

TR-EE 89-49
August 1989

**MODELING, SIMULATION, AND
ANALYSIS OF OPTICAL REMOTE
SENSING SYSTEMS**

**J. P. Kerekes
D. A. Landgrebe**

**School of Electrical Engineering
Purdue University
West Lafayette, Indiana 47907**

This research was supported in part by the National Science Foundation under Grant ECS 8507405 and National Aeronautics and Space Administration Grant NAGW-925.

TABLE OF CONTENTS

	Page
LIST OF TABLES.....	iv
LIST OF FIGURES.....	vi
LIST OF NOTATIONS.....	xii
ABSTRACT.....	xvii
CHAPTER 1 - INTRODUCTION.....	1
1.1 Background and Objective of the Investigation.....	1
1.2 Remote Sensing System Description.....	2
1.3 Related Work.....	8
1.4 Report Organization.....	10
CHAPTER 2 - REMOTE SENSING SYSTEM MODELING AND SIMULATION.....	11
2.1 Overview of System Model.....	11
2.2 Scene Models.....	13
2.2.1 Surface Reflectance Modeling.....	14
2.2.2 Solar and Atmospheric Modeling.....	25
2.3 Sensor Modeling.....	47
2.3.1 Sampling Effects.....	48
2.3.2 Electrical Noise Modeling.....	52
2.3.3 HIRIS Model.....	54
2.3.4 Radiometric Performance Measures.....	61
2.4 Processing.....	63
2.4.1 Radiometric Processing.....	65
2.4.2 Geometric Processing.....	65
2.4.3 Data Reduction.....	66
2.4.4 Class Separability Measures.....	67
2.4.5 Classification Algorithms.....	68
2.5 Summary and Discussion.....	69

	Page
CHAPTER 3 - ANALYTICAL SYSTEM MODEL.....	71
3.1 Model Overview	71
3.2 Analytical Expressions.....	73
3.2.1 Reflectance Statistics.....	73
3.2.2 Atmospheric Effects.....	74
3.2.3 Spatial Effects.....	75
3.2.4 Spectral Effects	77
3.2.5 Noise Model.....	78
3.2.6 Feature Selection	79
3.2.7 Error Estimation.....	79
3.3 Comparison Between the Analytical and Simulation Models.....	80
CHAPTER 4 - APPLICATION TO IMAGING SPECTROMETER SYSTEM ANALYSIS	83
4.1 Introduction	83
4.2 Radiometric Performance.....	84
4.3 Comparison of Simulation and Analytic Model Performance	99
4.4 System Parameter Studies.....	107
4.5 Interrelated Parameter Effects.....	123
4.6 Feature Selection Experiments.....	134
4.7 Summary and Conclusions	140
CHAPTER 5 - CONCLUSIONS AND SUGGESTIONS FOR FUTHER WORK.	143
LIST OF REFERENCES	147
APPENDICES	
Appendix A Expected Variance of a Two Dimensional Autoregressive Process.....	155
Appendix B Interpolation Algorithm.....	160
Appendix C LOWTRAN 7 Input File.....	162
Appendix D Sensor Descriptions.....	167
Appendix E Analytical System Model Program Listing	173

LIST OF TABLES

Table	Page
1.1 Simulation Studies.....	9
2.1 Typical Spatial Model Parameters	20
2.2 Spatial Correlation Coefficients for Hand County, South Dakota.....	21
2.3 Sequence in Generating a Simulated Surface Reflectance Array.....	24
2.4 Example LOWTRAN 7 Parameters.....	31
2.5 Diffuse Irradiance Constant Values.....	34
2.6 Default Values of Atmospheric Parameters.....	35
2.7 Data Set for Hand County, South Dakota, July 26, 1978.....	42
2.8 Description of Test Fields.....	43
2.9 Conversion Constants Between Radiance and Digital Counts	43
2.10 Scene Conditions at Time of Observations	44
2.11 LOWTRAN Settings for Experiment.....	44
2.12 Atmospheric Components for the Hand County Test Site	45
2.13 Comparison of Actual and Simulated Radiances (in mW/(cm ² -sr)) for Test Site in Hand County, SD	45
2.14 Sources and Types of Radiometric Errors	53
2.15 HIRIS Functional Parameters.....	54
2.16 Parameters of Detector Arrays in Terms of Electrons (e ⁻).....	59
2.17 Example Processing Functions.....	64

Table	Page
2.18 Summary of System Parameters Implemented in Simulation	70
3.1 System Factors Not Included In Analytical Model	80
4.1 Kansas Winter Wheat Data Set.....	84
4.2 Radiometric Study Baseline System Configuration.....	85
4.3 Radiometric Performance Parameters Studied and Their Variations.....	88
4.4 System Configuration for Comparison Test.....	100
4.5 Optimal Feature Set for Kansas Winter Wheat Data Set.....	102
4.6 Classification Accuracy of Base System Configuration.....	102
4.7 Increments Used in Ground Size Experiment.....	104
4.8 Classification Accuracies of Gaussian vs. Measured PSF	106
4.9 System Configuration for Parameter Studies.....	108
4.10 Parameters and Their Variation in Section 4.4.....	108
4.11 Summary Results for System Parameter Experiments.....	121
4.12 Parameter Interrelationship Studies	123
4.13 Wavelength Bands Combined for the Various Feature Sets.....	134
4.14 Classes and Fields Used to Compute Statistics for the Spring Wheat Test Scene.....	138
 Appendix Table	
D.1 MMS General Parameters	167
D.2 MMS Band and Noise Parameters.....	167
D.3 MSS General Parameters.....	169
D.4 MSS Band and Noise Parameters.....	169
D.5 TM General Parameters	171
D.6 TM Band and Noise Parameters.....	171

LIST OF FIGURES

Figure	Page
1.1 Remote Sensing System Pictorial Description	3
1.2 Noise Sources.....	6
1.3 Signal Sources	7
2.1 Remote Sensing System Model	12
2.2 Scene Model Block Diagram.....	13
2.3 Scene Geometry	15
2.4 Correlation Coefficients of Winter Wheat Field	22
2.5 Atmospheric Effects on Spectral Radiance Received by Sensor.....	27
2.6 Optical Thickness τ vs. Visibility	30
2.7 Optical Thickness vs. Wavelength.....	30
2.8 Ratio of Direct Irradiance to Total Irradiance vs. Total Optical Path Length.....	33
2.9 Effect of Meteorological Range on Direct Solar Spectral Irradiance	36
2.10 Effect of Solar Zenith Angle on Direct Solar Spectral Irradiance	36
2.11 Effect of Meteorological Range on Total Solar Spectral Irradiance	37
2.12 Effect of Solar Zenith Angle on Total Solar Spectral Irradiance	37
2.13 Effect of Meteorological Range on Diffuse Solar Spectral Irradiance	38
2.14 Effect of Solar Zenith Angle on Diffuse Solar Spectral Irradiance	38

Figure	Page
2.15 Effect of Meteorological Range on Spectral Transmittance.....	39
2.16 Effect of Sensor Zenith Angle on Spectral Transmittance	39
2.17 Effect of Meteorological Range on Path Spectral Radiance.....	40
2.18 Effect of Solar Zenith Angle on Path Spectral Radiance.....	40
2.19 Effect of Sensor Zenith Angle on Path Spectral Radiance	41
2.20 Effect of Surface Albedo on Path Spectral Radiance	41
2.21 Plot of Landsat vs. Simulated Radiances.....	46
2.22 Sensor System Components	47
2.23 Noise Model of Sensor.....	52
2.24 HIRIS Model Block Diagram.....	55
2.25 Spectral Transmittance of Optics.....	56
2.26 Normalized Spatial Response	57
2.27 Spectral Quantum Efficiency	58
2.28 Shot Noise vs. Signal Level.....	60
3.1 Analytical System Model Block Diagram	71
4.1 Mean and Variation of the Surface Reflectance of the Kansas Winter Wheat Data Set of Table 4.1.....	85
4.2 Mean and Variation of Image Vector as Received by HIRIS	86
4.3 Voltage and Power SNR for Typical Reflectance	87
4.4 $NE\Delta\rho$ for Typical Reflectance.....	87
4.5 SNR for Varying Meteorological Ranges	89
4.6 $NE\Delta\rho$ for Varying Meteorological Ranges	89
4.7 SNR for Varying Solar Angles.....	90
4.8 $NE\Delta\rho$ for Varying Solar Angles.....	90

Figure	Page
4.9 SNR for Varying View Angles.....	91
4.10 NE $\Delta\rho$ for Varying View Angles.....	91
4.11 SNR for Various Surface Albedoes.....	92
4.12 NE $\Delta\rho$ for Various Albedoes.....	92
4.13 SNR for Varying Factors of Shot Noise	93
4.14 NE $\Delta\rho$ for Varying Factors of Shot Noise	93
4.15 SNR for Varying Factors of Read Noise	94
4.16 NE $\Delta\rho$ for Varying Factors of Read Noise	94
4.17 SNR for Varying Radiometric Resolution	95
4.18 NE $\Delta\rho$ for Various Radiometric Resolutions	95
4.19 SNR for Various IMC Gain Settings	96
4.20 NE $\Delta\rho$ for Various IMC Gain Settings	96
4.21 SNR for Various Levels of Relative Calibration Error	97
4.22 NE $\Delta\rho$ for Various Levels of Relative Calibration Error	97
4.23 Simulated Image of Comparison Test Scene at $\lambda=1.70\ \mu\text{m}$	101
4.24 Classification Accuracy vs. Scene Spatial Correlation Coefficient.....	103
4.25 Classification Accuracy vs. Ground Size of Scene Cells.....	104
4.26 Classification Accuracy vs. Sensor View Angle.....	105
4.27 Classification Accuracy vs. Number of Training Samples	107
4.28 Effect of Spatial Correlation ($\rho=\rho_x=\rho_y$) on SNR.....	109
4.29 Effect of Spatial Correlation ($\rho=\rho_x=\rho_y$) on Classification Accuracy.....	109
4.30 Effect of Meteorological Range on SNR.....	110

Figure	Page
4.31 Effect of Meteorological Range on Classification Accuracy.....	110
4.32 Effect of Solar Zenith Angle on SNR.....	111
4.33 Effect of Solar Zenith Angle on Classification Accuracy.....	111
4.34 Effect of Sensor Zenith Angle on SNR.....	112
4.35 Effect of Sensor Zenith Angle on Classification Accuracy	112
4.36 Effect of Number of Scene Cells Within Sensor IFOV on SNR.....	113
4.37 Effect of Number of Scene Cells Within Sensor IFOV on Classification Accuracy	113
4.38 Effect of Shot Noise (Nominal = 1.0) on SNR.....	114
4.39 Effect of Shot Noise (Nominal = 1.0) on Classification Accuracy	114
4.40 Effect of Read Noise (Nominal = 1.0) on SNR.....	115
4.41 Effect of Read Noise (Nominal = 1.0) on Classification Accuracy	115
4.42 Effect of IMC Gain State on SNR	116
4.43 Effect of IMC Gain State on Classification Accuracy	116
4.44 Effect of Radiometric Resolution on SNR.....	117
4.45 Effect of Radiometric Resolution on Classification Accuracy.....	117
4.46 Effect of Relative Calibration Error on SNR	118
4.47 Effect of Relative Calibration Error on Classification Accuracy.....	118
4.48 Effect of Absolute Radiometric Error on SNR.....	119
4.49 Effect of Absolute Radiometric Error on Classification Accuracy.....	119
4.50 Effect of Number of Processing Features on SNR.....	120
4.51 Effect of Number of Processing Features on Classification Accuracy ...	120
4.52 Accuracy vs. Voltage SNR for System Parameter Experiments	122
4.53 Accuracy vs. Power SNR for System Parameter Experiments.....	122

Figure	Page
4.54 Effect of Meteorological Range and View Angle for $\theta_{\text{solar}}=0^\circ$	124
4.55 Effect of Meteorological Range and View Angle for $\theta_{\text{solar}}=30^\circ$	124
4.56 Effect of Meteorological Range and View Angle for $\theta_{\text{solar}}=60^\circ$	125
4.57 Effect of IFOV Size (in Scene Cells) and Spatial Correlation Coefficient	125
4.58 Effect of Meteorological Range and Shot Noise	126
4.59 Effect of Meteorological Range and Read Noise	126
4.60 Effect of Meteorological Range and IMC	127
4.61 Effect of Meteorological Range on Radiometric Resolution	127
4.62 Effect of Meteorological Range and Various Noise Sources Alone	128
4.63 Effect of Solar Angle and Shot Noise	128
4.64 Effect of View Angle and Shot Noise	129
4.65 Effect Solar Angle and IMC Gain State	129
4.66 Effect of View Angle and IMC Gain State	130
4.67 Effect of Meteorological Range and Number of Features	130
4.68 Effect of Solar Angle and Number of Features	131
4.69 Effect of Atmosphere With/Without Noise for Path Radiance Model With No Surface Reflectance Dependence	133
4.70 Voltage and Power SNR for the Various Feature Sets of Table 4.13	135
4.71 Classification Accuracy for the Various Feature Sets of Table 4.13	135
4.72 Feature Set Performance vs. Meteorological Range	136
4.73 Feature Set Performance vs. Solar Angle	137
4.74 Feature Set Performance vs. View Angle	137
4.75 SNR for Various Feature Sets and SW Variety Scene	139

Figure	Page
4.76 Classification Accuracy for Various Feature Sets and SW Variety Scene.....	139
Appendix	
Figure	
A.1 Quarter-Plane Image AR Model.....	156
D.1 MMS Spectral Response for Bands 1 through 5.....	168
D.2 MMS Spectral Response for Bands 6 through 10.....	168
D.3 MSS Spectral Response.....	170
D.4 MSS Spatial Response.....	170
D.5 TM Spectral Response	172
D.6 TM Spatial Response.....	172

LIST OF NOTATIONS

Symbols used for the various variables and parameters are defined below, along with the units where appropriate.

Symbol	Explanation (units)
A_x	Sum of $h_x(\bullet)$ coefficients
A_y	Sum of $h_y(\bullet)$ coefficients
a_{mn}, b_{mn}	Spatial model parameters for wavelengths m and n
B	Sensor spectral response matrix used in analytical model
B_{kl}	Bhattacharyya distance between classes k and l
$B(\lambda)$	Conversion factor relating the incident spectral radiance to the signal level in the sensor detectors
$B^+(\lambda)$	Product of the spectral radiance from a completely reflecting surface and the conversion to the signal level in the detectors
C_i	AR model spatial parameters
D	Fractal dimension
$d(i,j,l)$	Image level at pixel (i,j) for sensor band l
E_R	Absolute radiometric error level
$E_{\lambda, \text{Diffuse}}$	Diffuse solar spectral irradiance incident on Earth's surface ($\text{mW}/\text{cm}^2\text{-}\mu\text{m}$)
$E_{\lambda, \text{Direct}}$	Direct solar spectral irradiance incident on Earth's surface ($\text{mW}/\text{cm}^2\text{-}\mu\text{m}$)

$E_{\lambda,Exo}$	Exoatmospheric solar spectral irradiance incident on Earth's surface ($mW/cm^2-\mu m$)
$E_{\lambda,Total}$	Total (direct plus diffuse) solar spectral irradiance incident on Earth's surface ($mW/cm^2-\mu m$)
F	Band selection matrix for spectral compression
F	Full scale electron level in HIRIS model
G_x	Ground size of scene cell across scene (meters)
G_y	Ground size of scene cell down scene (meters)
$g_k(i,j)$	Value of discriminant function for class k at pixel (i,j)
g_x	Ground size of PSF step across scene (meters)
g_y	Ground size of PSF step down scene (meters)
H	Altitude of sensor (meters)
$h(u,v)$	2-dimensional point spread function of sensor
$h_x(\bullet)$	Across track line spread function
$h_y(\bullet)$	Down scene line spread function
J_F	Multiclass distance measure
K	Number of land cover classes in scene
L	Number of spectral bands in sensor
$L_{Full,l}$	Full scale radiance for sensor band l (mW/cm^2-sr)
$L_{\lambda,Scene}(\bullet)$	Scene spectral radiance (mW/cm^2-sr)
$L_{\lambda,Sensor}(x,y)$	Spectral radiance incident on sensor from scene location (x,y) ($mW/cm^2-\mu m-sr$)
$L_{\lambda,Path}$	Path spectral radiance incident on sensor ($mW/cm^2-\mu m-sr$)
$L_{\lambda,Path}^1$	Path spectral radiance with albedo = 1 ($mW/cm^2-\mu m-sr$)

$L_{\lambda,Path}^0$	Path spectral radiance with albedo = 0 (mW/cm ² -μm-sr)
$L_{\lambda,Path}^{1-0}$	Path spectral radiance difference for albedoes 0 and 1 (mW/cm ² -μm-sr)
M	Dimension of high resolution spectral reflectance vectors
N(l)	Spectral bandwidth normalizing factor for sensor band l
$n_1(\bullet), n_2(\bullet)$	Zero mean, unit variance Gaussian random numbers
O	Number of coefficients in across scene spatial response
P	Number of coefficients in down scene spatial response
\hat{P}_c	Estimate of classification accuracy
P_k	Apriori probability of class k
Q	Number of radiometric bits of sensor
$r(x,y)$	Surface scalar reflectance array
$r_{o,x}, r_{o,y}$	Radius of spatial response in analytical model
S	Received signal in detectors
S'	Received signal plus dark current in detectors
S''	Received signal plus noise and calibration error in detectors
S_b	L x L between class scatter matrix
S_k	L x L covariance matrix of image for class k
S_w	L x L within class scatter matrix
S_x	Across track ground sampling interval (meters)
S_y	Down scene ground sampling interval (meters)
$s_l(m)$	Spectral response of sensor
$T_{\lambda,Atm}$	Spectral transmissivity of atmosphere

V_{η}	Atmospheric surface meteorological range (Kilometers)
W_s	Spatial weighting function in sensor model
X_A	Adjacent surface reflectance
X_k	Surface reflectance vector for class k
\bar{Z}_k	Mean image or feature vector for class k
$z(\bullet)$	Zero mean, unit variance Gaussian random numbers
β	Volume extinction coefficient (Km^{-1})
$\Delta\lambda$	Spectral resolution of scene (μm)
ΔU	Angular distance between $h_x(\bullet)$ coefficients (radians)
ΔV	Angular distance between $h_y(\bullet)$ coefficients (radians)
ΔW	Across track sampling interval (radians)
ΔZ	Down scene sampling interval (radians)
Φ_k	$M \times M$ eigenvector matrix of spectral reflectance covariance matrix for class k
ϕ_{solar}	Azimuthal angle of solar illumination (degrees)
ϕ_{view}	Azimuthal angle of view (degrees)
Λ_k	$M \times M$ diagonal eigenvalue matrix of spectral reflectance covariance matrix for class k
Λ_{cal}	$L \times L$ diagonal matrix of relative calibration error variances
Λ_{quant}	$L \times L$ diagonal matrix of quantization noise variances
Λ_{read}	$L \times L$ diagonal matrix of read noise variances

Λ_{shot}	L x L diagonal matrix of shot noise variances
Λ_{therm}	L x L diagonal matrix of thermal noise variances
λ	Wavelength (μm)
\bar{P}_k	M x 1 mean vector of spectral reflectance for class k
$P(x,y)$	M x 1 vector of spectral reflectance of surface at location (x,y)
ρ_x, ρ_y	Spatial autocorrelation coefficients
Σ_A	Covariance matrix of average spectral reflectance
Σ_k	Covariance matrix of spectral reflectance or image features for class k
$\sigma_c(l)$	Calibration error standard deviation for sensor band l
$\sigma_s(l)$	Shot noise standard deviation for sensor band l
$\sigma_t(l)$	Thermal noise standard deviation for sensor band l
σ_u	Standard deviation of driving process for AR model
τ_λ	Spectral optical thickness of atmosphere
$\tau_{p,\lambda}$	Spectral optical path length
θ_{solar}	Zenith angle of solar illumination (degrees)
θ_{view}	Zenith viewing angle (degrees)

ABSTRACT

Kerekes, John Paul. Ph.D., Purdue University, August 1989. Modeling, Simulation, and Analysis of Optical Remote Sensing Systems. Major Professor: David A. Landgrebe.

Remote Sensing of the Earth's resources from space-based sensors has evolved in the past twenty years from a scientific experiment to a commonly used technological tool. The scientific applications and engineering aspects of remote sensing systems have been studied extensively. However, most of these studies have been aimed at understanding individual aspects of the remote sensing process while relatively few have studied their interrelations.

A motivation for studying these interrelationships has arisen with the advent of highly sophisticated configurable sensors as part of the Earth Observing System (EOS) proposed by NASA for the 1990's. These instruments represent a tremendous advance in sensor technology with data gathered in nearly 200 spectral bands, and with the ability for scientists to specify many observational parameters. It will be increasingly necessary for users of remote sensing systems to understand the tradeoffs and interrelationships of system parameters.

In this report, two approaches to investigating remote sensing systems are developed. In one approach, detailed models of the scene, the sensor, and the processing aspects of the system are implemented in a discrete simulation. This approach is useful in creating simulated images with desired characteristics for use in sensor or processing algorithm development.

A less complete, but computationally simpler method based on a parametric model of the system is also developed. In this analytical model the various informational classes are parameterized by their spectral mean vector and covariance matrix. These class statistics are modified by models for the atmosphere, the sensor, and processing algorithms and an estimate made of the resulting classification accuracy among the informational classes.

Application of these models is made to the study of the proposed High Resolution Imaging Spectrometer (HIRIS). The interrelationships among observational conditions, sensor effects, and processing choices are investigated with several interesting results.

Reduced classification accuracy in hazy atmospheres is seen to be due not only to sensor noise, but also to the increased path radiance scattered from the surface.

The effect of the atmosphere is also seen in its relationship to view angle. In clear atmospheres, increasing the zenith view angle is seen to result in an increase in classification accuracy due to the reduced scene variation as the ground size of image pixels is increased. However, in hazy atmospheres the reduced transmittance and increased path radiance counter this effect and result in decreased accuracy with increasing view angle.

The relationship between the Signal-to-Noise Ratio (SNR) and classification accuracy is seen to depend in a complex manner on spatial parameters and feature selection. Higher SNR values are seen to not always result in higher accuracies, and even in cases of low SNR feature sets chosen appropriately can lead to high accuracies.

CHAPTER 1

INTRODUCTION

1.1 Background and Objective of the Investigation

Remote sensing is defined (Swain and Davis, 1978) as "...the science of deriving information about an object from measurements made at a distance from the object, i.e., without actually coming in contact with it." In the context of observing the Earth, the sensing instruments have evolved from cameras tethered to balloons, aerial multispectral scanners, to satellite-borne imaging arrays. Applications have been many, and remote sensing of the Earth for land resource analysis has developed into a common and useful technological tool.

Countless projects have used remotely sensed data to assess crop production (MacDonald and Hall, 1978), crop disease (MacDonald, et al., 1972), urban growth (Jensen, 1981), and wetland acreage (Carter and Schubert, 1974) as a few examples. The technology of remote sensing has been studied extensively and is well documented in texts by Swain and Davis (1978), Colwell (1983), Richards (1986), and Asrar (1989).

While the various aspects of the remote sensing process have been well documented, the interrelationships among these process components have been studied comparatively little, especially in regard to sources of error or noise in the process. Landgrebe and Malaret (1986) looked at the effect of sensor noise on classification error in one of the few studies of this type, but there are many more parameters and effects that interrelate.

A motivation for studying these interrelationships has arisen with the forthcoming deployment of configurable sensors. As part of the Earth Observing System (EOS) program of the 1990's, several instruments will allow the

capability for a scientist to specify the observational conditions under which data are to be collected. It will become increasingly important to develop an understanding of how various parameters affect the collection of data and the resulting ability to extract the desired information.

The objectives of this report are to further this understanding of the remote sensing process through the following efforts:

- Document and model the remote sensing process from an overall systems perspective.
- Develop tools based on these models to allow the study of the interrelationships of system parameters.
- Investigate these interrelationships through the application of these tools to a variety of system configurations.

In this initial chapter, the concept of a remote sensing system is defined and described. Previous methods of studying the remote sensing process as a system are reviewed and commented upon. A description of the report organization then concludes the chapter.

1.2 Remote Sensing System Description

In this research, the term remote sensing will be used in the context of satellite- or aircraft-based imaging sensors that produce a digital image of the surface of the Earth below for land cover or Earth resource analysis. The imaging sensor will cover only the reflective portion of the optical spectrum with wavelengths approximately from 0.4 μm to 2.4 μm . This context includes many of the current and near future remote sensing instruments such as Landsat MSS and TM, SPOT, and HIRIS. The land use application of the imagery represents a significant application of the technology.

A pictorial description of a remote sensing system is given in Figure 1.1. This figure gives an overall view of the remote sensing process starting with the illumination provided by the sun. This incoming radiance passes through the atmosphere before being reflected from the Earth's surface in a manner indicative of the surface material. The reflected light then passes again through the atmosphere before entering the input aperture of the sensing instrument.

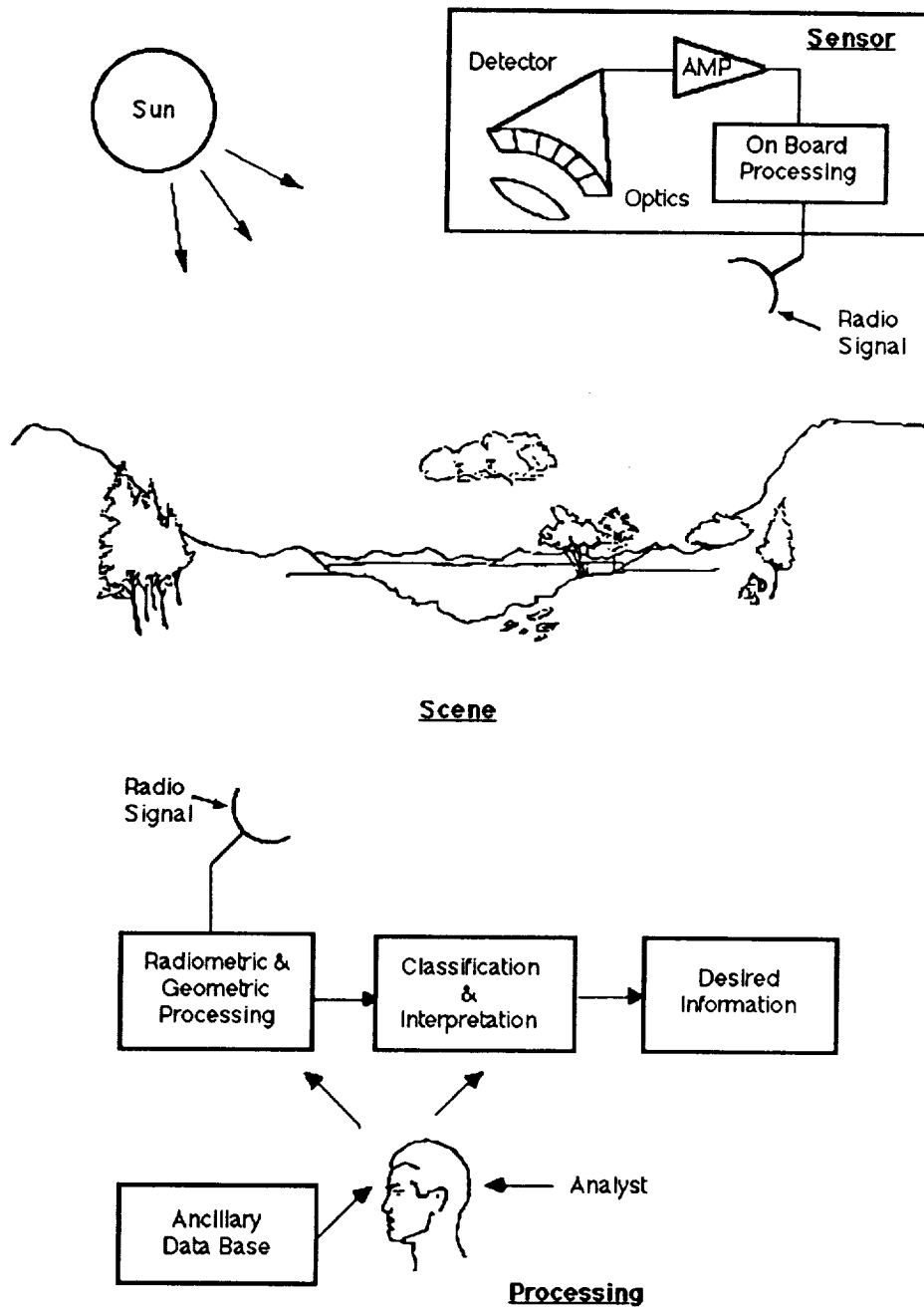


Figure 1.1 Remote Sensing System Pictorial Description.

At the sensor, the incoming optical energy is sampled spatially and spectrally in the process of being converted to an electrical signal. This signal is then amplified and quantized into discrete levels producing a multispectral scene characterization that is then transmitted to the processing facility.

At the processing stage, geometric registration and calibration may be performed on the image in order to be able to compare the data to other data sets. Feature extraction may also be performed to reduce the dimensionality of the data and to increase the separability of the various informational classes in the image. Lastly, the image undergoes a classification and interpretation stage, most often done with a computer under the supervision of a trained analyst using ancillary information about the scene.

The entire remote sensing process can be viewed as a system whose inputs include a vast variety of sources and forms. Everything from the position of the sun in the sky, the quality of the atmosphere, the spectral and spatial responses of the sensor, to the training fields selected by the analyst, etc., will influence the state of the system. The output of such a system is generally a spatial map assigning each discrete location in the scene to an appropriate land information class. Other outputs may be the amount of area covered by each class in the scene or the classification accuracy between the resulting classified map and the known ground truth of the scene.

In using this definition of a remote sensing system, it must be realized that it is a representation of the real world, and as such cannot be complete in characterizing all the inputs, states, or outputs. In this research, the problem is constrained by defining the system as well as one is able to do. It is an accepted fact that the system description will be incomplete and lacking; however, the model developed will represent the best that can be done from the current knowledge base and can be used as a starting point to increase system understanding.

To more fully describe a remote sensing system, it is helpful to begin to break the system down with natural boundaries between the various component systems. In Figure 1.1 we can readily see the system as being

comprised of three major subsystems: the scene, the sensor, and the processing subsystems. This division helps in providing structure to the system and facilitates identification of various components of the system.

The scene consists of all spectral and spatial sources and variations that contribute to the spectral radiance present at the input to the sensor. The sensor includes all spatial, spectral, and electrical effects of transforming the incident spectral radiance into a spatially and spectrally sampled discrete image. The processing subsystem consists of all possible forms of processing applied to the image to obtain the desired information.

Within this scene, sensor, and processing structure it is possible to further decompose these subsystems into major components and variations. As with all systems, there are components that represent desired, or signal, states or variations, and there are those that represent undesired, or noise, states or variations. Figure 1.2 shows a taxonomy of components and effects that can degrade the system. This structure is further described in Kerekes and Landgrebe (1987), and has grown out of the work reported by Anuta (1970). Likewise, a comparable taxonomy may be developed for signal, or desired, variations and states that contribute to the output of the system. Figure 1.3 is a signal taxonomy of such effects.

These taxonomies offer a framework in which remote sensing system effects can be grouped and located. The categories under the main subsystems delineate sources of major contributions to the system state. In some cases, effects or sources are listed in both signal and noise structures. These dual listings exemplify one of the major problems in understanding remote sensing systems. Depending on what type of information is desired, sources or effects may indeed represent both noise and signal effects.

After the system has been broken down into identifiable portions, one can take these blocks and build them back up into an overall system model. Through the synergism possible from this combination of models and their application the overall understanding of the entire process can be improved.

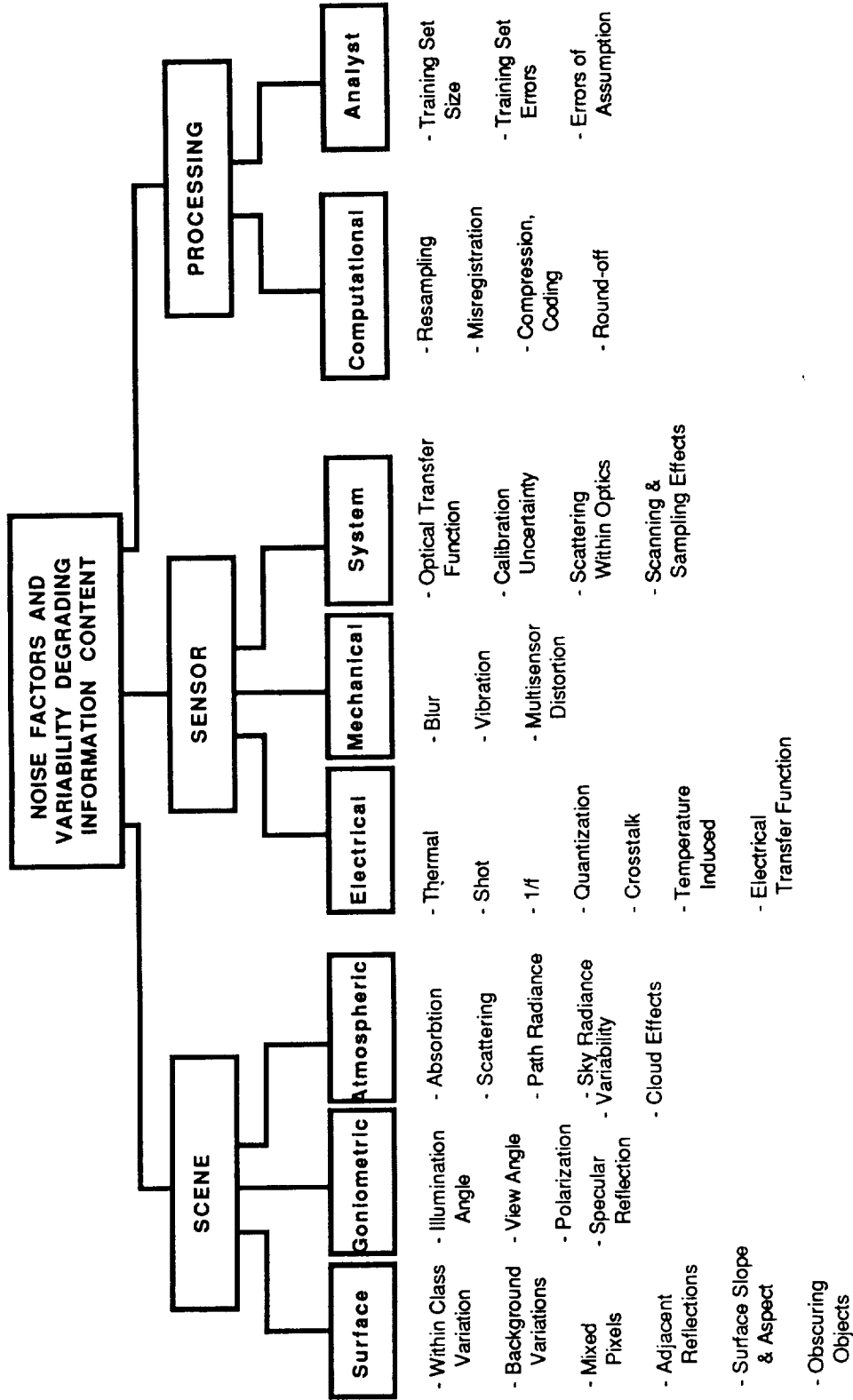


Figure 1.2 Noise Sources.

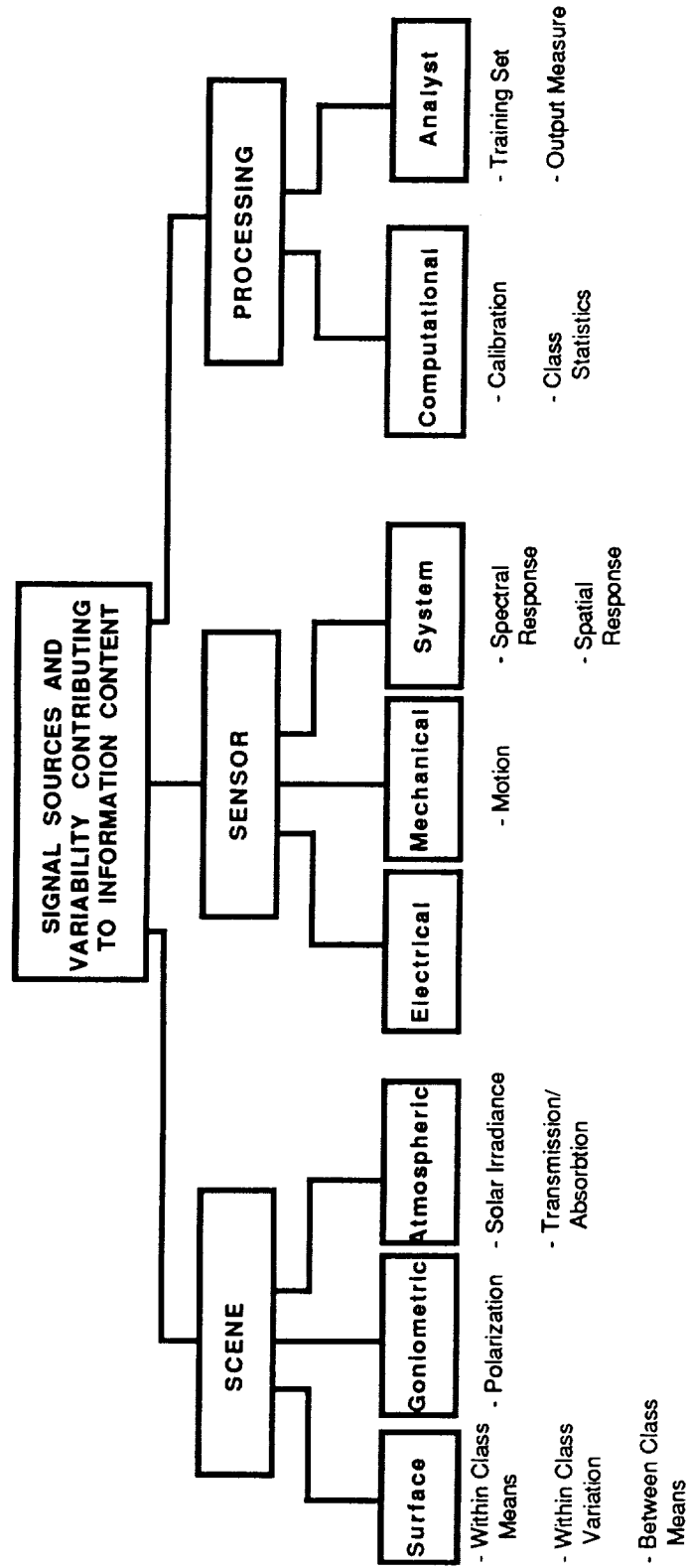


Figure 1.3 Signal Sources.

1.3 Related Work

The systems approach to the remote sensing process has been of interest for many years. In a tutorial paper by Landgrebe (1971), the differences between image based (photogrammetry) and numerically oriented remote sensing systems were described. The important factors to consider from an information point of view were delineated and described. The work described there helped to shape the ideas that are implemented in this research.

There have been many previous optical system simulation studies reported in the literature, including those done in the context of civilian remote sensing and those in a military context. Table 1.1 provides an overview of such studies including the reference and key characteristics of each.

Those studies fall into one of three categories: Landsat TM sensor parameter studies, basic parameter studies, and military studies. The Landsat TM sensor parameter studies were performed in preparation and analysis of the performance of Landsat-D Thematic Mapper. The basic parameter studies are ones that are most closely related to what the research in this report considers. They represent studies showing the tradeoffs of various system parameters and their effects on some output measure, usually classification error. A few military system studies are included to represent the unclassified literature in optical system simulation.

The combination of several characteristics of the research presented in this report distinguishes it from these previous studies. It presents a sophisticated framework in which detailed models of the various components of the system may be implemented. Flexibility has been built in to allow for expansion and growth. High spectral resolution has been used throughout the model in simulating the next generation of imaging spectrometers. Models from the scene, the sensor, and the processing portions have been integrated to create the ability to study cross system parameter interrelationship effects on the classification and noise performance. All of these features together make it an unique contribution to remote sensing science.

Table 1.1. Simulation Studies.

	Author	Type of Data	Primary Focus	State Space	Performance Measure
TM Studies	Landgrebe, Biehl, & Simmons (1977)	Aircraft	Sensor Noise, Spatial Resolution & Bands	Digital Image	ML & ECHO Classifiers
	Clark & Bryant (1982)	Aircraft	Spatial Resolution	Digital Image	ML Classifier
	Markham & Townshend (1981)	Aircraft	Spatial Resolution	Digital Image	ML Classifier
	Badhwar, et al (1982)	Field Spectrometer	TM vs. MSS	Digital Image	Clustering
	Toll (1985)	Landsat MSS & TM	Spatial, Spectral, & Quantization Effects	Digital Image	ML Classifier
Basic Parameter Studies	Billingsley (1982)	Deterministic Signature	Misregistration	Class Variances	Boxcar Classifier
	Maxwell (1976)	Landsat MSS	Noise Reduction	Transformed Data	ML Classifier
	Kaufman & Fraser (1984)	Laboratory Spectra	Atmosphere	Digital Image	Minimum Distance
	Pont (1982)	Spectral Model	MSS PSF & Scene Noise	Greeness/Brightness	Greeness/Brightness
	Huck, et al (1984)	Laboratory Spectra	Spectral Bands	Spectral Means & Covariances	ML & MSD Classifiers
	Mobasserri (1978)	Aircraft	Sensor Spatial Model	Spectral Means & Covariances	Bayes Multiclass
	Malaret (1982)	Aircraft	Sensor Noise	Spectral Means & Covariances	$\text{erfc}[\sqrt{2}u]$
	Mailia, Gleason, & Cicone (1977)	Reflectance Model	Atmosphere & Sensor Effects	Radiance Levels	Digital Image
	Lewis & Horgen (1979)	Radiance Model	Targetting	Voltage	Probability of Detection
	Pau & El Nahas (1983)	Radiance Model	Military System Simulation	Voltage	Target Identification
Military	Peters (1982)	Radiance Model	Time Delay	Detector Voltage	Time Delay

1.4 Report Organization

In this chapter, the objectives of the research were stated as being to document, model, and investigate the effects of various remote sensing system parameters on system performance. Also, the concept of a remote sensing system was defined. Chapter two discusses models and algorithms useful in simulating the remote sensing system process. Chapter three presents an alternative system model based on a parametric description of the system state, using analytical equations to describe the effect of the various system components. Chapter four presents results of applying these models to various system configurations based on an imaging spectrometer and studying the effect of system parameters on noise and classification performance. Chapter five concludes the report by discussing the results of these studies and possible future extensions of the work.

CHAPTER 2

REMOTE SENSING SYSTEM MODELING AND SIMULATION

2.1 Overview of System Model

In the modeling of a complex process, the goal is often to represent the process faithfully while reducing the complexity of the description. In the development of a model, we observe the process, take data measurements, and formulate an abstraction from these observations and data. This model then describes the process under varying conditions without having actually to duplicate it. Thus, the model serves as a documentation of our understanding of the process, as well as a tool useful in gaining insight into its operation. The models presented in this chapter serve both of these purposes.

The modeling of a system may be done at many levels of abstraction. The lowest level is the system itself. However this represents little knowledge of the system and is often impractical to use in studying its operation. The next level is with the use of detailed models of system components and simulation of the system operation. This chapter discusses component models useful in such a simulation. A still higher abstraction is a parametric and analytic description of the system. Chapter three presents a system model based on this type of a description.

The modeling of an optical remote sensing system is challenging because of its complexity. However, through the use of the taxonomies **developed** in the previous chapter this can be reduced to a **manageable task**. In chapter one the remote sensing process is described as a system and further divided into three subsystems: the scene, the sensor, and the processing subsystems. Figure 2.1 shows this division in the context of a system model that is described in this chapter for the simulation of the remote sensing process.

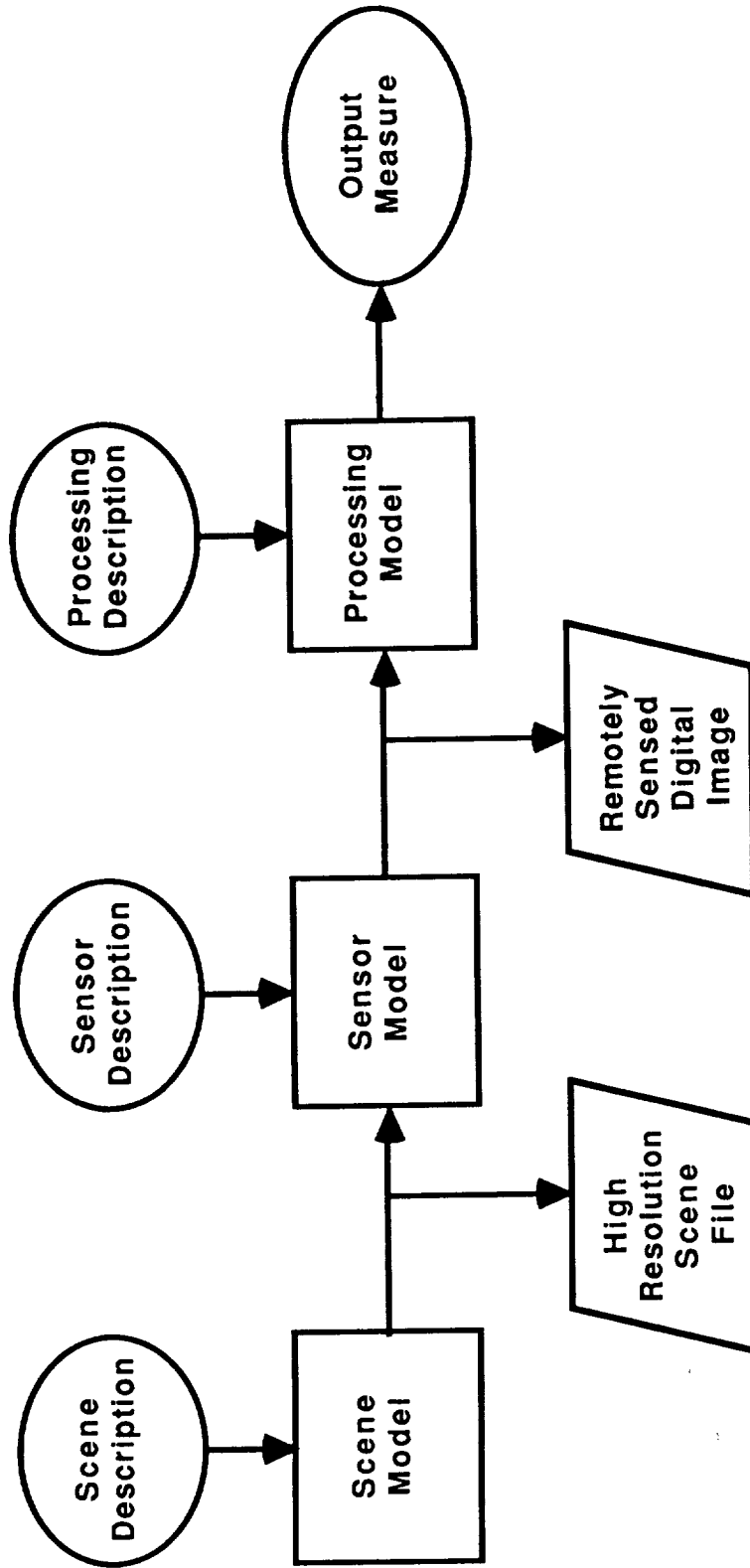


Figure 2.1 Remote Sensing System Model.

The following sections detail the models used for the scene, the sensor, and the processing subsystems. In each section various approaches to modeling or describing the processes involved are discussed. Section 2.2 discusses considerations in modeling the surface reflectance and the atmospheric effects and presents the model used in this report for simulating the scene. Section 2.3 describes the effects on the scene radiance introduced by the sensor, in both the remote sensing process and the simulation. Section 2.4 discusses approaches to extracting information from a multispectral image, as well as describing the options available in the simulation. Section 2.5 summarizes the models presented in this chapter.

2.2 Scene Models

The scene subsystem is by far the most complex, varied, and unknown of the remote sensing process. It is understood that no model can accurately represent all of the complex variations that make up the spectral radiance present at the input of the sensor. However, through the use of various simplifying assumptions, developing such a model becomes a reasonable task. In this section, approaches to modeling the scene are discussed.

From the taxonomies of chapter one, the scene is seen to consist of the solar illumination and atmospheric effects, the surface reflectance, and the goniometric effects due to the angles of illumination and view. In developing a model for the scene, models for the solar illumination and atmosphere, along with the surface reflectance are used, while the goniometric effects are embedded within the relationships between these two components. Figure 2.2 presents a block diagram of the basic scene model structure.

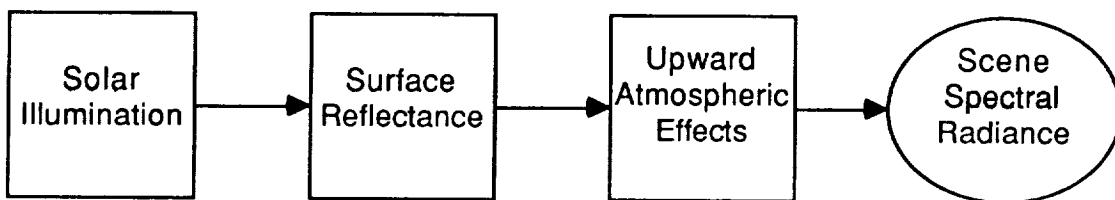


Figure 2.2 Scene Model Block Diagram.

To further describe the modeling of the scene, the rest of this section is divided into two parts. Section 2.2.1 discusses modeling of the surface in general terms, as well as describing in detail a model used to simulate the surface reflectance. Section 2.2.2 then discusses the solar illumination and the atmospheric effects present in optical remote sensing systems and their simulation implementation.

2.2.1 Surface Reflectance Modeling

In this section various methods of representing the reflectance of the surface are presented. The discussion begins with the most general way of describing this reflectance, followed by approaches using deterministic canopy models, and then concludes with models developed from the statistics of field reflectances. The model chosen for implementation in the simulation is then discussed.

The most general measurement of the reflectance of a surface is given by the Spectral Bidirectional Reflectance Distribution Function (SBRDF). This function is defined (chapter two of Swain and Davis, 1978) as in equation 2.1.

$$\rho_{\lambda}(\theta_{\text{solar}}, \phi_{\text{solar}}, \theta_{\text{view}}, \phi_{\text{view}}) = \frac{dL_{\lambda}(\theta_{\text{view}}, \phi_{\text{view}})}{dE_{\lambda}(\theta_{\text{solar}}, \phi_{\text{solar}})} \text{ sr}^{-1} \quad (2.1)$$

Here, $L_{\lambda}(\theta_{\text{view}}, \phi_{\text{view}})$ is the reflected spectral radiance observed at angles $\theta_{\text{view}}, \phi_{\text{view}}$, and $E_{\lambda}(\theta_{\text{solar}}, \phi_{\text{solar}})$ is the incident spectral irradiance at angles $\theta_{\text{solar}}, \phi_{\text{solar}}$. The geometry used here and in the rest of the report is shown in Figure 2.3.

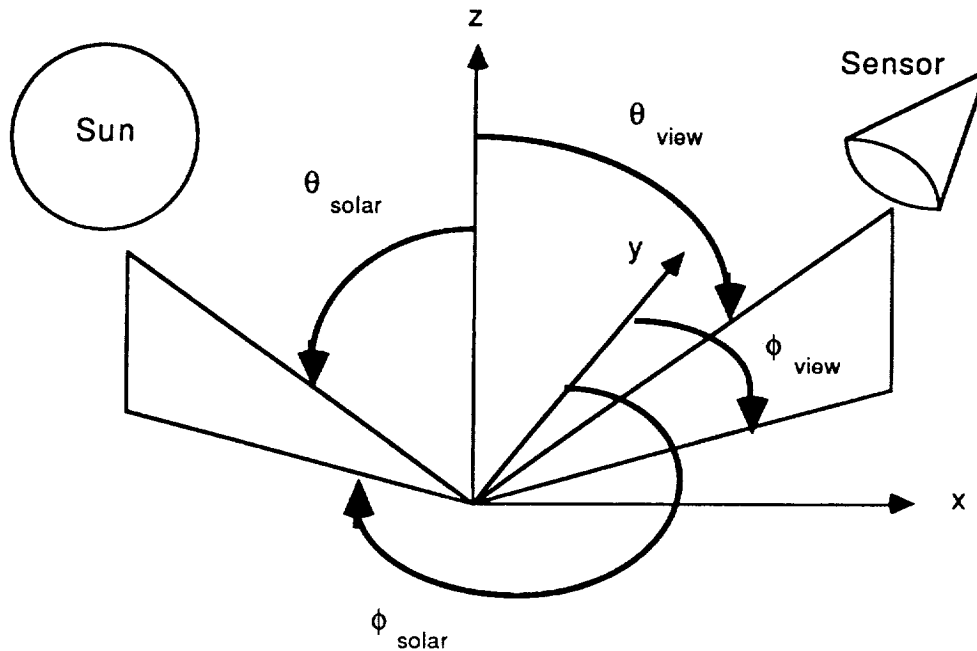


Figure 2.3 Scene Geometry.

The quantities θ_{solar} and θ_{view} are the zenith angles as measured from local vertical, while ϕ_{solar} and ϕ_{view} are the azimuthal angles as measured from North on a map.

The SBRDF gives the reflectance of an object from all angles of incidence and view and thus is the most complete representation of the surface reflectance. However, the accurate measurement of the SBRDF is a difficult task and few studies have been made.

A problem in obtaining the SBRDF arises due to spatial considerations. Typically, in remote sensing applications the scene is sampled spatially across two dimensions at some surface cell size G_x by G_y . A rectangular coordinate system is overlaid and an aggregate reflectance is obtained over each individual cell at spatial location (x,y) . An aggregate SBRDF is then a function of not only the geometry involved, but also the surface resolution cell size, the location in the scene, and the various materials contained within the cell.

$$\text{Aggregate SBRDF} = \rho_{\lambda,ag}(G_x, G_y, x, y, \theta_{solar}, \phi_{solar}, \theta_{view}, \phi_{view}) \quad (2.2)$$

Since the surface cell size G_x by G_y may be a number of meters square in typical remote sensing data sets, the measurement of the aggregate SBRDF on the surface is very inconvenient. Shibayma and Wiegand (1985) and Irons, Ranson, and Daughtry (1988) have reported some measurements of this type, but for limited crop species and over few wavelength intervals.

Thus, while the use of the measured SBRDF is the most complete way of representing the reflectance of the surface, it is impractical to use because of the difficulty in obtaining complete data for various cover types.

Strahler, Woodcock, and Smith (1986) discussed modeling of the scene for land resource remote sensing applications and divided surface models into two types: deterministic canopy models and stochastic image processing models. The term canopy comes about because these models attempt to calculate the SBRDF of vegetation by using radiative transport theory. Differential equations are used to compute the reflectance/transmittance of the several layers of leaves in a vegetative canopy.

Some examples of canopy models are the AGR model (Allen, Gayle, and Richardson 1970), the Suits model (Suits 1972a) with extensions for azimuthal (Suits 1972b) and row effects (Suits 1982), the SAIL model (Verhoef 1984), and the models by Park and Deering (1982), Cooper, Smith and Pitts (1982), and Kimes and Kirchner (1982). All of these models are based upon having precise knowledge of the reflectance, transmittance, and orientation of the leaves in each layer of the canopy. A model that used probability distributions in describing the orientations of the layers was described in Smith and Oliver (1974).

All of these canopy models, however, only consider the reflectance within a single surface cell, assuming the entire area covered by a particular surface type is homogeneous and with no regard to the spatial variability typical of almost all remotely sensed scenes. While they are capable of accurately modeling the SBRDF of a particular surface material, their lack of spatial

information limits their applicability for the type of system study undertaken in this research. However, it certainly would be conceivable, if one had the appropriate data, to extend a canopy model to be able to contain spatial information and develop a very accurate surface reflectance model. Unfortunately, this type of detailed database does not exist at the present time.

Image processing models, on the other hand, are not concerned with the reflectance structure within a scene resolution cell, but rather how the reflectances vary spatially and spectrally from cell to cell. In these models, the spectral reflectances of a surface area are taken to be multidimensional (across the spectral domain) random vectors with spectral and spatial correlation. While these models are usually developed from imagery that represent the radiance over an area, it can be assumed that the reflectances of the surface cells vary similarly in the spatial sense as do the image pixels. Also, the reflectance within each cell is assumed to be independent of illumination or viewing angle. This is known as Lambertian reflectance (Swain and Davis, 1978).

In the use of image processing models for the surface reflectance two assumptions are generally made about the spectral and spatial variation in the scene. The multispectral reflectance vectors are usually assumed to be samples from an M-dimensional multivariate normal (or Gaussian) probability distribution function. The form of this distribution is shown in equation 2.3.

$$p(x_1, x_2, \dots, x_M) = \frac{1}{(\sqrt{2\pi})^M (\sqrt{|\Sigma|})} \exp\left\{-\frac{1}{2}(X-\bar{X})^T \Sigma^{-1} (X-\bar{X})\right\} \quad (2.3)$$

Here, $X = \{x_1, x_2, \dots, x_M\}^T$ data vector, \bar{X} is the mean vector, and Σ is the covariance matrix.

The work that is often cited in justifying this assumption is that of Crane, Malila, and Richardson (1972). They worked with 12 band MSS data that was transformed to its principle component space and reduced to three bands.

Since the transformation produces uncorrelated variables, they tested each of the three bands for goodness-of-fit to Gaussian random variables. While the results showed a fairly good fit to the univariate Gaussian model, they ignored the fact that just because these random variables were Gaussian, that did not mean that the original 12 dimensional random vectors were multivariate Gaussian. This comes about because of the fact that combining Gaussian random variables into a vector does not necessarily result in jointly Gaussian random vectors. A much better test would be to use the procedures discussed in Koziol (1983) or Smith and Jain (1988) to check for multivariate normality.

Some early work done at LARS found the Gaussian assumption not to hold under the Chi-Square goodness-of-fit test. Members of the LARS Staff (1969) found that the Gaussian assumption did not hold for several multispectral data sets gathered from an airborne scanner. The results of this study may have been affected by the particular data they considered, or even the histogram cell interval used in the distribution test.

Nevertheless, the Gaussian assumption results in much simpler methods of generating and analyzing the data than those based upon more accurate, yet computational complex models.

Remotely sensed images have also been shown to have a pixel to pixel spatial correlation. Kettig (1975) used this fact in development of the ECHO spatial classifier. Also, Mobasseri (1978) developed a multispectral spatial model that was a separable (across and down scene) exponential model. This spatial model used by Mobasseri is specified by its spatial autocorrelation function $R_{mm}(\tau, \eta)$ for the scene reflectance r_m as given in equation 2.4.

$$E \{ r_m(x+\tau, y+\eta) r_m(x, y) \} = R_{mm}(\tau, \eta) = e^{-a_m |\tau|} e^{-b_m |\eta|} \quad (2.4)$$

Here, a_m and b_m are the across scene and down scene correlation parameters for wavelength m , and τ and η are the respective scene cell lag values. The coordinates (x, y) are the scene cell location.

Equation 2.4 may also be written in terms of the autocorrelation coefficients, $\rho_x = e^{-a}$ and $\rho_y = e^{-b}$, as in equation 2.5.

$$R_{mm}(\tau, \eta) = \rho_{m,x}^{-|\tau|} \rho_{m,y}^{-|\eta|} \quad (2.5)$$

This form of autocorrelation for a random field is equivalent to that of a wide-sense Markov random field with the neighbor set consisting of the quarter-plane causal neighbors, $\{(0,-1), (-1,0), (-1,-1)\}$ (chapter seven of Rosenfeld and Kak, 1982). This is also equivalent to a two-dimensional autoregressive (AR) model (Delp, et al., 1979) as given by equation 2.6.

$$r(x,y) = C_1 r(x-1,y) + C_2 r(x,y-1) + C_3 r(x-1,y-1) + \sigma_u z(x,y) \quad (2.6)$$

Here,

x, y - high resolution spatial column, row index in scene

$C_1 = \rho_x$

$C_2 = \rho_y$

$C_3 = -\rho_x \rho_y$

σ_u - standard deviation of Gaussian driving process, computed to retain unit variance for r (See algorithm given in Appendix A)

$z(x,y)$ - independent Gaussian random numbers with unit variance and zero mean.

Given arbitrary initial conditions, the AR model can easily generate a reflectance array with the desired spatial correlation. Other methods also exist to generate a random field with the spatial model of equation 2.4. Mobasseri (1978) used a Fourier-based technique, and Chellappa (1981) studied methods of generating spatially correlated arrays using arbitrary neighborhoods.

Using the Least Squared Error (LSE) estimation technique for the AR coefficients as described in Delp, et al., (1979) some typical coefficients for the AR model were calculated. Table 2.1 shows these typical values of the spatial parameters for a variety of scene types, computed from a line scanner image of an infrared band.

Table 2.1 Typical Spatial Model Parameters.

Full cover vegetation	$C_1=0.63$	$C_2=0.55$	$C_3= -0.35$
Just emergent row crops	$C_1=0.63$	$C_2=0.70$	$C_3= -0.44$
Bare soil field	$C_1=0.57$	$C_2=0.72$	$C_3= -0.41$

A problem with using line scanner imagery to compute the spatial statistics is that there is correlation introduced by the instrument itself, and as a result, computing the statistics from the image data does not truly represent the correlation of the original scene. This is difficult to prevent, as with any imaging sensor this effect will be present. It is known, however, (Papoulis, 1984) that the output correlation is greater than the input correlation for a linear system with the response similar to imaging systems. Thus, one can reasonably assume that the actual pixel to pixel correlation of the original scene was slightly less than that which was computed from the imagery.

An alternative method of gathering data to estimate spatial correlation is to use an instrument such as the Field Spectrometer System (FSS) described in Hixson, et al., (1978). With this instrument, spectral reflectance measurements were made with a spectral resolution of approximately 20 nm, and a ground field of view of approximately 25 meters. The instrument was mounted in a helicopter and flown over fields at a height of approximately 60 meters. The instrument made spectral radiance measurements that were converted into reflectance by comparison to the radiance measured over a known calibration panel. The report by Biehl, et al., (1982) describes the database of reflectance data measured by this and other instruments.

A comparison of the spatial correlation of imagery and spectrometer samples was made for two fields from Hand County, South Dakota. Both aircraft line scanner imagery and FSS reflectance data were obtained over fields 168 and 288 on July 26, 1978. Field 168 was mostly bare soil, while field 288 was ripe Millet with nearly 100% ground cover. The spatial correlation of the imagery was done in the same direction and over the same area that the FSS had acquired data. The direction was along the flightline for both instruments. Since the aircraft imagery had a ground field of view of

approximately eight meters, the correlation coefficients for the aircraft imagery were calculated at both one and three pixel lag values to be able to compare the coefficients with those of the FSS at a similar intersample distances. The correlation coefficients are computed with the estimate given in equation 2.7.

$$\rho(\tau) = \frac{\sum_{n=1}^{N-1} (x_n - \bar{x}) (x_{n+\tau} - \bar{x})}{\sum_{n=1}^N (x_n - \bar{x})^2} \quad (2.7)$$

Here, τ is the lag value, N is the number of data samples and \bar{x} is the sample mean. Table 2.2 shows the spatial correlation coefficients for two wavelengths in each field and two pixel distances of the aircraft scanner.

Table 2.2 Spatial Correlation Coefficients for Hand County, South Dakota.

Field Number	Wavelength	Aircraft 8 Meters	Aircraft 24 Meters	FSS 25 Meters
168 Bare Soil	0.56 μm	0.82	0.31	0.28
	1.00 μm	0.87	0.53	0.48
288 Ripe Millet	0.56 μm	0.61	0.44	0.25
	1.00 μm	0.67	0.20	0.16

The results of Table 2.2 show that as the distance between samples increase, the correlation coefficient decreases. Also, there seems to be a significantly higher correlation among the imagery pixels as compared to those of the spectrometer, even when they are computed using samples a similar distance apart. Thus, there does appear to be an increase in the correlation coefficient due to the characteristics of the line scanner.

To investigate the typical variation of the correlation across the spectrum, the spatial correlation coefficient was computed from some FSS data of a winter wheat field (number 151) from Finney County, Kansas taken on May 3, 1977. The wheat was beginning to ripen and there was approximately 30% ground cover. There were 58 samples across the field, each about 20 meters apart. The correlation coefficient for $\tau=1$ as calculated in equation 2.7 for each wavelength is shown in figure 2.4.

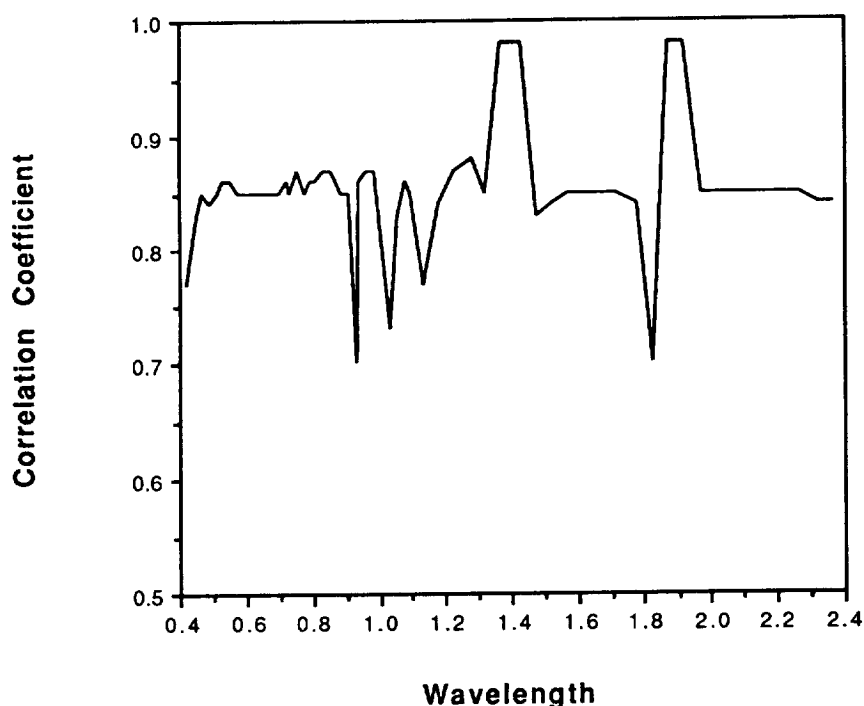


Figure 2.4 Correlation Coefficients of Winter Wheat Field.

The large peak around 1.4 and 1.9 μm is due to substituting 0.1% for the reflectance in the water absorption bands of the data. The other large peaks are also due to atmospheric absorption bands. The flat segments are from repeated values used in the plot due to the uneven spectral sampling of the FSS. For most of the wavelengths the correlation coefficient ranges around 0.85. This correlation among samples is significantly higher than those of Table

2.2. This is indicative of the high variability in correlation among surface cover types and conditions.

While the exponential model is one way of modeling spatial correlation, spatial models based on fractal geometry (Mandelbrot 1977, 1982, Gleick 1987, and Peitgen and Saupe 1988) have emerged as a powerful method for modeling natural phenomena. This is partly because its mathematical construction is similar to what is observed in natural scenes. In two spatial dimensions, the fractal random field $r(x,y)$ has the property shown in equation 2.8, where D is the fractal dimension ($2 < D < 3$).

$$E \left\{ \left| r(x_2, y_2) - r(x_1, y_1) \right|^2 \right\} \propto \left[(x_2 - x_1)^2 + (y_2 - y_1)^2 \right]^{3-D} \quad (2.8)$$

That is, the variance of the difference between pixel locations is proportional to the distance raised to a fractional power. Several experiments were conducted to measure the fractal dimension of typical agricultural scenes. Values for D ranged around 2.6 ± 0.1 for several cover types. See Dodd (1987) for an example in using fractal concepts to generate multispectral texture by computing the fractal dimension D from principle component images.

While several methods have been discussed for generating scenes with spatial correlation, the autoregressive model was chosen for implementation in the simulation. This model is efficient in generating a simulated reflectance array using computer-generated random numbers. Table 2.3 presents an overview of the technique used to simulate the surface reflectance, while the paragraphs following describe these steps in detail.

Table 2.3 Sequence in Generating a Simulated Surface Reflectance Array.

Step 1. Define scene size and class boundaries.
Step 2. Obtain spatial and spectral statistics of reflectance data for each class.
Step 3. Generate spatial correlated reflectance arrays for each wavelength, with each array being spectrally uncorrelated.
Step 4. Transform each reflectance vector to have the proper mean and covariance for the appropriate class.
Step 5. Interpolate resulting spectral reflectance vector to the desired spectral resolution of scene.

The scene is first defined by determining its size, X columns by Y rows, where each location (x,y) is a square scene cell with the distance on one side specified in meters. Each of these scene cells are assigned to one of the K classes. Class boundaries are specified by the upper left index and lower right index of the rectangular area containing the class.

Reflectance data for each class used in the simulation is obtained from the database of FSS measurements. Over the wavelength range considered in this report there are 60 wavelength samples in the FSS data. Thus, the spectral statistics are 60 dimensional. The across scene and down scene spatial coefficients are estimated from imagery over scenes similar to the one being simulated. Typically, the same spatial correlation is assumed for each wavelength, while no wavelength-to-wavelength spatial crosscorrelation is specified.

The AR model is used to generate the spatially correlated reflectance cells within the area defined for each class k, and for each wavelength band m as shown in equation 2.9,

$$r_m(x,y) = \rho_x r_m(x-1,y) + \rho_y r_m(x,y-1) - \rho_x \rho_y r_m(x-1,y-1) + \sigma_u z(x,y) \quad (2.9)$$

where the symbols are defined as in equation 2.6.

The individual arrays $\{r_m(x,y)\}$ are arranged as a spectral vector array, $\{R(x,y)\}$. Reflectance data of each class k are used to compute the mean vectors \bar{P}_k and covariance matrices Σ_k . The eigenvalues and eigenvectors of these covariance matrices are then computed and arranged as diagonal matrices Λ_k and column matrices Φ_k , respectively. The surface reflectance array $\{P(x,y)\}$ is then obtained by using equation 2.10, where for each scene cell location (x,y) the appropriate class transformation is applied.

$$P(x,y) = \bar{P}_k + \Phi_k \Lambda_k^{\frac{1}{2}} R(x,y) \quad (2.10)$$

The resultant reflectance array will be multivariate Gaussian with the mean and covariance of the original class statistics, and be spatially correlated according to the exponential model of equation 2.4.

While the FSS reflectance data covers the entire range from 0.4 to 2.4 μm , the wavelength sampling is uneven, ranging from 20 nm to 50 nm. In order to have a uniform spectral resolution for the scene model, an interpolation is performed on each spectral reflectance vector to yield 201 wavelengths spaced at 10 nm intervals. The algorithm used to perform this interpolation is given in Appendix B.

2.2.2 Solar and Atmospheric Modeling

In this section, the modeling of the solar illumination and the atmospheric effects present in optical remote sensing systems is discussed. Following a preliminary list of references to work in this area, a general model of the atmosphere is presented. This is followed by a discussion of measures of atmospheric quality. The model used in the simulation is then presented, along

with several curves showing the effect of various parameters on the atmospheric model. The section concludes with a comparison of the model atmosphere with real measurements for a particular test site.

The solar extraterrestrial flux and the atmosphere have been studied extensively over the years. Accurate measurements of the solar curve have been made and are well documented in the literature. For example, publications by Thekaekara (1974) and Bird (1982) contain solar standard curves. Discussions of the atmosphere may be found in chapter two of Swain and Davis (1978), Chahine (1983), and chapters five and six of Wolfe and Zisis (1978). Atmospheric simulation models have been reported in Kneizys, et al., (1983, 1988), Turner (1983), Diner and Martonchik (1984), and Herman and Browning (1975) among others.

The atmospheric effect on spectral radiance consists of two main mechanisms, scattering and absorption. Scattering is mainly due to the presence of particles in the atmosphere, while absorption comes about due to the energy transfer from the optical radiation to molecular motion of atmospheric gases. Both of these effects are wavelength dependent.

Figure 2.5 gives a pictorial view of the various atmospheric effects on the spectral radiance received by the sensor.

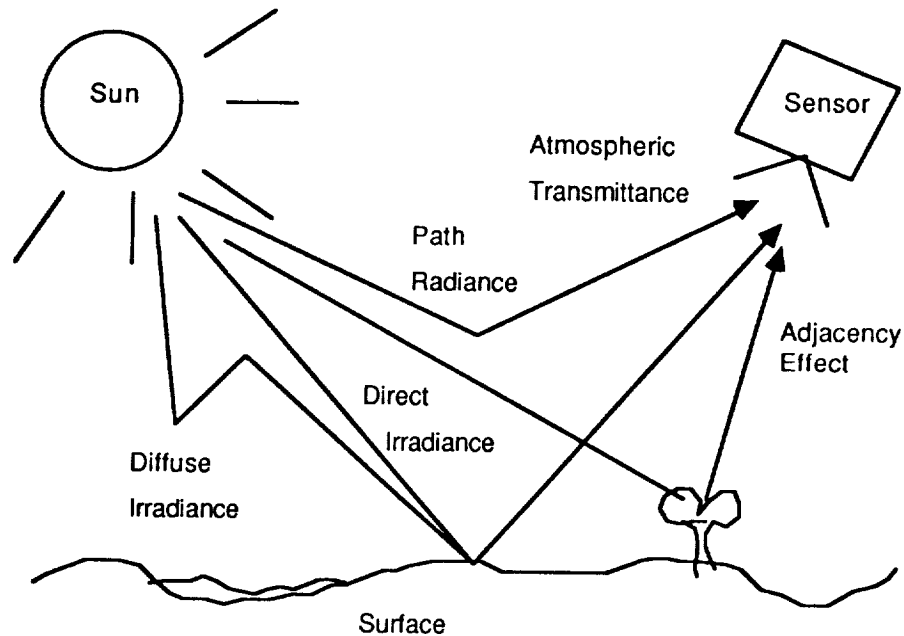


Figure 2.5 Atmospheric Effects on Spectral Radiance Received by Sensor.

From this figure, several main factors are seen to contribute to the radiance received by the sensor. The exoatmospheric spectral irradiance, $E_{\lambda, \text{Exo}}$, is attenuated and scattered by the atmosphere before reaching the surface as the direct spectral irradiance $E_{\lambda, \text{Direct}}$. Some of this scattered radiation also reaches the surface as $E_{\lambda, \text{Diffuse}}$, the diffuse spectral irradiance (or skylight irradiance.) The reflected spectral radiance $L_{\lambda, \text{Surface}}$ passes through the atmosphere and is attenuated by the spectral transmittance $T_{\lambda, \text{Atm}}$ of the atmosphere. Also, some of the solar irradiance that is scattered by the atmosphere finds its way into the sensor field of view as $L_{\lambda, \text{Path}}$, the path spectral radiance. This path radiance also includes that which may have been reflected off of the nearby surface (adjacency effect) before being scattered into the sensor field of view, as well as the background radiation of the atmosphere.

These factors contribute to the spectral radiance of the scene, as received by the sensor, in a manner described by equation 2.11.

$$L_{\lambda, \text{Sensor}} = \frac{1}{\pi} \left[\cos(\theta_{\text{solar}}) E_{\lambda, \text{Direct}} + E_{\lambda, \text{Diffuse}} \right] R_{\lambda} T_{\lambda, \text{Atm}} + L_{\lambda, \text{Path}} \quad (2.11)$$

Here, R_{λ} is the spectral reflectance of the surface. In the most general sense it is the Spectral Bidirectional Reflectance Factor (SBRF) that gives the reflectance for all angles of incidence and viewing. The other factors also depend upon the angles of illumination and viewing as well as the quality of the atmosphere.

Several other important aspects of the real atmosphere also influence the values in equation 2.11. One is the spatial dependence of the atmospheric scattering and absorption effects. The make-up of the atmosphere is not constant over a scene; however, it is unclear how the atmosphere changes from pixel to pixel over typical pixel sizes (20-30 meters), and is usually assumed to be constant. Another spatial effect of the atmosphere is the blurring that can be introduced by the scattering in the atmosphere. Kaufman (1985) has studied the atmosphere from this point of view, suggesting that the atmosphere be modeled with a spatial modulation transfer function (Goodman, 1978) similar to those used in the modeling of sensors. This could be implemented in the model in a spatial convolution with the scene radiance. Yet another effect that is often ignored is the time dependence of the atmospheric effects. Fast moving gases exist in the upper atmosphere and cause a changing effect on the scattering and absorption over the field of view of the sensor. The movement of clouds is an example of this time dependence.

The quality of the atmosphere may be represented by several different measures. The fundamental parameter for atmospheric quality is the spectral optical thickness τ_{λ} . The spectral transmittance $T_{\lambda, \text{Atm}}$ of the atmosphere between two points x_1 and x_2 is defined by equation 2.12 where $\beta(\lambda, z)$ is the volume extinction-coefficient with units of Km^{-1} .

$$T_{\lambda, \text{Atm}} = \exp \left[- \int_{x_1}^{x_2} \beta(\lambda, z) dz \right] \quad (2.12)$$

The integral inside the exponent of this equation is known as the spectral optical thickness τ_λ and is defined in equation 2.13.

$$\tau_\lambda = \int_{x_1}^{x_2} \beta(\lambda, z) dz \quad (2.13)$$

Visibility is also often used as a measure of the clarity of the atmosphere and is defined (Kneizys, et al., 1983) by "the greatest distance at which it is just possible to see and identify with the unaided eye in the daytime a dark object against the horizon sky." The surface meteorological range V_η is related to visibility (usually by a factor of 1 ± 0.3), but defined numerically, rather than by subjective judgement. For the typical atmospheres used in this report, it is assumed that the two terms can be used interchangeably. Surface meteorological range is related to the volume extinction-coefficient at $\lambda = 0.55 \mu\text{m}$ through equation 2.14.

$$V_\eta = \frac{3.912}{\beta_{\lambda=0.55}} \text{ Km} \quad (2.14)$$

Surface meteorological range (or visibility) is the measure commonly used in remote sensing for atmospheric quality. However, some experiments specify the optical thickness (also called optical depth for a vertical path). Data from Elterman (1970) was used to find an empirical relationship between optical thickness and visibility. Figure 2.6 shows points from Elterman's data along with a best fit curve. These data points are for $\lambda = 0.55 \mu\text{m}$. Optical thickness is also dependent upon wavelength. Data from Elterman (1968) was plotted in Figure 2.7 along with a best fit curve for the empirical data. This relationship is for a surface meteorological range of 25 Km.

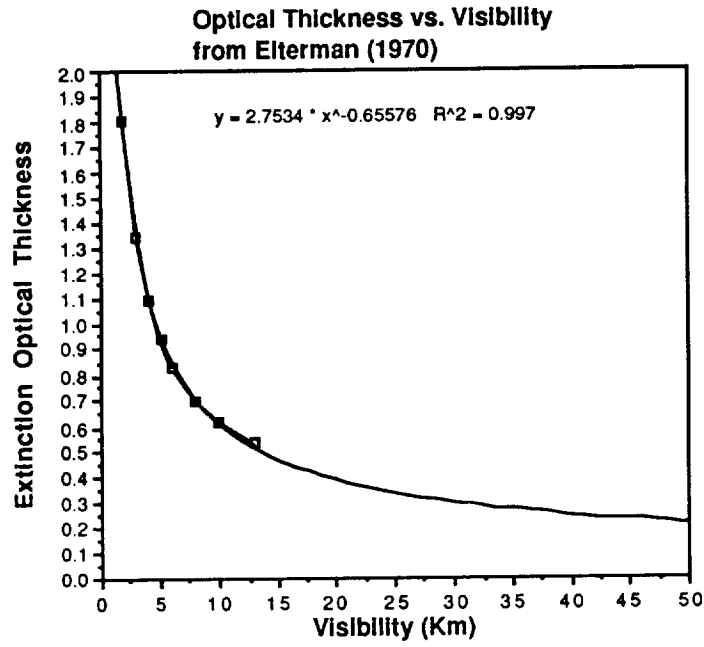


Figure 2.6 Optical Thickness τ vs. Visibility.

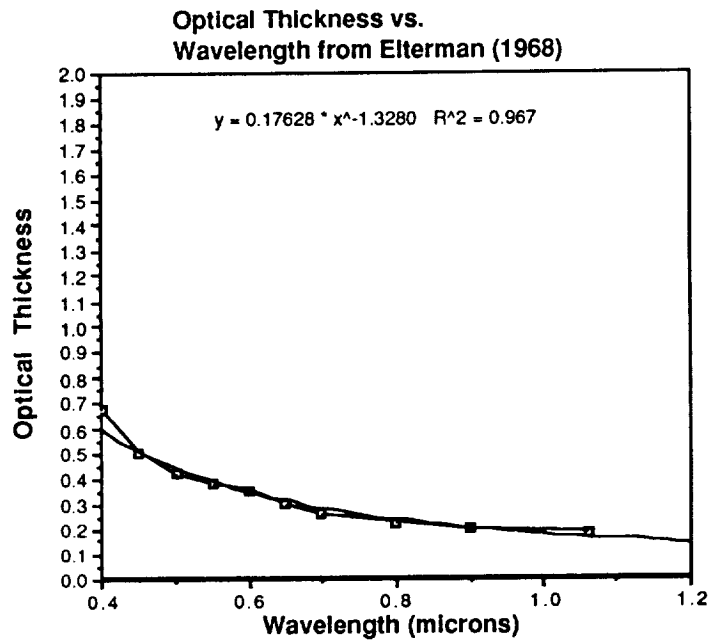


Figure 2.7 Optical Thickness vs. Wavelength.

These empirical relationships were used to derive equation 2.15 relating spectral optical thickness to meteorological range and wavelength.

$$\tau_{\lambda}(V_{\eta}) = 1.35\lambda^{-1.328}V_{\eta}^{-0.656} \quad (2.15)$$

This equation is assumed to be valid only over optical wavelengths and meteorological ranges from 2 to 50 Km.

In this research the solar and atmospheric model is implemented with the use of the computer code LOWTRAN 7 (Kneizys, et al., 1988). The program LOWTRAN has evolved over the years from simply an atmospheric transmittance code to one that is now capable of computing direct solar irradiance and multiply scattered atmospheric radiance.

LOWTRAN uses radiative transfer theory to compute the transmittance and radiance in each of 32 layers of the atmosphere. Well documented data tables embedded within the program give accurate spectral transmittance and radiance values at minimum wavenumber intervals of 20 cm⁻¹. This model compares favorably to ones developed by Diner and Martonchik (1984), and Herman and Browning (1975), because of its continuous spectral coverage and its inclusion of narrow absorption bands due to the various constituents of the atmosphere. A partial list of controllable parameters for LOWTRAN 7 is contained in Table 2.4.

Table 2.4 Example LOWTRAN 7 Parameters

Solar position
Meteorological range
Surface albedo
Atmospheric haze
Altitude of observer
Zenith angle of observer
Wavelength range and increment

LOWTRAN 7 is used along with the models discussed below for the diffuse irradiance and path radiance to compute the radiance received by the sensor. Appendix C contains the input file format used in the calls to LOWTRAN.

The spectral radiance present at the input to the sensor model in the simulation program is computed as in equation 2.16.

$$L_{\lambda, \text{Sensor}}(x, y) = \frac{1}{\pi} E_{\lambda, \text{Total}} P(x, y) T_{\text{Atm}} + L_{\lambda, \text{Path}} \quad (2.16)$$

The generation of the three atmospheric components of this equation is discussed below, while the spectral reflectance array $P(x, y)$ is as calculated in section 2.2.1.

1. Total Spectral Irradiance. This is the total downwelling spectral irradiance $E_{\lambda, \text{Total}}$ that is incident at the surface, and is equal to the sum of the direct and diffuse irradiances as shown in equation 2.17.

$$E_{\lambda, \text{Total}} = \cos(\theta_{\text{solar}}) E_{\lambda, \text{Direct}} + E_{\lambda, \text{Diffuse}} \quad (2.17)$$

Since LOWTRAN does not have an option to generate the diffuse component, a model was obtained from Chahine (1983). There, the total surface spectral irradiance $E_{\lambda, \text{Total}}$ is shown to be related to the direct spectral irradiance through the curve given in Figure 2.8. Also shown in the figure is an exponential model derived from the data.

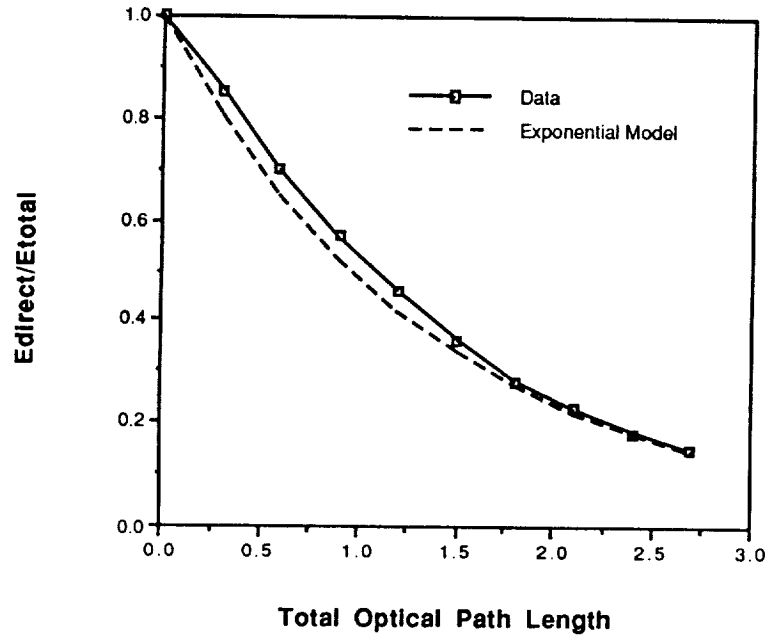


Figure 2.8 Ratio of Direct to Total Irradiance vs. Total Optical Path Length.

The total optical path length $\tau_{p,\lambda}$ is related to the optical thickness by multiplying by $\sec(\theta_{\text{solar}})$ as in equation 2.18.

$$\tau_{p,\lambda}(V_{\eta}, \theta_{\text{solar}}) = \tau_{\lambda}(V_{\eta}) \sec(\theta_{\text{solar}}) \quad (2.18)$$

This relationship between direct and total irradiance is given as a function of the total optical thickness of the atmosphere in equation 2.19. Thus, equation 2.19 can be used in conjunction with equation 2.15 to obtain the total surface spectral irradiance from the direct spectral irradiance, the surface meteorological range, the diffuse irradiance constant, and the solar zenith angle.

$$E_{\lambda, \text{Total}}(V_{\eta}, \theta_{\text{solar}}) = \frac{\cos(\theta_{\text{solar}}) E_{\lambda, \text{Direct}}(V_{\eta}, \theta_{\text{solar}})}{\exp[-K_D \tau_{\lambda}(V_{\eta}) \sec(\theta_{\text{solar}})]} \quad (2.19)$$

The diffuse irradiance constant K_D is dependent upon the type of atmosphere and the overall surface reflectance. In the discussion by Chahine (1983) from which Figure 2.8 was taken, the author stated that the curve was for a nonabsorbing atmosphere and surface albedo $< 15\%$. It was also indicated that for absorbing atmospheres and higher albedoes the curve would be steeper. While no specific values were given in the reference, Table 2.5 shows some estimates of K_D for different conditions. The model shown in Figure 2.8 was with $K_D = 0.73$.

Table 2.5 Diffuse Irradiance Constant Values.

K_D	Type of Atmosphere	Surface Reflectance
0.73	nonabsorbing	low ($< 15\%$)
0.84	absorbing	low ($< 15\%$)
1.00	absorbing	medium (15 - 30 %)
1.26	absorbing	high ($> 30\%$)

2. Atmospheric Spectral Transmittance. This is directly computed using LOWTRAN for a path from the surface to the sensor. This may be a vertical or slant path through the atmosphere, depending on the zenith angle of the sensor. It represents the path loss due to scattering and absorption.

3. Path Spectral Radiance. This is computed by using two calls to LOWTRAN. It is called once for a surface albedo of 0 and once for an albedo of 1. The total path radiance received by the sensor is then computed by interpolating between these extremes as in equation 2.20, where (x,y,m) specifies the spatial location x,y and wavelength m . $\rho_{m,ave}(x,y)$ is the average surface reflectance for wavelength m in the neighborhood of x,y . In implementing this model in the simulation the entire scene is used in computing $\rho_{m,ave}(x,y)$.

$$L_{\lambda,Path}(x,y,m) = L_{\lambda,Path}^{alb=0}(m) + \rho_{m,ave}(x,y) \cdot \left[L_{\lambda,Path}^{alb=1}(m) - L_{\lambda,Path}^{alb=0}(m) \right] \quad (2.20)$$

This formulation of path radiance allows for its dependence on the surface reflectance. This does not truly represent the situation in the real system, as the path radiance there is dependent upon the reflectance of the surface for each particular path the illumination follows before arriving at the sensor, and there are many paths the illumination may take. However, this simple linear model offers good compromise between accuracy and computational complexity.

On the following pages, examples of how various scene parameters affect these atmospheric model components. For these examples the default parameters of Table 2.6 were used.

Table 2.6 Default Values of Atmospheric Parameters.

Parameter	Default
Model	1976 U.S. Standard
Atmospheric Haze	Rural Extinction
Surface Meteorological Range	16 Km
Diffuse Irradiance Constant	0.73
Solar Zenith Angle	30°
View Zenith Angle	0°
Surface Albedo	0.10

The following figures 2.9 through 2.14 show the direct, diffuse, and total spectral irradiance for several meteorological ranges and solar zenith angles. The curves for the diffuse irradiance were computed as the difference between the total and direct spectral irradiances. Figures 2.15 and 2.16 show how atmospheric transmittance varies for several meteorological ranges and view angles. Figures 2.17 through 2.20 show how the path radiance component is affected by meteorological range, solar angle, view angle and surface albedo.

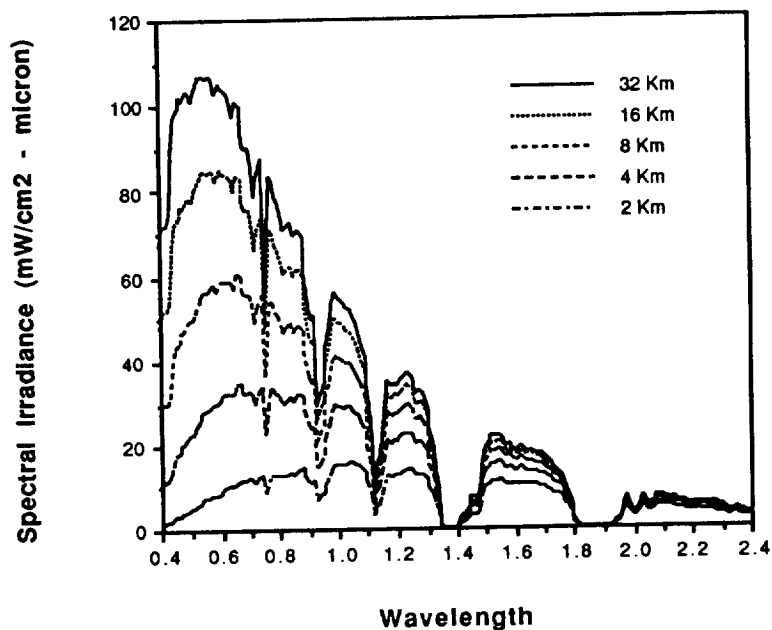


Figure 2.9 Effect of Meteorological Range on Direct Solar Spectral Irradiance.

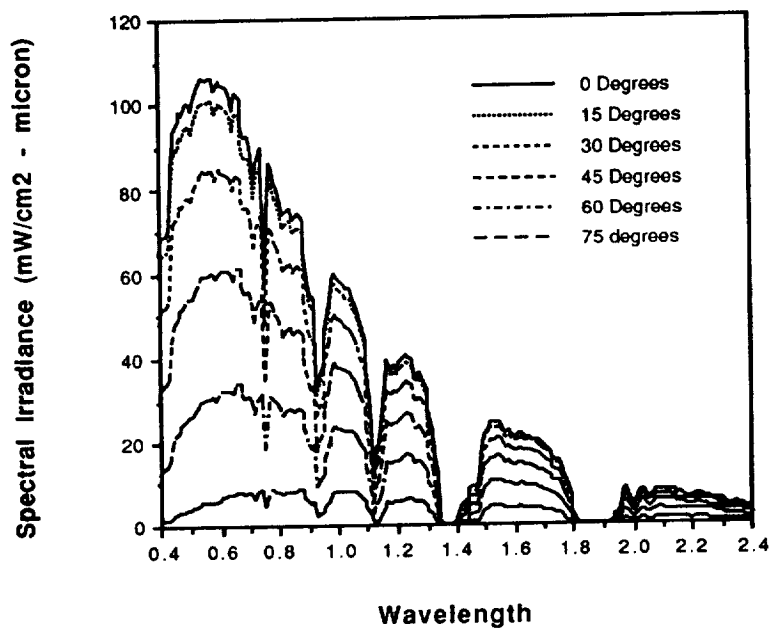


Figure 2.10 Effect of Solar Zenith Angle on Direct Solar Spectral Irradiance.

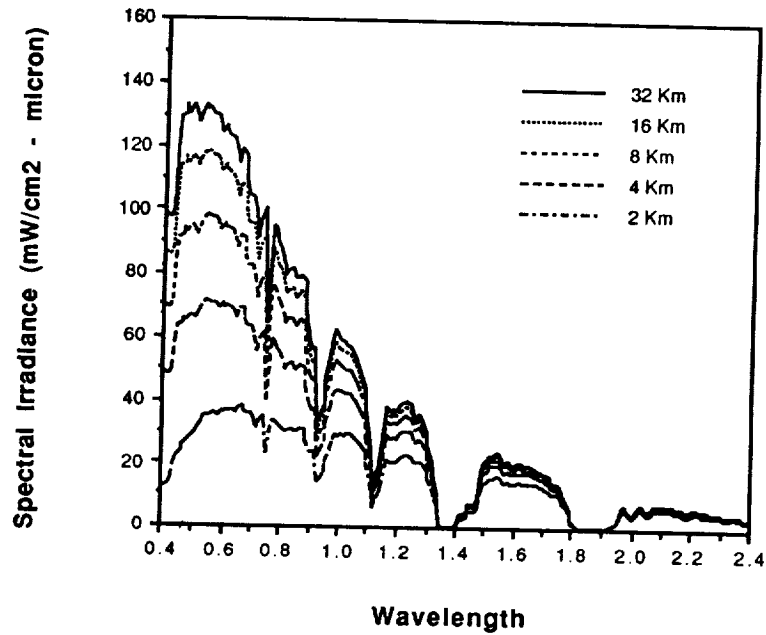


Figure 2.11 Effect of Meteorological Range on Total Solar Spectral Irradiance.

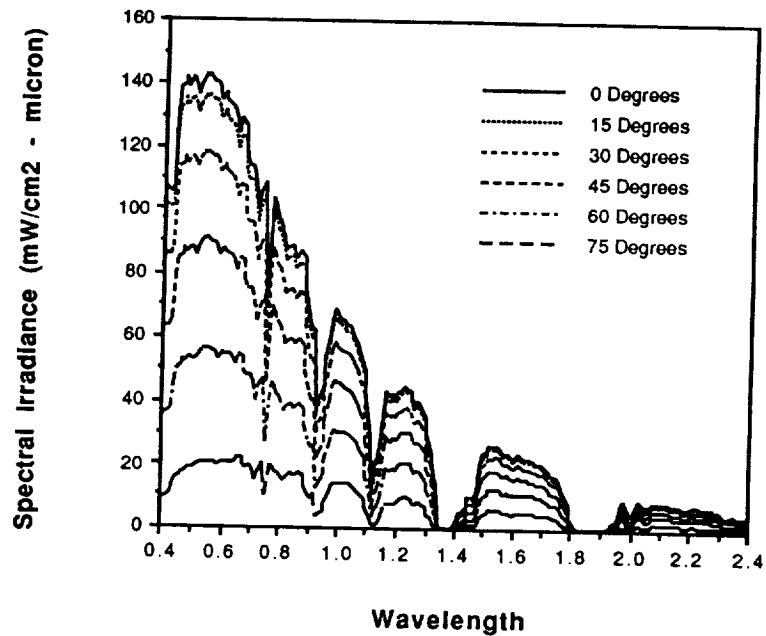


Figure 2.12 Effect of Solar Zenith Angle on Total Solar Spectral Irradiance.

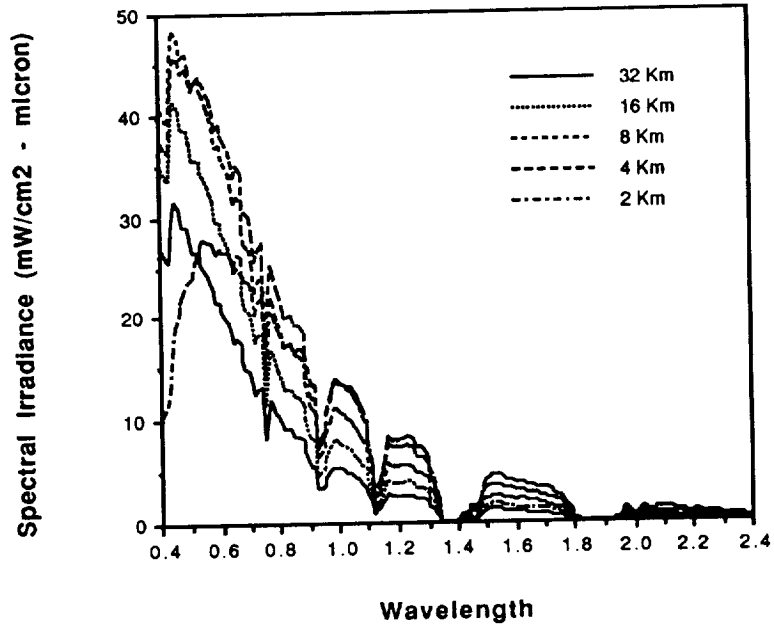


Figure 2.13 Effect of Meteorological Range on Diffuse Solar Spectral Irradiance.

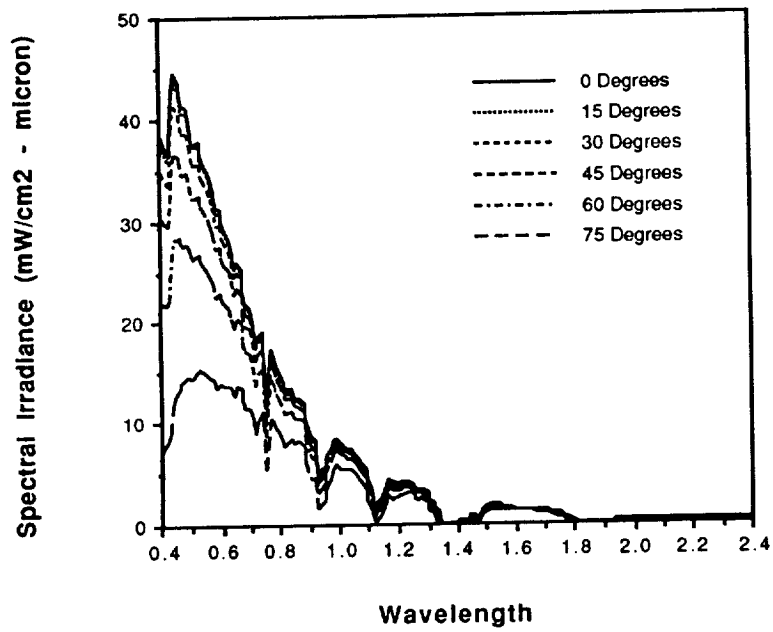


Figure 2.14 Effect of Solar Zenith Angle on Diffuse Solar Spectral Irradiance.

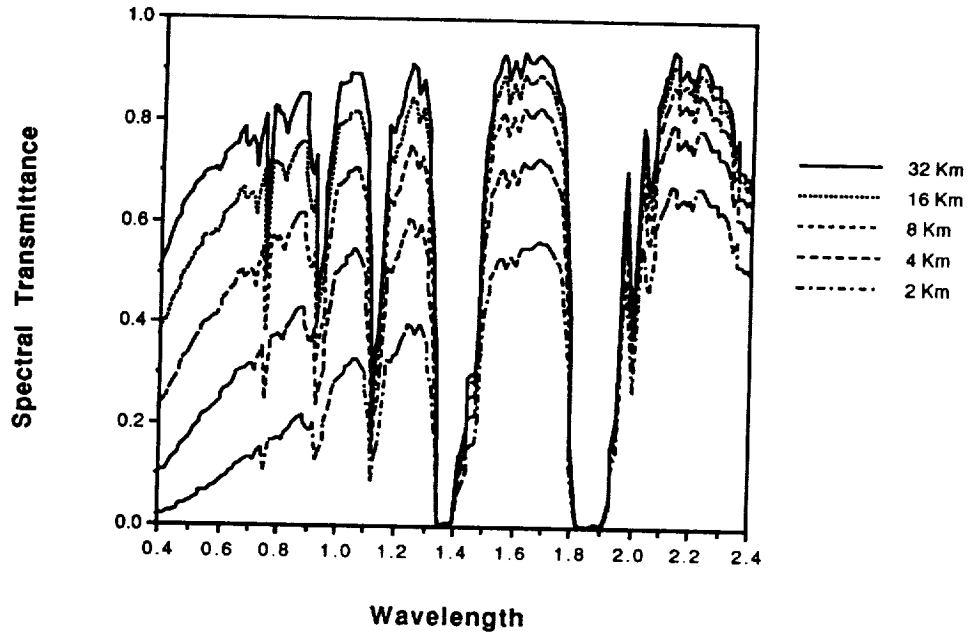


Figure 2.15 Effect of Meteorological Range on Spectral Transmittance.

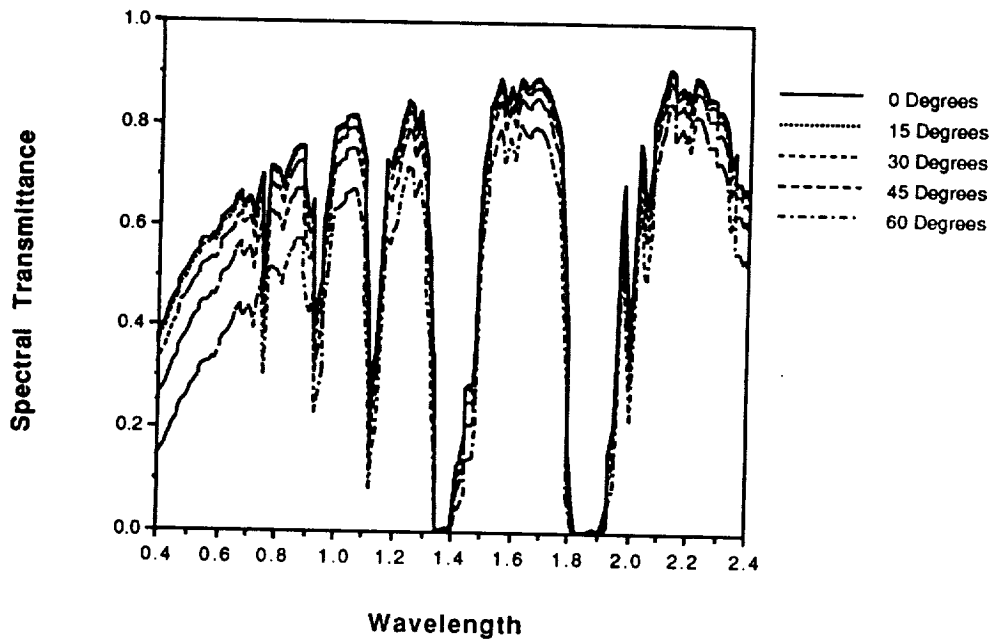


Figure 2.16 Effect of Sensor Zenith Angle on Spectral Transmittance.

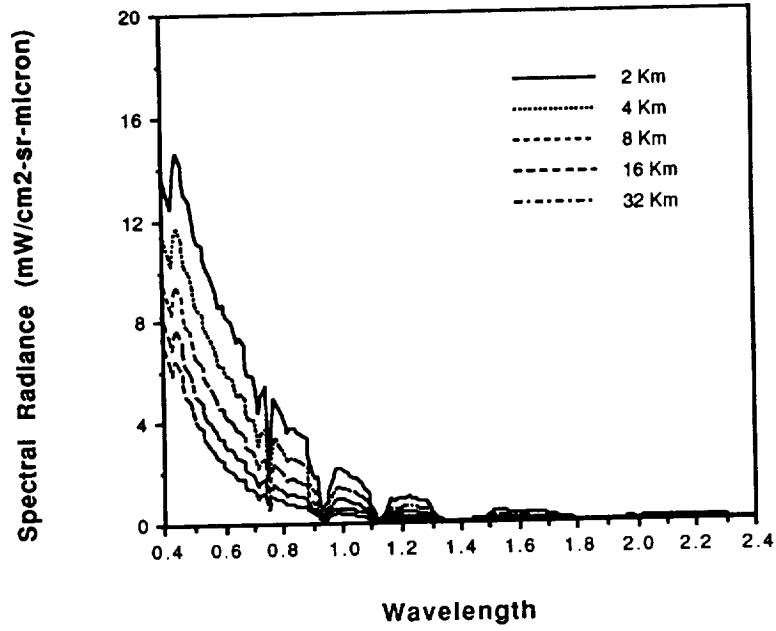


Figure 2.17 Effect of Meteorological Range on Path Spectral Radiance.

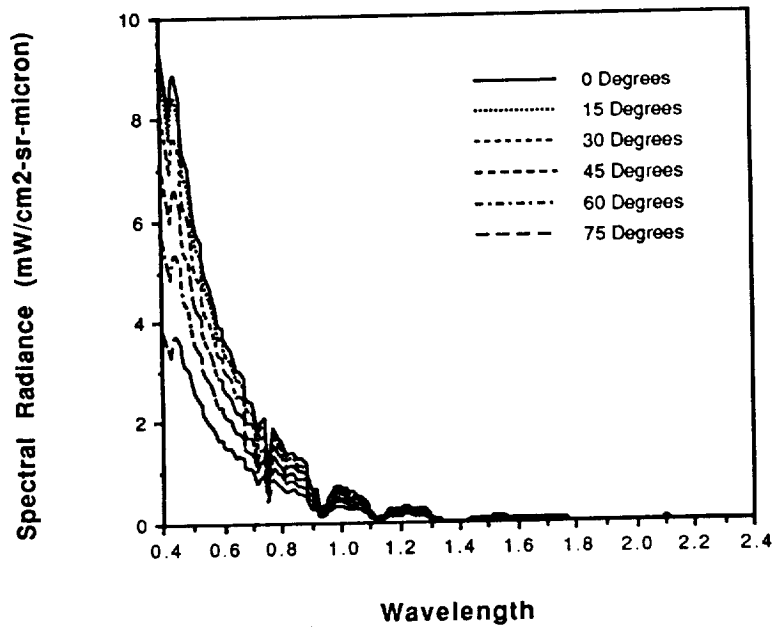


Figure 2.18 Effect of Solar Zenith Angle on Path Spectral Radiance.

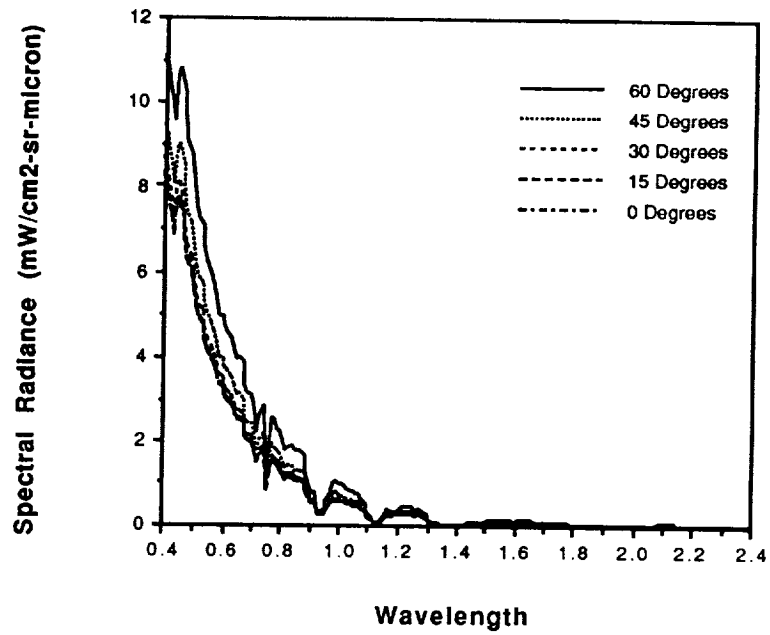


Figure 2.19 Effect of Sensor Zenith Angle on Path Spectral Radiance.

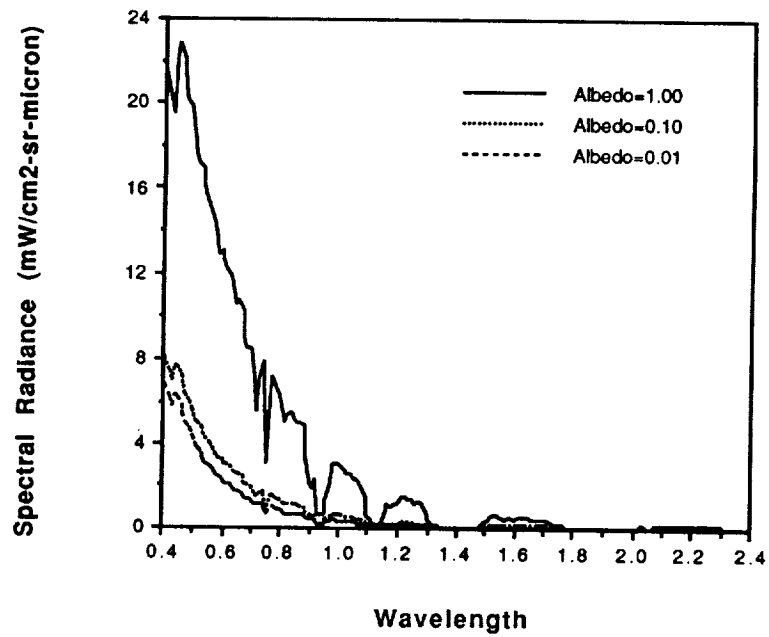


Figure 2.20 Effect of Surface Albedo on Path Spectral Radiance.

These curves give an indication how the components of the atmospheric model vary under different conditions. In general, they show how a hazier atmosphere will allow less radiance to be received by the sensor from the surface, yet increases the path radiance, and how the angle of illumination or view can decrease the signal radiance as well as increase the path radiance. The path radiance is also seen to increase with surface albedo.

An experiment was performed to test the suitability of the atmospheric model by comparing the radiance received by a satellite to that simulated by the model from a description of the scene conditions and the reflectance of the surface. A test site in Hand County, South Dakota was chosen from data gathered as part of the LACIE program (Hixson, et al., 1978). On July 26, 1978, reflectance data was gathered at approximately the same time as the Landsat 2 MSS passed over the area. The parameters of these sensors are shown in Table 2.7.

Table 2.7 Data Set for Hand County, South Dakota, July 26, 1978.

Landsat 2 Multispectral Scanner	
Spectral Channels	4 bands, 0.4 - 1.1 μm
Scene	21281-16232
Altitude	918 Km
Ground Size of IFOV	80 Meters
Time	1623 GMT
Helicopter Field Spectrometer System	
Spectral Channels	60 bands, 0.4 - 2.4 μm
Altitude	60 Meters
Ground Size of FOV	25 Meters
Time	1505 - 1601 GMT

A particular area having four large nearly square fields was selected for test. Table 2.8 contains the field numbers from the LACIE experiment and the crop types.

Table 2.8 Description of Test Fields.

Field Number	Crop Type	Ground Cover
Field 290	Spring Wheat	30 Percent
Field 168	Millet	10 Percent
Field 289	Spring Wheat	30 Percent
Field 288	Millet	90 Percent

In order to compute the radiances received by the MSS, a table of conversion constants was obtained from the work by Richardson, et al., (1980). Table 2.9 shows the A_i and B_i used to compute from the digital counts DC_i the radiance present at the input of Landsat 2 MSS in band i . Equation 2.21 shows how these constants are used to compute the radiance. The units of A are $mW/(cm^2\text{-sr-digital count})$ and for B are $mW/(cm^2\text{-sr})$.

Table 2.9 Conversion Constants Between Radiance and Digital Counts.

Band	A	B
1	0.0201	0.08
2	0.0134	0.06
3	0.0115	0.06
4	0.0603	0.11

$$L_i = A_i DC_i + B_i \quad (2.21)$$

In generating the simulated radiance, the atmospheric model described earlier in this chapter was used with the radiances integrated over the nominal wavelength intervals of each band of the MSS sensor. Thus, the radiance in each band i was generated as in equation 2.22.

$$L_i = \frac{1}{\pi} E_{i,Total} T_{i,Atm} R_i + \left(L_{i,Path}^1 - L_{i,Path}^0 \right) R_i + L_{i,Path}^0 \quad (2.22)$$

Here, R_i is the average reflectance in band i . Table 2.10 gives the atmospheric and goniometric conditions present at the time of observations.

Table 2.10 Scene Conditions at Time of Observations.

Meteorological Range (V_{η})	31 Km
Solar Zenith Angle (θ_{solar})	39°
Solar Azimuth Angle (ϕ_{solar})	119°
Diffuse Irradiance Constant (K_D)	1.26

Table 2.11 contains the LOWTRAN settings used in generating the simulated atmospheric effects.

Table 2.11 LOWTRAN Settings for Experiment.

Atmospheric Model	1976 U. S. Standard
Atmospheric Haze	Rural Extinction
Atmospheric Scattering	Multiple
Aerosol Phase Functions	Mie-generated
Aerosol Profile	Background Stratospheric

All other LOWTRAN parameters were set to zero, or the default. Table 2.12 shows the atmospheric components generated by LOWTRAN for each of the spectral bands, while Table 2.13 compares the simulated to the actual radiances received by the satellite.

Table 2.12 Atmospheric Components for the Hand County Test Site.

Band	$E_{\text{Total}} \left(\frac{\text{mW}}{\text{cm}^2} \right)$	T_{atm}	$L_{\text{Path},1} \left(\frac{\text{mW}}{\text{cm}^2 \cdot \text{sr}} \right)$	$L_{\text{Path},0} \left(\frac{\text{mW}}{\text{cm}^2 \cdot \text{sr}} \right)$
1	16.296	0.684	1.131	0.248
2	14.036	0.746	0.735	0.128
3	10.843	0.764	0.434	0.068
4	19.329	0.774	0.524	0.071

Table 2.13 Comparison of Actual and Simulated Radiances (in $\text{mW}/(\text{cm}^2\text{-sr})$) for Test Site in Hand County, SD.

	FSS Reflectance	MSS Average Digital Count	Landsat Radiance	Simulated Radiance	Percent Error
Field 290					
Band 1	0.063	21.5	0.512	0.527	+2.9
Band 2	0.083	26.9	0.421	0.455	+8.1
Band 3	0.166	44.2	0.568	0.566	-0.4
Band 4	0.240	20.7	1.358	1.323	-2.6
Field 168					
Band 1	0.068	23.7	0.556	0.549	-1.3
Band 2	0.088	31.0	0.475	0.475	0.0
Band 3	0.121	36.8	0.483	0.431	-10.8
Band 4	0.182	16.6	1.111	1.020	-8.2
Field 289					
Band 1	0.058	22.1	0.524	0.505	-3.6
Band 2	0.078	27.6	0.430	0.435	+1.2
Band 3	0.143	43.2	0.557	0.497	-10.8
Band 4	0.208	20.1	1.322	1.156	-12.6
Field 288					
Band 1	0.043	18.3	0.448	0.439	-2.0
Band 2	0.031	14.8	0.258	0.250	-3.1
Band 3	0.252	66.1	0.820	0.825	+0.6
Band 4	0.388	36.6	2.317	2.094	-9.6

A scatter plot of the simulated radiances versus the measured ones is shown in Figure 2.21. The solid line is a best linear fit to the points with a regression coefficient of 0.99, while the dashed line represents the ideal of equal radiances.

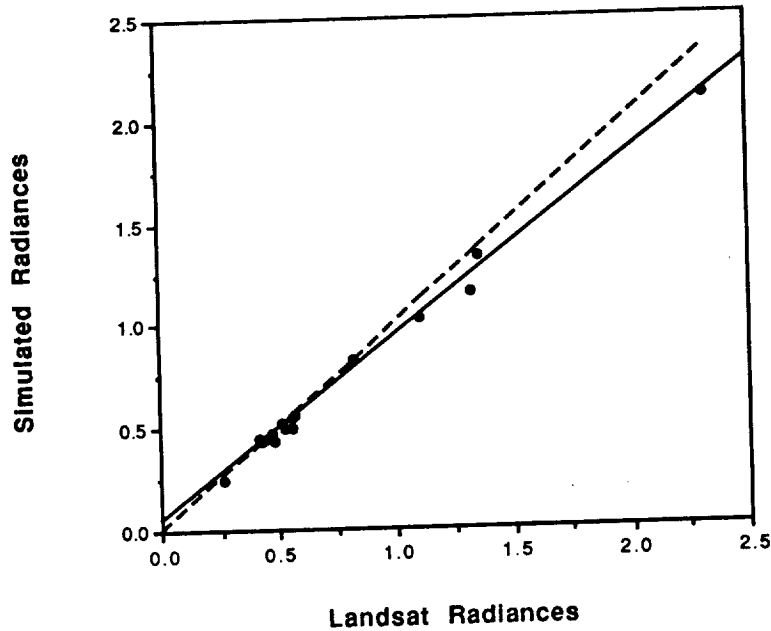


Figure 2.21. Plot of Landsat vs. Simulated Radiances.

The error between the Landsat and the simulated radiances seems to be equally distributed (+ and -) for bands 1 and 2, while the radiances in bands 3 and 4 seem to be consistently underestimated by the model. The greater error at the longer wavelengths may be due to several factors. The diffuse irradiance component may be on the low side because of the high reflectances of the surrounding area. Also, LOWTRAN may be underestimating the path radiance calculation.

Overall, there seems to be a close match between the Landsat radiance and the simulated radiance. It would seem then, that this atmospheric model is reasonably satisfactory.

2.3 Sensor Modeling

The sensor portion of optical remote sensing systems performs the task of sampling the continuous spectral radiance of the scene in the spectral, spatial, radiometric, and temporal domains. This results in a digital multispectral image of a scene at a certain moment in time, with a discrete number for the radiance at each spot in the scene and for each spectral region.

The modeling of imaging sensors can be quite complex indeed. One may consider the propagation of the optical waves through the sensor optics (including aberrations), the conversion from light to electrons in the detector material, and the effects in the signal conditioning electronics. Goodman (1968) provides a good discussion of the propagation of optical waves in imaging systems from a linear systems point of view. Texts by Hudson (1969), Pinson (1985), and Wyatt (1987), and chapter eight of Colwell (1983) cover the entire detection process from the optical system through the detector electronics.

In this research, the modeling of sensors is approached from a lumped systems perspective. Figure 2.22 shows a block diagram of the major components of a multispectral sensor.

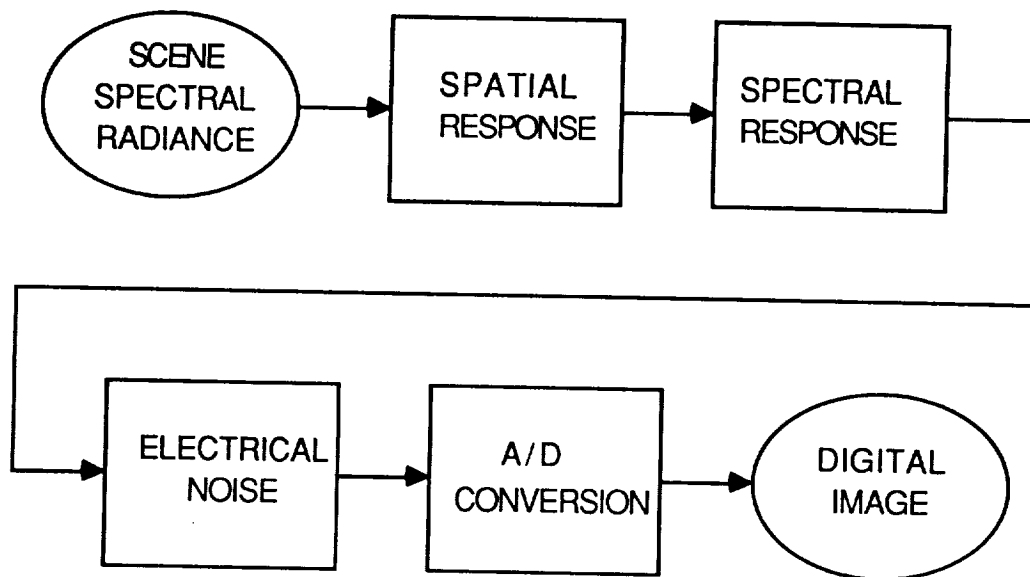


Figure 2.22 Sensor System Components.

The scene is sampled spatially by its being imaged onto a detector array that is either scanned sequentially down the scene, or consists of a focal plane array that gathers the two-dimensional image in a small but finite time interval. These sampled pixels are also dispersed onto separate detectors for each spectral band to perform the spectral sampling.

The signals from these detectors are then amplified (electrical noise effects occur here) and calibrated before being quantized into discrete values.

The model shown here is very general and could be enhanced to include very detailed effects such as the aberrations in the optical propagation in the optical system, spatial misalignment of the detectors, or electrical bandwidth of the amplifiers. But in this report, the model will be relatively simple within this generality. The model will be limited to a simple point spread function for the spatial response, a simple multiplication of the sensor response for the spectral response, and a noise model containing electrical noise, calibration error, and quantization effects.

In the following subsections 2.3.1 and 2.3.2, models are presented for the sampling and noise processes. In subsection 2.3.3, a detailed model is presented for a future remote sensing imaging spectrometer. Appendix D contains complete descriptions of several multispectral scanners. In subsection 2.3.4, the computation of radiometric performance measures is discussed.

2.3.1 Sampling Effects

In the creation of the digital image the continuous spectral radiance of the scene is sampled spatially, spectrally, and radiometrically (ie., A/D conversion). The following paragraphs describe these forms of sampling.

1. Spatial Sampling. The optical Point Spread Function (PSF) is the two-dimensional analog of the system impulse response in linear system theory (Goodman, 1968). It is the response of the optical system to an infinitely bright point source, usually represented by the Dirac delta function $\delta(x,y)$.

In the simulation model, no parametric form for the PSF is assumed. Rather, a table of values derived from measurements of the real devices is used to define the PSF. Thus, this form includes many of the aberrations present in the instrument optics.

The discrete representation of the response of the optical system is given by equation 2.23. The PSF $h(u,v)$ is represented as the product of separable line spread functions $h_x(\cdot)$, and $h_y(\cdot)$, across the two spatial dimensions. The response is normalized to unit area by dividing by the area under it.

$$h(u,v) = \frac{1}{(A_x g_x)(A_y g_y)} \sum_{o=1}^{O+1} \sum_{p=1}^{P+1} h_x(o)h_y(p) \delta(u - g_x o, v - g_y p) \quad (2.23)$$

Where,

(u,v) - spatial domain locations (meters)

A_x - sum of across scene line spread function coefficients

A_y - sum of down scene line spread function coefficients

$g_x = \Delta UH$ - ground interval between h_x coefficients (meters)

$g_y = \Delta VH$ - ground interval between h_y coefficients (meters)

ΔU - angular distance between h_x coefficients (radians)

ΔV - angular distance between h_y coefficients (radians)

H - height of sensor (meters).

Also, $O+1$ and $P+1$ represent the number of coefficients in the across scan and down track line spread functions, respectively, and $h_x(P/2)$ and $h_y(O/2)$ contain the maximum response.

Equation 2.23 gives the response for a vertical viewing sensor. For sensor zenith angles $> 0^\circ$, the distance on the ground between the coefficients must be rotated by the azimuthal angle ϕ_{view} , and scaled by the zenith angle θ_{view} . This is shown in equation 2.24.

$$\begin{bmatrix} g'_x \\ g'_y \end{bmatrix} = \begin{bmatrix} \cos(\phi_{\text{view}}) & \sin(\phi_{\text{view}}) \\ -\sin(\phi_{\text{view}}) & \cos(\phi_{\text{view}}) \end{bmatrix} \begin{bmatrix} g_x \\ \frac{g_y}{\cos(\theta_{\text{view}})} \end{bmatrix} \quad (2.24)$$

In applying this spatial response to the scene spectral radiance function derived in section 2.2.3, equation 2.25 is used. This equation is repeated for all image pixel locations (i,j) and scene wavelengths m.

$$L_{\lambda, \text{Sensor}}(i,j,m) = \frac{G_x G_y}{(A_x g'_x)(A_y g'_y)} \sum_{o=1}^{O+1} \sum_{p=1}^{P+1} L_{\lambda, \text{Scene}} \left(\frac{iS_x - og'_x}{G_x}, \frac{jS_y - pg'_y}{G_y}, m \right) \cdot h_x \left(\frac{og'_x}{G_x} \right) h_y \left(\frac{pg'_y}{G_y} \right) \quad (2.25)$$

S_x and S_y are the across scene and down track sampling intervals for the image pixels. In the case of off-nadir viewing these also must be scaled and rotated as the ground coefficient intervals were in equation 2.24. Note that since the scene radiance array has discrete pixel locations all index quotients are rounded to the nearest integer. Also, at the edges, the extreme row or column is repeated as necessary to allow for the complete application of the spatial response.

The PSF is often approximated by a truncated Gaussian curve. Measured PSF's often are nonsymmetrical and can include ringing at the tails of the response; thus the Gaussian shape does not truly represent the actual PSF. Although in some cases, it can be close enough to justify its use in theoretical modeling.

2. Spectral Sampling. The spectral response of a multispectral sensor consists of the continuous response of each channel to the spectral radiance received by the sensor. In the simulation, the application of the discrete response to the incoming spectral radiance $L_{\lambda, \text{Sensor}}(i,j,m)$ is as shown in equation 2.26.

$$L_{\text{Image}}(i,j,l) = \Delta\lambda \sum_{m=1}^M L_{\lambda,\text{Sensor}}(i,j,m) \frac{s_l(m)}{N(l)} \quad (2.26)$$

Where,

$\Delta\lambda$ - scene wavelength increment in μm

$s_l(m)$ - normalized response of band l to spectral wavelength m

$L_{\text{Image}}(i,j,l)$ - radiance received by band l at pixel location (i,j)

$L_{\lambda,\text{Sensor}}(i,j,m)$ - incoming spectral radiance from pixel location (i,j)
at wavelength m

$N(l)$ - normalizing factor for nominal bandwidth variations.

The normalizing factor $N(l)$ is the ratio between the actual bandwidth as measured by the area under the normalized response curve and the nominal bandwidth of the channel. This factor is often necessary to match the published gain setting between the real instrument and a modeled version. Price (1987) discusses calibration problems of this sort and presents tables of the actual bandwidth for several multispectral scanners.

For the imaging spectrometers modeled in this report, the spectral resolution of the sensor is the same as the scene. Thus, for these sensors there is only one term present in equation 2.26.

3. Radiometric Sampling. After the continuous spectral radiance across the scene has been sampled spectrally, and spatially, and the noise (discussed in the following subsection) has been added in, the received value is converted to a discrete level by equation 2.27.

$$d(i,j,l) = \text{nint} \left\{ \frac{L_{\text{Image}}(i,j,l)}{L_{\text{Full}}} \cdot (2^Q - 1) \right\} \quad (2.27)$$

Here, Q is the number of radiometric bits of the sensor, and L_{Full} is the published full scale equivalent radiance for sensor band l. This introduces

quantization noise uniformly distributed with an equivalent radiance variance shown in equation 2.28 for each sensor band.

$$\sigma_{\text{quant},l}^2 = \frac{1}{12} \left(\frac{L_{\text{Full},l}}{2^Q - 1} \right)^2 \quad (2.28)$$

2.3.2 Electrical Noise Modeling

Malaret (1982) performed a study of the general noise effects in multispectral sensor systems and their impact on data analysis. In this research, his model for the electrical noise present in these types of sensors will be used, augmented by models for radiometric and calibration errors. Figure 2.23 contains a block diagram of this noise model showing the signal dependent shot noise, thermal noise, radiometric error, and calibration error.

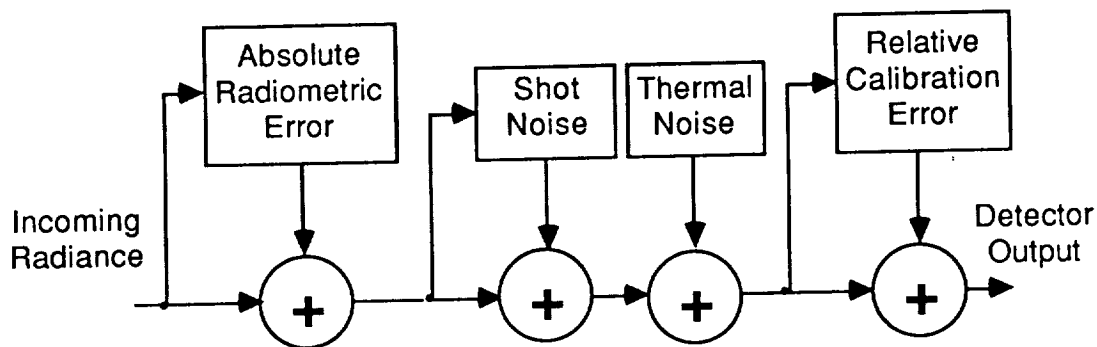


Figure 2.23 Noise Model of Sensor.

In his work, Malaret showed how the shot noise in a multispectral sensor can be modeled as a zero mean Gaussian process with its variance proportional to the signal level (assuming the typical signal levels associated with Landsat sensors.) In this research, the shot noise signal dependence is implemented by having the variance of a Gaussian random number generator proportional to the signal level. These random numbers are then added to the signal level.

Thermal noise has been shown to have a Gaussian distribution also with zero mean and a variance proportional to the product of detector temperature, bandwidth, and resistance. These factors are assumed to be relatively constant, and thus the level of the thermal noise is fixed. It is implemented as a Gaussianly distributed random number added in to the signal level received by the sensor.

Two types of radiometric error are found in the sensor system, absolute and relative calibration error. Absolute errors imply a deterministic change in output level, while relative errors are manifested as stochastic noise. Table 2.14 shows several causes for these errors and the type of error produced.

Table 2.14 Sources and Types of Radiometric Errors.

Error Source	Error Type
Change in transmittance of optics	absolute
Change in gain of detector amplifiers	absolute
Change in characteristics of calibration standard	absolute
Change in detector quantum efficiency	relative

Absolute errors are introduced in the model through additive offset. The level of error is constant across the detectors, but is signal and wavelength dependent. The model for the relative calibration error has been developed under the assumption that each detector channel in the imaging array may undergo a random and independent change in its response over time. Thus, the radiance level required for a given output may differ from detector to detector.

From the statistics given in Castle, et al. (1984) it was determined that the actual output of detectors may vary as much as 1% from the calibrated output given the same input. Assuming an uniform distribution for this error, then the multiplier for the uniform random number generator would be chosen to be $\pm 1\%$ of the signal level. The standard deviation of this error is given in equation 2.29.

$$\sigma_{cal} = \frac{2 * 0.01}{\sqrt{12}} \{ \text{signal level} \} \quad (2.29)$$

Depending on the spatial arrangement of the detectors, the relative calibration error may be constant in one spatial direction. For example, a linear array of detectors may cause relative errors across the image, but since the rest of the image is formed by the motion of the sensor platform, the relative error is constant down the columns of the image. This may cause a vertical striping effect. Or, for a line scanning detector array, the striping may be horizontal as was found in early Landsat MSS sensors. Thus, in implementing the calibration error model, the type and arrangement of detectors must be considered.

2.3.3 HIRIS Model

In this subsection, a model for the High Resolution Imaging Spectrometer (HIRIS) is presented. The instrument is described in Goetz and Herring (1989). HIRIS is meant to be used in an on-demand mode of operation, gathering data at the request of a science investigator. Kerekes and Landgrebe (1989a) present a full description of this instrument and its performance. Table 2.15 contains a brief overview of the instrument and its general design parameters.

Table 2.15 HIRIS Functional Parameters.

Design Altitude	705 Km
Ground IFOV	30 m
Swath Width	20 Km
Spectral Coverage	0.4 - 2.5 μm
	192 Bands
Average Spectral Sample Interval	
0.4 - 1.0 μm	9.4 nm
1.0 - 2.5 μm	11.7 nm
Pointing	
Down-track	+60°/-30°
Cross-track	+20°/-20°
Data Encoding	12 bits/pixel
Maximum Internal Data Rate	512 MBPS
Maximum Output Data Rate	300 MBPS
Image Motion Compensation Gain	1, 2, 4, or 8

For this research the model shown in Figure 2.24 is used for the HIRIS instrument. This model version has 201 equally spaced (10 nm intervals) spectral bands from 0.4 to 2.4 μm and includes most major spectral, spatial, and radiometric effects of the instrument.

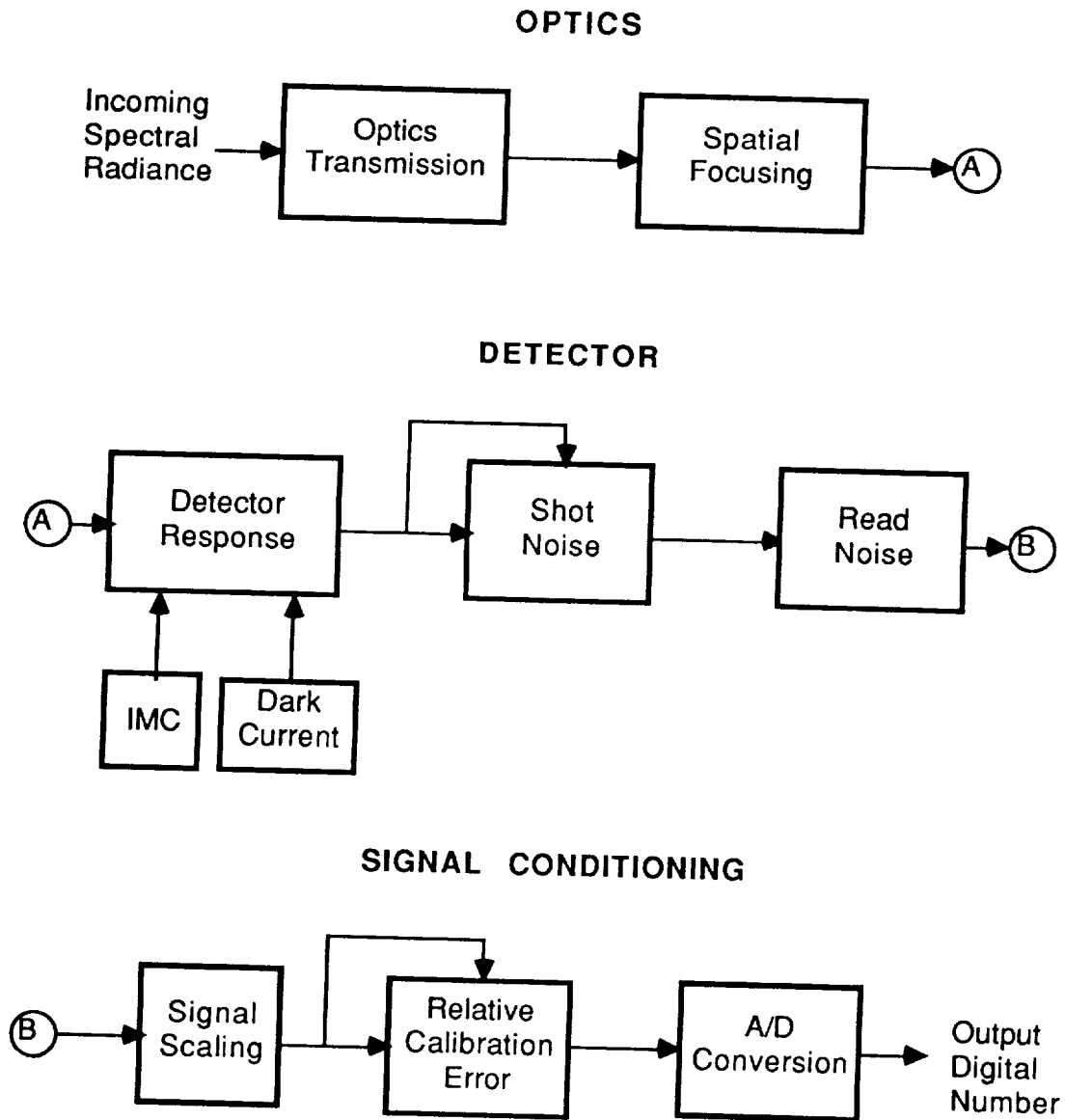


Figure 2.24 HIRIS Model Block Diagram.

Instrument parameters have been obtained from a progress report by JPL (1987). These parameter levels are based upon preliminary specifications and prototype testing. The following paragraphs and figures detail the blocks in the overall diagram and present relevant parameter values.

The sensor has two detector arrays to cover the entire spectral response. The Very Near Infrared (VNIR) array covers 0.4 - 1.0 μm , while the Short Wave Infrared (SWIR) array covers 1.0 - 2.5 μm . The scene is imaged line by line as the sensor passes over. Each scene line is sampled spectrally by being dispersed across the detector arrays.

The spectral transmittance of the instrument optics is shown in Figure 2.25. Note the low response at the spectral gap between the VNIR and the SWIR arrays at 1.0 μm .

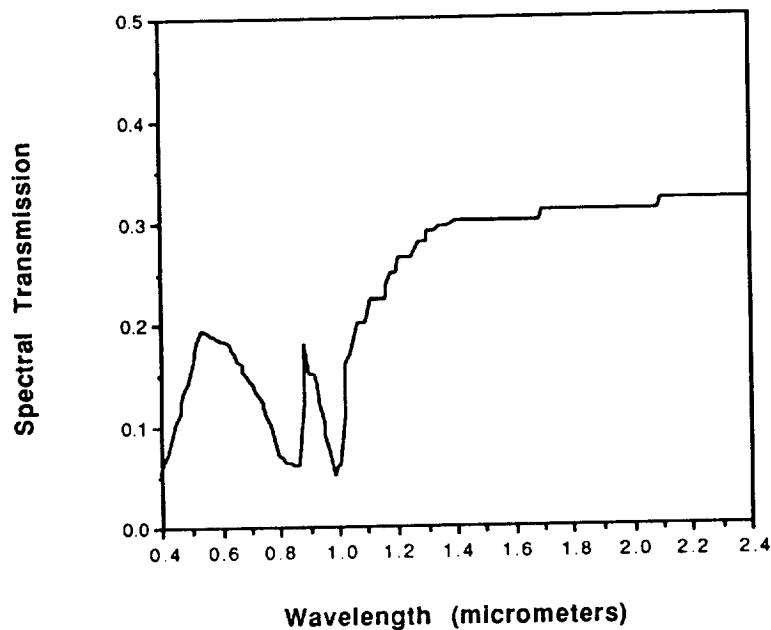


Figure 2.25 Spectral Transmittance of Optics.

The normalized spatial response of the optics and field stop is assumed to be similar to the that of the Landsat Thematic Mapper instrument, as they both

have a Ground Instantaneous Field of View (GIFOV) of 30 meters. Figure 2.26 shows the measured down scene and across scene normalized responses as a function of angular distance for the TM, taken from Markham (1985). The data points shown are the discrete values used in the simulation. At the nominal altitude of the HIRIS instrument, the distance on the ground between these points is approximately seven meters.

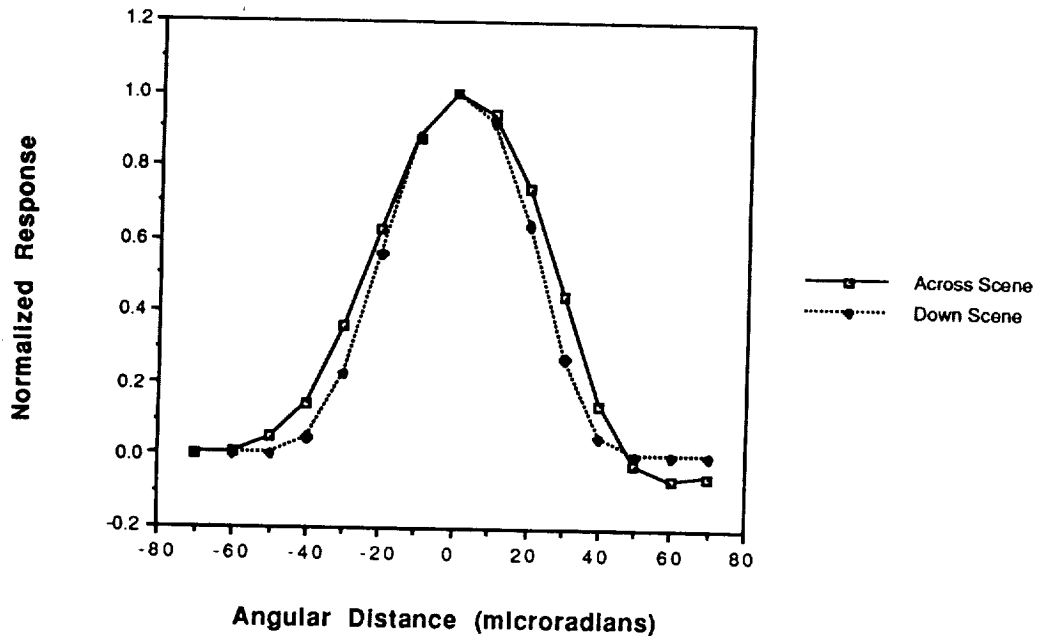


Figure 2.26 Normalized Spatial Response.

The radiometric conversion from the incoming spectral radiance ($\text{mW}/\text{cm}^2\text{-sr-}\mu\text{m}$) is accomplished by dividing by 1000 mW/W , multiplying by the transmittance of the optics and by the $A\Omega$ (the product of the detector area and the solid angle of view) of the optics. The output of the optics model P_λ , the incident spectral power, is then in units of $\text{watts}/\mu\text{m}$. The $A\Omega$ used in the model is $1.44 \times 10^{-6} \text{ cm}^2\text{-sr}$.

The spectral quantum efficiency η of the detectors is shown in Figure 2.27. The incident spectral power P_λ at wavelength λ is converted to a number of electrons S at the detector by the integration of the incident photon level over

the pixel integration time. Thus, the overall radiometric conversion is shown in equation (2.30).

$$S = L_{\lambda, \text{Scene}} \cdot \frac{1000 \text{ mW}}{1 \text{ W}} \cdot A\Omega \cdot T_{\text{optics}} \cdot \Delta\lambda \cdot \eta \cdot \frac{\lambda}{hc} \cdot t \quad (2.30)$$

Where,

$\Delta\lambda = 0.01 \mu\text{m}$, wavelength interval of spectral samples

$\lambda =$ wavelength of interest (μm)

$h = 6.62 \times 10^{-34}$ Joule-sec, Planck's constant

$c = 3 \times 10^8$ meters/sec, the speed of light

$t = 0.0045$ seconds, pixel integration time

$\eta =$ detector quantum efficiency.

Since the noise level data and full scale specifications were obtained in terms of number of electrons, the signal level is stated in these same terms and is unitless.

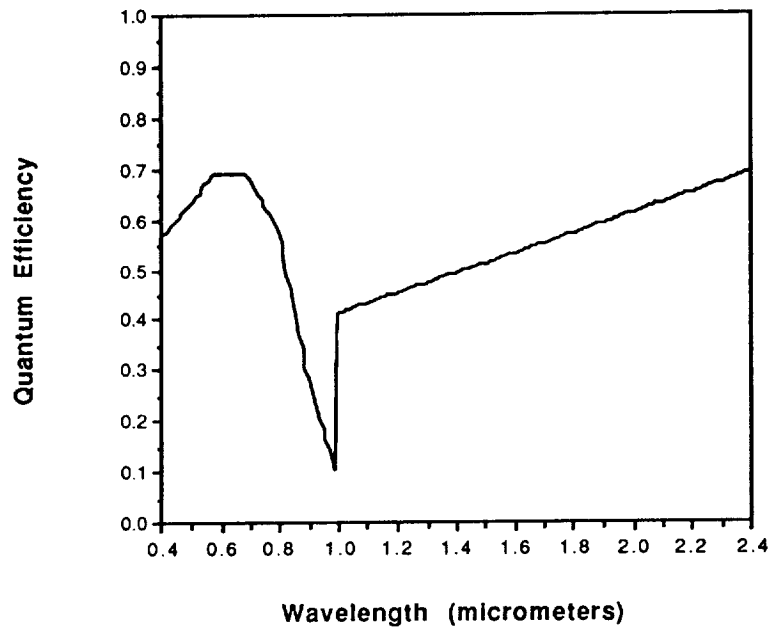


Figure 2.27 Spectral Quantum Efficiency.

The Image Motion Compensation (IMC) is implemented through movement of the down-track pointing mirror to offset the platform speed and effectively multiply the pixel integration time by the gain state selected: 2, 4, or 8.

The noise in this model consists of a deterministic dark signal level and absolute radiometric error, and random shot noise, read noise, and relative calibration error. Thermal noise has been found to be insignificant. All noise is considered to be stochastically independent between noise types and spectral bands. Table 2.16 contains several parameters of the detector arrays.

Table 2.16 Parameters of Detector Arrays in Terms of Electrons (e^-).

	<u>VNIR</u>	<u>SWIR</u>
Dark Current	0 e^-	27000 e^-
Read Noise Standard Deviation	300 e^-	1000 e^-
Full Scale Level	577,395 e^-	1,441,440 e^-

The dark current is simply added to the received signal level in the model. The absolute radiometric error is included in the detector portion of the model by multiplying the total signal by $(1 + E_R)$, where E_R is the decimal level of error. Read noise is added in as a zero mean Gaussian random number with a standard deviation as in Table 2.16. Within each detector array, the read noise level is assumed to be constant over wavelength.

The shot noise in the model consists of zero mean Gaussian random numbers with a standard deviation equal to a function of the total signal level in the detectors. This total signal is comprised of the incoming radiance, and the dark current level mentioned above. Figure 2.28 shows several points relating total signal and shot noise levels taken from the JPL report, along with a curve showing the square root of the total signal. It can be seen that the shot noise level is almost exactly the square root of the total signal level.

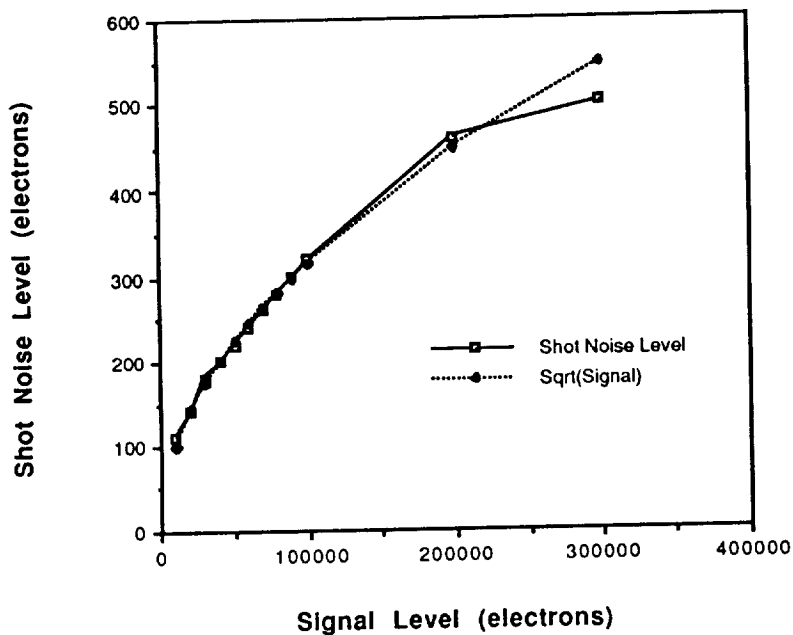


Figure 2.28 Shot Noise vs. Signal Level.

Thus, the standard deviation of the shot noise process is given by equation 2.31.

$$\sigma_{\text{shot}} = \sqrt{S'} \quad (2.31)$$

S' is the total (sum of received signal and dark current) detector signal level in electrons. Note that this relationship is assumed to be independent of wavelength.

The relative calibration error is implemented by adding in uniform random numbers with zero mean and a standard deviation as was given in equation 2.29.

The conversion from the e^- levels S'' (received signal plus noise and calibration error) to a digital number (DN) occurs as in equation 2.32.

$$DN = \text{nint} \left\{ \frac{S''}{IMC \cdot F} \cdot (2^Q - 1) \right\} \quad (2.32)$$

where,

IMC = IMC Gain State

F = Full Scale Electron Level (shown in Table 2.16)

Q = Number of radiometric bits (nominally 12)

The division by the IMC gain state is included to preserve the dynamic range of the detectors over the various gain states.

2.3.4 Radiometric Performance Measures

Several measures of the radiometric performance of remote sensing instruments are commonly used. All of these measures are a function of wavelength, atmospheric conditions, sensor response, and sensor electrical noise. In this subsection, two common ones are described and defined as they are used in this research.

Noise Equivalent change in Reflectance ($NE\Delta\rho$) is used in identifying the smallest differences in the surface reflectance that are detectable by the sensor. It is defined as being the equivalent change in the reflectance of the surface to match the total noise level in the sensor. In terms of the parameters used in this report, this is given in equation 2.33. Note that these parameters are dependent upon the sensor spectral band for which the calculation is being made.

$$NE\Delta\rho = \frac{\sqrt{\sigma_{\text{shot}}^2 + \sigma_{\text{therm}}^2 + \sigma_{\text{read}}^2 + \sigma_{\text{quant}}^2 + \sigma_{\text{cal}}^2}}{\frac{1}{\pi} E_{\lambda, \text{Total}} T_{\lambda, \text{Atm}} B(\lambda)} \quad (2.33)$$

$B(\lambda)$ is the conversion from incident spectral radiance to the signal level in the detector for the appropriate band. For general multispectral scanners,

this is the summation given in equation 2.26, while for the HIRIS model it is the right side of equation 2.30. The resulting signal level is then scaled by the absolute radiometric error $(1+E_R)$.

The Signal-to-Noise Ratio (SNR) is another common measure of performance of a remote sensing instrument. It is commonly expressed as the log of the ratio of the signal level of interest to the total noise level.

In many Earth resource analysis remote sensing applications, the output product is some form of classification map of the observed area. The classification is usually obtained by a computer algorithm that uses the mean and covariances of the multispectral image data to distinguish between the classes. Thus, in this application not only are signal levels important, but so are signal power variations.

In this report, two types of SNR are defined. One based on the mean signal level, while the other is based on the covariance of the received signal. The voltage SNR is useful for determining the dynamic range required of the sensor, while the power SNR is useful for studying the sensitivity of the sensor in discriminating among surface class types.

The voltage SNR is defined for a sensor band by dividing the mean signal level in that band by the square root of the sum of the noise levels for that band, as in equation 2.34.

$$\text{Voltage SNR} = 20 \log_{10} \left\{ \frac{\frac{1}{\pi} E_{\lambda, \text{Total}} T_{\text{Atm}} \bar{\rho} B(\lambda)}{\sqrt{\sigma_{\text{shot}}^2 + \sigma_{\text{therm}}^2 + \sigma_{\text{read}}^2 + \sigma_{\text{quant}}^2 + \sigma_{\text{cal}}^2}} \right\} \quad (2.34)$$

Here, $\bar{\rho}$ is the mean reflectance of the surface, and $B(\lambda)$ is defined as above. The power SNR is defined for one wavelength m in the HIRIS model to be as in equation 2.35.

$$\text{Power SNR} = 10 \log_{10} \left\{ \frac{\sigma_m^2 \left[\frac{1}{\pi} E_{\lambda, \text{Total}} T_{\lambda, \text{Atm}} B(\lambda=m) \right]^2}{\sigma_{\text{shot}}^2 + \sigma_{\text{read}}^2 + \sigma_{\text{quant}}^2 + \sigma_{\text{cal}}^2} \right\} \quad (2.35)$$

Here, σ_m^2 is the variance of the surface reflectance for wavelength m . In calculating the SNR for a particular scene, the mean and variance of the surface reflectance are usually calculated from the combined data set of all classes represented in the scene.

In computing the power SNR for the multispectral scanners, or for features derived from the HIRIS sensor by combining bands, the signal levels cannot be simply added because of the band-to-band correlation present in the reflectance data. In these cases, the signal variance is the sum of the individual variances, plus terms due to the covariance between each pair of wavelengths m and n , combined in the feature as in equation 2.36.

$$\text{Combined Power SNR} = 10 \log_{10} \left\{ \frac{\sum_{m=1}^{M_L} \sum_{n=1}^{M_L} \sigma_{mn} B^+(\lambda=m) B^+(\lambda=n)}{\sigma_{\text{shot}}^2 + \sigma_{\text{therm}}^2 + \sigma_{\text{read}}^2 + \sigma_{\text{quant}}^2 + \sigma_{\text{cal}}^2} \right\} \quad (2.36)$$

M_L is the number of wavelengths combined for the band or feature, while $B^+(\lambda)$ is the product of the radiance received from a completely reflecting surface and the conversion to the signal level in the sensor for the appropriate wavelength. The m,n entry in the reflectance spectral covariance matrix is denoted here as σ_{mn} . Also, the noise variances as used here are the sum of the individual wavelength variances combined appropriately.

2.4. Processing

Processing plays the most important role in remote sensing systems as it is the part that provides the information that the system is designed to acquire. Aspects of processing in remote sensing are discussed in chapters 17 through

24 of Colwell (1983), chapters three through six of Swain and Davis (1978), and in the text by Richards (1986). Numerous other texts and articles have been published dealing with the processing of remotely sensed images.

Table 2.17 shows a list of typical functions used in the processing of remotely sensed images. The task of the processing portion of the system is to **take the multispectral image** from the sensor, and any other input data or algorithms, and then compute an output information product. This product may be a classification map showing to which of the informational classes each pixel belongs, or it may be a summary of the total area within the image that belongs to each of the classes. The processing functions shown in Table 2.17 aid in this task by allowing the information to be obtained efficiently and accurately.

Table 2.17 Example Processing Functions.

<u>Processing Type</u>	<u>Example</u>
Radiometric	Calibration Scaling Compression/ Decompression
Geometric	Registration Resampling
Data Reduction	Feature Extraction Feature Compression
Class Separability	Training Field Selection Interclass Distance Intraclass Distance
Classification	Unsupervised (Clustering) Supervised Class Area Measures

In the rest of this section these processing functions are discussed, and where appropriate, models are presented for use in the simulation of remote sensing systems.

2.4.1 Radiometric Processing

The goal of radiometric processing is to allow accurate and repeatable calibration of the radiance levels represented by the digital numbers in the multispectral image. This is important when comparing images over the same area from different dates or sensors. Price (1987) discusses the accurate calibration of several sensors for comparative purposes. Papers by Fischel (1984), Murphy, et al., (1984), and Castle, et al., (1984) discuss the calibration of the Landsat Thematic Mapper sensor.

For modeling purposes, the calibration models presented in section 2.3.2 are useful in studying the effect of these radiometric errors.

2.4.2 Geometric Processing

Geometric processing is generally concerned with correcting spatial distortions in the multispectral image due to scanning variations, detector misalignment, or view angle effects. The aim of such processing is again to allow comparison of images, or to match images to other forms of spatial data such as topographical or land use maps.

Spatial distortions are often corrected by developing a mapping function from the image to the control map by using identifiable features (control points) in the scene. Pixels in between these points are often resampled to give a desired spatial resolution. The papers by Park, et al., (1982 and 1984), and Schowengerdt, et al., (1984) discuss the effects of these corrections.

Another form of geometric distortion is known as misregistration, and is due to the effective misalignment of detectors of the various spectral bands. This may occur due to distortion in the imaging optics, or to the physical location of the detectors. It effectively causes the pixels of different bands to be imaged from a slightly different part of the scene. Misregistration has been studied by Cicone, et al., (1976), Billingsley (1982), and Swain, et al., (1982). In the study by Swain, et al., it was found that misregistration by as little as 0.3 pixels can affect classification accuracy.

Although they would be relatively straightforward to implement in the sensor spatial model, these forms of geometric distortion were not studied in this research.

2.4.3 Data Reduction

In most cases it is either necessary, or at least advantageous, to reduce the amount of data in a multispectral image without diminishing the informational content. In the case of the upcoming HIRIS instrument the normal operating mode produces data at a rate exceeding the capabilities of the satellite's communication channel, thus necessitating some form of on-board editing. For lower dimensional sensors such as Landsat TM or aircraft scanners, it has been shown that under conditions of limited training samples, classification accuracy decreases as more spectral bands are used in the classification (see Hughes, 1968, and Chandrasekaran, 1975.)

This data reduction may be accomplished spatially, spectrally, or by reducing the radiometric resolution of the data. The spatial reduction may be as simple as deleting every other pixel or reducing the swath width of the sensor, or as complex as a scheme described in Ghassemian (1988) which retains much of the spatial detail in the image while reducing the data to a set of features. Reducing the radiometric resolution may be used and usually will not increase the noise level significantly, unless the quantization error becomes the dominant source of noise in the image.

Spectral reduction through the Karhunen-Loeve (or principal component) transformation was studied in Ready and Wintz (1974). This method has proved to be useful in reducing dimensionality while retaining class separability, even in cases of limited training samples (Kalayeh, et al., 1983, and Muasher and Landgrebe, 1983). However, it requires computation of the eigenstructure of the covariance matrix and thus is not easily implemented at high data rates.

With the advent of imaging spectrometers such as HIRIS, on-board feature selection algorithms that can be implemented through simple programmable operations, such as summations, have been studied. Chen and Landgrebe (1988) have extended a method first proposed by Wiersma and

Landgrebe (1980) to select spectral regions to be combined. The algorithm uses training samples from similar data, or ground reflectance, and selects wavelengths to be combined based upon the eigenfunctions of the spectral covariance matrix. A simple set of summation coefficients may then be transmitted to the satellite and used to reduce the data rate. Factors of data reduction of 10 or more have been found to be possible with little loss in the class recognition accuracy (Chen, 1988).

In the simulation program developed in this report, data reduction may be accomplished for the HIRIS model through the combination or weighted summation of spectral bands.

2.4.4 Class Separability Measures

Class separability measures are computed from the statistics of known class samples, and are used to obtain an idea of the statistical distance between informational classes. These measures have been studied both as a feature selection technique (Swain and King, 1973), as well as an estimate of error probability (Kailath, 1967, and Whitsitt and Landgrebe, 1977.)

Many of these separability measures are for two classes, and are computed from the mean vectors and covariance matrices. As an example, the Bhattacharyya distance B_{kl} is given in equation 2.37 between class k and class l with mean vectors \bar{Z}_k and \bar{Z}_l , and covariance matrices Σ_k and Σ_l .

$$B_{kl} = \frac{1}{8} (\bar{Z}_k - \bar{Z}_l)^T \left(\frac{\Sigma_k + \Sigma_l}{2} \right)^{-1} (\bar{Z}_k - \bar{Z}_l) + \frac{1}{2} \log_e \left[\frac{\left| \frac{\Sigma_k + \Sigma_l}{2} \right|}{\sqrt{|\Sigma_k| |\Sigma_l|}} \right] \quad (2.37)$$

Multiclass separability measures can be obtained from apriori class probability weighted pairwise summations of such two class separability measures. Whitsitt and Landgrebe (1977) discuss this and other ways of measuring multiclass separability.

Fukanaga (1972) also presents a multiclass separability measure that is used in canonical analysis to reduce the dimensionality of data through a linear transformation (Merembeck and Turner, 1980). This measure J_F is described by equation 2.38.

$$J_F = \text{tr } S_W^{-1} S_b \quad (2.38)$$

where,

$$S_W = \sum_{k=1}^K P_k \Sigma_k$$

$$S_b = \sum_{k=1}^K P_k (\bar{Z}_k - \bar{Z}_0) (\bar{Z}_k - \bar{Z}_0)^T$$

$$\bar{Z}_0 = \sum_{k=1}^K P_k \bar{Z}_k$$

In these equations, P_k is the apriori probability of class k , and the mean vectors and covariance matrices are noted above.

In the simulation program, both a pairwise summation of the Bhattacharyya distance and the Fukanaga multiclass measure are implemented. The class statistics are computed from designated areas within the known class areas.

2.4.5 Classification Algorithms

The classification of a multispectral image into informational classes may be done in an unsupervised manner by a computer algorithm, or in a supervised approach by an analyst working interactively with the computer. In either case, the accuracy of such a classification can then be computed by comparing the resulting class map to a known class map of the area. Classification accuracy has also been estimated from the class statistics. Fukanaga and Krile (1969) present an analytical method for estimating accuracy in the two class Gaussian case, while Whitsitt and Landgrebe (1977) discuss several considerations in multiclass error estimation.

In unsupervised classification, the data vectors are grouped into separable classes through clustering algorithms (Duda and Hart, 1973.) These algorithms group data vectors that are "similar" in a statistical sense into spectral classes. These spectral classes are then either subdivided or combined to form the desired informational classes.

Supervised classification is done by developing training statistics, either through locating known class areas in the image, or by applying a clustering algorithm to help identify possible classes. Various classification algorithms can then be applied to all of the pixels in the image and assign them to an informational class.

For the simulation program, a supervised classification technique using the Maximum Likelihood (ML) classification algorithm has been implemented. The ML classifier uses the standard Gaussian assumption with class apriori probabilities dependent on the numbers of pixels in each class. Since the scene is defined in the simulation, the class boundaries are known in the image and a classification accuracy can be computed directly. Class statistics are computed from designated training areas. The classification can be done on the original image, or on the compressed image if the sensor was an imaging spectrometer type.

The classifier works by assigning each pixel the class label that provides the maximum value of probability as coming from that class. That is, a pixel $Z(i,j)$ is assigned to class k' if $g_{k'}(i,j) > g_k(i,j)$ for all classes k in the scene, where g_k is defined in equation 2.39. L is the dimension of the class statistics.

$$g_k(i,j) = \frac{P_k}{(2\pi)^{L/2} |\Sigma_k|^{1/2}} \exp \left\{ -\frac{1}{2} [Z(i,j) - \bar{Z}_k]^T \Sigma_k^{-1} [Z(i,j) - \bar{Z}_k] \right\} \quad (2.39)$$

2.5 Summary and Discussion

In this chapter, the modeling of optical remote sensing systems has been discussed from a general viewpoint as well as one of simulation. The models

discussed represent an understanding of the system. Obviously, these models cannot describe all of the effects and processes in the real system, but they represent a level of understanding of duplicating the real world in the computer laboratory.

Table 2.18 presents a summary of the various aspects of the remote sensing system that have had models described in this chapter and implemented in the system simulation program RSSIM (Kerekes and Landgrebe, 1989b).

Table 2.18 Summary of System Parameters Implemented in Simulation.

Scene	Sensor	Processing
Spectral Means	Spatial Response	Training Field Selection
Spectral Covariance	Spectral Response	Feature Selection
Spatial Correlation	Electrical Noise (Shot, Thermal, and Read)	Class Separability
Spatial Layout	Absolute Radiometric Error	Class Accuracy
Direct Solar Irradiance	Relative Calibration Error	Classification Map
Diffuse Solar Irradiance	Radiometric Resolution	
Atmospheric Transmittance	Detector Gain	
Scattered Path Radiance		
Zenith Angle of Sun		
Zenith Angle of Sensor		
Meteorological Range		

While there are many effects not described in this table, it represents a comprehensive framework from which to study their interrelated effects on system performance.

CHAPTER 3

ANALYTICAL SYSTEM MODEL

3.1 Model Overview

The system model described in chapter two gave a tool to allow accurate modeling and simulation of a remote sensing system. However, because of the flexibility and completeness, it may represent too much detail for some system studies. A simpler approach may be obtained by using some of the component models described in chapter two, and the work of several previous researchers, to develop a purely analytical system model.

Figure 3.1 shows a block diagram of the analytical model presented in this chapter. At each stage in the system model, the mean vector and covariance matrix of each class are modified by the function in that block.

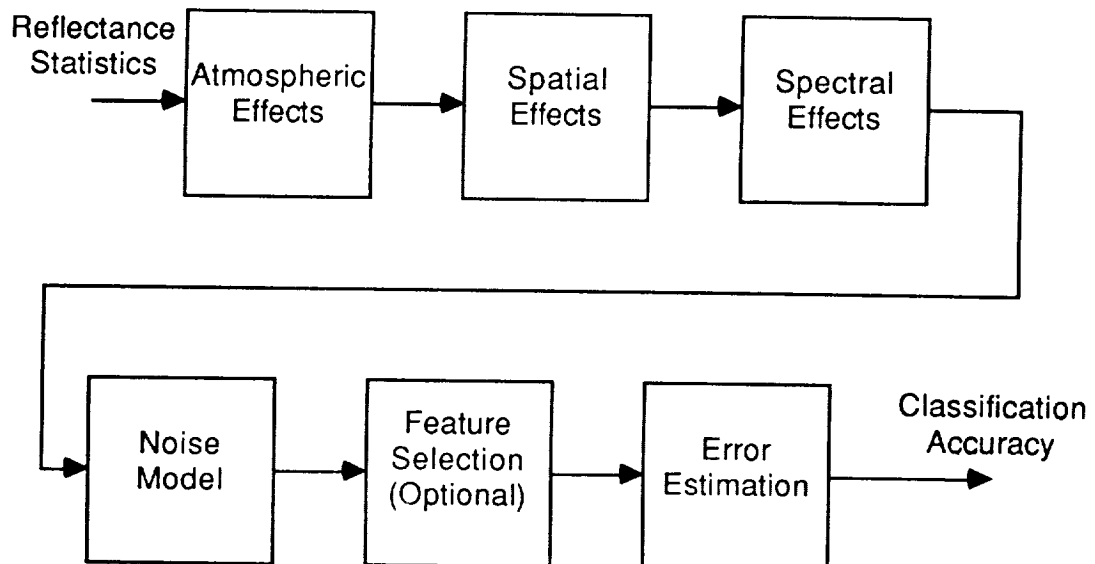


Figure 3.1 Analytical System Model Block Diagram.

A brief description of these blocks and their assumptions is given in the following paragraphs.

Reflectance Statistics - Each surface cover class is assumed to be multivariate Gaussian described by the mean vector and covariance matrix of the reflectance. The surface reflectance is also assumed to have a separable exponential spatial correlation.

Solar Illumination and Atmosphere - The linear atmospheric effects model described in chapter two is used here.

Spatial Effects - The spatial response of the sensor is assumed to have the shape of a Gaussian probability distribution function and be circularly symmetric.

Spectral Effects - This is a linear transformation to convert the scene spectral radiance to the received signal in the spectral bands of the sensor. In the case of the HIRIS model, the spectral resolutions are equal and this matrix is diagonal.

Noise Model - The various types of noise described in chapter two are added in here. They are assumed to be zero mean, and uncorrelated between noise type and spectral band.

Feature Selection - This is another linear transformation, and is used to combine sensor bands together for spectral compression.

Error Estimation - The pairwise Bhattacharyya distance is calculated from the modified class statistics, and used to estimate the error. Equal a priori probabilities are assumed and the multiclass error is the sum of the pairwise errors.

A listing of the FORTRAN program implementing the model discussed in this chapter for the model HIRIS sensor is included in Appendix E.

3.2 Analytical Expressions

This section presents the equations that form the analytical model. The model first applies the system functions to the statistics of each of the K classes, then computes the pairwise error estimates.

3.2.1 Reflectance Statistics

The surface reflectance is assumed to be spectrally multivariate Gaussian with a spatial correlation described by a separable exponential model.

The spectral reflectance statistics are computed from the database of FSS field spectra. To take full advantage of the spectral resolution considered in this research, the data is first interpolated to 10 nm wavelength spacing by using the algorithm presented in Appendix B. Thus, for each class k the mean vector \bar{X}_k and the covariance matrix Σ_k will have $M = 201$ dimensions.

The spatial model has a crosscorrelation function for wavelengths m and n as shown in equation 3.1.

$$R_{mn}(\tau, \eta) = e^{-a_{mn}|\tau|} e^{-b_{mn}|\eta|} \quad (3.1)$$

This form yields spatial crosscorrelation coefficients $\rho_{mn,x}$ for across the scene, and $\rho_{mn,y}$ for down scene as shown in equations 3.2 and 3.3.

$$\rho_{mn,x} = e^{-a_{mn}} \quad (3.2)$$

$$\rho_{mn,y} = e^{-b_{mn}} \quad (3.3)$$

For the model implemented in this chapter, the spatial correlation coefficients have been assumed to be constant across all spectral wavelengths.

3.2.2 Atmospheric Effects

The atmospheric effects model converts the scene reflectance to the spectral radiance received by the sensor. Equation 3.4 shows the spectral radiance L_λ received by the sensor.

$$L_\lambda = L_{\lambda,S} X + L_{\lambda,Path}^0 + \left[L_{\lambda,Path}^1 - L_{\lambda,Path}^0 \right] X_A \quad (3.4)$$

X is the surface reflectance in the sensor IFOV, while X_A is the average reflectance around this area and represents the source of the adjacency effect discussed in chapter two. For this model, the adjacent reflectance X_A is considered to be the average reflectance of all K classes. It is also considered to be uncorrelated with the reflectance within the sensor IFOV.

$L_{\lambda,Path}^1$, and $L_{\lambda,Path}^0$ are the path spectral radiance components for surface albedoes of 1 and 0, respectively. $L_{\lambda,S}$, the spectral radiance reflected from a perfectly reflecting surface, is as shown in equation 3.5.

$$L_{\lambda,S} = \frac{1}{\pi} \left[\cos(\theta_{solar}) E_{\lambda,Direct} + E_{\lambda,Diffuse} \right] T_{\lambda,Atm} \quad (3.5)$$

Thus after the application of the atmospheric effects function, the mean and covariance of the signal radiance is as follows. The mean spectral radiance is given by equation 3.6.

$$\overline{L}_\lambda = L_{\lambda,S} \overline{X} + L_{\lambda,Path}^0 + L_{\lambda,Path}^{1-0} \overline{X}_A \quad (3.6)$$

$L_{\lambda,Path}^{1-0}$ is the difference between the path radiances for a surface albedo of 1 and 0. The spectral radiance covariance matrix Σ_{L_λ} is derived as follows for each row m , column n entry $\sigma_{L,mn}$.

$$\sigma_{L,mn} = E\left\{\left(L_m - \bar{L}_m\right)\left(L_n - \bar{L}_n\right)\right\} \quad (3.7)$$

$$= E\left\{\left(\begin{array}{l} \left(L_{m,S}X_m + L_{m,Path}^0 + L_{m,Path}^{1-0}X_{A,m} - L_{m,S}\bar{X}_m - L_{m,Path}^0 - L_{m,Path}^{1-0}\bar{X}_{A,m}\right) \cdot \\ \left(L_{n,S}X_n + L_{n,Path}^0 + L_{n,Path}^{1-0}X_{A,n} - L_{n,S}\bar{X}_n - L_{n,Path}^0 - L_{n,Path}^{1-0}\bar{X}_{A,n}\right) \end{array}\right)\right\} \quad (3.8)$$

$$= L_{m,S}\sigma_{X,mn}L_{n,S} + L_{m,Path}^{1-0}\sigma_{A,mn}L_{n,Path}^{1-0} \quad (3.9)$$

Here, $\sigma_{X,mn}$ is the mn entry of the reflectance covariance matrix Σ_k , while $\sigma_{A,mn}$ is the mn entry of the covariance matrix Σ_A of the averaged reflectance, which is given in equation 3.10.

$$\Sigma_A = \frac{1}{K^2} \left(\Sigma_1 + \Sigma_2 + \dots + \Sigma_K \right) \quad (3.10)$$

In the derivation of Σ_A , the reflectances averaged are considered to be uncorrelated with each other.

3.2.3 Spatial Effects

The spatial effects function uses the results of Mobasseri, et al., (1978) to modify the spectral radiance covariance matrix. The separable exponential spatial correlation model of equation 3.1 is assumed for the scene, along with a Gaussian PSF for the sensor as shown in equation 3.11.

$$h(u,v) = \frac{1}{2\pi\sigma_o^2} \exp\left(-\frac{u^2 + v^2}{2\sigma_o^2}\right) \quad (3.11)$$

Since σ_o is related to the size of the sensor IFOV in scene cells, as the sensor look angle changes it must be modified to reflect the change in ground

size of the IFOV. The spatial direction that this occurs is dependent upon the relative azimuthal angle of the sensor and the ground reference axis. For simplicity, the sensor azimuth is defined to be 0° . Thus, in terms of $r_{o,x}$, and $r_{o,y}$, parameters used below in the weighting function, σ_o is modified as in equations 3.12, and 3.13.

$$r_{o,x} = \sqrt{2} \sigma_o \quad (3.12)$$

$$r_{o,y} = \frac{\sqrt{2} \sigma_o}{\cos(\theta_{\text{view}})} \quad (3.13)$$

Mobasseri defined a weighting matrix W_s that is a function of the spatial model and PSF parameters. Following his results, the sensor spatial response modifies each mn entry in Σ_{L_λ} as in equation 3.14.

$$\sigma_{L,mn}^S = W_s^{mn} \sigma_{L,mn} \quad (3.14)$$

Where,

$$W_s^{mn} = 4 \exp\left\{\left(\frac{a_{mn}^2 + b_{mn}^2}{2}\right) r_{o,x} r_{o,y}\right\} \text{erfc}(a r_{o,x}) \text{erfc}(b r_{o,y}) \quad (3.15)$$

and, $\text{erfc}(\cdot)$ is defined as in equation 3.16.

$$\text{erfc}(\alpha) = \frac{1}{\sqrt{2\pi}} \int_{\alpha}^{\infty} e^{-\frac{x^2}{2}} dx \quad (3.16)$$

Since the spatial correlation coefficients have been assumed to be constant across spectral wavelengths, the parameter W_s^{mn} is constant for all mn . If one uses differing a and b , care must be taken to ensure the resulting covariance matrix remains nonsingular.

Thus, equation 3.14 gives a new $\sum_{L_\lambda}^S$ that represents the spectral radiance covariance matrix after application of the spatial effects. The mean spectral radiance vector is unchanged by the spatial model as shown in equation 3.17.

$$\overline{L_\lambda^S} = \overline{L_\lambda} \quad (3.17)$$

3.2.4 Spectral Effects

The sensor spectral effects are applied by a linear transformation matrix B which converts the spectral radiance to the signal levels in each of the sensor image bands. For the line scanner sensors with L bands, this matrix is L rows by M columns, with each row consisting of the normalized response of that band to each of the M wavelengths of the spectral radiance. Also, each entry in the matrix is multiplied by $\Delta\lambda$, the spectral resolution of the spectral radiance vectors. The resulting signals will be in terms of radiances. Thus, this matrix B is formed as in equation 3.18.

$$B = \Delta\lambda \begin{bmatrix} \text{Band 1 Response} \\ \text{Band 2 Response} \\ \vdots \\ \text{Band L Response} \end{bmatrix} \quad L \times M \quad (3.18)$$

For the HIRIS imaging spectrometer with the same spectral resolution as the scene, the matrix will be diagonal M by M with each entry b_{mm} as shown in equation 3.19.

$$b_{mm} = A\Omega \cdot \Delta\lambda \cdot \frac{\lambda}{hc} \cdot t \cdot T_{\text{optics}} \cdot \eta \quad (3.19)$$

The various symbols are defined in section 2.3.3 of chapter two. The resulting signal will be in electrons.

For either sensor type, the mean received signal vector is thus obtained by

$$\bar{S} = B L_{\lambda}^{\bar{S}} \quad (3.20)$$

while the signal covariance is as shown in equation 3.21.

$$\Sigma_S = B \Sigma_{L_{\lambda}^S} B^T \quad (3.21)$$

3.2.5 Noise Model

The noise effects are modeled as zero mean random processes, except for the deterministic absolute radiometric error E_R and detector dark current D . These deterministic effects are added directly to the mean signal vector to yield the noisy mean vector \bar{Y} as in equation 3.22.

$$\bar{Y} = \bar{S} (1 + E_R) + D \quad (3.22)$$

The random noise sources modeled include shot noise, thermal noise, read noise, quantization error, and relative calibration error. The form of these models was discussed in section 2.3.2 of chapter two. In his thesis, Malaret (1982) showed how these sources of noise affect the covariance matrix of the signals received by the sensor. The result used here is that while some of the noise may be dependent upon the signal (shot and calibration error), they are still uncorrelated with the signal and the variances add directly. Also, each noise source is assumed to be independent of the others and uncorrelated from spectral band to spectral band. Thus, the signal covariance is modified as in equation 3.23.

$$\Sigma_Y = (1+E_R)^2 \Sigma_S + \Lambda_{\text{therm}} + \Lambda_{\text{shot}} + \Lambda_{\text{read}} + \Lambda_{\text{quant}} + \Lambda_{\text{cal}} \quad (3.23)$$

Here, the Λ 's are diagonal matrices of the variances in each sensor band of the various noise sources.

3.2.6 Feature Selection

Feature selection is optionally applied by combining the sensor bands according a weighting matrix F to create the features Z as in equations 3.24 and 3.25.

$$\bar{Z} = F\bar{Y} \quad (3.24)$$

$$\Sigma_Z = F \Sigma_Y F^T \quad (3.25)$$

To transform the L-dimensional vectors Y to the N-dimensional feature space, F is N rows by L columns of weighting coefficients. For the spectral feature compression scheme described in section 2.4.3 of chapter two, these coefficients are just 0 and 1 to appropriately skip or combine the sensor bands.

As an example, consider a transformation for the output of the HIRIS model to two features. Let feature 1 be the combination of the first five wavelengths 0.40 - 0.44 μm , while feature 2 be the combination of the last five wavelengths 2.36 - 2.40 μm . The matrix F for this example is shown in equation 3.26.

$$F = \begin{bmatrix} 1 & 1 & 1 & 1 & 1 & 0 & 0 & \dots & 0 & 0 & 0 & 0 & 0 & 0 & 0 \\ 0 & 0 & 0 & 0 & 0 & 0 & 0 & \dots & 0 & 1 & 1 & 1 & 1 & 1 \end{bmatrix}_{2 \times 201} \quad (3.26)$$

3.2.7 Error Estimation

After the class statistics of each class has been modified by the above functions, an estimate of the probability of error is made. Whitsitt (1977) discussed a pairwise error estimate based upon the mean and covariance

statistics and found it to be closely related to the actual classification error. Equation 3.27 shows this estimate of probability of error P_e which uses the Bhattacharyya distance B_{kl} between classes k and l defined in section 2.4.4 of chapter two.

$$P_e^{kl} = \text{erfc} \left\{ \sqrt{2B_{kl}} \right\} \quad (3.27)$$

Whitsitt also discussed an upper bound on the probability of error in the multiclass case as being the sum of the pairwise error estimates. Thus, in the model the following estimate for the classification accuracy \hat{P}_c (in percent) is used.

$$\hat{P}_c = 100 \left[1 - \sum_{k=1}^K \sum_{l=1 \neq k}^K P_e^{kl} \right] \quad (3.28)$$

Since the summation of the pairwise errors is an upper bound, this estimate of the classification accuracy will be pessimistic in multiclass experiments.

3.3 Comparison Between the Analytical and Simulation Models

While the analytical model offers the advantages of being simpler, and computationally more efficient, it lacks in being able to accurately represent the real world as compared to the simulation model. Table 3.1 lists several factors that the analytical model is not able to represent at present.

Table 3.1 System Factors Not Included In Analytical Model.

Size and Spatial Arrangements of Fields Mixed Pixels at Field Borders Non Gaussian Sensor PSF Training Field Selection and Size
--

These factors can be significant. Section 4.3 of chapter four presents some results of comparing the accuracy estimate of the analytical and simulation models.

Another difference between the modeling approaches is that the analytical model works in a parametric space, while the simulation model produces multispectral images that can be displayed and processed like real ones. This advantage of the simulation approach is useful for the development of processing algorithms when "real" data is not available.

CHAPTER 4

APPLICATION TO

IMAGING SPECTROMETER SYSTEM ANALYSIS

4.1 Introduction

In this chapter, the system models presented in this report are applied to the study of system performance using a proposed imaging spectrometer. The HIRIS (Goetz and Herring, 1989) instrument is proposed as part of the Earth Observing System program that will drive the international remote sensing effort into the 1990's. It was chosen for study for the following reasons.

- It leads the next generation of sophisticated remote sensing instruments.
- Being in the design phase, its performance can only be predicted through modeling and simulation.
- Since it will be operated in an on-demand mode, it is important to develop an understanding of the system performance under varying observational conditions.
- Because of its flexibility of parameters, it may be used to simulate other sophisticated sensors and study their performance.
- The complexity of the instrument puts it close to the fundamental limits of technology, and its study helps gain a basic understanding of the remote sensing process.

The following sections describe the performance of this instrument for a variety of system configurations and performance measures. The first part presents the radiometric performance of the sensor with curves showing the Signal-to-Noise Ratio (SNR) and Noise Equivalent Change in Reflectance ($NE\Delta\rho$) under a variety of conditions. It is followed by a comparison of the

performance of the simulation and analytical modeling approaches to system analysis. This section is included to illustrate the limits of each approach. The rest of the chapter explores the effect on classification performance of several system parameters.

For many of the experiments performed in this chapter, the reflectance statistics used were from a test site in Finney County, Kansas. Table 4.1 provides a description of this data set.

Table 4.1 Kansas Winter Wheat Data Set.

Location	Finney County, Kansas	
Date	May 3, 1977	
LARS Experiment Number	77102207	
LARS Data Tape Number	4260	
<u>Spectral Classes</u>	<u>Number of Fields</u>	<u>Number of Samples</u>
Winter Wheat	25	658
Summer Fallow	6	211
Unknown	39	682

4.2 Radiometric Performance

To gain an understanding of the radiometric performance of HIRIS under a variety of conditions, the model described in chapter two was used to examine their effect on SNR and $NE\Delta\rho$.

For the results included in this section, the system configuration shown in Table 4.2 was used as a baseline. The solar illumination and atmospheric effects were obtained using the LOWTRAN 7 computer code.

Before presenting the results of these noise studies, it may be helpful to present an example of instrument performance for a typical vegetative scene. Reflectance data from all three classes from the data set of Table 4.1 were combined to form a new data ensemble. The mean reflectance and variation of this ensemble are plotted in Figure 4.1.

Table 4.2 Radiometric Study Baseline System Configuration.

Atmospheric Model	1976 US Standard
Haze Parameter	Rural Extinction
Aerosols	Mie-Generated
Diffuse Irradiance Constant	0.84
Surface Meteorological Range	16 Km
Solar Zenith Angle	30°
Solar Azimuth Angle	180°
View Zenith Angle	0°
View Azimuth Angle	0°
Surface Albedo	0.10
IMC Gain State	1
Shot and Read Noise	Nominal
Radiometric and Calibration Error	0%
Radiometric Resolution	12 bits

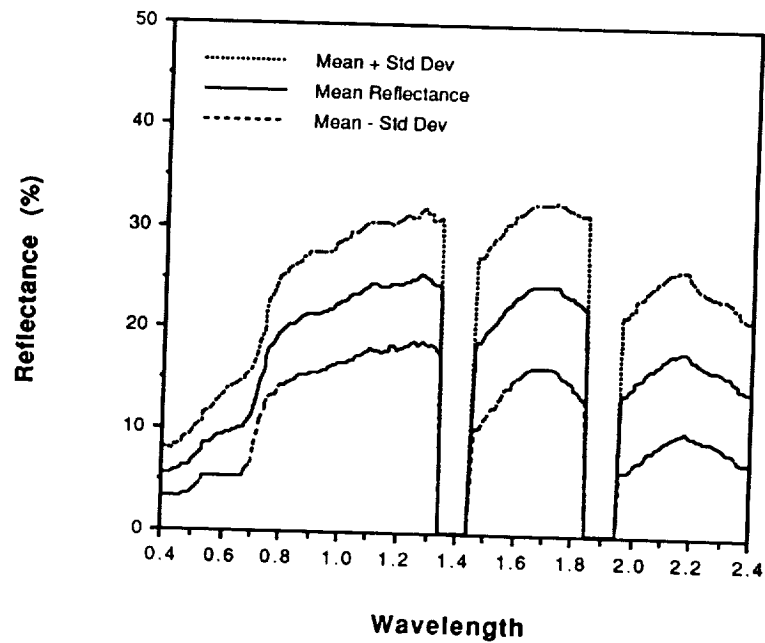


Figure 4.1 Mean and Variation of the Surface Reflectance of the Kansas Winter Wheat Data Set of Table 4.1.

To obtain an idea of how this reflectance is modified by the atmosphere and sensor response, a simulated image was created using the baseline system configuration. The resulting mean digital counts and their variation are shown in Figure 4.2. Several effects are immediately noticeable. The absorption bands of the atmosphere are present, as well as a reversal in the relative values of the visible and infrared amplitudes. This reversal is due to the effects of the solar illumination and gain settings of the sensor.

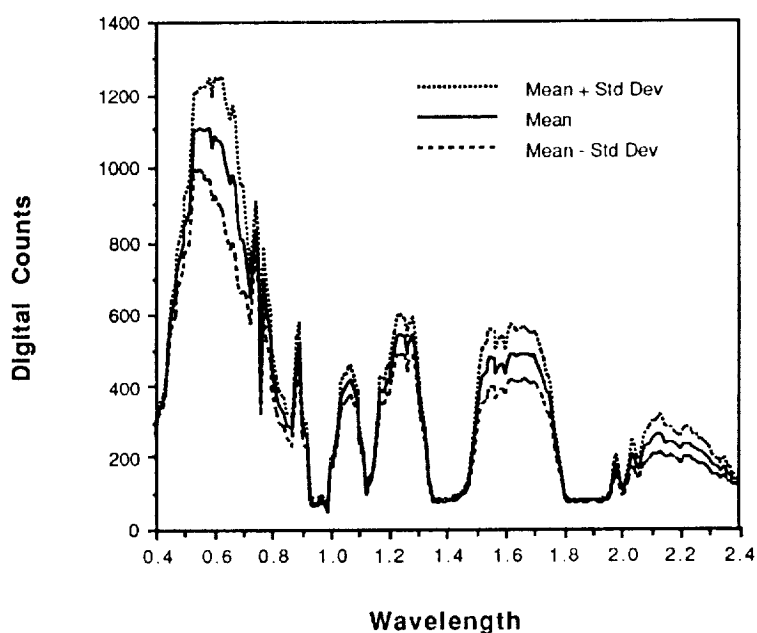


Figure 4.2 Mean and Variation of the Image Vector as Received by HIRIS.

The voltage and power SNR for this configuration and typical surface reflectance are shown in Figure 4.3. The power SNR shown here and in the rest of the chapter was calculated with the signal covariances scaled by the spatial weight function W_s^{mn} discussed in chapter three. The $NE\Delta\rho$ is shown in Figure 4.4.

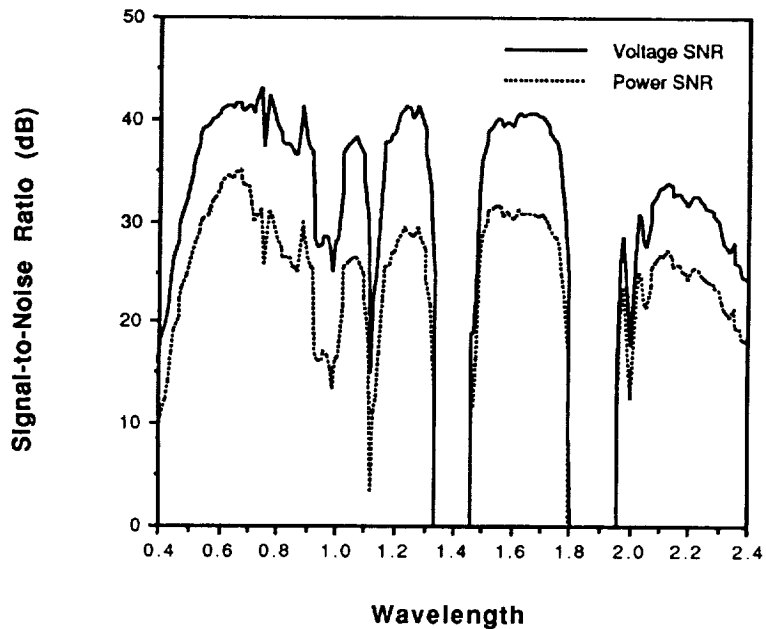


Figure 4.3 Voltage and Power SNR for Typical Reflectance.

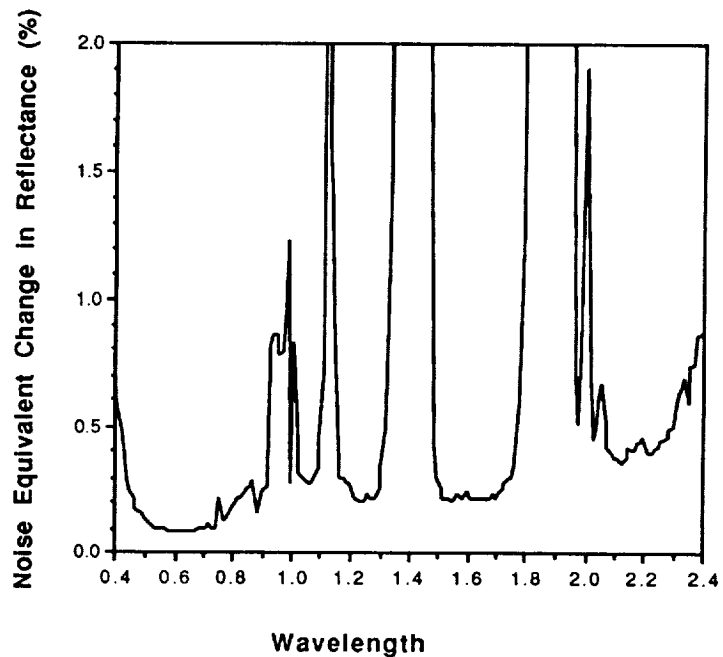


Figure 4.4 $NE\Delta\rho$ for Typical Reflectance.

The following Figures 4.5 through 4.22 show the Voltage SNR and $NE\Delta\rho$ variations as a function of the parameters shown in Table 4.3.

Table 4.3 Radiometric Performance Parameters Studied and Their Variations.

Meteorological Range	2, 4, 8, 16, 32 Km
Solar Zenith Angle	0°, 30°, 60°
View Zenith Angle	0°, 30°, 60°
Surface Albedo	0.03, 0.10, 0.30
Shot Noise Level	0.25, 1.0, 4.0
Read Noise Level	0.25, 1.0, 4.0
Radiometric Resolution	8, 12, 16 bits
IMC Gain State	1, 2, 4, 8
Relative Calibration Error Level	0.0, 0.5, 1.0, 2.0%

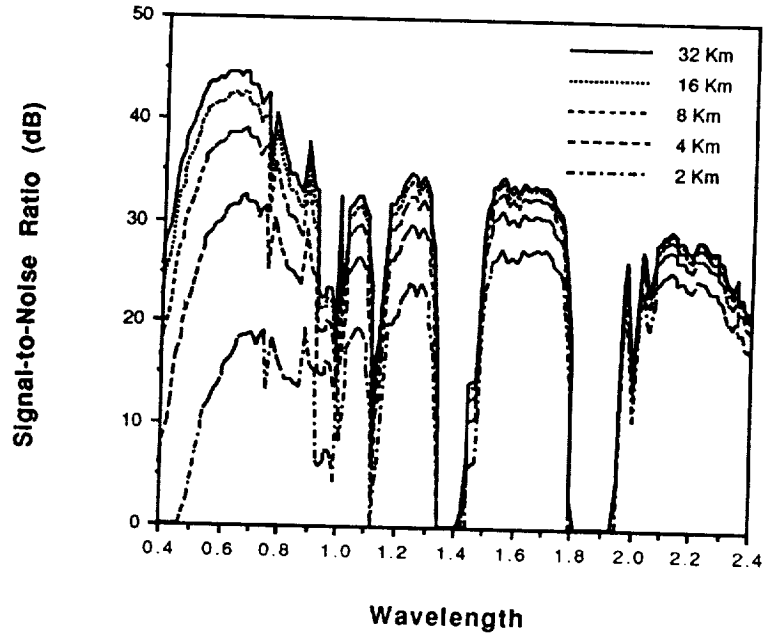


Figure 4.5 SNR for Varying Meteorological Ranges.

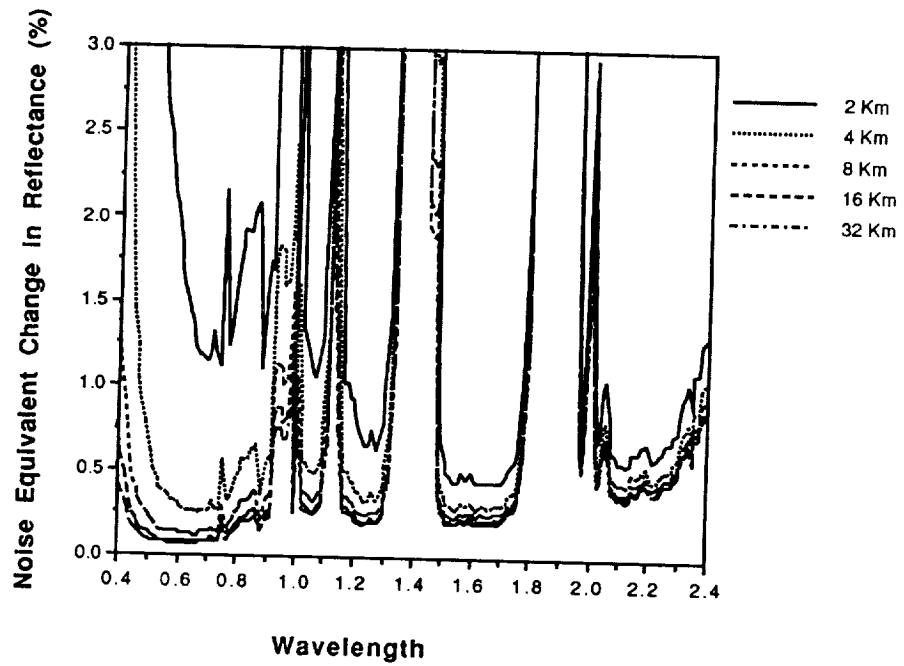


Figure 4.6 NEΔρ for Varying Meteorological Ranges.

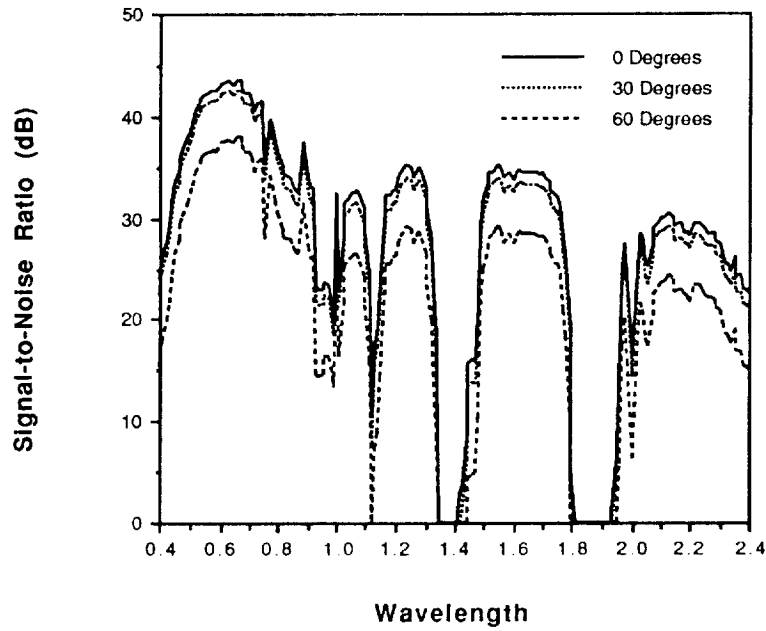


Figure 4.7 SNR for Varying Solar Angles.

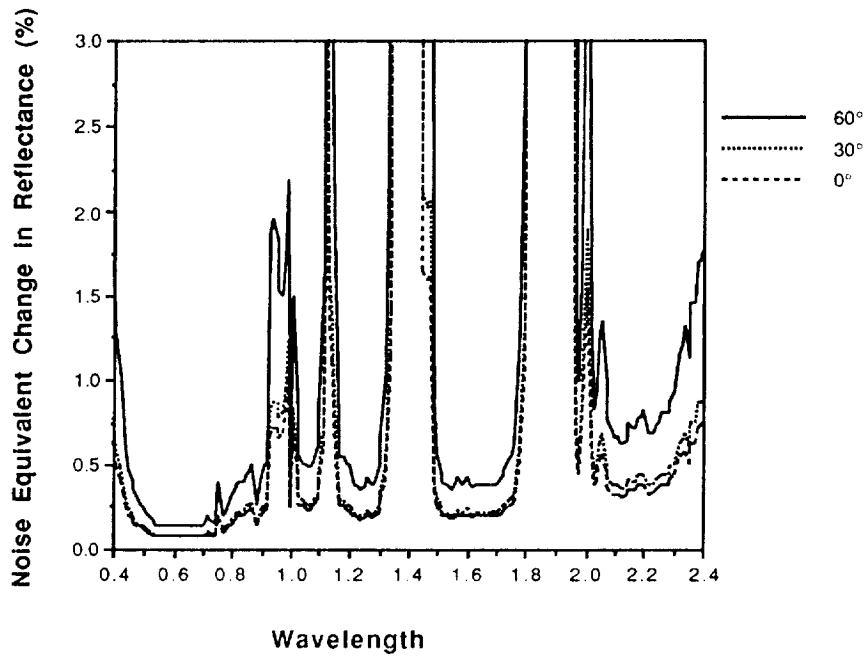


Figure 4.8 NE $\Delta\rho$ for Varying Solar Angles.

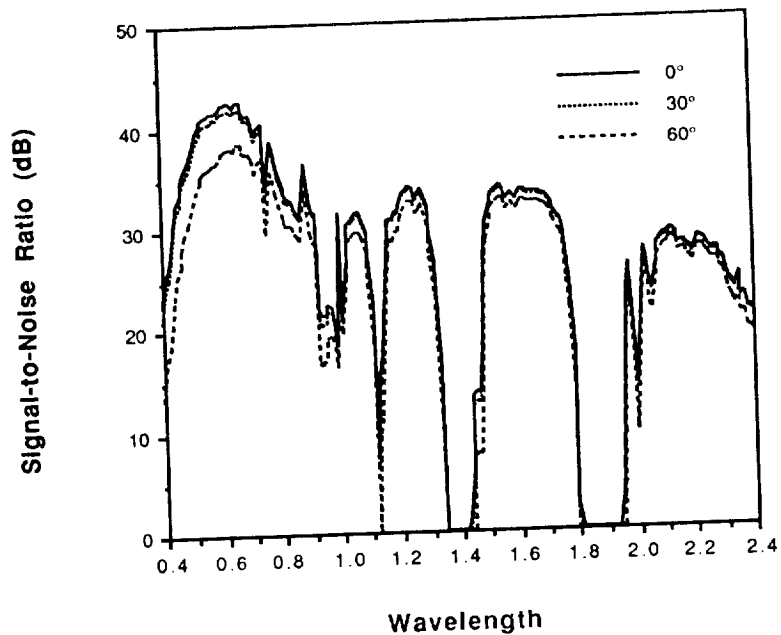


Figure 4.9 SNR for Varying View Angles.

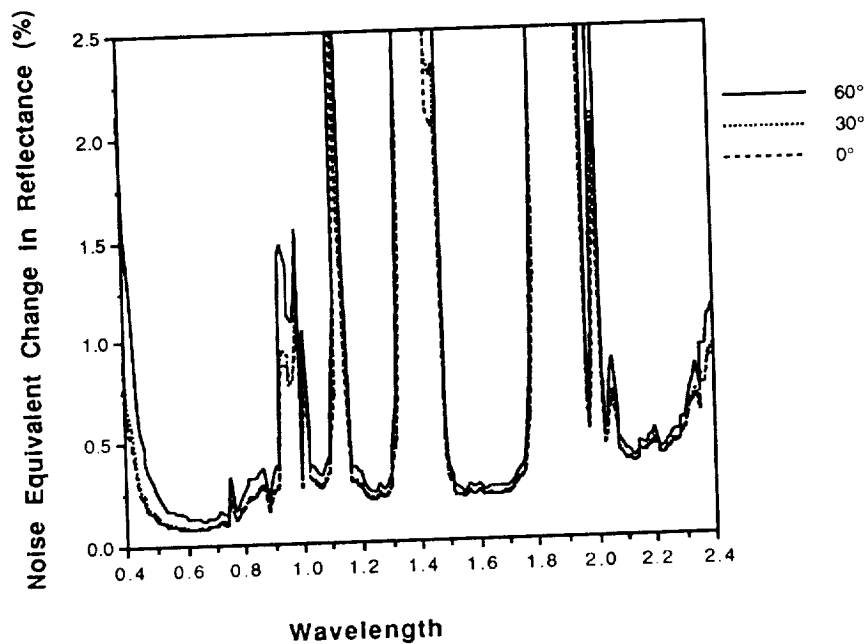


Figure 4.10 $NE\Delta\rho$ for Varying View Angles.

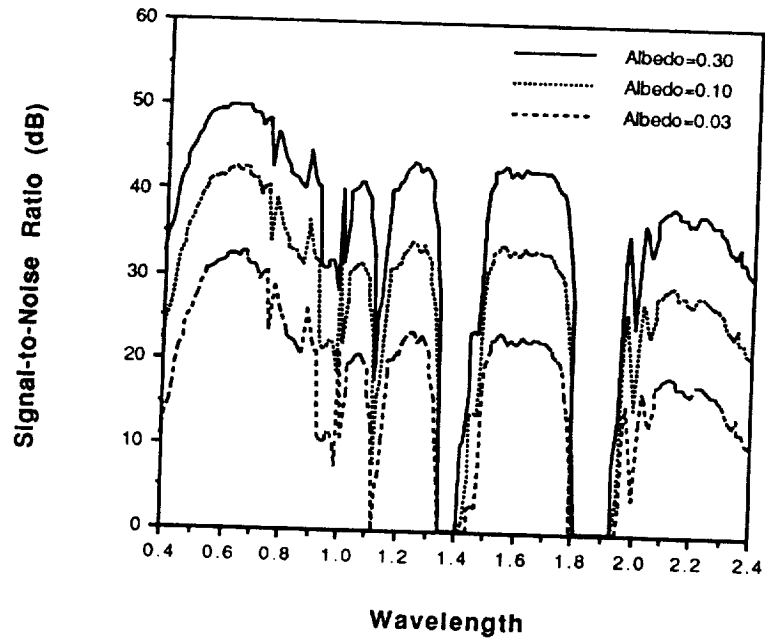


Figure 4.11 SNR for Various Surface Albedoes.

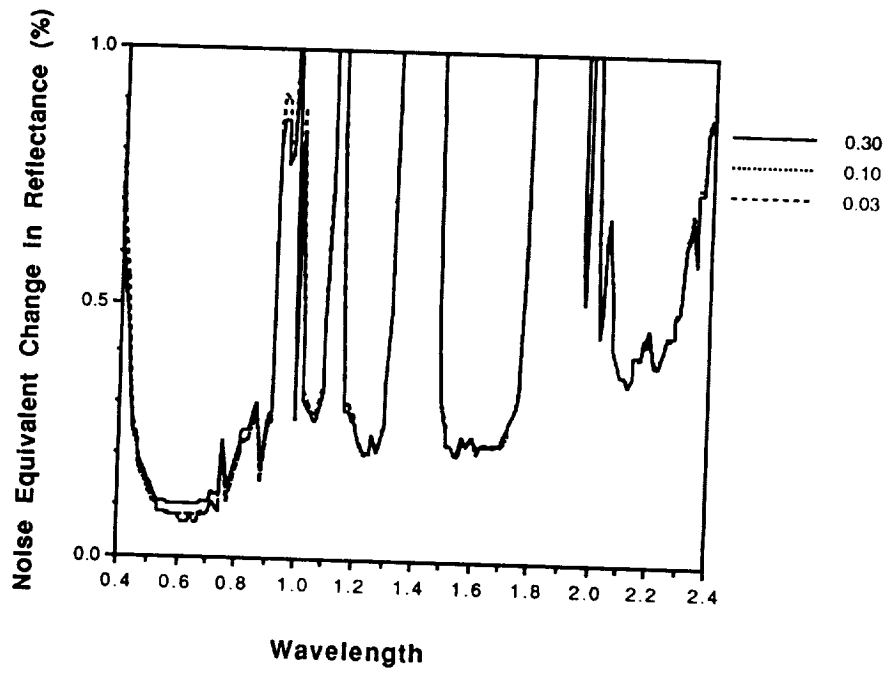


Figure 4.12 NE $\Delta\rho$ for Various Albedoes.

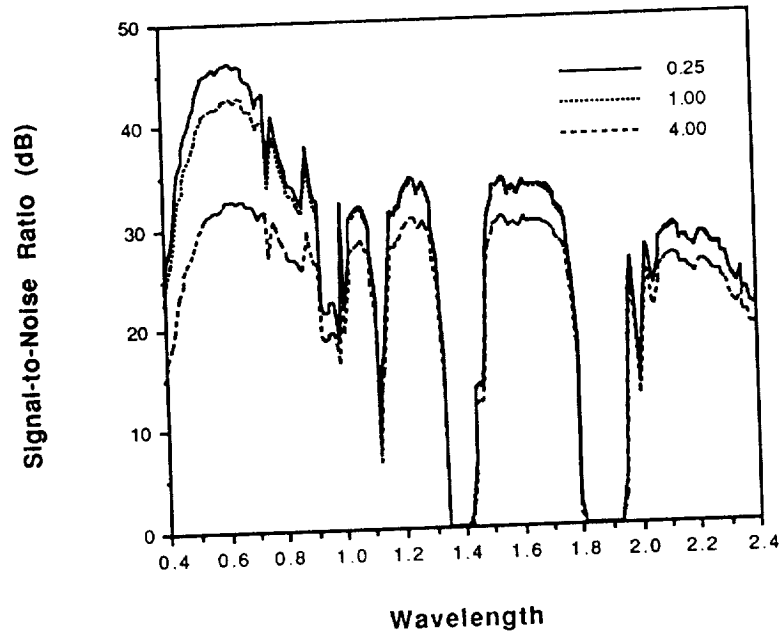


Figure 4.13 SNR for Varying Factors of Shot Noise.

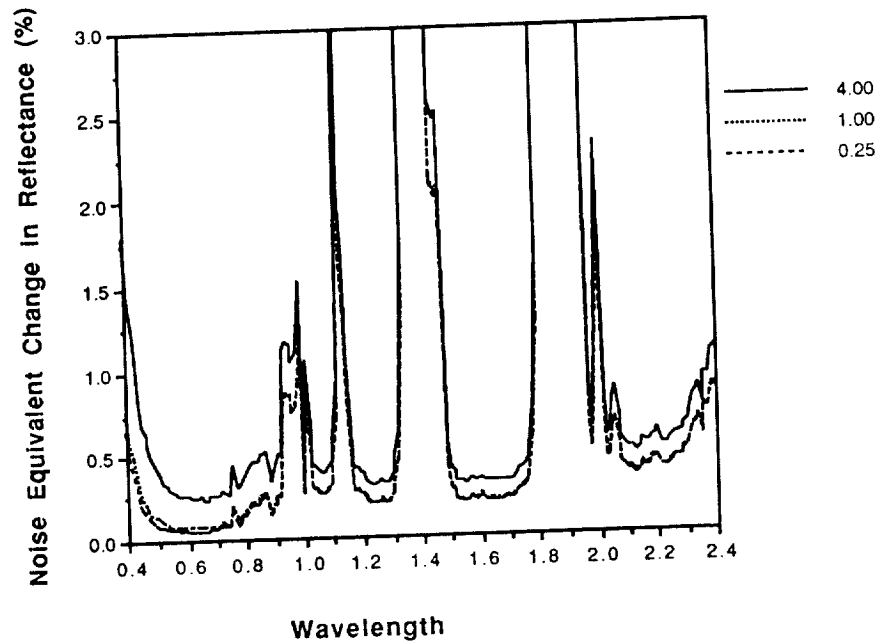


Figure 4.14 NE $\Delta\rho$ for Varying Factors of Shot Noise.

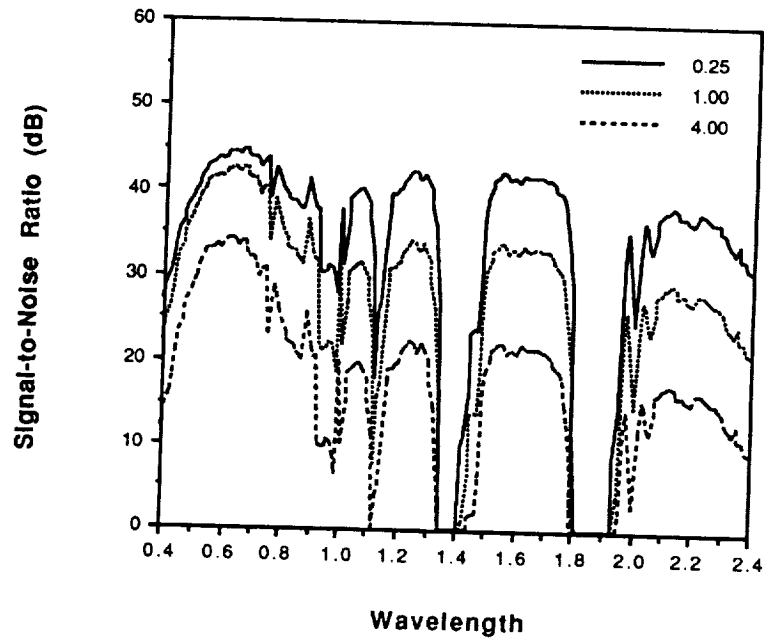


Figure 4.15 SNR for Varying Factors of Read Noise.

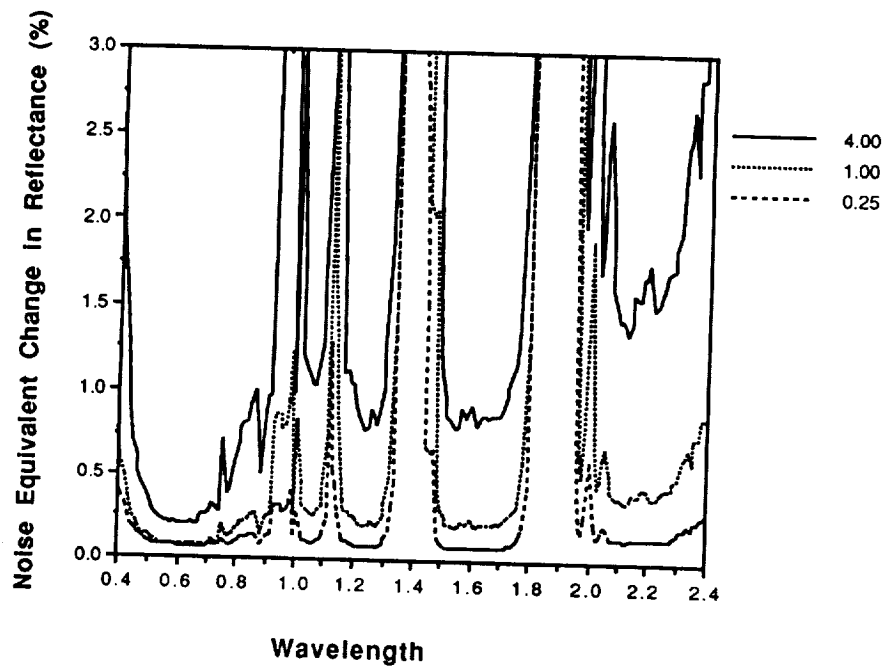


Figure 4.16 NE $\Delta\rho$ for Varying Factors of Read Noise.

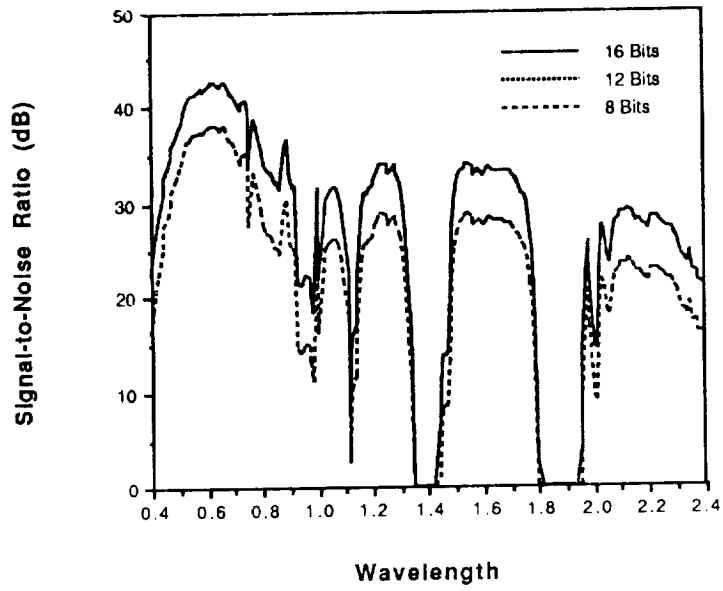


Figure 4.17 SNR for Varying Radiometric Resolution. The SNR for 12 and 16 Bits is Identical.

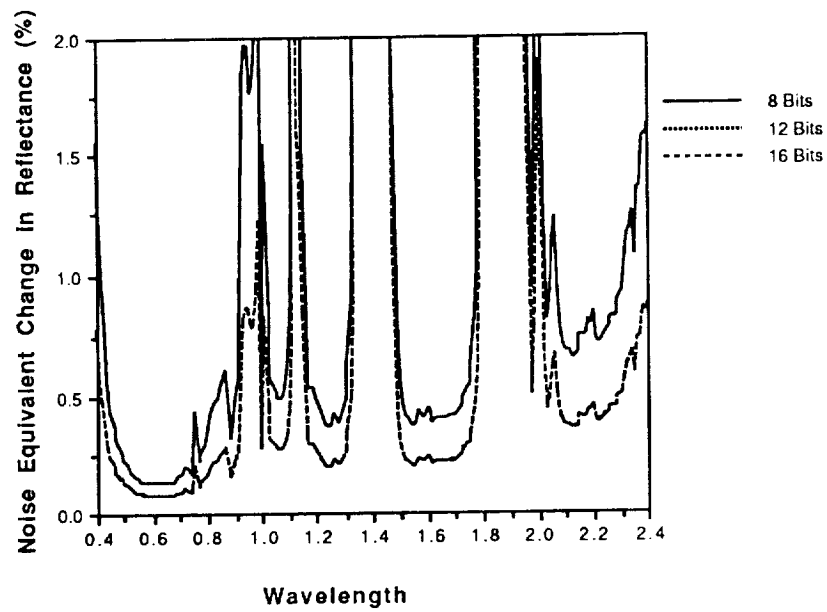


Figure 4.18 $NE\Delta\rho$ for Various Radiometric Resolutions. The $NE\Delta\rho$ for 12 and 16 Bits is Identical.

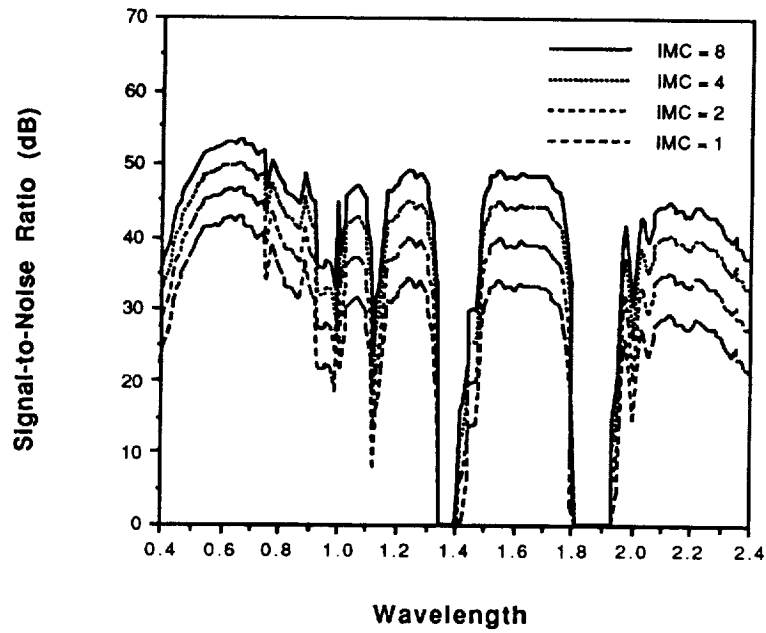


Figure 4.19 SNR for Various IMC Gain Settings.

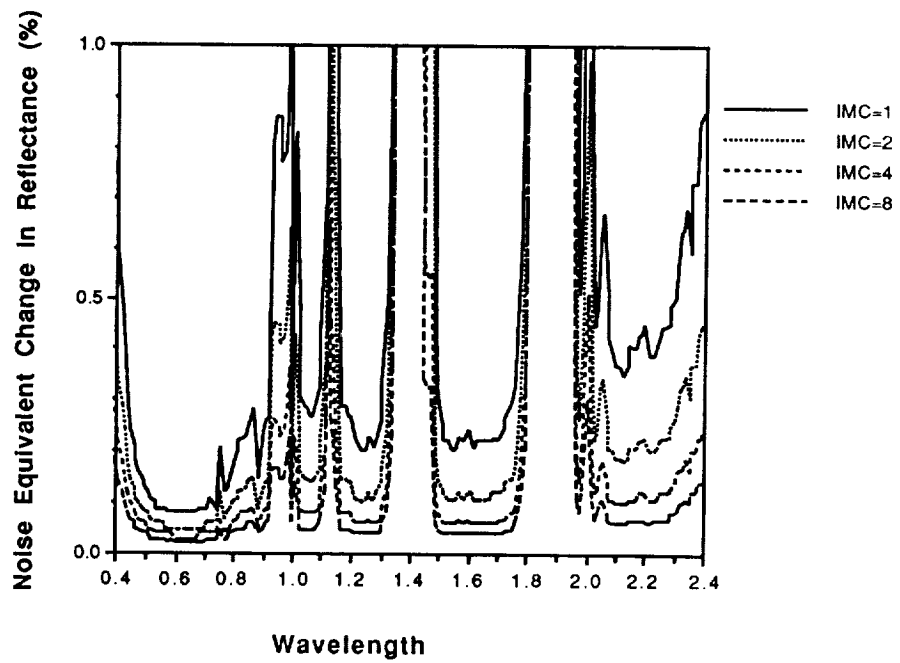


Figure 4.20 NE $\Delta\rho$ for Various IMC Gain Settings.

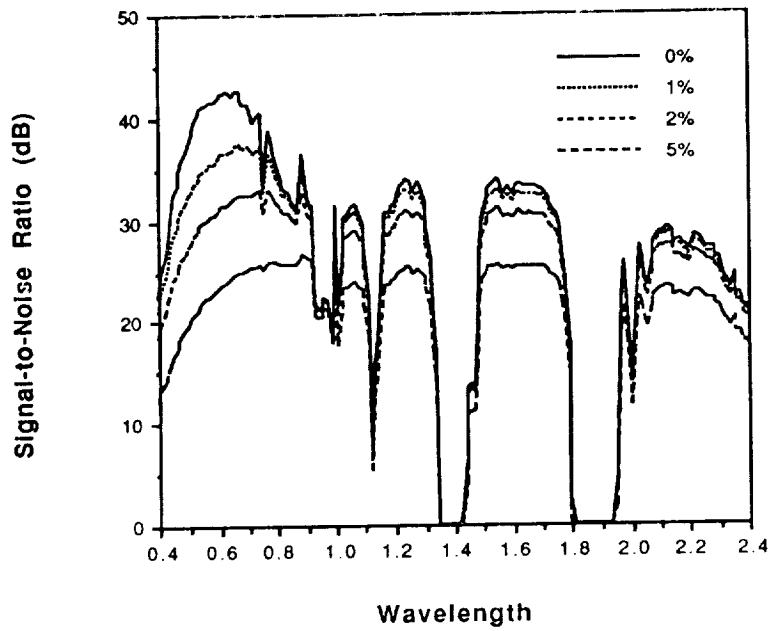


Figure 4.21 SNR for Various Levels of Relative Calibration Error.

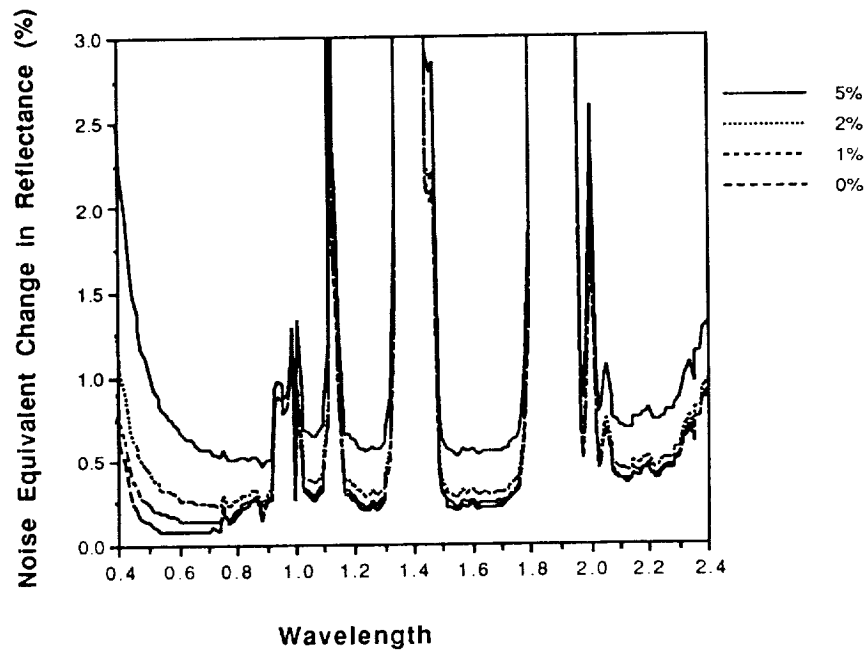


Figure 4.22 NE $\Delta\rho$ for Various Levels of Relative Calibration Error.

These figures show much about the radiometric performance of the HIRIS instrument for the various parameters studied. A common observation from all of these results is the presence of the many absorption bands in the atmosphere. The main water absorption bands around 1.4 and 1.9 μm make these wavelengths and those nearby useless, while the several other absorption bands present reduce the utility of those wavelengths for sensing of the Earth's surface. The following paragraphs discuss the effect of each of the parameters studied.

Meteorological Range (Figures 4.5 and 4.6). In general, a decreasing meteorological range results in a lower SNR and higher $\text{NE}\Delta\rho$, but the effect is seen to be much more significant in the visible and near infrared spectral regions. This parameter's effect becomes significant at ranges less than 16 Km.

Solar Zenith Angle (Figures 4.7 and 4.8). This angle is seen to have little effect at zenith angles less than 30° . At angles greater than this, the effect on SNR is constant across the wavelength, while the effect on $\text{NE}\Delta\rho$ is seen to be greater at the longer wavelengths. This is due to the lower signal levels at these wavelengths which require a greater $\Delta\rho$ to match the dominant read noise (see below).

View Zenith Angle (Figures 4.9 and 4.10). The effect of this angle is also minimal for angles less than 30° . At angles higher than this, the effect is greatest in the visible region because the path radiance (which increases with zenith angle) is more significant at these wavelengths.

Surface Albedo (Figures 4.11 and 4.12). While this parameter has a significant effect on SNR, its effect on $\text{NE}\Delta\rho$ is minimal. In the calculation of $\text{NE}\Delta\rho$, the only term that depends on albedo is the shot noise. Since shot noise is most significant in the visible wavelengths (see below), the effect of albedo on $\text{NE}\Delta\rho$ is only noticeable there.

Shot and Read Noise (Figures 4.13, 4.14, 4.15, and 4.16). Both the SNR and $\text{NE}\Delta\rho$ curves show that shot noise has a more significant effect over the

VNIR array wavelengths (0.4 - 1.0 μm), while read noise is dominant in the SWIR array (1.0 - 2.4 μm).

Radiometric Resolution (Figures 4.17 and 4.18). The nominal radiometric resolution of 12 bits yields a quantization error that is not significant when compared to the other noise sources. However, at 8 bits of resolution, the quantization error becomes significant. Also, it can be seen from the $NE\Delta\rho$ curves that this error is more significant at the lower signal levels of the longer wavelengths.

Image Motion Compensation (Figures 4.19 and 4.20). At higher gain states of IMC the SNR curves show a constant improvement across all wavelengths. Looking at the $NE\Delta\rho$ curves, it can be seen that the improvement in detecting the $\Delta\rho$ of the surface is greater for the lower signal levels of the long wavelengths.

Relative Calibration Error (Figures 4.21 and 4.22). Since the calibration error is signal dependent, its effect is seen to be greater for the higher signal levels of the visible wavelengths. At these shorter wavelengths 1% error is significant, while at the longer wavelengths the error is not significant until levels of nearly 5%.

4.3 Comparison of Simulation and Analytic Model Performance

Several experiments were performed to be able to compare the results between the simulation and analytical models. The system configuration was matched as closely as possible for the comparison.

A test scene was defined to be 80 rows by 80 columns of scene cells and divided at the middle into two classes. The reflectance data used for these classes were the Summer Fallow, and Unknown class from the data set described in Table 4.1. These classes were chosen for their low separability. Table 4.4 gives the details of the system configuration used in the test.

Table 4.4. System Configuration for Comparison Test

<u>Scene</u>		
Surface Meteorological Range		16 Km
Atmospheric Model		1976 US Standard
Haze Parameter		Rural Extinction
Diffuse Constant		0.84
Solar Zenith Angle		30°
View Zenith Angle		0°
Across scene spatial correlation ρ_x		0.6
Down scene spatial correlation ρ_y		0.6
Ground Size of Scene Cells		15 Meters
<u>Sensor (HIRIS Model)</u>		
Spatial Radius		
Analytical model r_0		1.4 Scene Cells
Simulator PSF IFOV		30 Meters
Point Spread Function		Gaussian
Read Noise Level		Nominal
Shot Noise Level		Nominal
IMC Gain State		1
Relative Calibration Error		0%
Absolute Radiometric Error		0%
Radiometric Resolution		12 Bits
<u>Processing</u>		
Training Fields		100% of Class Area
Feature Selection		First 6 Features of Table 4.5

Figure 4.23 shows an image of this scene with the model HIRIS sensor at $\lambda=1.70 \mu\text{m}$. This image was created using a scene cell ground size of 30 meters, resulting in 80 columns and 80 rows. The division between the classes is barely visible along a vertical line in the center of the image. However, the two classes are well separable when several features are used in the classification algorithm.

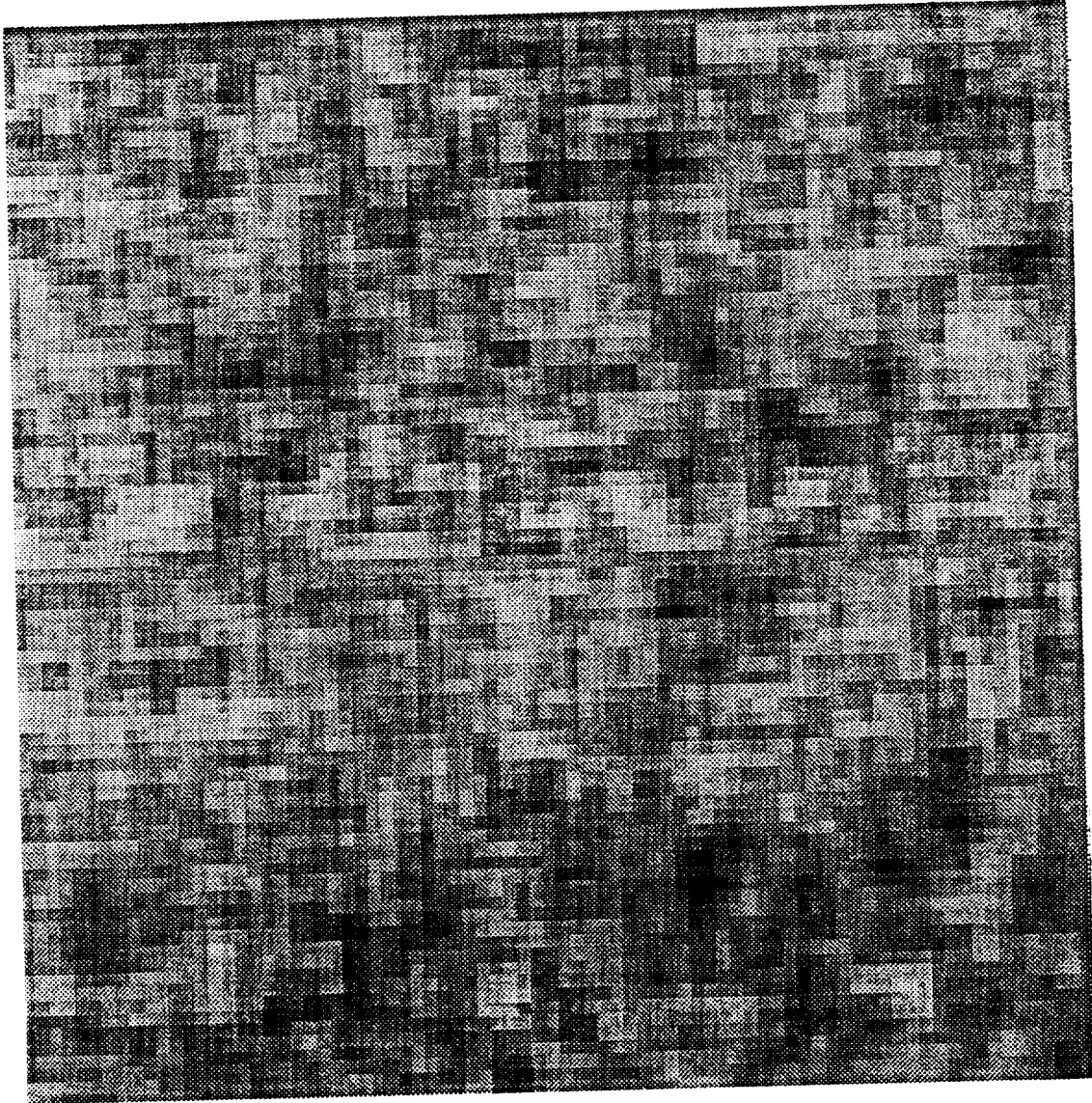


Figure 4.23 Simulated Image of Comparison Test Scene at $\lambda=1.70 \mu\text{m}$.

In Chen's thesis (Chen and Landgrebe, 1988), he listed the feature set that his algorithm designed for the data set of Table 4.1. This feature set is shown in Table 4.5 following.

Table 4.5 Optimal Feature Set for Kansas Winter Wheat Data Set.

Feature	Wavelength (μm)
1	0.70 - 0.92
2	1.98 - 2.20
3	2.20 - 2.40
4	0.66 - 0.84
5	1.48 - 1.64
6	0.52 - 0.66
7	1.64 - 1.78
8	1.16 - 1.28
9	0.96 - 1.06
10	1.04 - 1.12
11	0.94 - 1.00
12	0.44 - 0.50
13	1.12 - 1.16
14	0.92 - 0.96
15	0.40 - 0.44
16	1.00 - 1.04

For each of these tests, the simulation model was run five times and the resulting accuracies averaged together. Also, the classification accuracy shown is the average of the two individual class accuracies.

For the base system configuration shown in Table 4.4, the accuracies obtained are shown in Table 4.6. The values are with 1% of each other, indicating that, at least for this configuration, the simulation model and the analytic model predict similar performance.

Table 4.6. Classification Accuracy of Base System Configuration.

Simulation Model	88.06%
Analytical Model	87.78%

The first test was to compare the effect on accuracy of the spatial model parameters. Figure 4.24 shows the result of changing the spatial correlation $\rho = \rho_x = \rho_y$ of the scene cells.

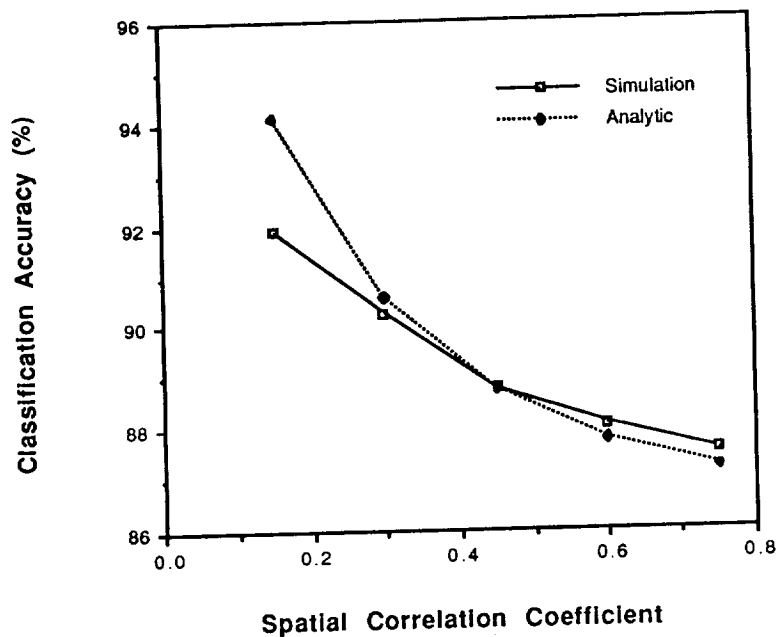


Figure 4.24 Classification Accuracy vs. Scene Spatial Correlation Coefficient.

As can be seen, the simulation model and analytical model track the change in accuracy due to the spatial correlation. This validates the equivalence of the autoregressive and exponential spatial models, and supports the work by Mobasseri in analyzing the effect of the spatial model on class spectral statistics.

Another comparison test of the spatial model was performed by allowing the ground size of the scene cells to change and observing the effect on classification performance. The change in scene cell size for the simulation model is equivalent to changing the PSF radius of the analytical model. The IFOV of the sensor was held constant at 30 meters in the simulation model. Table 4.7 presents the increments used in this experiment.

Table 4.7. Increments Used in Ground Size Experiment.

Ground Size of Cell	Radius of Analytic PSF (r_p)	Resulting Image Size
30 Meters	0.7 cells	80 rows by 80 columns
15 Meters	1.4 cells	40 rows by 40 columns
7 Meters	2.8 cells	20 rows by 20 columns
4 Meters	5.6 cells	10 rows by 10 columns
2 Meters	11.2 cells	5 rows by 5 columns

Figure 4.25 shows the results of this experiment. Both models show an increase in accuracy as the scene cell size decreases. However, while the analytical model continues this trend at cell sizes less than 10 meters, the simulation model shows the effects of mixed pixels at the border between the classes and reduced training set size to dramatically reduce the accuracy.

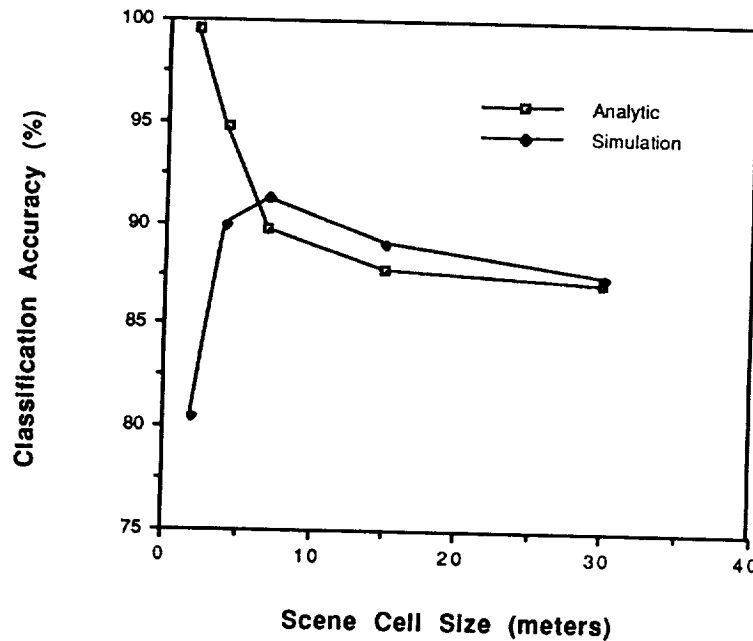


Figure 4.25 Classification Accuracy vs. Ground Size of Scene Cells.

The next test was to compare the effect of sensor view angle on the performance predicted by each model. The results are shown in Figure 4.26.

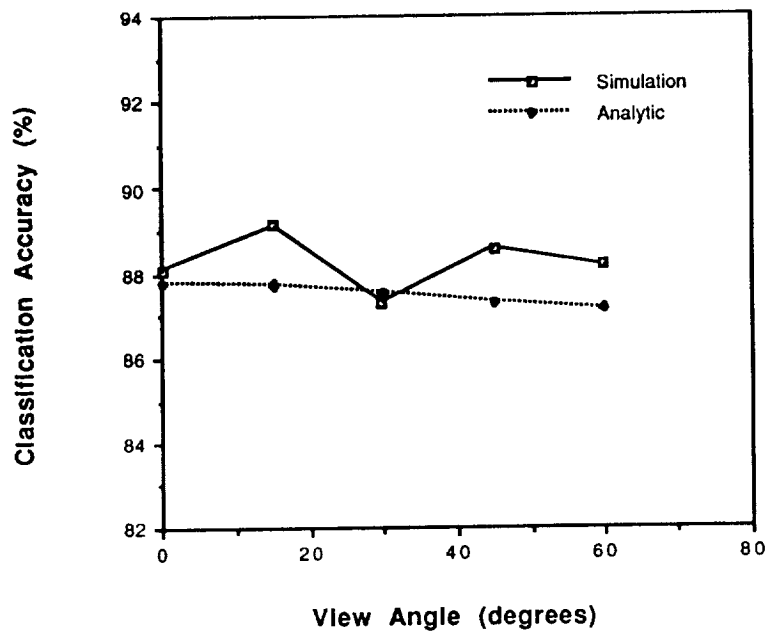


Figure 4.26 Classification Accuracy vs. Sensor View Angle.

The analytical model shows a slight continuous decrease in accuracy, while the simulation model seems to seesaw with a slightly decreasing trend. There are two offsetting effects on the system as the viewing angle increases. There is the increase in path radiance which results in higher shot noise and *decreasing* accuracy, while the ground size of the sensor IFOV increases thereby decreasing the variation in the scene and *increasing* accuracy.

In the analytical model this change in ground size happens continuously, while in the simulation model it is a discrete change as scene cells are combined in integer increments. In this case, for angles 0°, 15°, and 30°, four scene cells are within the sensor IFOV, while at 45° six are combined, and at 60° eight fill the field of view. As the number of scene cells within the IFOV increases, the size of the resulting image decreases, and fewer pixels result for each class. This can also affect the accuracy through mixed pixel effects.

It is important to point out that the surface model used in both the simulation and analytic models does not account for variation in reflectance with illumination and view angle. Thus, this experiment does not predict how actual classification accuracy may be affected by the changing view angle in a general sense, but it does serve to illustrate factors that may influence the result.

Another test was done to compare the accuracy obtained when using a Gaussian versus the measured shape of the PSF of the sensor. Table 4.8 shows the result of the simulation model using the two PSF types.

Table 4.8 Classification Accuracies of Gaussian vs. Measured PSF.

Gaussian PSF	90.15%
Tabulated PSF	89.75%

The assumption of a Gaussian shape is seen to give a slightly higher accuracy than when using the actual curve of the sensor. Thus, assuming a Gaussian PSF is seen to be slightly optimistic.

An experiment was also performed to illustrate the effect of reducing the number of training samples used for the classifier. Each of the two classes has 800 pixels in the image produced during the simulation. The result is shown in Figure 4.27.

Obviously, the analytical model shows no effect, as it is only based on the class statistics and no "training" is involved. The simulation model shows the decreased accuracy as fewer samples are used. This illustrates one of the limitations of the analytical model in representing the real system.

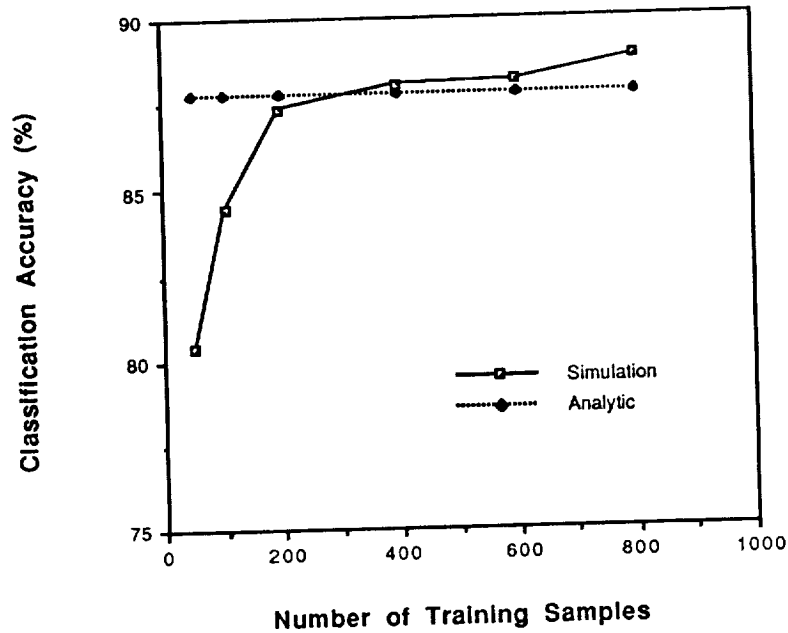


Figure 4.27 Classification Accuracy vs. Number of Training Samples.

In general, the simulation and analytical models compare well. In some cases, the differences between the two are indicative of real world constraints, while in others the difference is artificial due to limitations of the model. The results concerning the scene cell sizes and the training samples show limitations of the analytical model. The irregular shape of the simulation result for the view angle effects show the potential problems in using a discrete simulation. Both approaches have their advantages, however, and with the proper interpretation can be used productively.

4.4 System Parameter Studies

In this section results are presented showing the effect of system parameters on SNR and classification accuracy using the analytical model.

The scene reflectance was the Kansas Winter Wheat data set of Table 4.1. Table 4.9 shows the baseline system configuration used in this study.

Table 4.10 shows the parameters that were varied and the range of their variation. Figures 4.28 through 4.51 show the results of these experiments.

Table 4.9 System Configuration for Parameter Studies.

<u>Scene</u>	
Surface Meteorological Range	16 Km
Atmospheric Model	1976 US Standard
Haze Parameter	Rural Extinction
Diffuse Constant	0.84
Solar Zenith Angle	30°
View Zenith Angle	0°
Across and Down Scene Spatial Correlation	0.6
<u>Sensor (HIRIS Model)</u>	
Spatial Radius (analytical model r_0)	1.4 Scene Cells
Read Noise Level	Nominal
Shot Noise Level	Nominal
IMC Gain State	1
Relative Calibration Error	0.5%
Absolute Radiometric Error	0%
Radiometric Resolution	12 Bits
<u>Processing</u>	
Feature Selection	First 6 Features of Table 4.5

Table 4.10 Parameters Studied and Their Variation in Section 4.4.

Spatial Correlation	0, 0.15, 0.30, 0.45, 0.60, 0.75, 0.90
Meteorological Range	2, 4, 8, 16, 32 Km
Solar Zenith Angle	0°, 15°, 30°, 45°, 60°
View Zenith Angle	0°, 15°, 30°, 45°, 60°
Sensor IFOV On a Side	1, 2, 4, 8, 16 Scene Cells
Shot Noise Factor	0, 0.5, 1.0, 2.0, 4.0
Read Noise Factor	0, 0.5, 1.0, 2.0, 4.0
IMC Gain State	1, 2, 4, 8
Number of Bits	6, 8, 10, 12, 14, 16
Relative Calibration Error	0, 0.5, 1.0, 2.0, 4.0 %
Absolute Radiometric Error	-10, -5, -2, 0, 2, 5, 10 %
Number of Features	1 through 16

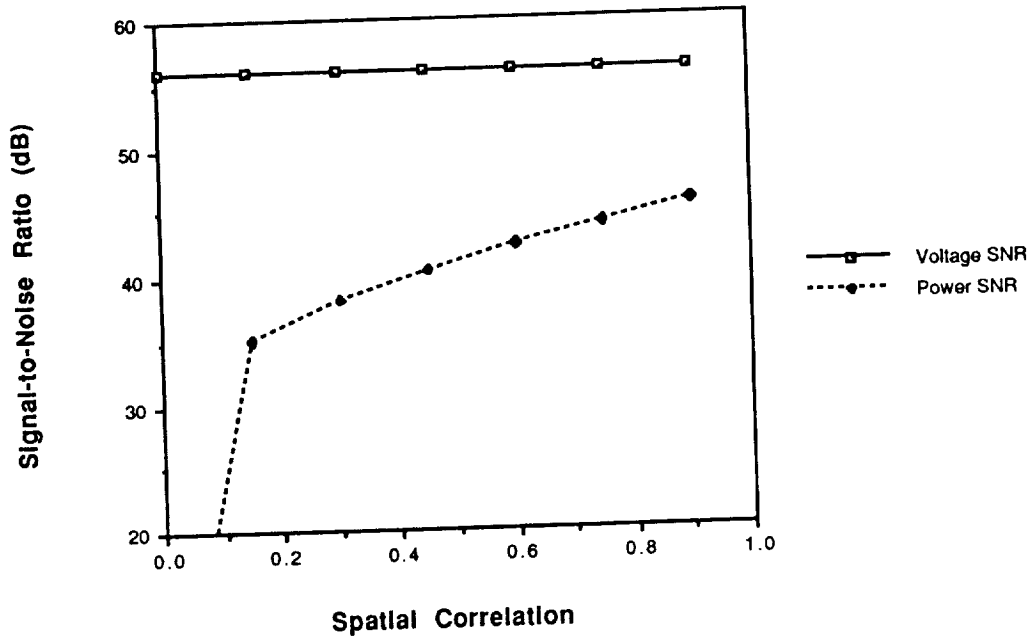


Figure 4.28 Effect of Spatial Correlation ($\rho = \rho_x = \rho_y$) on SNR.

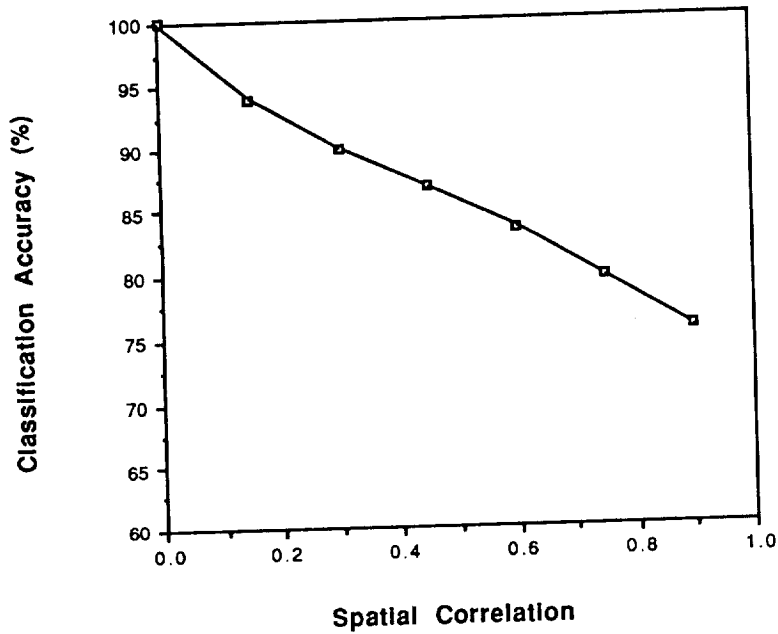


Figure 4.29 Effect of Spatial Correlation ($\rho = \rho_x = \rho_y$) on Classification Accuracy.

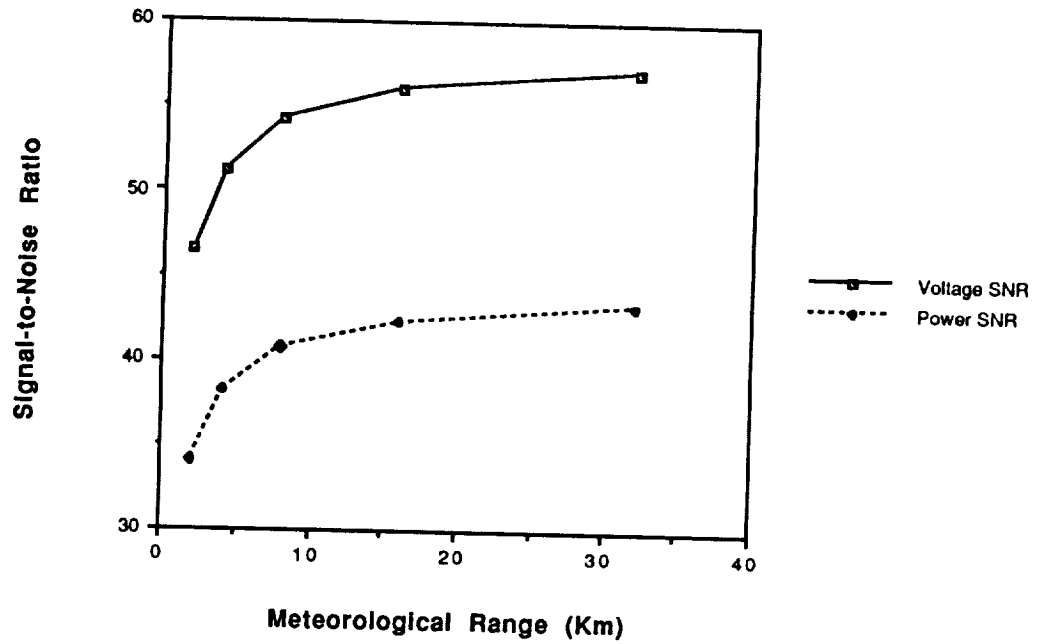


Figure 4.30 Effect of Meteorological Range on SNR.

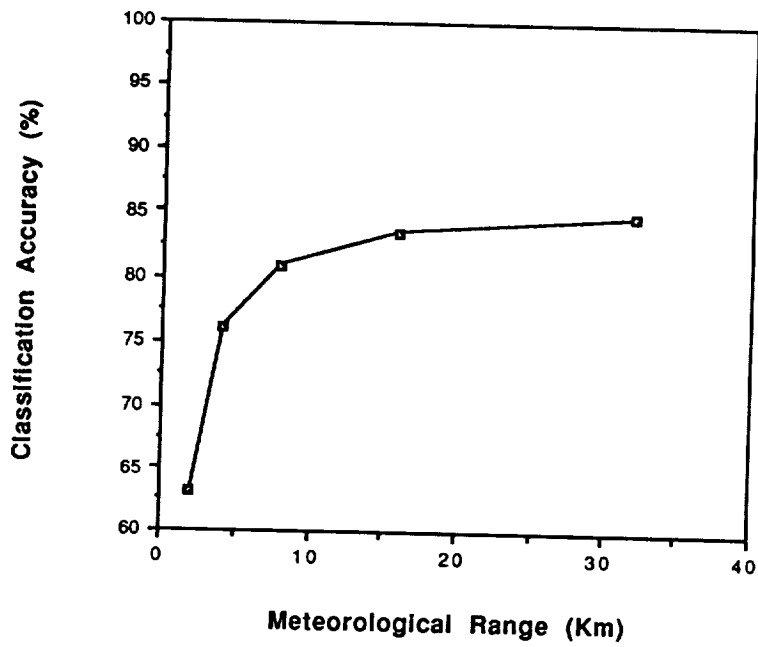


Figure 4.31 Effect of Meteorological Range on Classification Accuracy.

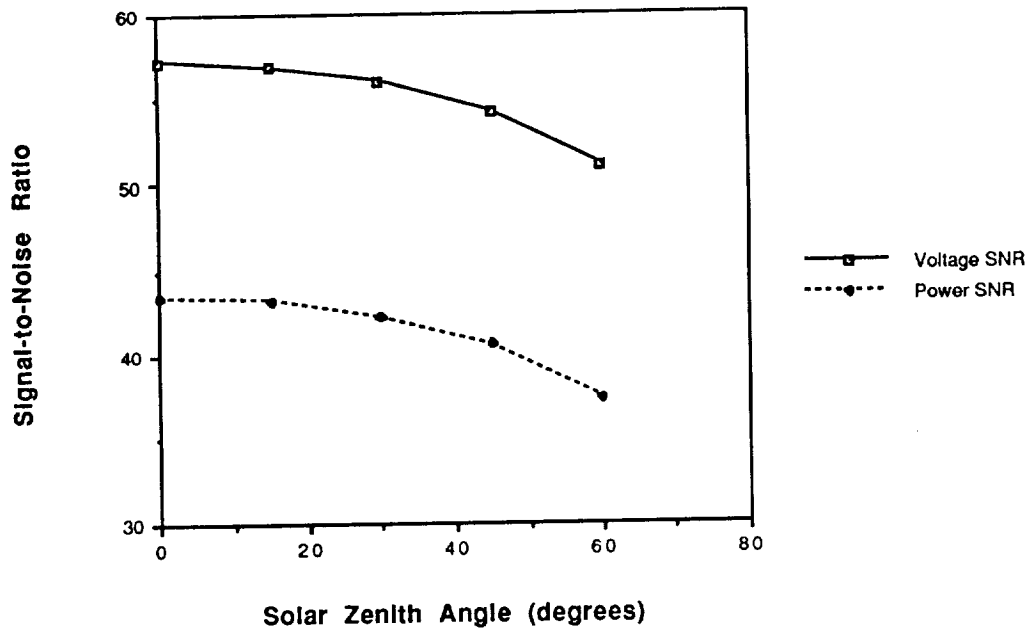


Figure 4.32 Effect of Solar Zenith Angle on SNR.

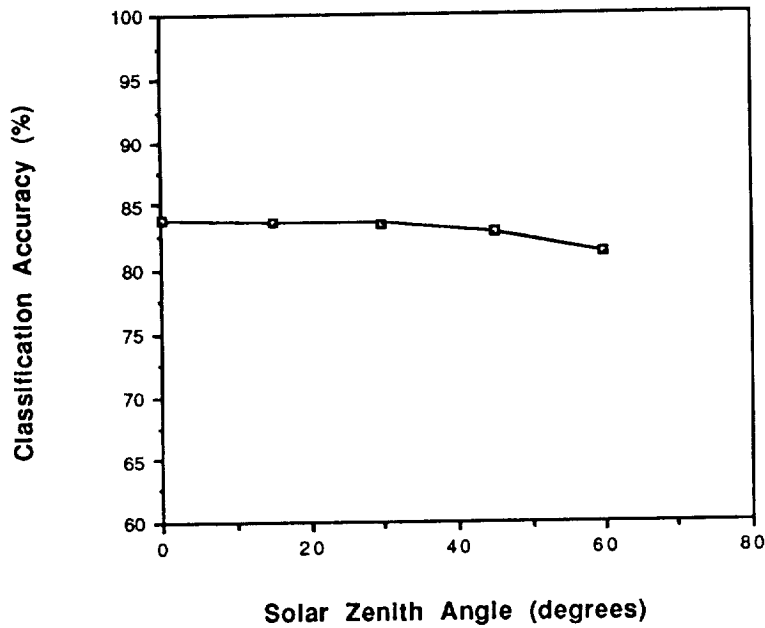


Figure 4.33 Effect of Solar Zenith Angle on Classification Accuracy.

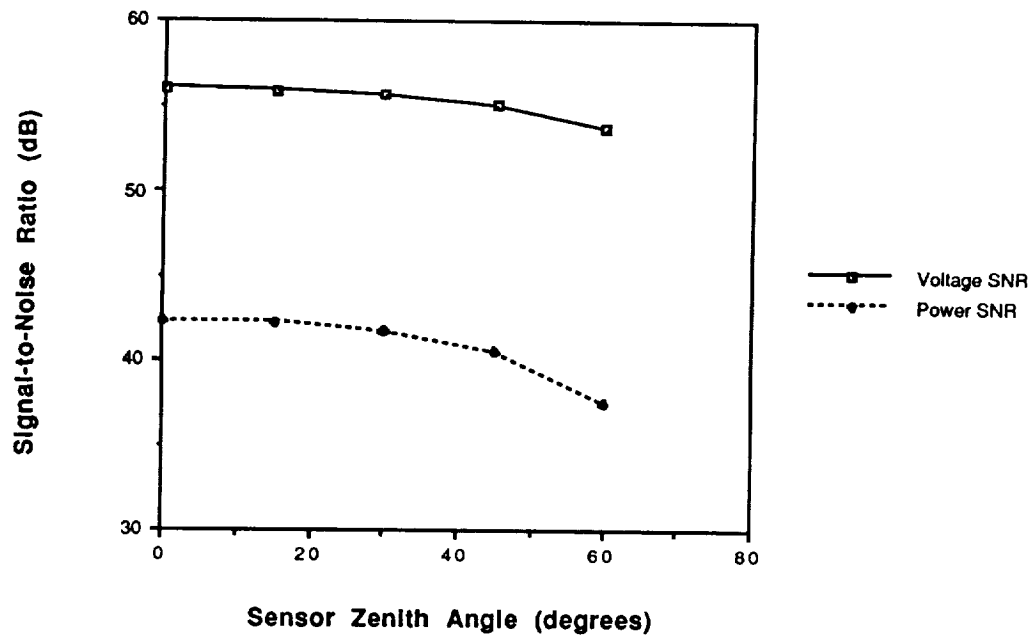


Figure 4.34 Effect of Sensor Zenith Angle on SNR.

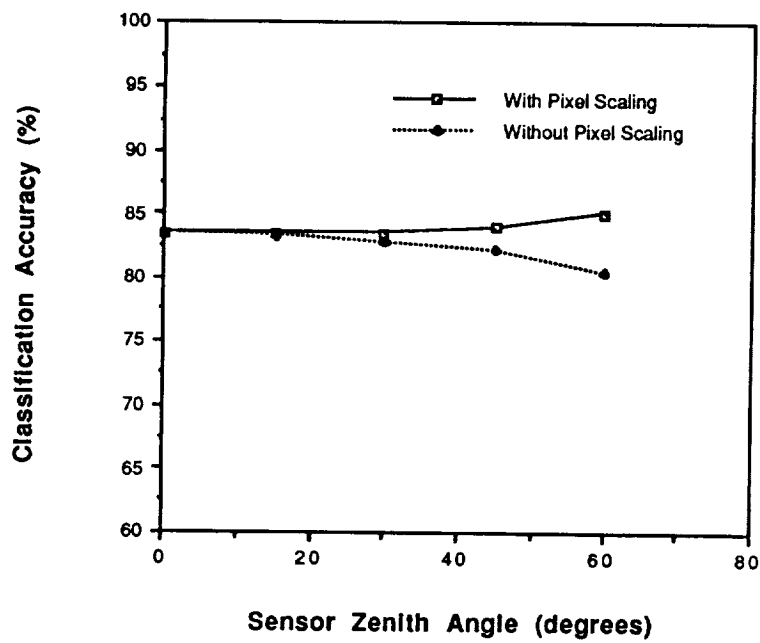


Figure 4.35 Effect of Sensor Zenith Angle on Classification Accuracy.

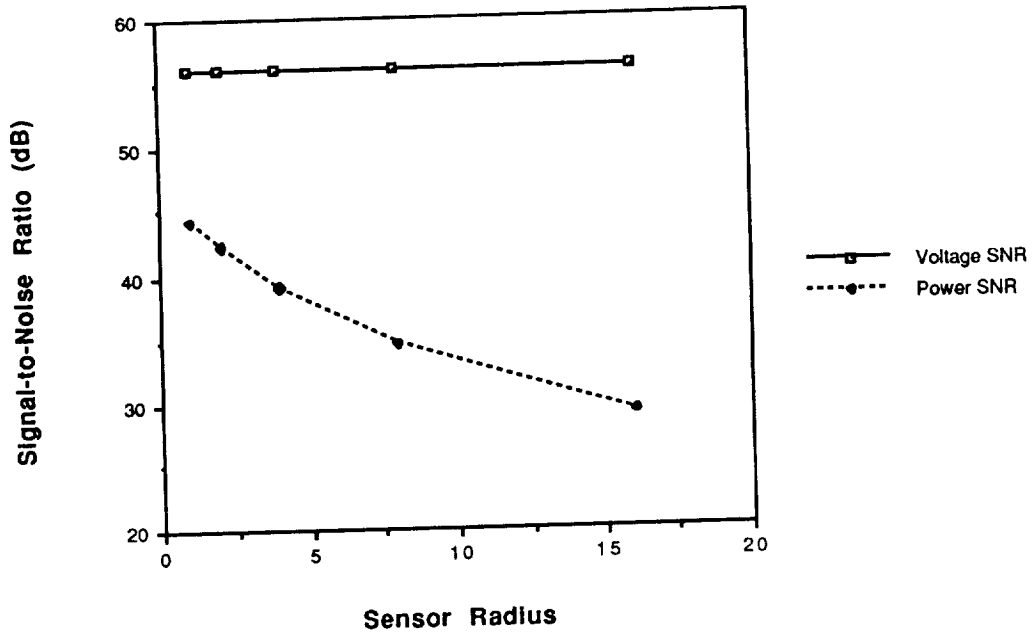


Figure 4.36 Effect of Number of Scene Cells Within Sensor IFOV on SNR.

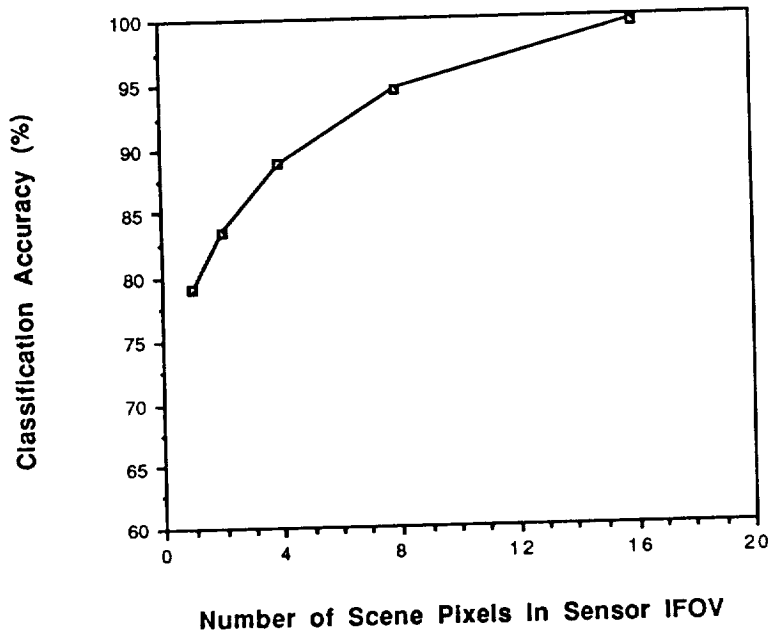


Figure 4.37 Effect of Number of Scene Cells Within Sensor IFOV on Classification Accuracy.

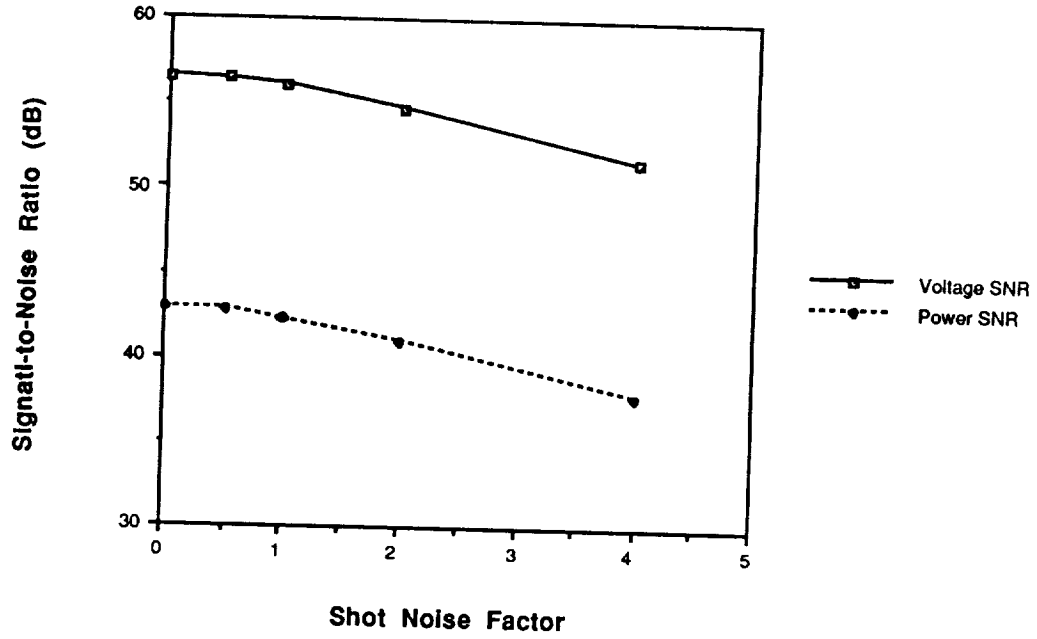


Figure 4.38 Effect of Shot Noise (Nominal = 1.0) on SNR.

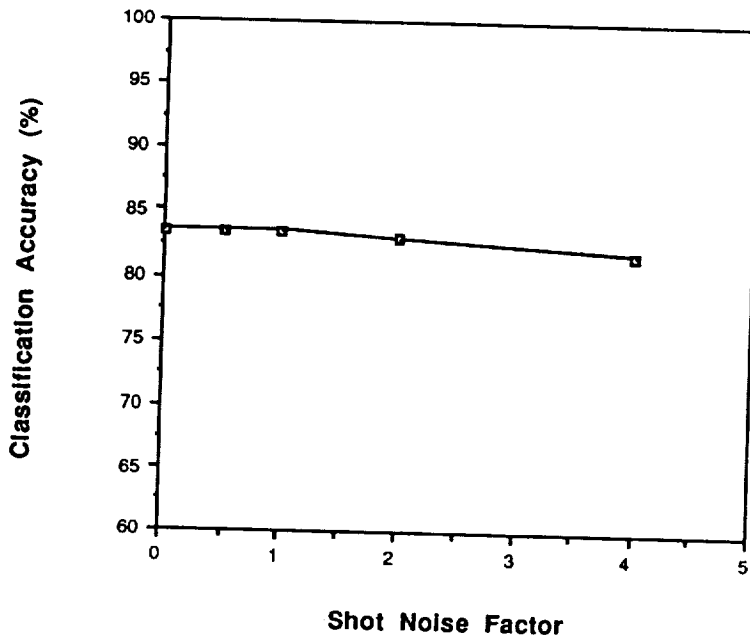


Figure 4.39 Effect of Shot Noise (Nominal = 1.0) on Classification Accuracy.

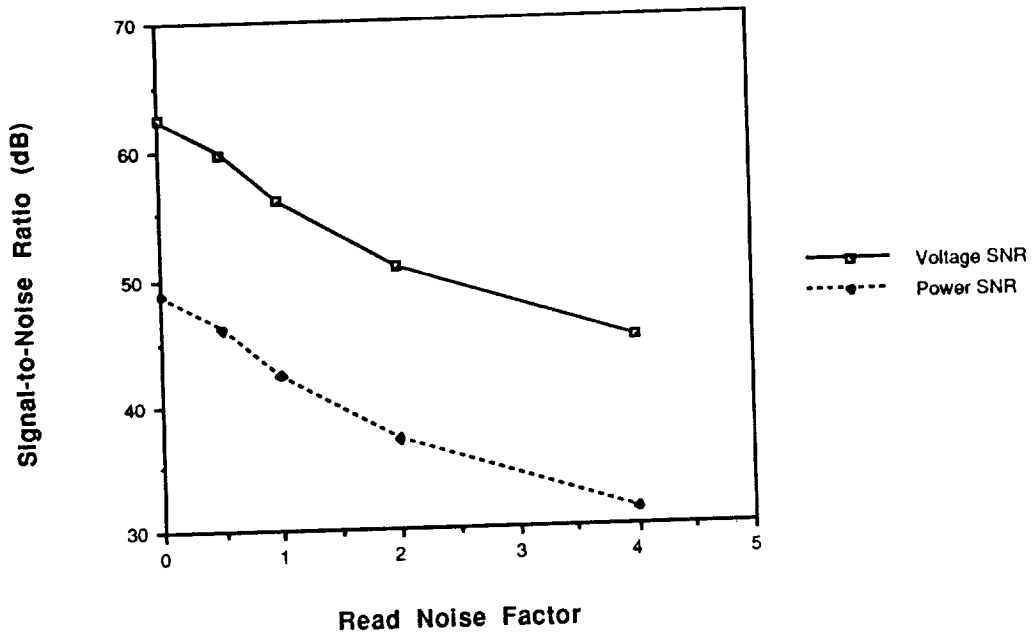


Figure 4.40 Effect of Read Noise (Nominal = 1.0) on SNR.

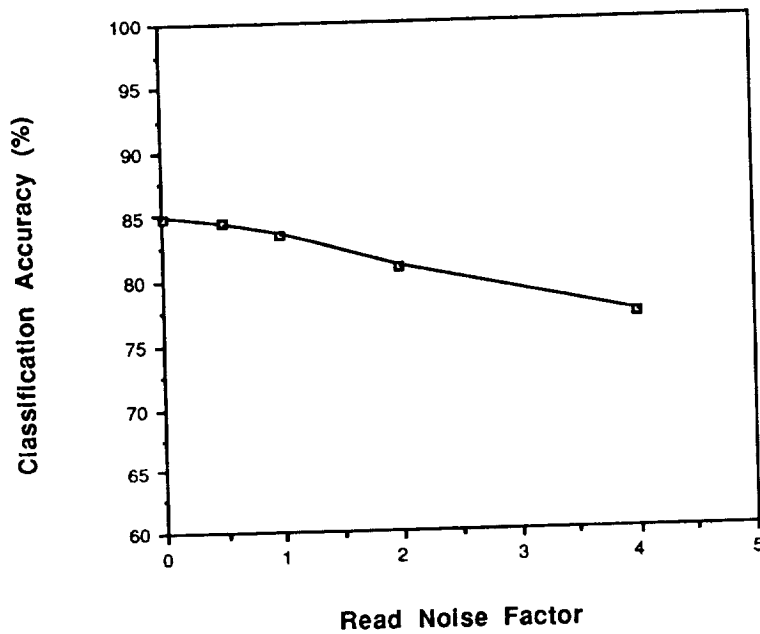


Figure 4.41 Effect of Read Noise (Nominal = 1.0) on Classification Accuracy.

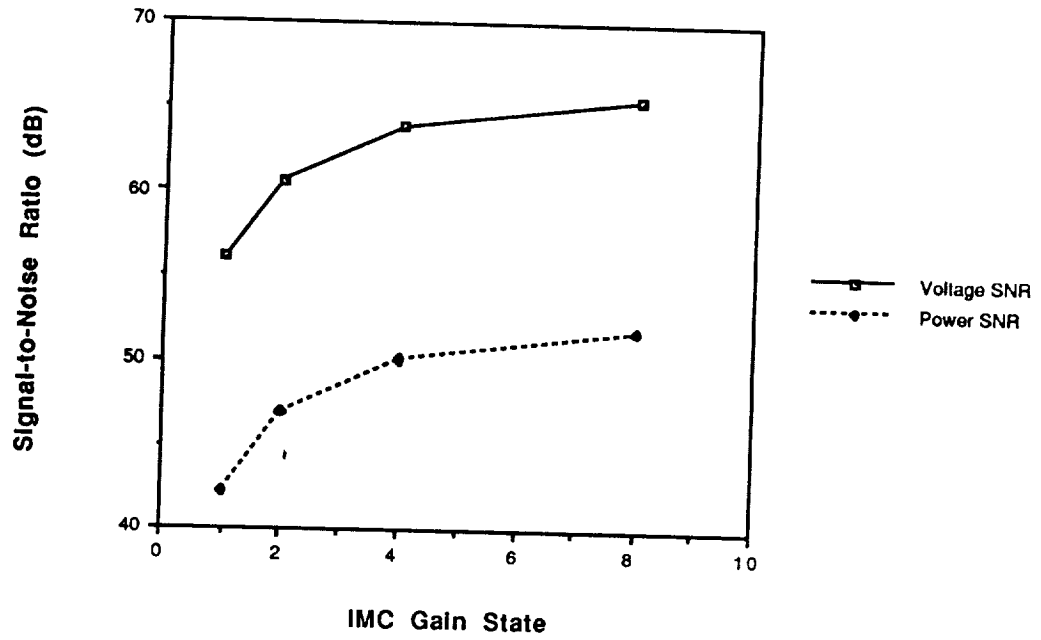


Figure 4.42 Effect of IMC Gain State on SNR.

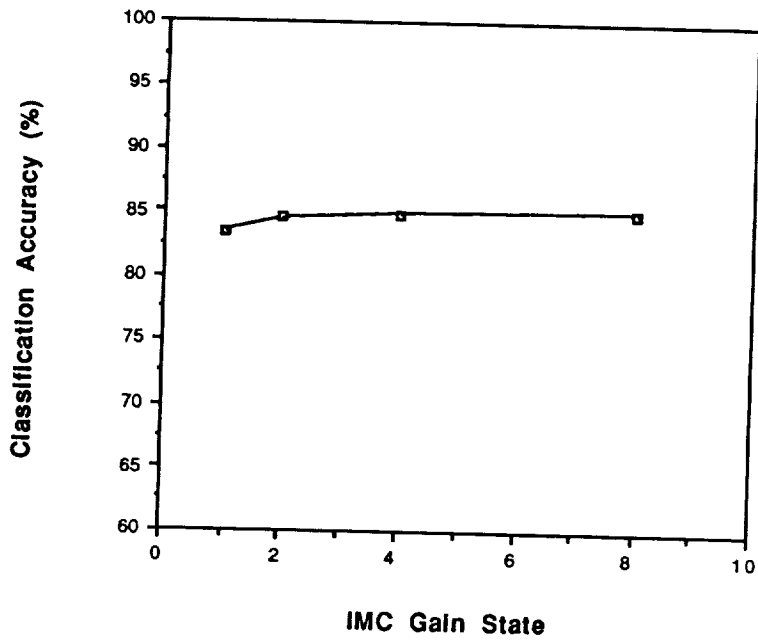


Figure 4.43 Effect of IMC Gain State on Classification Accuracy.

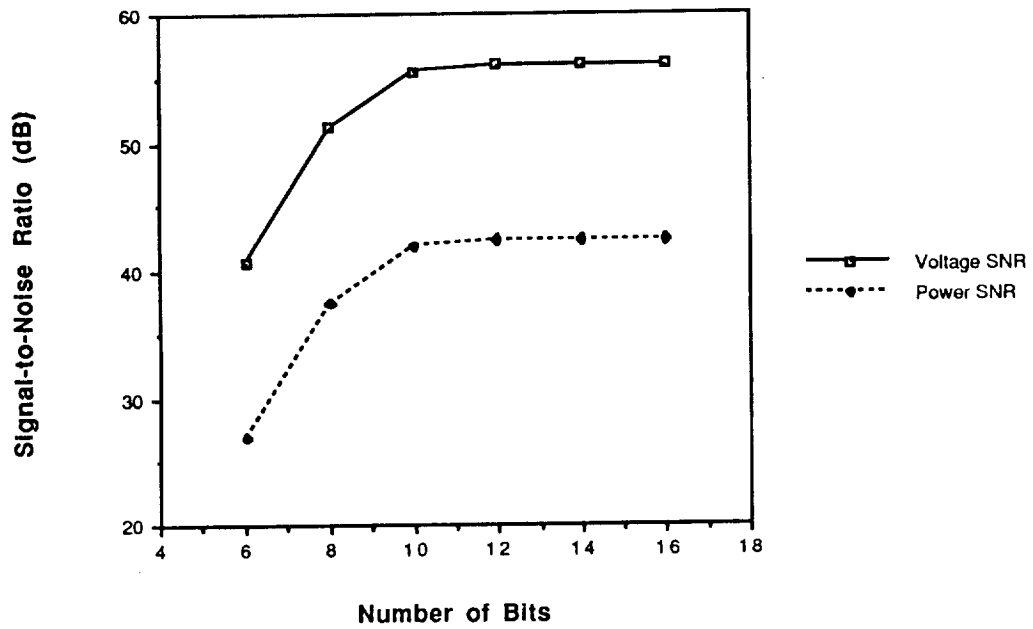


Figure 4.44 Effect of Radiometric Resolution on SNR.

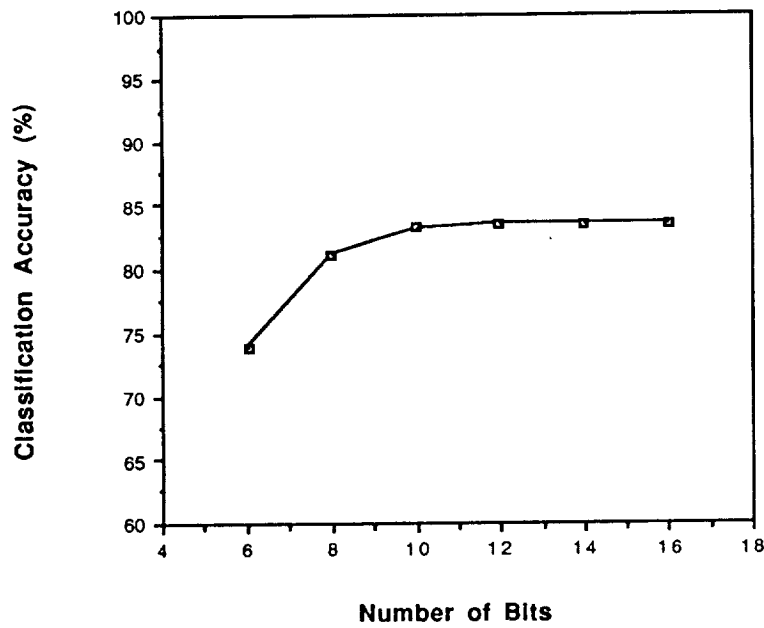


Figure 4.45 Effect of Radiometric Resolution on Classification Accuracy.

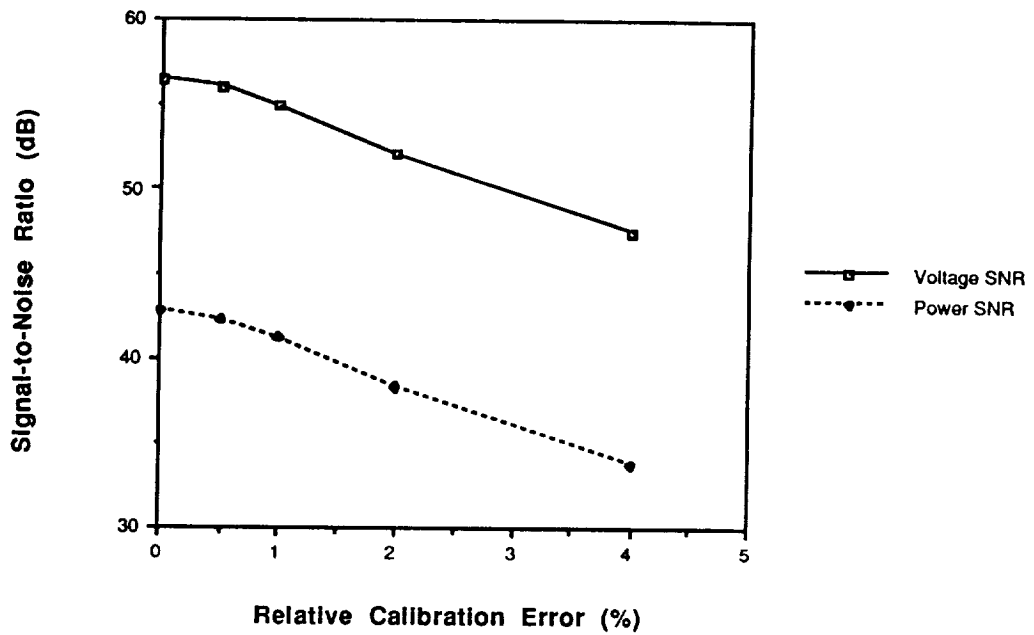


Figure 4.46 Effect of Relative Calibration Error on SNR.

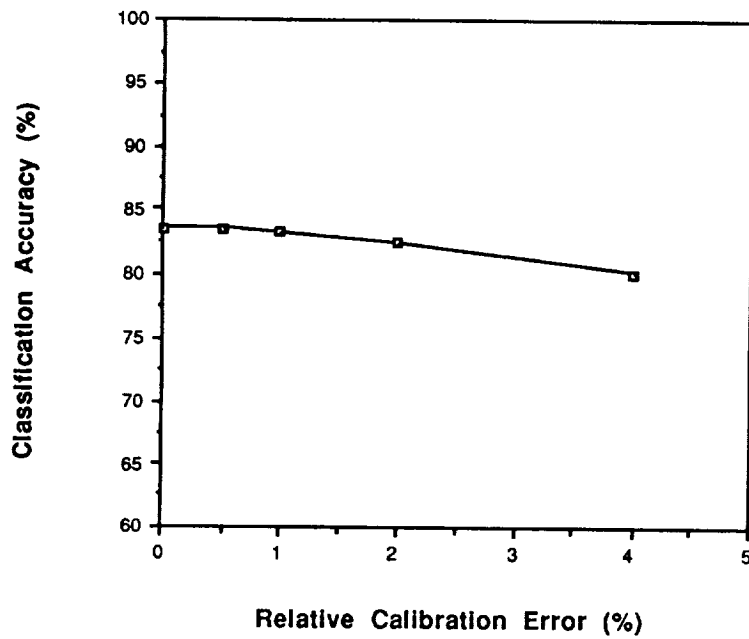


Figure 4.47 Effect of Relative Calibration Error on Classification Accuracy.

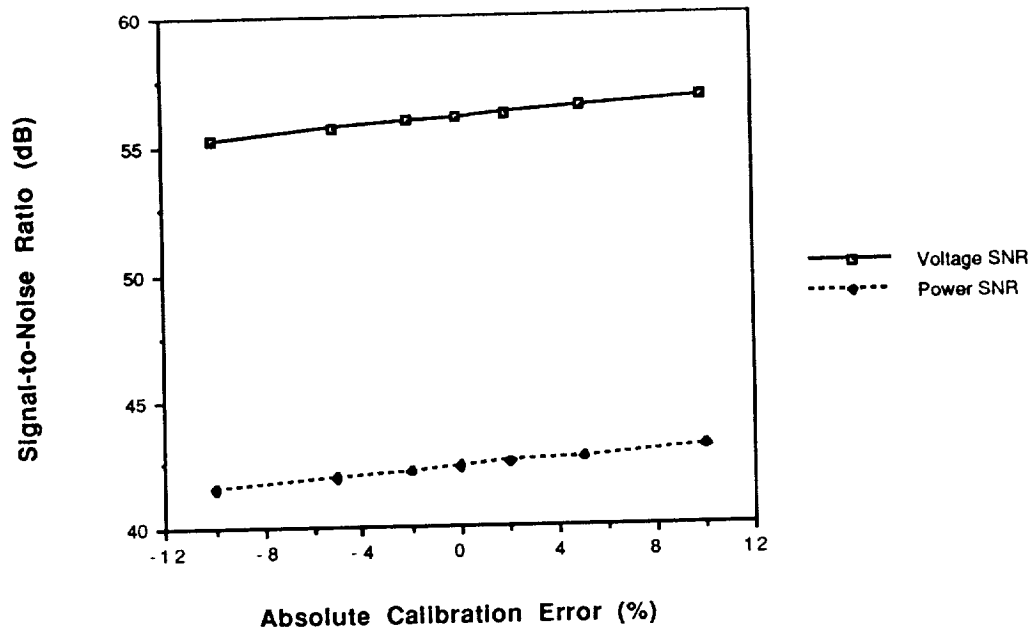


Figure 4.48 Effect of Absolute Radiometric Error on SNR.

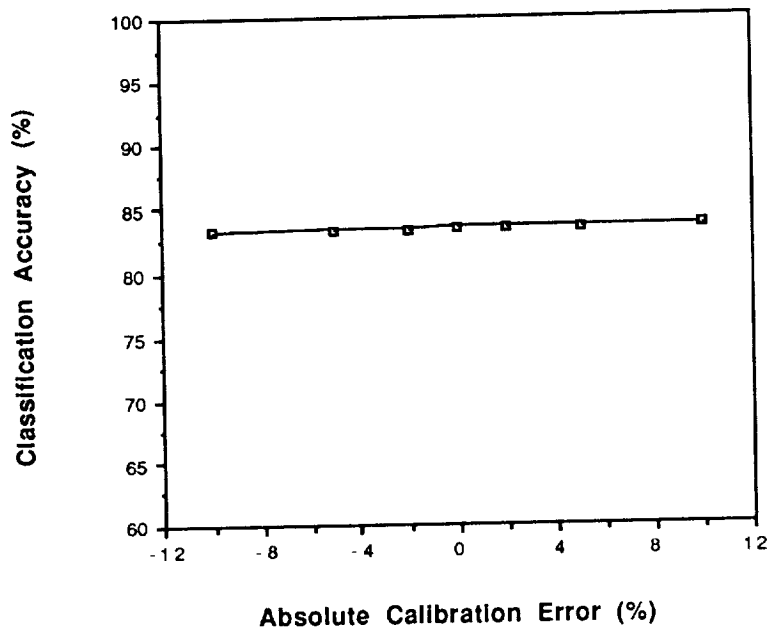


Figure 4.49 Effect of Absolute Radiometric Error on Classification Accuracy.

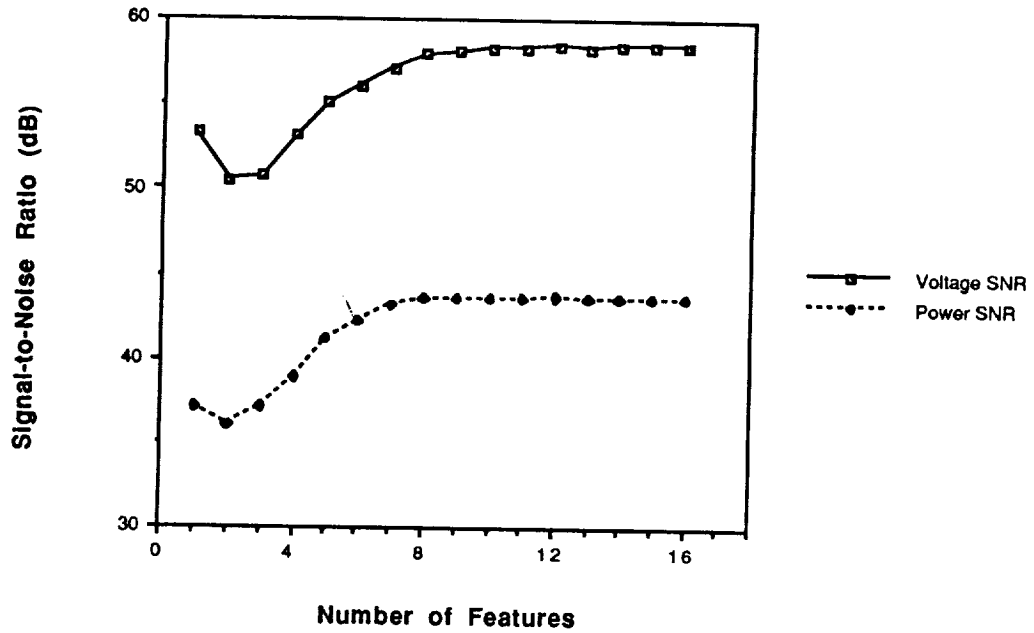


Figure 4.50 Effect of Number of Processing Features on SNR.

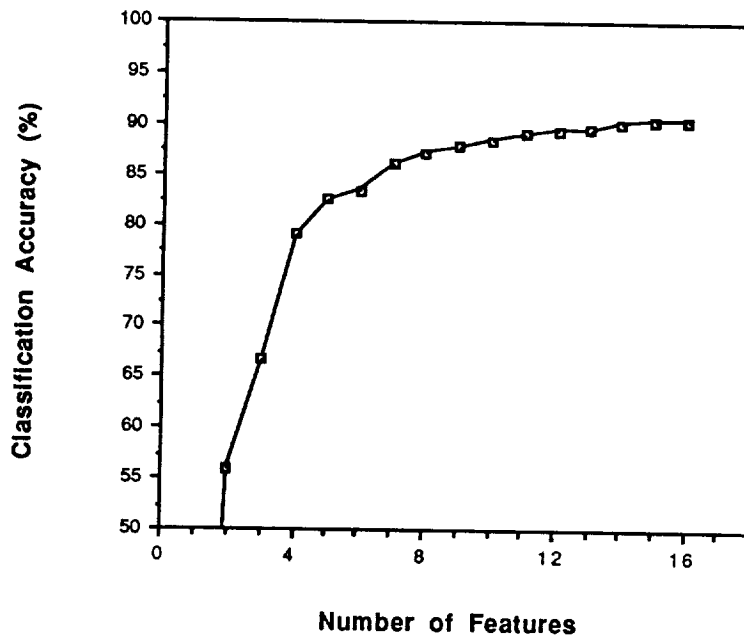


Figure 4.51 Effect of Number of Processing Features on Classification Accuracy.

In computing the SNR values, the method described in section 2.3.4 of chapter two for a feature was extended for combining all of the features and computing one value. Also, in computing the power SNR, the weighting function W_s described in chapter three was used to modify the class variances. The reflectance statistics used in these computations were for the combined data set. The results of these experiments are summarized in Table 4.11.

Table 4.11 Summary Results for System Parameter Experiments.

System Parameter (Increasing)	Figures	Voltage SNR	Power SNR	Accuracy
Scene				
Spatial Correlation	4.28, 4.29	No Change	Increase	Decrease
Meteorological Range	4.30, 4.31	Increase	Increase	Increase
Solar Zenith Angle	4.32, 4.33	Decrease	Decrease	Decrease
View Zenith Angle	4.34, 4.35	Decrease	Decrease	Increase
Sensor				
Sensor Radius	4.36, 4.37	No Change	Decrease	Increase
Shot Noise	4.38, 4.39	Decrease	Decrease	Decrease
Read Noise	4.40, 4.41	Decrease	Decrease	Decrease
IMC Gain	4.42, 4.43	Increase	Increase	Increase
Radiometric Resolution	4.44, 4.45	Increase	Increase	Increase
Relative Calibration Error	4.46, 4.47	Decrease	Decrease	Decrease
Absolute Radiometric Error	4.48, 4.49	Increase	Increase	Increase
Processing				
Number of Features	4.50, 4.51	Increase	Increase	Increase

In Figures 4.52 and 4.53, the results of this section are displayed in a scatter plot to show the relationships between classification accuracy and signal-to-noise ratio. As can be seen, there is no direct relationship. While there appears a significant trend of higher classification accuracy resulting from higher SNR, it is not always the case.

The spatial correlation and sensor IFOV radius are cases in point. While their variation had a significant effect on both classification accuracy and power SNR, the effect was opposite. These spatial parameters come into the noise model only through the modification of the signal covariance matrix thus there is no effect on voltage SNR.

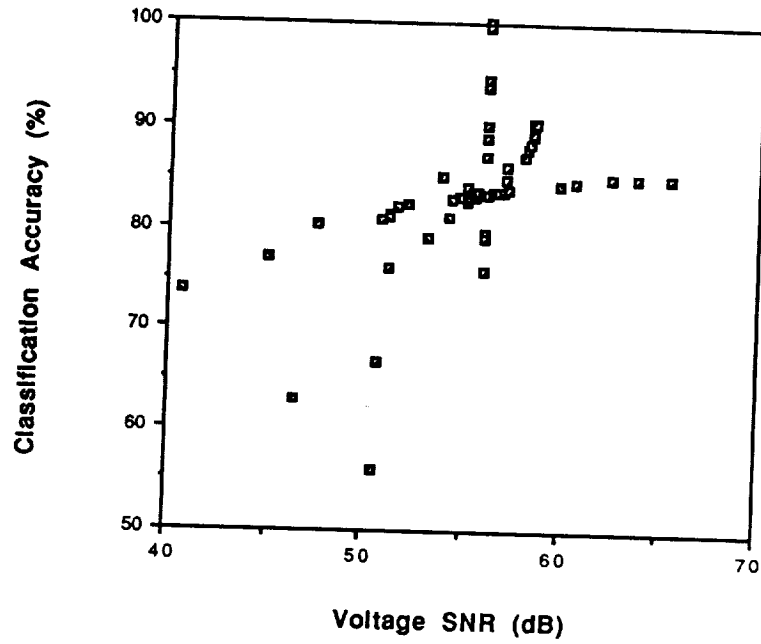


Figure 4.52 Accuracy vs. Voltage SNR for System Parameter Experiments.

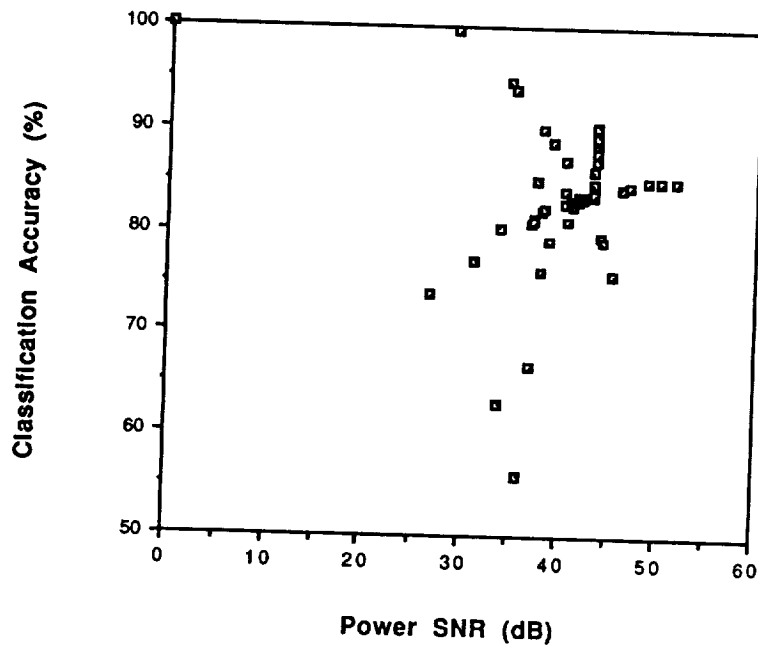


Figure 4.53 Accuracy vs. Power SNR for System Parameter Experiments.

These results are mostly intuitively appealing, except for the sensor view angle. Figure 4.35 contained two curves. The one labelled "with scaling" was obtained using the $1/\cos(\theta_{\text{view}})$ scaling of the ground size of the sensor IFOV as θ_{view} was changed. The other curve labelled "without scaling" did not. It shows the effects due solely to the decreased atmospheric transmittance and increased path radiance. Thus, it seems the increase in accuracy due to the IFOV scaling overrides the decrease due to the atmospheric effects. Of course, this experiment assumes a Lambertian surface reflectance and no effects due to field size and mixed pixels. Also, the atmosphere chosen was relatively clear. In the next section results are presented to show that in hazier atmospheres, the effect of the atmosphere on view angle is much more pronounced.

4.5 Interrelated Parameter Effects

In this section results showing the interrelated effects of parameters are presented. The analytical model is again utilized and the system configuration is as defined in section 4.4. The parameters studied and their variation are given in Table 4.12 below.

Table 4.12 Parameter Interrelationship Studies.

Meteorological Range and Sensor View Angle ($\theta_{\text{solar}} = 0^\circ$)
Meteorological Range and Sensor View Angle ($\theta_{\text{solar}} = 30^\circ$)
Meteorological Range and Sensor View Angle ($\theta_{\text{solar}} = 60^\circ$)
Spatial Correlation and Sensor IFOV Size
Meteorological Range and Shot Noise
Meteorological Range and Read Noise
Meteorological Range and IMC
Meteorological Range and Number of Bits
Meteorological Range and Noise Sources Alone
Solar Zenith Angle and Shot Noise
Sensor View Angle and Shot Noise
Solar Zenith Angle and IMC
Sensor View Angle and IMC
Meteorological Range and Number of Features
Solar Zenith Angle and Number of Features

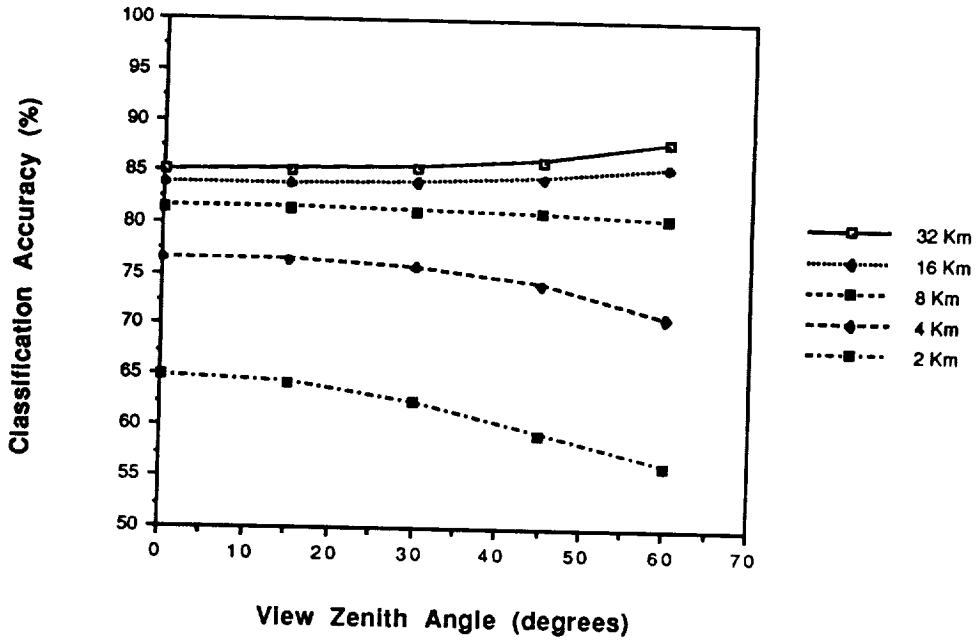


Figure 4.54 Effect of Meteorological Range and View Angle for $\theta_{\text{solar}} = 0^\circ$.

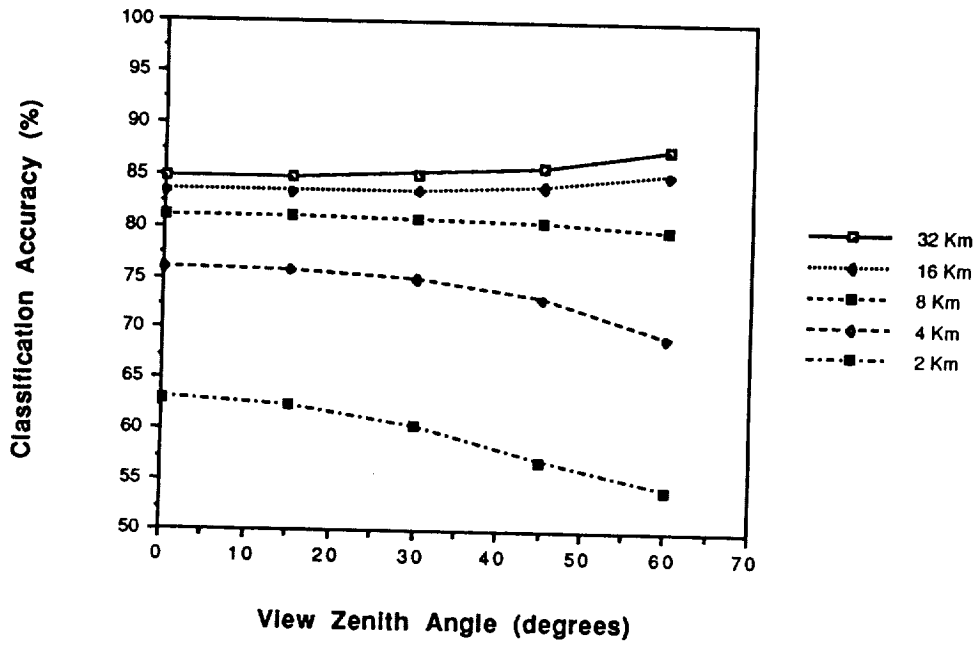


Figure 4.55 Effect of Meteorological Range and View Angle for $\theta_{\text{solar}} = 30^\circ$.

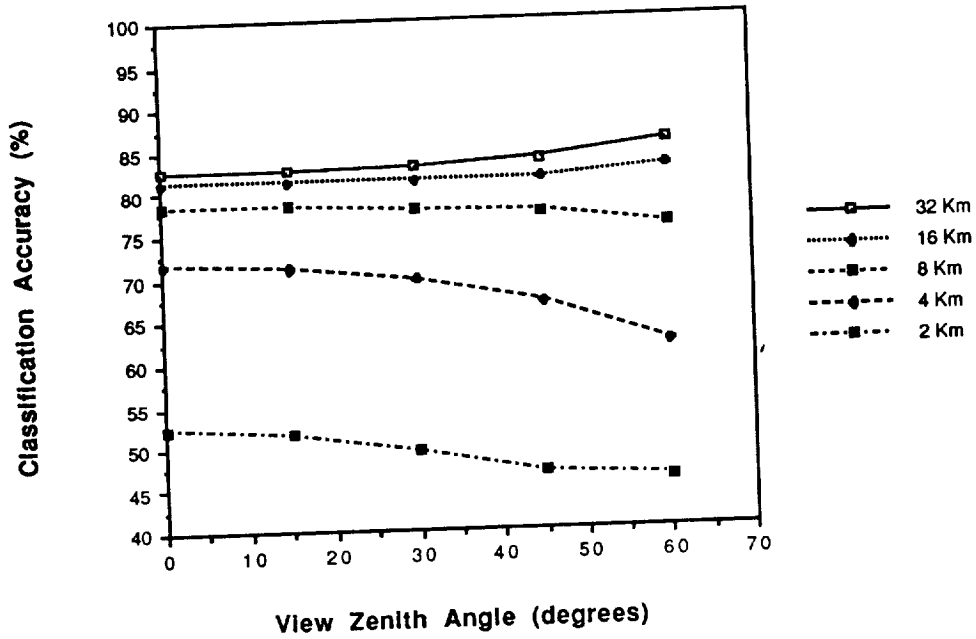


Figure 4.56 Effect of Meteorological Range and View Angle for $\theta_{\text{solar}} = 60^\circ$.

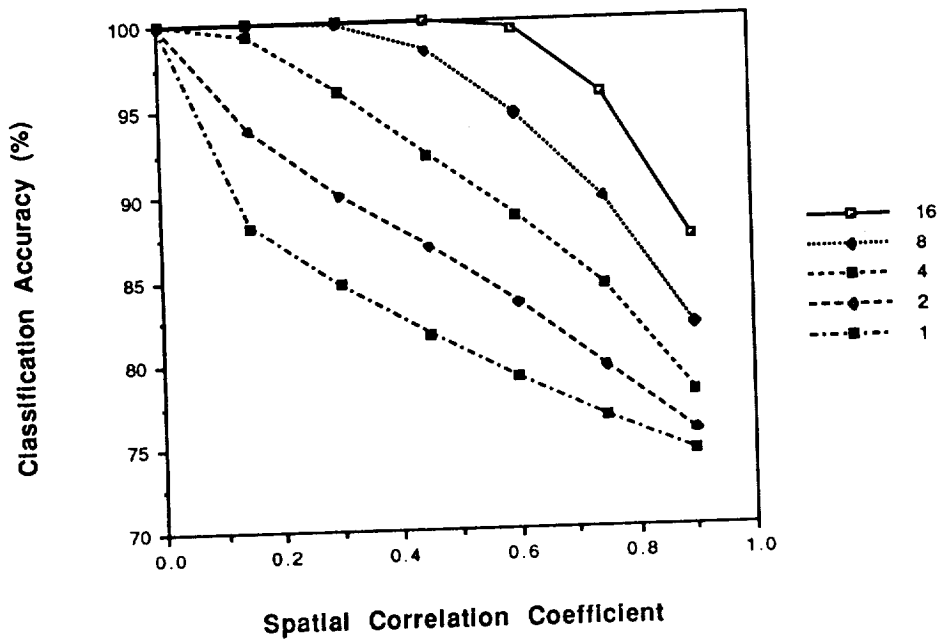


Figure 4.57 Effect of IFOV Size (in Scene Cells) and Spatial Correlation Coefficient.

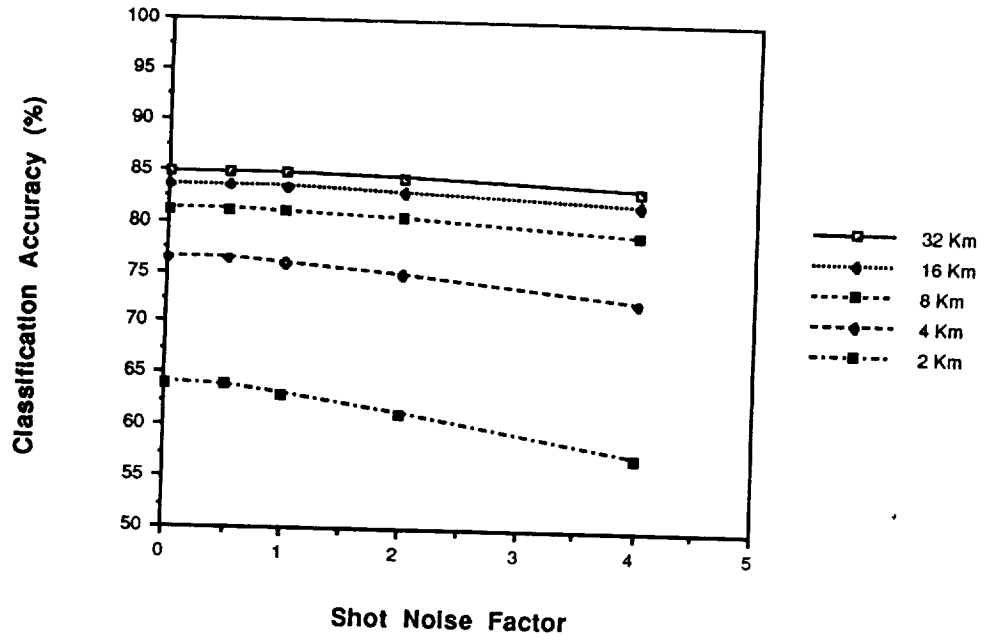


Figure 4.58 Effect of Meteorological Range and Shot Noise.

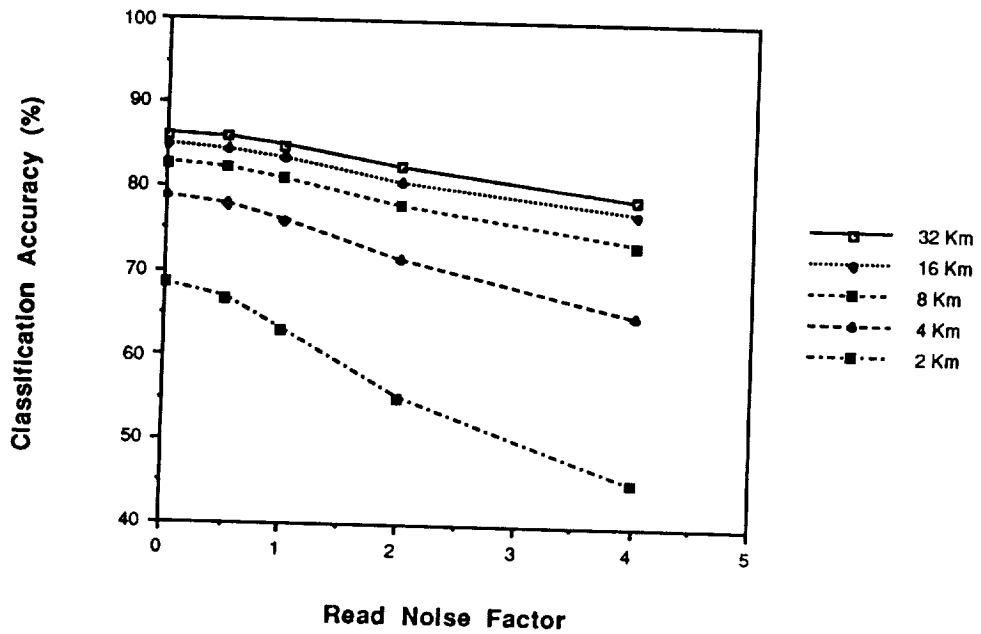


Figure 4.59 Effect of Meteorological Range and Read Noise.

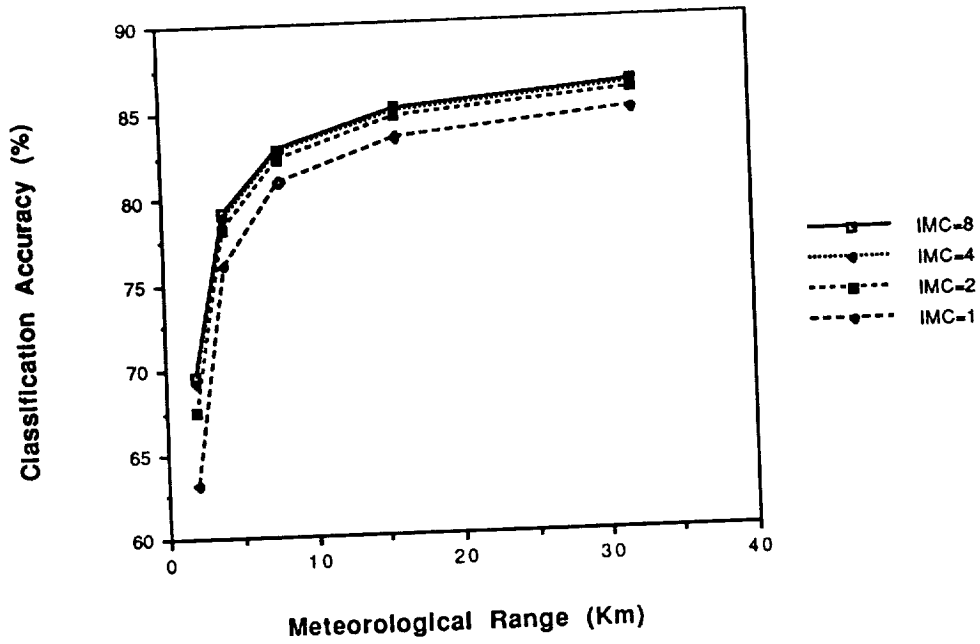


Figure 4.60 Effect of Meteorological Range and IMC.

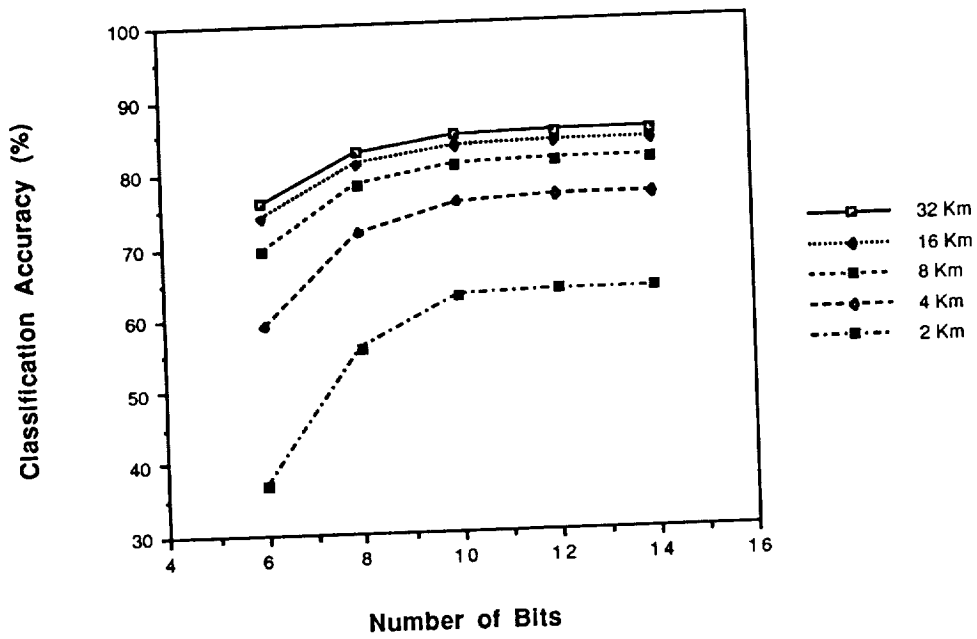


Figure 4.61 Effect of Meteorological Range and Radiometric Resolution.

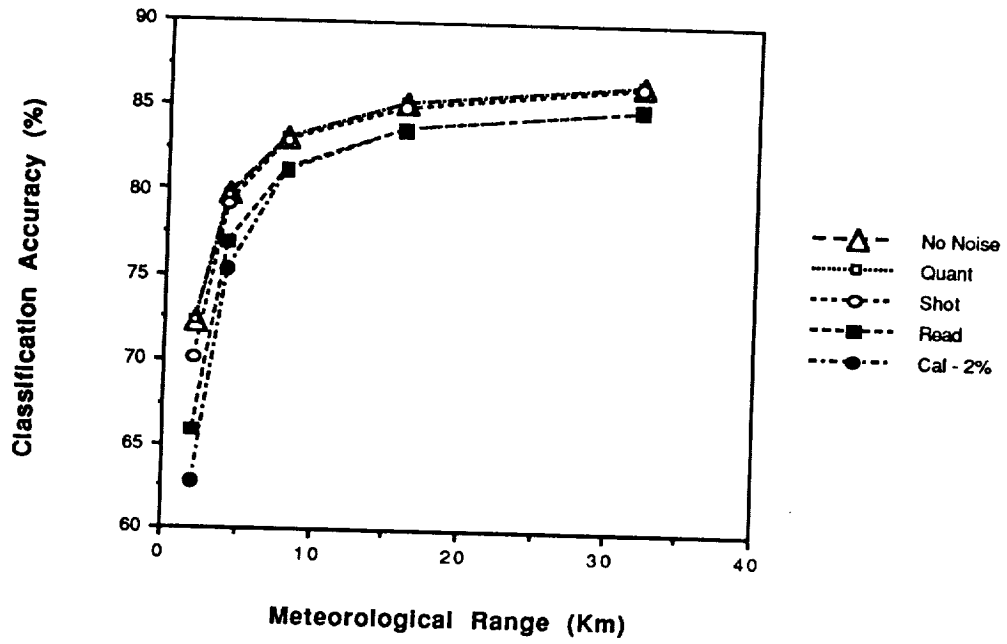


Figure 4.62 Effect of Meteorological Range and Various Noise Sources Alone.

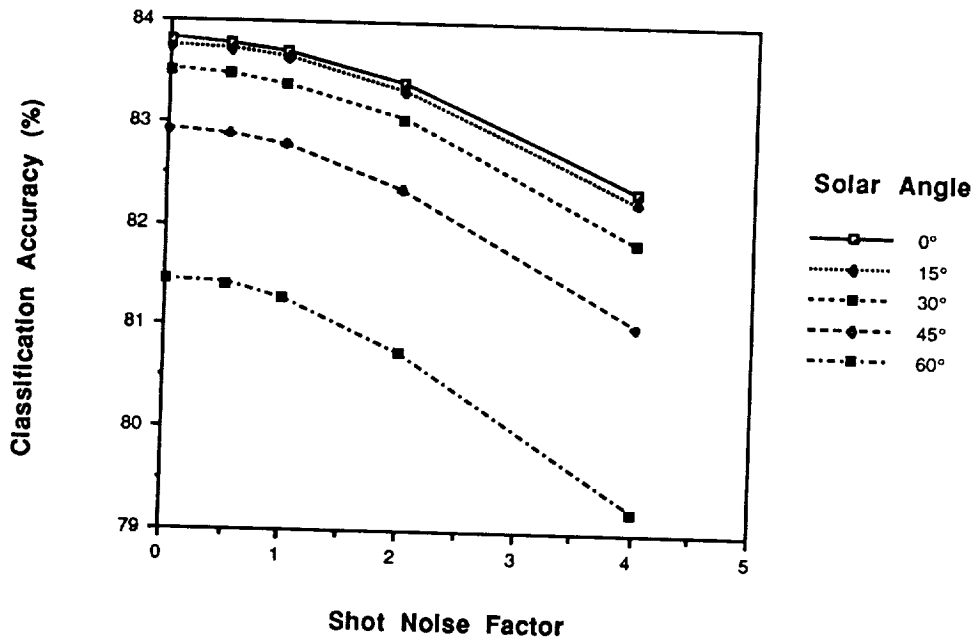


Figure 4.63 Effect of Solar Angle and Shot Noise.

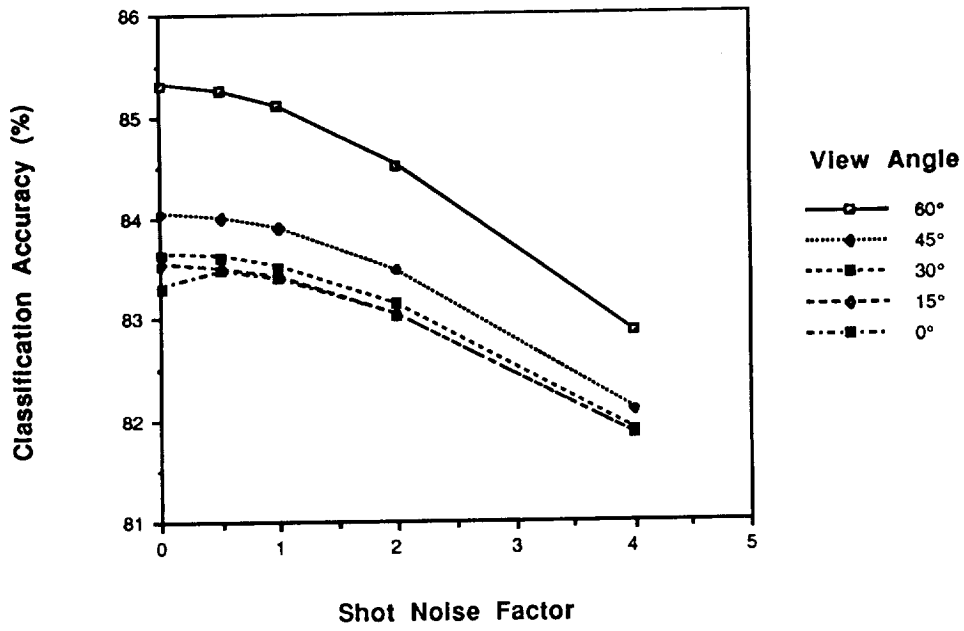


Figure 4.64 Effect of View Angle and Shot Noise.

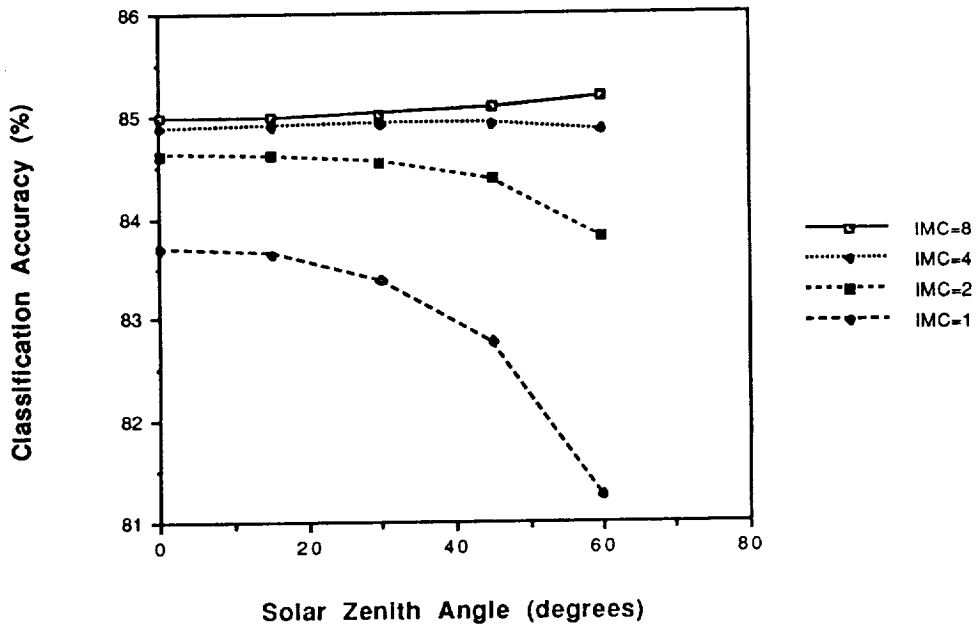


Figure 4.65 Effect of Solar Angle and IMC Gain State.

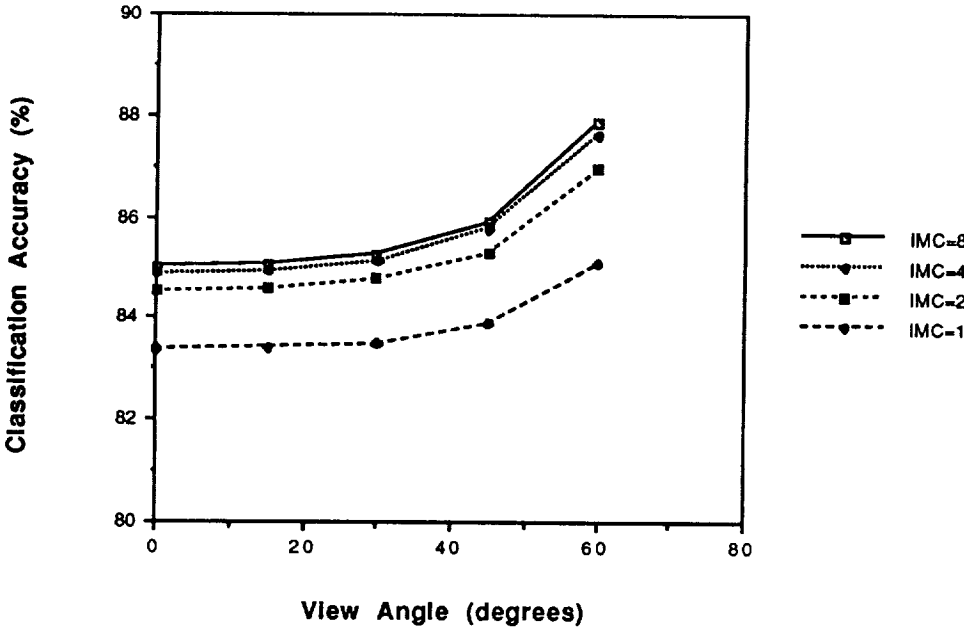


Figure 4.66 Effect of View Angle and IMC Gain State.

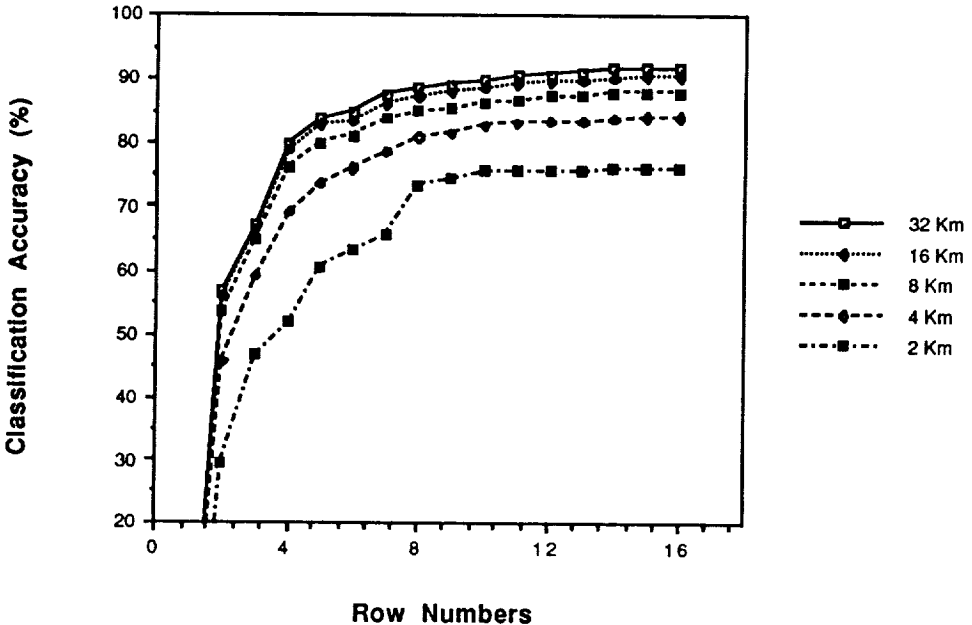


Figure 4.67 Effect of Meteorological Range and Number of Features.

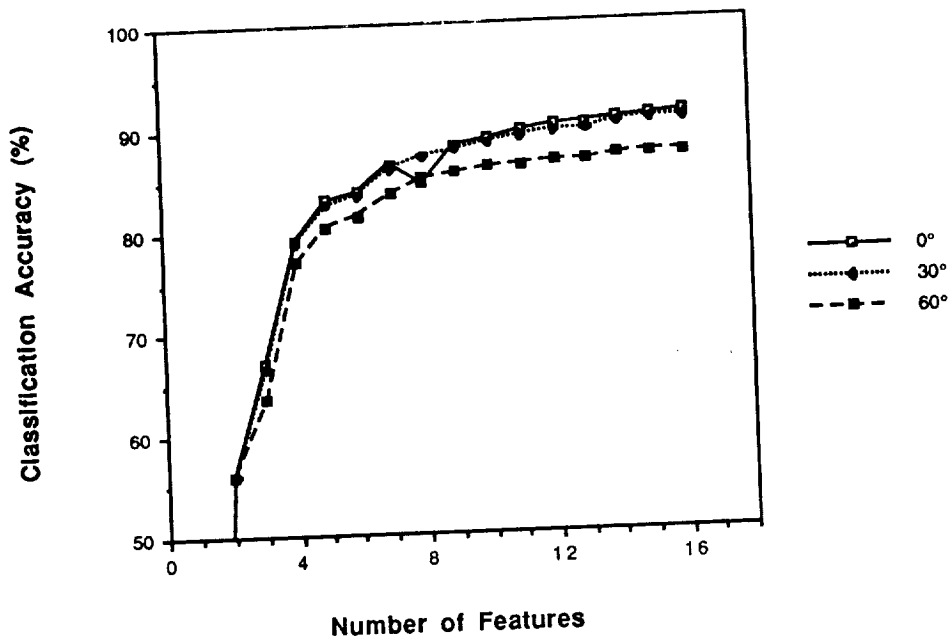


Figure 4.68 Effect of Solar Angle and Number of Features.

The results of these experiments are discussed in the following paragraphs.

Figures 4.54 through 4.56 help understand the relationships between meteorological range, sensor view angle, and solar zenith angle. In clear atmospheres, the increase in accuracy due to the geometry of higher view angles is evident. However, as the atmosphere becomes hazy, the decreased signal levels and increased path radiance become dominant and accuracy is then decreased for higher view angles. The effects due to the atmosphere are seen to be more significant for higher solar zenith angles.

Figure 4.57 shows a complex relationship between the spatial correlation of scene cells, and the number of cells in a sensor IFOV side. With increasing correlation, the accuracy for small cells (many cells per IFOV side) falls sharply before decreasing at a constant rate, while the accuracy for large scene cells (few cells per IFOV side) remains constant before falling sharply at high

correlations. While this result shows the tradeoffs on classification accuracy of scene cell size and spatial correlation for constant sensor IFOV, it is interesting to consider this in the light of the results of Table 2.2. There it was shown that spatial correlation decreases with increasing scene cell size. Thus, for typical remote sensing data sets large scene cells have low spatial correlation, while small cells have high correlation. These tradeoffs form an imaginary horizontal line across Figure 4.57 and indicate that classification accuracy is relatively independent of scene cell size.

Figures 4.58 and 4.59 show that the effects due to increased noise are more significant in hazy atmospheres, while Figure 4.60 shows the improvement by using IMC to be greater in hazy atmospheres. Figure 4.61 demonstrates how the increase in quantization error of fewer radiometric bits can be more significant in hazy atmospheres.

In Figure 4.62, it can be seen that the read noise and relative calibration errors are more significant for all meteorological ranges, while the effect of shot noise is greater at low ranges due to the increase in path radiance. It is interesting to compare the effect of the atmosphere with no noise sources present shown here with that of Landgrebe and Malaret (1986). Their result showed the atmosphere had no effect when no sensor noise was present, while Figure 4.62 shows a significant effect. The difference in these results is due to the path radiance model used in this report. Malaret's model considered path radiance as a constant additive source, while the model used here is dependent upon the surface reflectance. Figure 4.69 shows the effect of the atmosphere with and without sensor noise for the system model modified to remove the surface reflectance dependence on path radiance. As can be seen, the atmosphere has little effect on accuracy when this dependence is removed. It is known that path radiance is dependent upon surface reflectance in the real world, thus the results shown in Figure 4.62 are judged to be more realistic.

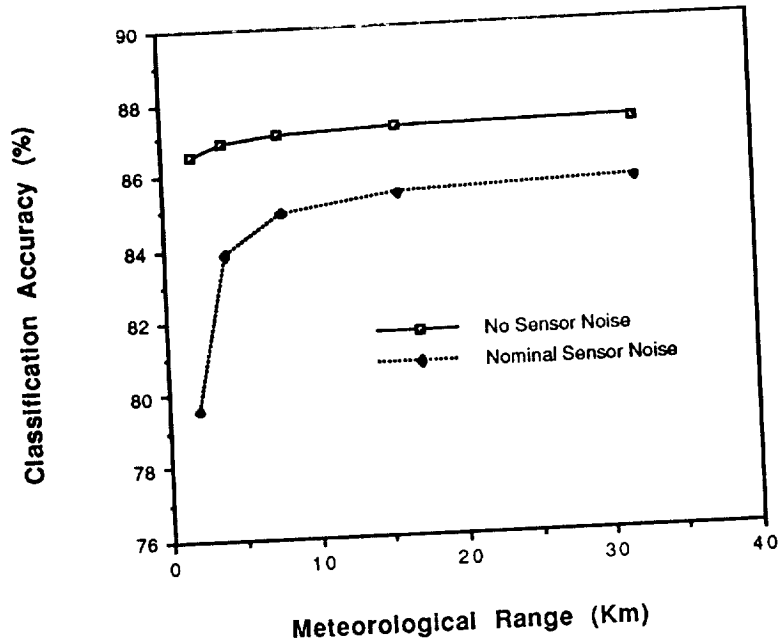


Figure 4.69 Effect of Atmosphere With/Without Noise For Path Radiance Model With No Surface Reflectance Dependence.

Figures 4.63 and 4.64 contain some interesting results. In Figure 4.63, the effect of shot noise is seen to be greater at high solar zenith angles, while in Figure 4.64, just the opposite is seen for high view angles. In both cases, the effect due to the shot noise alone is to decrease accuracy more at higher angles, but for the view angle case the increase in accuracy due to the geometry overrides the shot noise effect.

Figure 4.65 shows how the IMC can be used to overcome the combination of low signal levels and high read noise to actually increase accuracy at high solar zenith angles. In Figure 4.66, a similar effect is seen as the IMC increases accuracy by a greater amount at high view angles.

Figures 4.67 and 4.68 show how, up to a point, more features can be used in classification to overcome the effects of the atmosphere or solar angle.

However, it can be seen that the accuracy increases level out after a certain number of features and increases beyond that level are not significant.

Overall, the results of these experiments show the complex interaction of system parameters in determining their effect on classification accuracy. This demonstrates the importance of considering the interdependence of parameters when considering their specification in the design of a remote sensing experiment.

4.6 Feature Selection Experiments

Several sets of six features (shown in Table 4.13) were used to evaluate their classification performance for a variety of system parameter variations and scenes. This section presents the results of these experiments.

Table 4.13 Wavelength Bands Combined for the Various Feature Sets. The Various Feature Sets are Defined as SFD = Spectral Feature Design Algorithm, TM = Landsat Thematic Mapper, WSNR = Wide Signal-to-Noise Ratio, NSNR = Narrow Signal-to-Noise Ratio, SSFD = Single Band Spectral Feature, SSNR = Single Band Signal-to-Noise Ratio.

Feature	SFD	TM	WSNR	NSNR	SSFD	SSNR
1	0.52-0.66	0.45-0.52	0.40-0.70	0.51-0.56	0.59	0.54
2	0.66-0.84	0.52-0.60	0.77-0.90	0.81-0.86	0.75	0.84
3	0.70-0.92	0.63-0.69	1.00-1.10	1.02-1.07	0.81	1.04
4	1.48-1.64	0.76-0.90	1.15-1.30	1.20-1.25	1.56	1.11
5	1.98-2.20	1.45-1.75	1.50-1.74	1.59-1.64	2.10	1.61
6	2.20-2.40	2.08-2.35	1.97-2.40	2.16-2.21	2.30	2.19

The SNR features were chosen based upon spectral regions of high SNR. These various sets were chosen to see how classification accuracy and combined signal-to-noise ratios compared. Figure 4.70 shows the voltage and power SNR for the various feature sets and the combined reflectance statistics of the data set in Table 4.1, while Figure 4.71 shows the resultant classification accuracy for the baseline system of Table 4.9.

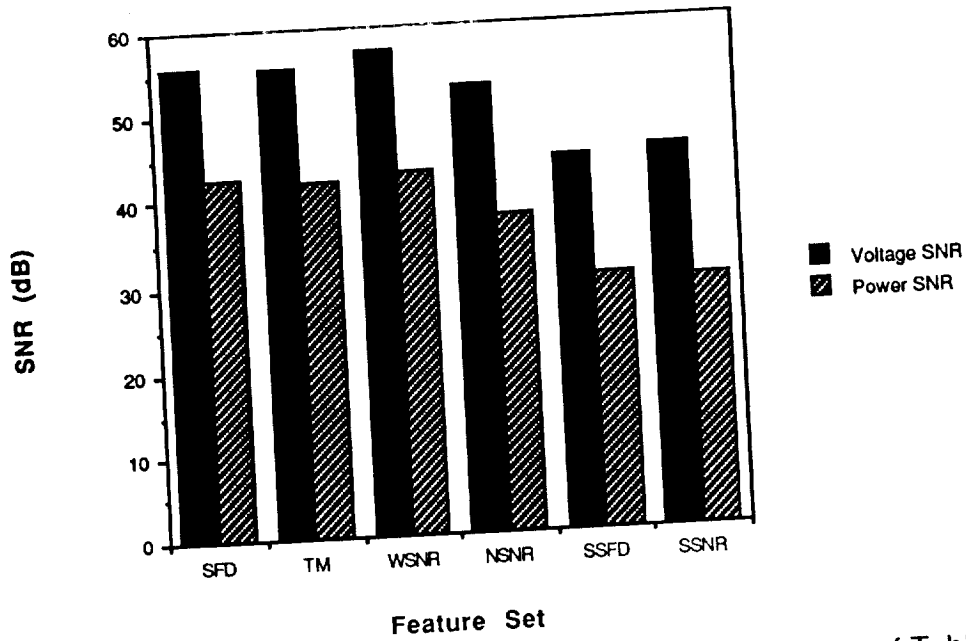


Figure 4.70 Voltage and Power SNR for the Various Feature Sets of Table 4.13.

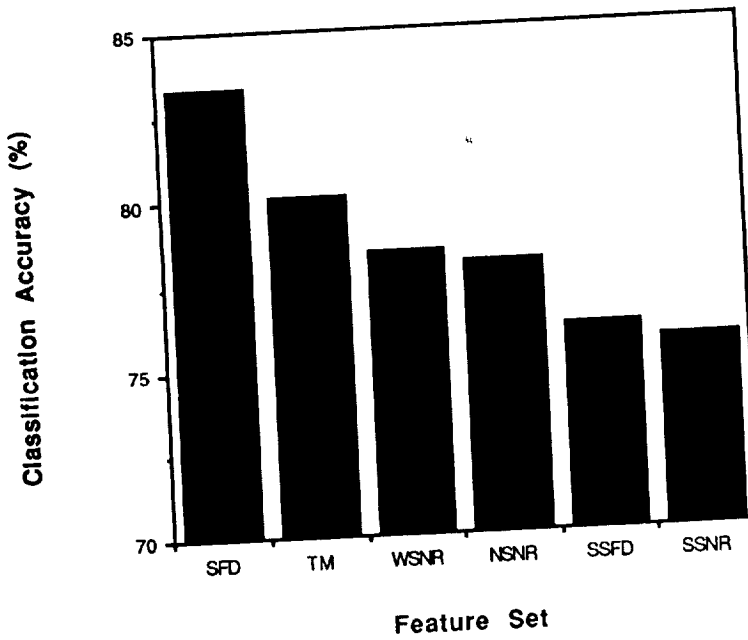


Figure 4.71 Classification Accuracy for the Various Feature Sets of Table 4.13.

In this case, the SFD features performed the best for this data set, even though they did not have highest SNR. However, since they were derived from the data used to generate the scene, it is expected that they perform well.

Several experiments were run to compare the performance of the various feature sets over varying scene conditions. Figures 4.72, 4.73, and 4.74 show the classification performance of the feature sets for various meteorological ranges, solar zenith angles, and view angles.

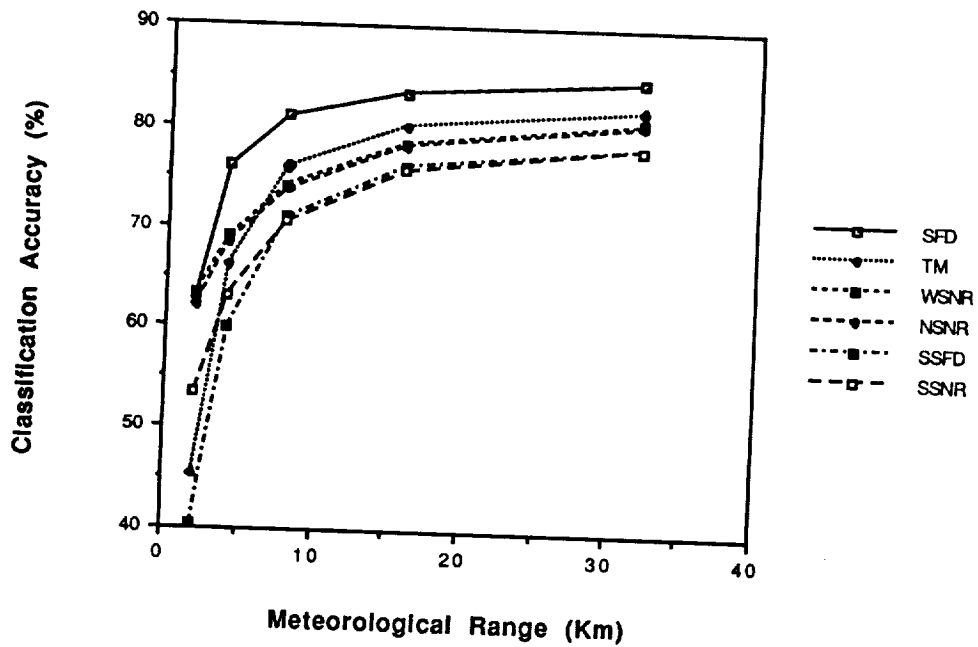


Figure 4.72 Feature Set Performance vs. Meteorological Range.

From these curves, it can be seen that the features derived from high SNR regions are less susceptible to changes in the scene parameters. However, they give overall less accuracy than the features obtained from the SFD algorithm. Also, the features that are obtained from only one spectral band perform poorly under all conditions.

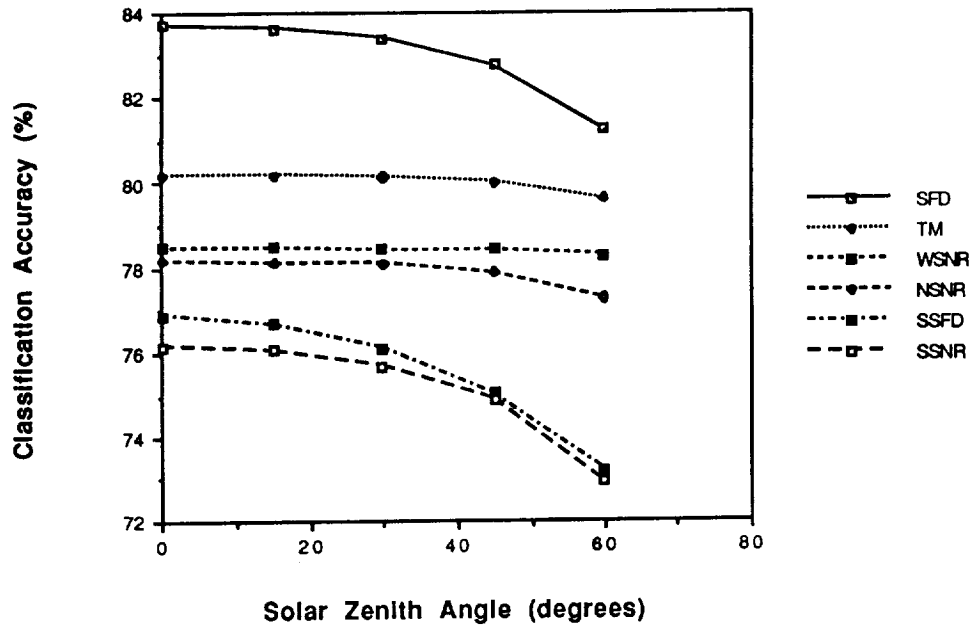


Figure 4.73 Feature Set Performance vs. Solar Angle.

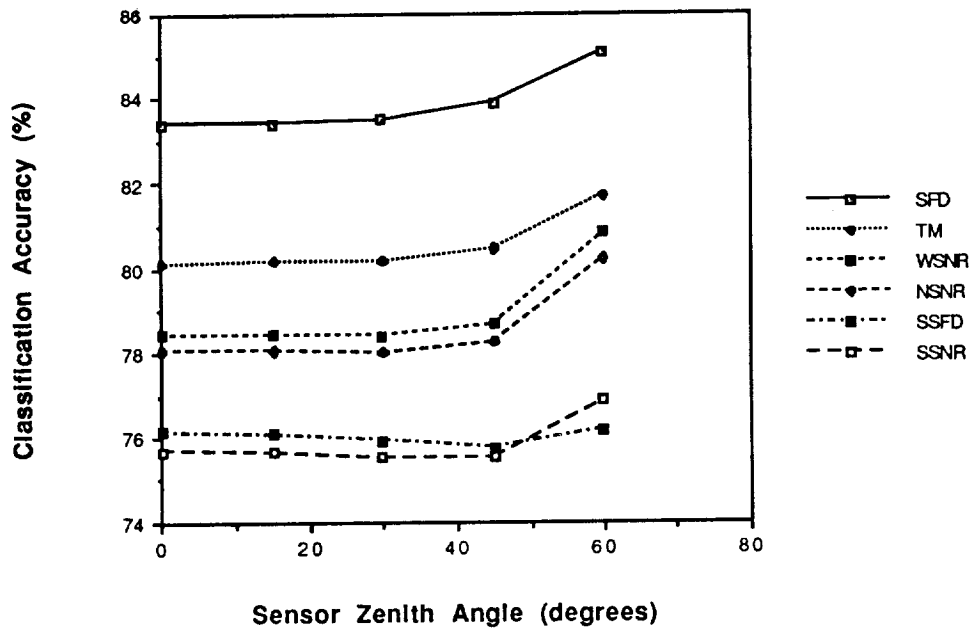


Figure 4.74 Feature Set Performance vs. View Angle.

The robustness of the spectral feature design algorithm was then studied by comparing the accuracy of the various feature sets in classifying a scene created from a different data set than that from which the features were derived. A scene was created from reflectance data of three varieties of spring wheat. Table 4.14 gives the specific fields from the LARS field data base.

Table 4.14. Classes and fields used to compute statistics for the Spring Wheat test scene. The data is from Hand County, South Dakota, on July 26, 1978.

Classes	Field	Number of Observations
Spring Wheat	118	13
	154	29
	199	28
	291	28
	292	16
	Total = 114	
SW 1809	296	28
	303	58
	Total = 86	
SW Mix	75	13
	281	55
	Total = 68	

The system configuration was as shown in Table 4.9. Figure 4.75 shows the voltage and power SNR of the Spring Wheat test scene for the various feature sets, while Figure 4.76 presents the resulting classification accuracy.

In all cases, the features formed from the wavelengths used in the Landsat TM and the ones from high SNR regions performed the best. Compared to these feature sets, the SFD feature set did not perform as well.

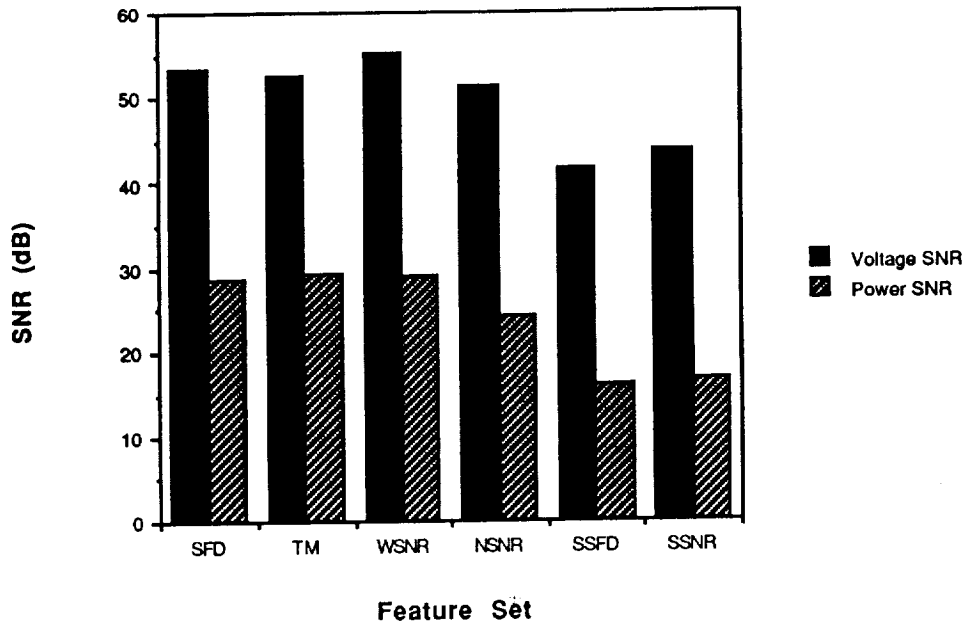


Figure 4.75 SNR for Various Feature Sets and SW Variety Scene.

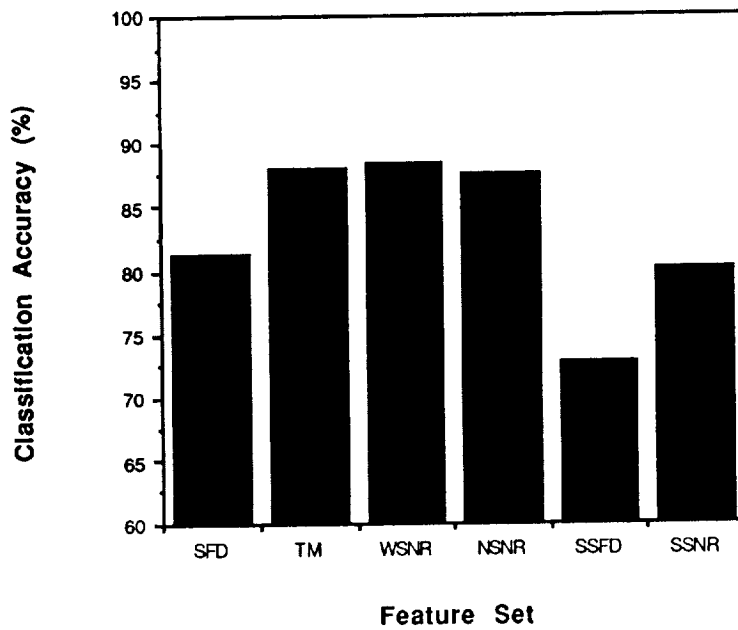


Figure 4.76 Classification Accuracy for Various Feature Sets and SW Variety Scene.

These results imply that over varying scenes the features derived from the reflectance of a different crop type perform less well at classification than features derived from signal-to-noise regions of the instrument, or even the wavelength bands used in the Thematic Mapper. This is not surprising since the SFD procedure is intended to be case-specific; it is intended to provide features optimal for its design case, as compared to being optimal in the general case.

4.7 Summary and Conclusions

In this chapter the system models presented in chapters two and three have been applied to the study of a remote sensing system based on the proposed imaging spectrometer HIRIS. System performance measured by signal-to-noise ratios and classification accuracy has been studied under a variety of system parameter configurations. While the results of these experiments have been discussed at the end of each of the sections, the following paragraphs briefly summarize the main conclusions.

In section 4.2 the Signal-to-Noise Ratio (SNR) and Noise Equivalent Change in Reflectance ($NE\Delta\rho$) of HIRIS was studied. The results illustrated how the atmosphere affects each of the spectral bands, and what noise sources are the most dominant under a variety of conditions. Hazier atmospheres were seen to have more significant effects on the shorter wavelength bands than the longer wavelengths. Shot noise was seen to be more significant at the high signal levels at the wavelengths of the VNIR detector array, while read noise was the dominant noise source in the longer wavelengths of the SWIR array.

Section 4.3 investigated the similarities and differences between the simulation model of chapter two and the analytical model of chapter three. The results indicated that the approaches gave similar results, except in cases where mixed pixels or the training of a classifier were involved.

Section 4.4 presented the results of applying the analytical model to the study of the individual effect of several parameters on SNR and classification accuracy. The results generally showed a trend of increased SNR resulting in increased accuracy, except for parameters involved with spatial variation. Here,

the spatial parameters resulting in lower power SNR gave an increase in classification by increasing the separability of the classes.

In section 4.5 the interdependence of system parameters was investigated. Significant relationships were seen between system parameters, especially those involving pixel size variations and signal dependent noise.

Section 4.6 presented several results comparing various methods of choosing spectral feature sets under a variety of system conditions. The results indicated that feature sets based on high SNR were the most robust under system parameter variations, but feature sets derived from the original reflectance data were optimum for scenes created from that data.

These results have been presented to show the relative importance of the system parameters. In no way are these results intended to be used to predict the actual performance of the system. Rather, they are useful in discovering the relative effects and tradeoffs in specifying the various parameters.

CHAPTER 5

CONCLUSIONS AND SUGGESTIONS FOR FURTHER WORK

In pursuing this research, the goals were to: 1) document and model the remote sensing process from an overall systems perspective; 2) develop a tool to allow the study of the interrelationships of identifiable system parameters; 3) apply this tool to the study of optical remote sensing systems.

Chapters one and two described the remote sensing process from a systems perspective. It was seen to be comprised of three major components: the scene, the sensor, and the processing algorithms. Modeling of these components was discussed from a general point of view, and a framework was described for implementing a subset of these models in a simulation of the entire system. The simulation used the scene models to produce a spectral radiance function over a defined scene consisting of various informational classes arranged spatially. The sensor models then converted this function into a digital multispectral image, similar to that produced by real sensors. Various processing algorithms were then applied to this image to extract a performance measure of the system.

Chapter three presented an alternative to the simulation approach with the development of a parametric model to describe the remote sensing process. This model used analytical equations to describe the effects of the various system parameters.

Each of these approaches are useful as a tool to study remote sensing systems, and the choice of their use is dependent upon the goal of the study.

The simulation method is useful in the following example cases.

- The spatial layout of the various classes is of interest.
- A particular scene or image is desired to be simulated under a variety of conditions.
- An image with desired characteristics is needed for the study of various processing algorithms.
- One scene needs to have several different sensors applied to it to compare the resulting images.
- It is desired to use a very accurate and detailed model for the sensor spatial, spectral, and noise effects.
- It is desired to introduce spatial effects in the scene such as clouds, shadows, or in the sensor such as geometric distortion or misregistration.

The parametric model is useful for the following examples.

- Parameter tradeoff studies where detail of models can be sacrificed for speed of results.
- The scene has a large number of classes with no particular constraints on spatial layout.

These are only a few of the possible uses of both approaches, but they are listed to illustrate some of the kinds of studies that are possible under the modeling framework developed in this report.

Chapter four presented a detailed study of the system performance of a future imaging spectrometer. The goals were to evaluate the noise and classification performance of the instrument under a variety of system configurations. For the majority of the results, the analytical model was implemented. This allowed the tradeoff study of several parameters to help determine the interrelationships among them. Although the results were for the particular instrument and scene defined, the general trends were observed and are believed to hold for similar systems.

Some of the significant results of this study of HIRIS include the following.

- Atmospheric visibility and scattered path radiance influence the sensitivity of the instrument to ground reflectance changes much more in the visible wavelengths than in the infrared.
- While classification accuracy is usually related directly to SNR, it is not always the case.
- The effect of the atmosphere on sensor viewing angle varies significantly with visibility.
- Lower classification accuracies in hazy atmospheres are not only because of noise sources in the sensor, but also the increased path radiance scattered from the surface.
- While feature sets chosen from spectral regions of high SNR are robust across system parameter variations, feature sets derived using analytical approaches from field databases perform optimally for scenes created from the data.

The work presented here has been but one step on the road to modeling and understanding optical remote sensing systems. It has built upon the work of many previous researchers, and hopefully, will stand as a foundation for future efforts.

While almost every component of the system model could be improved, several particular areas deserve to be pointed out. The surface reflectance model assumption of Lambertian reflectance could be replaced by a description of the bidirectional reflectance. Embedded within this function should be the spectral and spatial variation of the reflectance. Another assumption used in the scene spatial model that needs work is the spatial crosscorrelation between high spectral resolution reflectance data.

Two aspects of the atmospheric model could be extended. The relationship between the total surface irradiance and the direct irradiance needs to be more adequately defined. Also, spatial blurring and spatial variability of the atmosphere could be implemented.

Geometric distortion and spectral band misregistration could be implemented in the sensor model.

This simulation approach could be used today to generate realistic high dimensional multispectral images for use in processing algorithm study. These may be studies of hyperspectral image display or classification algorithm development.

These are but a few of the possible extensions and uses of the modeling approaches. Indeed, it would seem to be an axiom of modeling that one can always improve one's model, especially when part of the subject is the natural world.

LIST OF REFERENCES

- Allen, W.A., T.V. Gayle, and A.J. Richardson, "Plant Canopy Irradiance Specified By Duntley Equations," *Journal Optical Society of America*, vol. 60, pp. 372-376, 1970.
- Anuta, P.E., "LARS/University of Michigan Aircraft Scanner Data System Parameter Identification Study," LARS Information Note 091470, Laboratory for Applications of Remote Sensing, Purdue University, West Lafayette, IN 47907, September 1970.
- Asrar, G., Editor, **Theory and Applications of Optical Remote Sensing**, Wiley-Interscience, New York, NY, 1989.
- Badhwar, G.D., K.E. Henderson, D.E. Pitts, W.R. Johnson, M.L. Sestak, T. Woolford, J. Carnes, "A Comparison of Simulated Thematic Mapper Data and Multispectral Scanner Data for Kingsbury County, South Dakota," *Proceedings of 1982 Machine Processing of Remotely Sensed Data Symposium*, West Lafayette, IN, 1982.
- Badhwar, G.D., W. Verhoef, and N.J.J. Bunick, "Comparative Study of Suits and SAIL Canopy Reflectance Models," *Remote Sensing of Environment*, vol. 17, pp. 179-195, 1985.
- Bartlett, D.S., R.W. Johnson, M.A. Hardisky, and V. Klemas, "Assessing Impact of Off-Nadir Observation on Remote Sensing of Vegetation: Use of the Suits Model," *Int. J. Remote Sensing*, vol. 7, no. 2, pp. 247-264, February 1986.
- Biehl, L.L., M.E. Bauer, B.F. Robinson, C.S.T. Daughtry, L.F. Silva, and D.E. Pitts, "A Crops and Soils Data Base for Scene Radiation Research," *Proceedings of the 8th International Symposium on Machine Processing of Remotely Sensed Data*, pp. 169-177, Purdue University, West Lafayette, IN, 1982.
- Billingsley, F.C., "Modelling Misregistration and Related Effects on Multispectral Classification," *Photogrammetric Engineering and Remote Sensing*, vol. 48, pp. 421-430, 1982.
- Bird, R.E., "Terrestrial Solar Spectral Modeling," *Solar Cells*, vol. 7, no. 1-2, pp. 107-118, November 1982.
- Carter, V. and J. Schubert, "Coastal Wetlands Analysis From ERTS MSS Digital Data and Field Spectral Measurements," *Proceedings of the Ninth International Symposium on Remote Sensing of the Environment*, Ann Arbor, MI, pp. 1241-1260, 1974.
- Castle, K.R., R.G. Holm, C.J. Kastner, J.M. Palmer, P.N. Slater, M. Dinguirard, C.E. Ezra, R.D. Jackson, and R.K. Savage, "In-Flight Absolute Radiometric Calibration of the Thematic Mapper," *IEEE Transactions on Geoscience and Remote Sensing*, Vol. GE-22, No. 3, pp. 251-255, May 1984.
- Catanzariti, E., "Satellite Image Understanding Through Synthetic Images," in **Pictorial Analysis**, ed. R.M. Haralick, pp. 369-383, Springer-Verlag, 1983.

- Chahine, M.T. "Interaction Mechanisms Within the Atmosphere," Chapter 5 in **Manual of Remote Sensing**, 2nd Edition, edited by R.N. Colwell, American Society of Photogrammetry, Falls Church, VA, 1983.
- Chance, J.E. and W.E. LeMaster, "Suits Reflectance Models for Wheat and Cotton: Theoretical and Experimental Tests," *Applied Optics*, vol. 16, no. 2, pp. 407-412, February 1977.
- Chandrasekaran, B. and A.K. Jain, "Independence, Measurement Complexity, and Classification Performance," *IEEE Transactions on Systems, Man, and Cybernetics*, vol. SMC-5, no. 2, pp. 240-244, March 1975.
- Chellappa, R., "Stochastic Models in Image Analysis and Processing," Ph.D. Thesis, Purdue University, West Lafayette, IN 47907, August 1981.
- Chen, C.-C. T., and D.A. Landgrebe, "Spectral Feature Design In High Dimensional Multispectral Data," TR-EE 88-35, School of Electrical Engineering, Purdue University, West Lafayette, IN, August 1988.
- Cicone, R.C., W.A. Malila, J.M. Gleason, and R.F. Nalepka, "Effects of Misregistration on Multispectral Recognition," *Proceedings of the Symposium on the Machine Processing of Remotely Sensed Data*, Purdue University, West Lafayette, IN, pp. 4A-1 to 4A-8, 1976.
- Clark, J., and N.A. Bryant, "LANDSAT-D Thematic Mapper Simulation Using Aircraft Multispectral Scanner Data," *Proceedings of the 15th Environmental Research Institute of Michigan Symposium*, 1982.
- Colwell, R.N., Editor, **Manual of Remote Sensing**, 2nd Edition, American Society of Photogrammetry and Remote Sensing, Falls Church, VA, 1983.
- Cooper, K., J. Smith, and D. Pitts, "Reflectance of a Vegetation Canopy Using the Adding Method," *Applied Optics*, vol. 21, pp. 4112-4118, 1982.
- Craig, R.G., "The Spatial Structure of Terrain: A Process Signal in Satellite Digital Images," *Proceedings of the Ninth Pecora Remote Sensing Symposium*, pp. 51-54, IEEE Computer Society Press, October 1984.
- Crane, R.B., W.A. Malila, and W. Richardson, "Suitability of the Normal Density Assumption for Processing Multispectral Scanner Data," *IEEE Transactions on Geoscience Electronics*, Vol GE-10, No. 4, October 1972.
- Crutchfield, J.P., J.D. Farmer, N.H. Packard, R.S. Shaw, "Chaos," *Science*, December 1986.
- Dave, J.V., "Extensive Datasets of the Diffuse Radiation in Realistic Atmospheric Models with Aerosols and Common Absorbing Gases," *Solar Energy*, vol. 21, pp. 361-369, 1978.
- Delp, E.J., R.L. Kashyap, and O.R. Mitchell, "Image Data Compression Using Autoregressive Time Series Models," *Pattern Recognition*, vol. 11, pp. 313-323, 1979.
- Diner, D.J. and V.V. Martonchik, "Atmospheric Transfer of Radiation Above an Inhomogeneous Non-Lambertian Reflective Ground I. Theory," *Journal Quant. Spectros. Rad. Transfer*, Vol. 31 pp. 97-125, 1984.
- Dodd, N., "Multispectral Texture Synthesis Using Fractal Concepts," *IEEE Transactions on Pattern Analysis and Machine Intelligence*, Vol. PAMI-9, No. 5, pp. 703-707, September 1987.

- Duda, R.O., and P.E. Hart, **Pattern Classification and Scene Analysis**, John Wiley and Sons, New York, NY, 1973.
- Elterman, L., "UV, Visible, and IR Attenuation for Altitudes to 50 Km," AFCRL 68-0153, AFCEP ERP 285, Air Force Cambridge Research Laboratories, Bedford MA, 1968.
- Elterman, L., "Vertical Attenuation Model with Eight Surface Meteorological Ranges, 2 to 13 km," Report 70-0200, Air Force Cambridge Research Laboratory, Bedford, MA, 1970.
- Fischel, D., "Validation of the Thematic Mapper Radiometric and Geometric Correction Algorithms," *IEEE Transactions on Geoscience and Remote Sensing*, vol. GE-22, no. 3, pp. 237-242, May 1984.
- Foley, D.H., "Considerations of Sample and Feature Size," *IEEE Transactions on Information Theory*, Vol. IT-18, No. 5, September 1972.
- Friedlander, B., "On the Computation of the Cramer-Rao Bound for ARMA Parameter Estimation," *IEEE Transactions on Acoustics, Speech, and Signal Processing*, vol. ASSP-32, no. 4, pp. 721-727, August 1984.
- Fukanaga, K. and T.F. Kriple, "Calculation of Bayes' Recognition Error for Two Multivariate Gaussian Distributions," *IEEE Transactions on Computers*, vol. C-18, no. 3, pp. 220-229, March 1969.
- Fukanaga, K., **Introduction to Statistical Pattern Recognition**, Academic Press, 1972.
- Ghassemian, H. and D.A. Landgrebe, "An Unsupervised Feature Extraction Method for High Dimensional Image Data Compaction," *Proceedings of the Systems, Man and Cybernetics Conference*, Alexandria, VA October 20-23, 1987.
- Gleick, J., **Chaos: Making a New Science**, Viking Penguin, 1987.
- Goetz, A.F.H. and M. Herring, "The High Resolution Imaging Spectrometer (HIRIS) for Eos," *IEEE Transactions on Geoscience and Remote Sensing*, Vol. GE-27, No. 2, pp. 136-144, March, 1989.
- Goodman, J.W. **Introduction to Fourier Optics**, McGraw Hill, 1968.
- Haralick, R.M., "Statistical and Structural Approaches to Texture," *Proceedings of the IEEE*, vol. 67, no. 5, pp. 786-804, May 1979.
- Herman, S.M. and S.R. Browning, "The Effect of Aerosols on the Earth Atmosphere Albedo," *Journal of Atmospheric Science*, vol. 32, pp. 1430-1445, 1975.
- Hixson, M.M., M.E. Bauer, and L.L. Biehl, "Crop Spectra From LACIE Field Measurements," LARS CR 011578, Laboratory for Applications of Remote Sensing, Purdue University, West Lafayette, IN, 1978.
- Horn, B.K.P. and B.L. Bachman, "Using Synthetic Images to Register Real Images with Surface Models," *Communications of the ACM*, vol. 21, no. 11, November 1978.
- Huck, F.O., R.E. Davis, C.L. Fales, R.M. Aherron, R.F. Arduini, and R.W. Samms, "Study of Remote Sensor Spectral Responses and Data Processing Algorithms for Feature Classification," *Optical Engineering*, vol. 23, no. 5, pp. 650-666, September/October 1984.
- Hudson, R.D., Jr., **Infrared System Engineering**, Wiley-Interscience, New York, NY, 1969.

- Hughes, G.F., "On the Mean Accuracy of Statistical Pattern Recognizers," *IEEE Transactions on Information Theory*, vol. IT-14, no. 1, pp. 55-63, January 1968.
- Irons, J.R., K.J. Ranson, and C.S.T. Daughtry, "Estimating Big Bluestem Albedo From Directional Reflectance Measurements," *Remote Sensing of Environment*, vol. 25, pp. 185-199, 1988.
- JPL, "High-Resolution Imaging Spectrometer (HIRIS): Phase A Final Report," JPL D-4782, Jet Propulsion Laboratory, California Institute of Technology, Pasadena, CA, November 1987. Also, data was obtained from viewgraphs used in a presentation by V. Wright of JPL on October 6, 1987 to the Imaging Spectrometer Science Advisory Group (ISSAG).
- Jensen, J.R., "Urban Change Detection Mapping Using Landsat Digital Data," *The American Cartographer*, vol. 8, pp. 127-147, 1981.
- Johnson Space Center, "Modular Multiband Scanner (MMS)", JSC Internal Note No. 74-FM-47, Johnson Space Center, Houston Texas, July, 1974.
- Kay, S., "Generation of the Autocorrelation Sequence of an ARMA Process," *IEEE Transactions on Acoustics, Speech, and Signal Processing*, vol. ASSP-33, no. 3, pp. 733-734, June 1985.
- Kailath, T., "The Divergence and Bhattacharyya Distance Measures in Signal Selection," *IEEE Transactions on Communication Technology*, vol. COM-15, no. 1, pp. 52-60, February 1967.
- Kalayeh, H.M., M.J. Muasher, and D.A. Landgrebe, "Feature Selection with Limited Training Samples," *IEEE Transactions on Geoscience and Remote Sensing*, vol. GE-21, no. 4, pp. 434-438, October 1983.
- Kaufman, Y.J. and R. S. Fraser, "Atmospheric Effect on Classification of Finite Fields," *Remote Sensing of Environment*, vol. 15, no. 2, pp. 95-118, March 1984.
- Kaufman, Y.J., "Atmospheric Effect on Spatial Resolution of Surface Imagery," *Applied Optics*, Vol. 23, No. 19, pp. 3400-3408, 1 October 1984.
- Kaufman, Y.J., "Atmospheric Effect on the Separability of Field Classes Measured from Satellites," *Remote Sensing of Environment*, pp. 21-34, August 1985.
- Kerekes, J.P. and D.A. Landgrebe, "A Noise Taxonomy for Remote Sensing Systems," in *Proceedings of IGARSS '87 Symposium*, pp. 903-908, Ann Arbor, MI, 18-21 May, 1987.
- Kerekes, J.P. and D.A. Landgrebe, "HIRIS Performance Study," TR-EE 89-23, School of Electrical Engineering, Purdue University, West Lafayette, IN, April, 1989a.
- Kerekes, J.P. and D.A. Landgrebe, "RSSIM: A Simulation Program for Optical Remote Sensing Systems," TR-EE 89-48, School of Electrical Engineering, Purdue University, West Lafayette, IN, August, 1989b.
- Kettig, R.L., "Computer Classification of Remotely Sensed Multispectral Image Data by Extraction and Classification of Homogeneous Objects," PhD Thesis, School of Electrical Engineering, Purdue University, West Lafayette, IN, May 1975. Also available as LARS TR 050975.
- Kimes, D.S. and J.A. Kirchner, "Radiative Transfer Model for Heterogeneous 3-D Scenes," *Applied Optics*, vol. 21, no. 22, pp. 4119-4129, 15 November 1982.

- Kneizys, F.X., et al., "Atmospheric Transmittance/Radiance: Computer Code LOWTRAN 6," AFGL-TR-83-0187, ERP No. 846, Air Force Geophysics Laboratory, Hanscom Air Force Base, MA, August 1983.
- Kneizys, F.X., E.P. Shettle, L.W. Abreu, J.H. Chetwynd, G.P. Anderson, W.O. Gallery, J.E.A. Selby, and S.A. Clough, "Users' Guide to LOWTRAN 7," AFGL-TR-88-0177, ERP No. 1010, Air Force Geophysics Laboratory, Hanscom Air Force Base, MA, August 1988.
- Koziol, J.A., "On Assessing Multivariate Normality," *Journal of Royal Statistical Society B*, vol. 45, no. 3, pp. 358-361, 1983.
- Landgrebe, D.A., "Systems Approach to the Use of Remote Sensing," LARS Information Note 041571, Laboratory for Applications of Remote Sensing, Purdue University, West Lafayette, IN 47907, April 1971.
- Landgrebe, D.A., L.L. Biehl, and W.R. Simmons, "An Empirical Study of Scanner System Parameters," *IEEE Transactions on Geoscience and Remote Sensing*, vol. GE-15, no. 3, pp. 120-130, July 1977.
- Landgrebe, D.A., and E.R. Malaret, "Noise in Remote Sensing Systems: The Effect on Classification Error," *IEEE Transactions on Geoscience and Remote Sensing*, vol. GE-24, no. 2, March, 1986.
- LARS Staff, "Testing the Gaussian Assumption on Aircraft Data," LARS Information Note 040469, Laboratory for Applications of Remote Sensing, Purdue University, West Lafayette, IN 47907, April 1969.
- Lewis, R.D. and C.H. Horgen, "Optical Sensor System Simulation," *Optical Engineering*, vol. 18, no. 3, May-June 1979.
- MacDonald, R.B., M.E. Bauer, R.D. Allen, J.W. Clifton, J.D. Ericson, and D.A. Landgrebe, "Results of the 1971 Corn Blight Watch Experiment," in *Proceedings of the Eighth International Symposium on Remote Sensing of Environment*, Ann Arbor, MI, pp. 157-190, 1972.
- MacDonald, R.B., and F.G. Hall, "LACIE: An Experiment in Global Crop Forecasting, in *Proceedings of LACIE Symposium*, JSC-14551, NASA, Johnson Space Center, Houston, TX, October 13-26, 1978.
- Malaret, E.R., "The Relationship of Sensor Parameters to Applications Data Analysis," Master's Thesis, Purdue University, August 1982.
- Malila, W.A., J.M. Gleason, and R.C. Cicone, "Multispectral System Analysis Through Modeling and Simulation," *Proceeding of 11th International Symposium on Remote Sensing*, Ann Arbor, MI, pp. 1319-1328, 1977.
- Mandelbrot, B.B. *Fractals: Form, Chance, and Dimension*, W.H. Freeman and Company, 1977.
- Markham, B. L. and J. R. G. Townshend, "Land Cover Classification as a Function of Sensor Spatial Resolution," *Proceedings of the 15th Annual International Symposium on Remote Sensing*, vol. 15, Ann Arbor, MI, 1981.
- Markham, B.L., and J.L. Barker, "Spectral Characterization of the Landsat-4 MSS Sensors," *Photogrammetric Engineering and Remote Sensing*, vol. 49, no. 6, pp 811-833, June 1983.

- Markham, B.L., and J.L. Barker, "Spectral Characterization of the Landsat Thematic Mapper Sensors," *International Journal of Remote Sensing*, vol. 6, no. 56, pp 697-716, 1985.
- Markham, B.L., "The Landsat Sensors' Spatial Responses," *IEEE Transactions on Geoscience and Remote Sensing*, vol. GE-23, No. 6, pp. 864-875, November 1985.
- Maxwell, E.L., "Multivariate System Analysis of Multispectral Imagery," *Photogrammetric Engineering and Remote Sensing*, vol. 42, no. 9, pp. 1173-1186, September 1976.
- McClatchey, R.A., R.W. Fenn, J.E.A. Selby, J.S. Garing, F.E. Volz, "Optical Properties of the Atmosphere," AFCRL-70-0527, Air Force Cambridge Research Laboratories, Bedford MA, 1970.
- Merembeck, B.F. and B.J. Turner, "Directed Canonical Analysis and the Performance of Classifiers Under its Associated Linear Transformation," *IEEE Transactions on Geoscience and Remote Sensing*, vol. GE-18, pp. 190-196, 1980.
- Mobasser, B.G., C.D. McGillem, and P.E. Anuta, "Parametric Multiclass Bayes Error Estimator for Multispectral Scanner Spatial Model Performance Evaluation," LARS Technical Report 061578, Purdue University, West Lafayette, IN 47906, June 1978.
- Muasher, M.J., and P.H. Swain, "A Multispectral Data Simulation Technique," LARS TR 070980, Purdue University, West Lafayette, IN 47907, 1980.
- Muasher, M.J. and D.A. Landgrebe, "A Binary Tree Feature Selection Technique for Limited Training Sample Size," *Remote Sensing of Environment*, vol. 16, pp. 183-194, 1984.
- Muasher, M.J. and D.A. Landgrebe, "The K-L Expansion as an Effective Feature Ordering Technique for Limited Training Sample Size," *IEEE Transactions on Geoscience and Remote Sensing*, vol. GE-21, no. 4, pp. 438-441, October 1983.
- Murphy, J.M., T. Butlin, P.F. Duff, and A.J. Fitzgerald, "Revised Radiometric Calibration Technique for Landsat-4 Thematic Mapper Data," *IEEE Transactions on Geoscience and Remote Sensing*, vol. GE-22, no. 3, pp. 243-250, May 1984.
- Nagata, Motoyasu, "Image Processing for Boundary Extraction of Remotely Sensed Data," *Pattern Recognition*, vol. 14, pp. 275-282, 1981.
- Papoulis, A. **Probability, Random Variables, and Stochastic Processes**, 2nd Edition, McGraw-Hill Book Company, 1984.
- Park, J.K. and D.W. Deering, "Simple Radiative Transfer Model for Relationships Between Canopy Biomass and Reflectance," *Applied Optics*, Vol 21, No. 2, pp 303-309, 15 January 1982.
- Park, S.K. and R.A. Schowengerdt, "Image Sampling, Reconstruction, and the Effect of Sample-Scene Phasing," *Applied Optics*, vol. 21, no. 17, pp. 3142-3151, 1 September 1982.
- Park, S.K., R. Schowengerdt, and M.-A. Kaczynski, "Modulation-Transfer-Function Analysis for Sampled Image Systems," *Applied Optics*, vol. 23 no. 15, pp. 2572-2582, 1 August 1984.
- Pau, L.-F., and M.Y. El Nahas, **An Introduction to Infrared Image Acquisition and Classification Systems**, John Wiley & Sons, Inc., New York, NY, 1983.
- Peitgen, H-O and D. Saupe, **The Science of Fractal Images**, Springer-Verlag, 1988.

- Peters, P.J., "An Extension of Image Quality: Computer Modeling a Complete Electro-Optical system," *Optical Engineering*, vol. 21, no. 1, pp. 38-42, January/February 1982.
- Pinson, L.J., *Electro-Optics*, John Wiley & Sons, New York, NY, 1985.
- Pont, W.F. Jr., "Spatial and Spectral Simulation of Landsat Images of Agricultural Areas," in *Proceedings of 1982 Machine Processing of Remotely Sensed Data Symposium*, pp. 149-153, July 1982.
- Price, J.C., "Calibration of Satellite Radiometers and the Comparison of Vegetation Indices," *Remote Sensing of Environment*, vol. 21, pp. 15-27, 1987.
- Ready, P.J., P.A. Wintz, S.J. Whitsitt, and D.A. Landgrebe, "Effects of Compression and Random Noise on Multispectral Data," in *Proc. of Seventh Int. Symp. on Remote Sensing of the Environment*, Ann Arbor, Michigan, 1971.
- Ready, P.J. and P.A. Wintz, "Information Extraction, SNR Improvement, and Data Compression in Multispectral Imagery," *IEEE Transactions on Communications*, vol. COM-21, no. 10, pp. 1123-1131, October 1974.
- Richards, J.A., *Remote Sensing Digital Image Analysis: An Introduction*, Springer-Verlag, 1986.
- Richardson, A.J., D.E. Escobar, H.W. Gausman, J.H. Everitt, "Comparison of Landsat-2 and Field Spectrometer Reflectance Signatures of South Texas Rangeland Plant Communities," *Proceedings of 1980 Machine Processing of Remotely Sensed Data Symposium*, pp. 88-97, 1982.
- Rosenfeld, A. and L.S. Davis, "Image Segmentation and Image Models," *Proceedings of the IEEE*, vol. 67, no. 5, pp. 764-772, May 1979.
- Salomonson, V.V., P.L. Smith, Jr., A.B. Park, W.C. Webb, and T.J. Lynch, "An Overview of Progress in the Design and Implementation of Landsat-D Systems," *IEEE Transactions on Geoscience and Remote Sensing*, Vol. GE-18, No. 2, April 1980.
- Schowengerdt, R., S.K. Park, and R. Gray, "Topics in the Two-Dimensional Sampling and Reconstruction of Images," *International Journal of Remote Sensing*, vol. 5, no. 2, pp. 333-347, 1984.
- Shibayma, M. and C.L. Wiegand, "View Azimuth and Zenith, and Solar Angle Effects on Wheat Canopy Reflectance," *Remote Sensing of Environment*, vol. 18, no. 1, pp. 91-103, 1985.
- Smith, J.A. and R.E. Oliver, "Effects of Changing Canopy Directional Reflectance on Feature Selection," *Applied Optics*, vol. 13, no. 7, pp. 1599-1604, July 1974.
- Smith, S.P. and A.K. Jain, "A Test to Determine the Multivariate Normality of a Data Set," *IEEE Transactions on Pattern Analysis and Machine Intelligence*, vol. 10, no. 5, pp. 757-761, September 1988.
- Strahler, A.H., C.E. Woodcock, and J.A. Smith, "On the Nature of Models in Remote Sensing," *Remote Sensing of Environment*, vol. 20, no. 2, pp. 121-139, October 1986.
- Suits, G.H., "The Calculation of the Directional Reflectance of a Vegetation Canopy," *Remote Sensing of Environment*, vol. 2, pp. 117-125, 1972a.

- Suits, G.H., "The Cause of Azimuthal Variations in Directional Reflectance of Vegetative Canopies," *Remote Sensing of Environment*, vol. 2 p. 175, 1972b.
- Suits, G.H., "The Extension of a Uniform Canopy Reflectance Model to Include Row Effects," SR-E1-04065 NASA. Scientific and Technical Information Facility, P.O. Box 33, College Park, MD, 20740, 1982.
- Summers, R.A., "Systems Analysis Techniques in Earth Resources Satellite Systems Planning," *Proceedings of the 7th Symposium on Remote Sensing of the Environment*, pp. 237-246, 1971.
- Swain, P.H. and S.M. Davis, Eds., **Remote Sensing: The Quantitative Approach**, McGraw-Hill, 1978.
- Swain, P.H., V.C. Vanderbilt, and C.D. Jobusch, "A Quantitative Applications-Oriented Evaluation of Thematic Mapper Design Specifications," *IEEE Transactions on Geoscience and Remote Sensing*, vol. GE-20, no. 3, pp. 370-377, July 1982.
- Thekaekara, M.P., "Extraterrestrial Solar Spectrum 3000-6100 Å at 1 Å Intervals," *Applied Optics*, vol. 13, no. 3, pp. 518-522, March 1974.
- Toll, D.L., "Effect of Landsat Thematic Mapper Sensor Parameters on Land Cover Classification," *Remote Sensing of Environment*, vol. 17, pp. 129-140, 1985.
- Turner, R.E., "A Stochastic Atmospheric Model for Remote Sensing Applications," NASA-CR-172181, pp. 1-33, August 1983.
- Vane, G., "Airborne Visible/Infrared Imaging Spectrometer (AVIRIS)," JPL Publication 87-38, Jet Propulsion Laboratory, California Institute of Technology, Pasadena, California, November 1987.
- Verhoef, W., "Light Scattering by Leaf Layers with Application to Canopy Reflectance Modeling: the SAIL Model," *Remote Sensing of Environment*, vol. 16, pp. 125-141, 1984.
- Whitsitt, S.J., and D.A. Landgrebe, "Error Estimation and Separability Measures in Feature Selection for Multiclass Pattern Recognition," LARS Publication 082377, Laboratory for Applications of Remote Sensing, Purdue University, West Lafayette, IN, August 1977.
- Wiersma, D.J. and D.A. Landgrebe, "Analytical Design of Multispectral Sensors," *IEEE Transactions of Geoscience and Remote Sensing*, vol. 18, no. 2, pp. 180-189, 1980.
- Wiswell, E.R., "Analytic Techniques for the Study of Some Parameters of Multispectral Scanner Systems for Remote Sensing," Ph. D. Thesis, School of Electrical Engineering, Purdue University, West Lafayette, IN, 1978. Also available as LARS TR 061778.
- Wolfe, W.L., and G.J. Zissis, Editors, **The Infrared Handbook**, Office of Naval Research, Dept. of the Navy, Washington, DC. 1978.
- Wyatt, C.L., **Radiometric System Design**, Macmillan Publishing Company, New York, NY, 1987.

Appendix A Expected Variance of a Two Dimensional Autoregressive Process

This appendix provides a straightforward method of computing the expected variance of a two dimensional autoregressive (AR) process. While the method is similar to discussions presented in Friedlander (1984) and Kay (1985), it is developed here in the context of image modeling and presented in an intuitively simple manner.

The zero mean Mth order AR process $y(k)$ is defined as in equation A.1.

$$y(k) = \sum_{m=1}^M \theta_m y(k-m) + u(k) \quad k=1, \dots, N \quad (\text{A.1})$$

where

- $y(k)$ - process data value at point k in sequence
- θ_m - model coefficient at lag m
- $u(k)$ - Gaussian white noise sequence with zero mean and variance σ_u^2

The process will be stationary if the zeros of $F(z)$ lie outside of the unit circle in the complex plane, where $F(z)$ is defined as in equation A.2.

$$F(z) = 1 - \theta_1 z - \theta_2 z^2 - \dots - \theta_M z^M \quad (\text{A.2})$$

Autoregressive models have been applied to image modelling and compression (Delp, Kashyap, and Mitchell 1979) through the use of a line scanning formulation. The two-dimensional image is row concatenated to form a one dimensional sequence. Figure A.1 shows the arrangement for a quarter plane AR model applied to a P row x P column image.

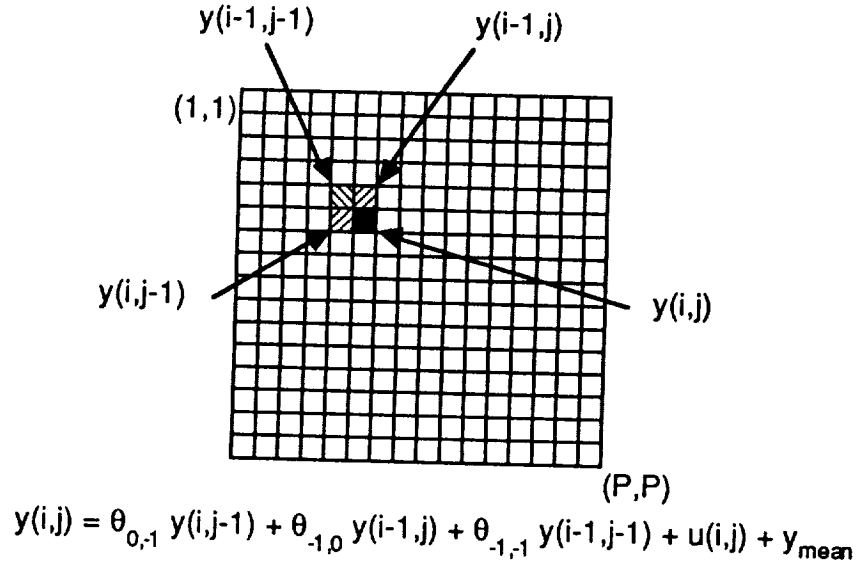


Figure A.1 Quarter-Plane Image AR Model.

This model may be reformulated as a one dimensional sequence by letting the index $k = (i-1)P + j$. This is shown in equation A.3.

$$y(k) = \theta_1 y(k-1) + \theta_P y(k-P) + \theta_{P+1} y(k-P-1) + u(k) + y_{\text{mean}} \quad \text{for } k=P+1, \dots, P^2 \quad (\text{A.3})$$

The AR model is now of order $M = P + 1$, but with only coefficients θ_1 , θ_P , and θ_{P+1} being nonzero. Also, the initial conditions of the model become the first row and the first pixel of the second row. Usually these are set to the mean of the image as in equation A.4.

$$y(k) = y_{\text{mean}} \quad \text{for } k = 1, 2, \dots, P+1. \quad (\text{A.4})$$

The Yule-Walker (YW) equations are obtained by multiplying equation A.1 by $y(k-l)$ and taking the expectation. This results in equation A.5.

$$E\{y(k) y(k-l)\} = E\left\{ \sum_{m=1}^M \theta_m y(k-m) y(k-l) + u(k) y(k-l) \right\} \quad (\text{A.5})$$

For $l > 0$, this results in equation A.6,

$$\sigma_y^2(l) = \sum_{m=1}^M \theta_m \sigma_y^2(m-l) \quad (\text{A.6})$$

where $\sigma_y^2(l)$ is the covariance between data points l lags apart. This result comes about due to the stationarity of the process and the fact that $u(k)$ is an uncorrelated sequence.

Writing equation A.5 for $l=1$ to M and normalizing by the variance $\sigma_y^2 = \sigma_y^2(0)$, we obtain the YW relations as equation A.7.

$$\begin{aligned} \rho_1 &= \theta_1 + \theta_2 \rho_1 + \dots + \theta_M \rho_{M-1} \\ \rho_2 &= \theta_1 \rho_1 + \theta_2 + \theta_3 \rho_1 + \dots + \theta_M \rho_{M-2} \\ &\vdots \\ \rho_M &= \theta_1 \rho_{M-1} + \theta_2 \rho_{M-2} + \dots + \theta_M \end{aligned} \quad (\text{A.7})$$

Observe that in the above we have used the fact that $\rho_0 = 1$, and that $\rho_{-1} = \rho_1$. Also, note that

$$\rho_m = \frac{\sigma_y^2(m)}{\sigma_y^2}$$

Equation A.7 can be reformulated as in equation A.8.

$$\left[I_{M \times M} - \Theta_A - \Theta_B \right] \begin{bmatrix} \rho_1 \\ \rho_2 \\ \vdots \\ \rho_M \end{bmatrix} = \begin{bmatrix} \theta_1 \\ \theta_2 \\ \vdots \\ \theta_M \end{bmatrix} \quad (\text{A.8})$$

Where $I_{M \times M}$ is an $M \times M$ identity matrix, and Θ_A and Θ_B are defined as follows,

$$\Theta_A = \begin{bmatrix} \theta_2 & \theta_3 & \dots & \theta_M & 0 \\ \theta_3 & \theta_4 & \dots & \theta_M & 0 & 0 \\ \dots & \dots & \dots & \dots & \dots & \dots \\ \dots & \theta_M & 0 & \dots & \dots & 0 \\ \theta_M & 0 & \dots & \dots & \dots & 0 \\ 0 & 0 & \dots & \dots & \dots & 0 \end{bmatrix} \quad \Theta_B = \begin{bmatrix} 0 & 0 & \dots & \dots & 0 \\ \theta_1 & 0 & 0 & \dots & 0 \\ \theta_2 & \theta_1 & 0 & \dots & 0 \\ \dots & \dots & \dots & \dots & \dots \\ \theta_{M-1} & \dots & \theta_2 & \theta_1 & 0 \end{bmatrix}$$

The elements of Θ_A and Θ_B can be filled by the following pseudo-code.

For Θ_A ,

```

for i = 1 to M {
  for j = 1 to M {
    if (i+j ≤ M) then  $\Theta_A(i,j) = \theta_{i+j}$ 
    else  $\Theta_A(i,j) = 0$ 
  }
}

```

For Θ_B ,

```

for i = 1 to M {
  for j = 1 to M {
    if (i-j ≥ 1) then  $\Theta_B(i,j) = \theta_{i-j}$ 
    else  $\Theta_B(i,j) = 0$ 
  }
}

```

Equation A.8 is in the form of a system of linear equations, and the autocorrelation coefficients $\rho_1, \rho_2, \dots, \rho_M$, can then be obtained by using any standard linear algebra routine.

Using the relationship between the coefficients, the autocorrelations, and the process variance from Box and Jenkins (1970), we can solve for the variance of the process as in equation A.9.

$$\sigma_y^2 = \frac{\sigma_u^2}{1 - \sum_{m=1}^M \theta_m \rho_m} \quad (\text{A.9})$$

Appendix B Interpolation Algorithm

The following routine was used to convert the 60 dimensional FSS reflectance into the 201 dimensional vectors used in the system models. The FSS data covered 0.4 to 2.40 μm , in spectral samples ranging from 20 nm to 50 nm. The system model uses a constant 10 nm wavelength spacing across this range.

The conversion is accomplished by first placing samples that correspond directly in wavelength, then performing several levels of interpolation to match the wavelength spacing as closely as possible.

The two arrays are defined as `fssref(1:60)`, the FSS reflectance, and `hiref(1:201)`, the resulting interpolated array.

```

c
c      Do direct placements first
c
      hiref(1)=fssref(1)
      do 10 i=2,8
10         hiref(2*i)=fssref(i)
      do 20 i=9,11
20         hiref(2*i+1)=fssref(i)
      do 30 i=12,13
30         hiref(2*i+2)=fssref(i)
      do 40 i=14,18
40         hiref(2*i+3)=fssref(i)
      do 50 i=19,28
50         hiref(2*i+2)=fssref(i)
      hiref(59)=fssref(29)
      do 60 i=30,34
60         hiref(2*i+3)=fssref(i)
      hiref(75)=fssref(35)
      hiref(80)=fssref(36)
      do 62 i=37,60
62         hiref(5*(i-37)+84)=fssref(i)
c
c      Next interpolate simply
c
      do 70 i=1,7
70         hiref(2*i+1)=0.5*(fssref(i)+fssref(i+1))
      do 80 i=8,11
80         hiref(2*i+2)=0.5*(fssref(i)+fssref(i+1))
      hiref(27)=0.5*(fssref(12)+fssref(13))
      do 90 i=13,17
90         hiref(2*i+4)=0.5*(fssref(i)+fssref(i+1))
      do 100 i=19,27

```

```

100     hiref(2*i+3)=0.5*(fssref(i)+fssref(i+1))
        hiref(61)=0.5*(fssref(29)+fssref(30))
        do 110 i=30,33
110     hiref(2*i+4)=0.5*(fssref(i)+fssref(i+1))
        hiref(73)=0.5*(fssref(34)+fssref(35))
        hiref(77)=0.5*(fssref(35)+fssref(36))
        hiref(82)=0.5*(fssref(36)+fssref(37))
        hiref(87)=0.5*(fssref(37)+fssref(38))
        do 115 i=38,59
115     hiref(5*(i-38)+91)=0.5*(fssref(i)+fssref(i+1))
c
c     Now interpolate interpolations
c
        hiref(2)=0.5*(hiref(1)+hiref(3))
        hiref(17)=0.5*(hiref(16)+hiref(18))
        hiref(25)=0.5*(hiref(24)+hiref(26))
        hiref(29)=0.5*(hiref(28)+hiref(30))
        hiref(60)=0.5*(hiref(59)+hiref(61))
        hiref(62)=0.5*(hiref(61)+hiref(63))
        do 120 i=72,78,2
120     hiref(i)=0.5*(hiref(i-1)+hiref(i+1))
        hiref(81)=0.5*(hiref(80)+hiref(82))
        hiref(83)=0.5*(hiref(82)+hiref(84))
        do 125 i=86,92,2
125     hiref(i)=0.5*(hiref(i-1)+hiref(i+1))
        do 130 i=110,195,5
130     hiref(i)=0.5*(hiref(i-1)+hiref(i+1))
c
c     Now interpolate interpolations of the interpolations
c
        hiref(79)=0.5*(hiref(78)+hiref(80))
        hiref(85)=0.5*(hiref(84)+hiref(86))
        hiref(93)=0.5*(hiref(92)+hiref(94))
        do 135 i=112,197,5
135     hiref(i)=0.5*(hiref(i-1)+hiref(i+2))
        do 140 i=113,198,5
140     hiref(i)=0.5*(hiref(i-1)+hiref(i+1))
c
c     Set water absorption bands to 0.001
c
        do 143 i=96,106
143     hiref(i)=0.001
        do 147 i=146,156
147     hiref(i)=0.001
c
c     Set up repeated values
c
        hiref(95)=hiref(94)
        hiref(107)=hiref(109)
        hiref(108)=hiref(109)
        hiref(145)=hiref(144)
        hiref(157)=hiref(159)
        hiref(158)=hiref(159)
        hiref(200)=hiref(199)
        hiref(201)=hiref(199)

```

Appendix C LOWTRAN 7 Input File

The atmospheric simulation program LOWTRAN 7 is implemented in the simulation by setting up an input file, calling the program through a UNIX system command, then reading the resultant output file created.

The following variables and default values were used in the implementation of LOWTRAN 7. See Kneizys, et al., (1988) for a complete description.

ANGLE - Angle parameter

DV - Incremental wavenumber

GNDALT - Altitude of surface

H1 - Initial altitude

H2 - Final altitude

ICLD - Cirrus cloud parameter

ICSTL - Ocean parameter

IEMSCT - Execution mode parameter

= 0 program calculates transmittance

= 1 program calculates atmospheric radiance

= 2 program calculates atmospheric and singly scattered solar/lunar radiance

= 3 program calculates directly transmitted solar irradiance

IHAZE - Atmospheric haze parameter

= 0 for a clear atmosphere

= 1 for a rural atmosphere

= 5 for an urban atmosphere

IM - Radiosonde parameter

IMULT - Multiple scattering control parameter

= 0 program executed without multiple scattering

= 1 program executed with multiple scattering

IPARM - Geometry specification controlling parameter

IPH - Aerosol phase function parameter

IRPT - repetition parameter

= 0 no more input cards follow

= 1 more input cards follow

ISEASN - season parameter (0=default)

ISOURC - Extraterrestrial source parameter

- = 0 source is sun
- = 1 source is moon

ITYPE - Atmospheric path parameter

- = 1 for a horizontal path
- = 2 for a vertical or slant path between two altitudes
- = 3 for a vertical or slant path to space

IVSA - Vertical structure algorithm parameter

IVULCN - Volcanic activity parameter

M1 through M6 - Altitude profile parameters

MODEL - Atmospheric model type parameter

- = 1 selects Tropical Model Atmosphere
- = 2 selects Midlatitude Summer
- = 3 selects Midlatitude Winter
- = 4 selects Subarctic Summer
- = 5 selects Subarctic Winter
- = 6 selects 1976 U. S. Standard

NOPRT - Normal operation parameter

PARM1 - Azimuthal angle between observer and sun

PARM2 - Solar zenith angle ($=\theta_{\text{solar}}$)

RAINRT - Rain rate parameter

SALB - Surface albedo

V1 - Initial wavenumber

V2 - Final wavenumber

VIS - Surface meteorological range ($=V_{\eta}$)

The following default values were used for the experiments and simulations used in this report.

GNDALT=0	<i>/* Surface at sea level */</i>
ICLD=0	<i>/* No clouds */</i>
ICSTL=1	<i>/* No effect, only used over oceans */</i>
IDAY=180	<i>/* Day of year */</i>
IHAZE=1	<i>/* Rural atmosphere */</i>
IM=0	<i>/* No radiosonde data */</i>

```

IMULT = 1           /* Multiple scattering */
ISEASN=0           /* Season determined by MODEL */
ISOURC             /* Source is Sun */
IVSA=0            /* Vert. Structure Algorithm not used */
IVULCN=0          /* No volcanic profile */
M1=0              /* Normal operation */
M2=0              /* Normal operation */
M3=0              /* Normal operation */
MODEL=6           /* 1976 U. S. Standard atmosphere */
NOPRT=1           /* Normal operation */
RAINRT=0.0        /* No rain */
VIS=Vη

```

Four calls to LOWTRAN are set up within the input file. The first call calculates the direct solar spectral irradiance at the surface. The second calculates the transmittance of the path from the surface to the sensor. The third and fourth calls calculate the path radiance seen by the sensor for surface albedoes of 0 and 1. LOWTRAN reads from an input file named TAPE5. The lines below labelled CARD contain the actual variables in the file TAPE5.

The following lines set up the direct solar irradiance call.

```

ITYPE=3
IEMSCT=3
H1=0.0
ANGLE=θsolar
IRPT=1

```

```

CARD 1    MODEL,ITYPE,IEMSCT,IMULT,M1,M2,M3,M4,M5,M6,MDEF,IM,
          NOPRT,SALB
CARD 2    IHAZE,ISEASN,IVULCN,ICSTL,ICLD,IVSA,VIS,RAINRT,GNDALT
CARD 3    H1, ANGLE, ISOURC
CARD 4    V1,V2,DV
CARD 5    IRPT

```

The following lines set up the transmittance call.

```

ITYPE=2
IEMSCT=0
H1=0.0
H2=H /* Altitude of sensor */
ANGLE= $\theta_{\text{view}}$ 
IRPT=1

```

```

CARD 6    MODEL,ITYPE,IEMSCT,IMULT,M1,M2,M3,M4,M5,M6,MDEF,IM,
          NOPRT,SALB
CARD 7    IHAZE,ISEASN,IVULCN,ICSTL,ICLD,IVSA,VIS,RAINRT,GNDALT
CARD 8    H1,H2,ANGLE
CARD 9    V1,V2,DV
CARD 10   IRPT

```

The following lines set up one path radiance call.

```

ITYPE=2
IEMSCT=2
H1=H
ANGLE= $180.0 - \theta_{\text{view}}$ 
IPARM=2
IPH=2
PARM1= $(\phi_{\text{view}} - \phi_{\text{solar}})/2$ 
PARM2= $\theta_{\text{solar}}$ 
SALB=0.0 /* or = 1.0 */

```

```

CARD 11   MODEL,ITYPE,IEMSCT,IMULT,M1,M2,M3,M4,M5,M6,MDEF,IM,
          NOPRT,SALB
CARD 12   IHAZE,ISEASN,IVULCN,ICSTL,ICLD,IVSA,VIS,RAINRT,GNDALT
CARD 13   H1,ANGLE,LEN
CARD 14   IPARM,IPH,IDAY,ISOURC
CARD 15   PARM1,PARM2
CARD 16   V1,V2,DV

```

CARD 17 IRPT

The program generates a file named TAPE7 with the output data. Since LOWTRAN uses wavenumber increments across the spectrum, a conversion is done to put the result into wavelength units. Since the resolution of the call to LOWTRAN results in one or more wavenumber samples per wavelength interval, this conversion is accomplished by averaging over the appropriate wavenumbers to obtain the resulting wavelength value.

Appendix D Sensor Descriptions

In the following descriptions the radiance levels are given in mW/(cm²-sr). The shot noise constants are computed from data and can be used to compute the standard deviation as in equation D.1.

$$\sigma_{\text{shot}} = K_{\text{shot}} \sqrt{\text{Signal Level}} \quad (\text{D.1})$$

D.1. Modular Multispectral Scanner

This is an airborne sensor flown for LARS in the early 1970s. The spectral response and noise levels were estimated from data given in the report by NASA's Johnson Space Center (1974). Details are given in Tables D.1 and D.2, and Figures D.1, and D.2. The noise values are estimated assuming equivalent shot and thermal noise for one-half full scale radiance signals.

Table D.1 MMS General Parameters.

Altitude	3030 Meters
Sampling Interval	2.3 millirads
Number of Bands	10
Number of Bits	8

Table D.2 MMS Band and Noise Parameters.

Band	Full Scale Radiance	Shot Noise Constant	Thermal Noise Equivalent Radiance
1	0.338	0.0151	0.00450
2	0.640	0.0042	0.00160
3	1.114	0.0039	0.00160
4	1.253	0.0037	0.00150
5	1.314	0.0035	0.00150
6	1.333	0.0028	0.00150
7	1.170	0.0024	0.00140
8	1.020	0.0018	0.00140
9	0.983	0.0034	0.00300
10	0.259	0.0061	0.00250

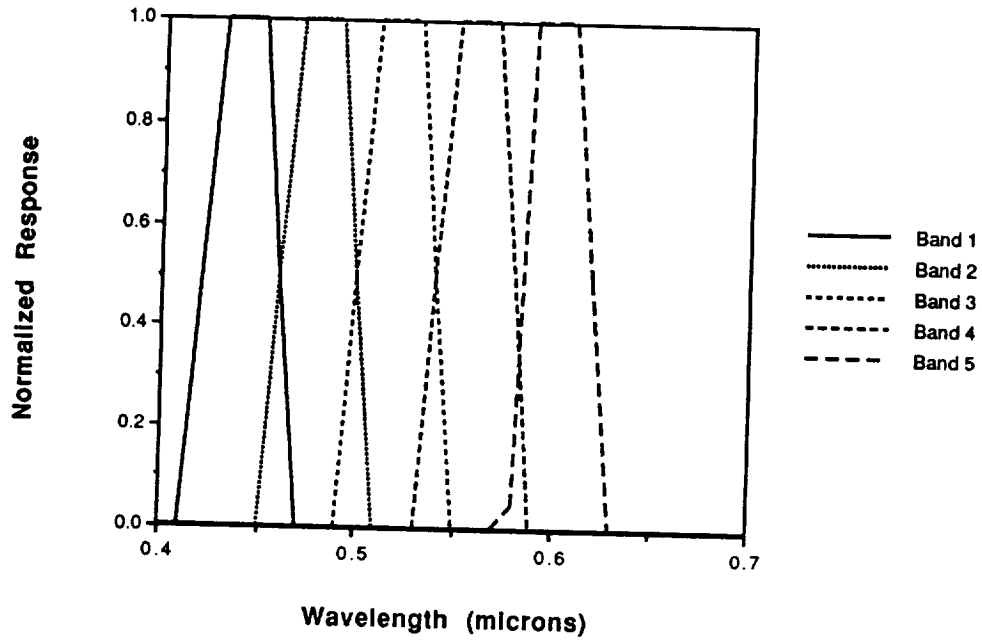


Figure D.1 MMS Spectral Response for Bands 1 though 5.

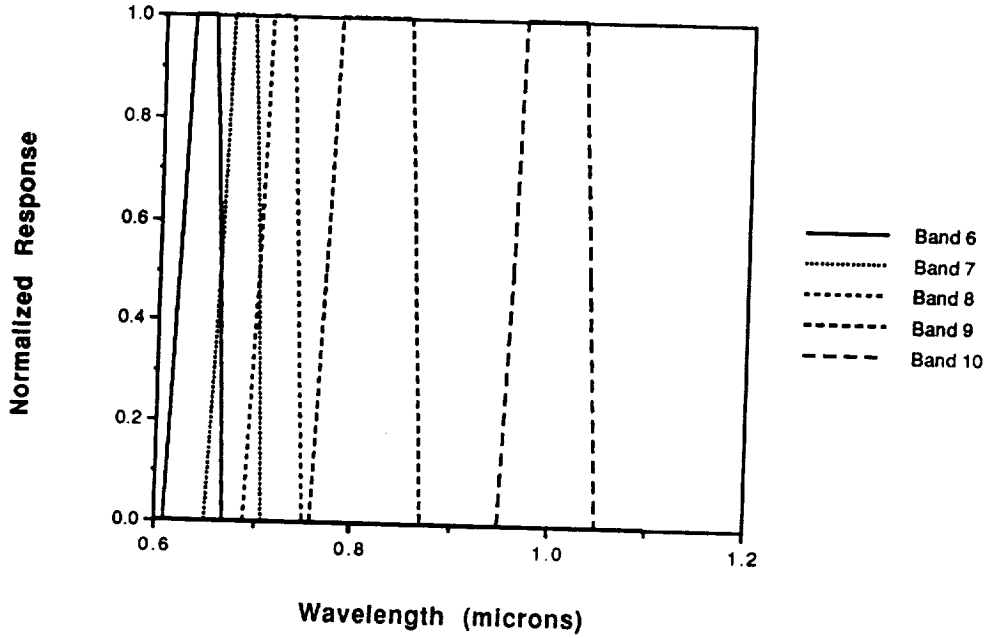


Figure D.2 MMS Spectral Response Bands 6 through 10.

The spatial response of the MSS is assumed to be Gaussian with a standard deviation of 1.25 milliradians.

D.2. Landsat MSS

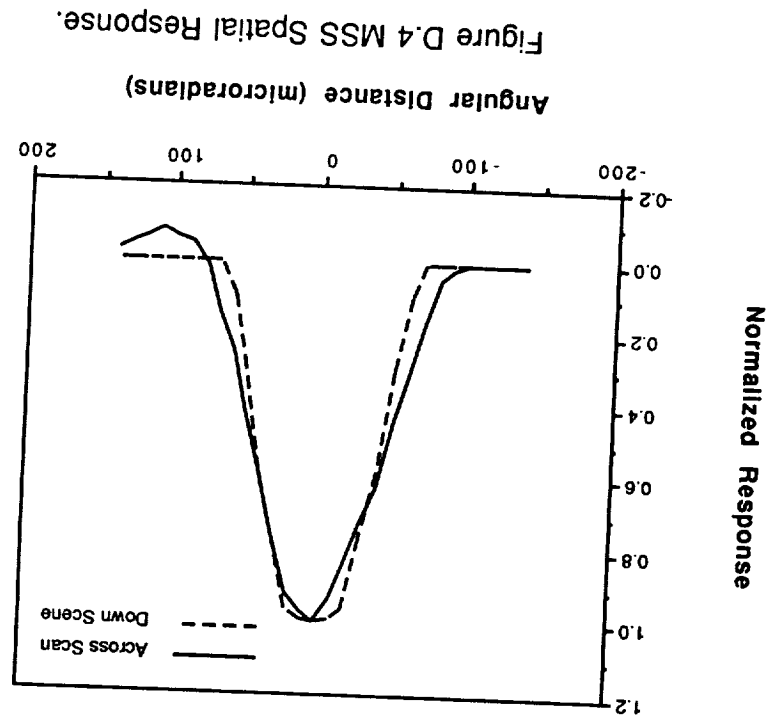
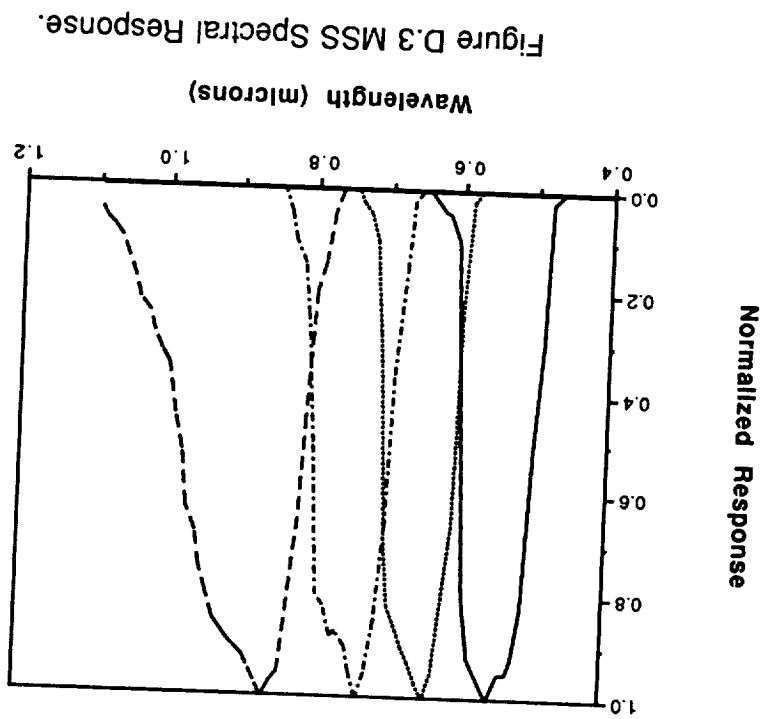
The following data are for the Landsat MSS instrument. The spectral response was taken from Markham and Barker (1983), the spatial response from Markham (1985), and the noise levels set similar to those of the Thematic Mapper instrument. The rest of the information is from Salomonson, et al. (1980).

Table D.3 MSS General Parameters.

Altitude	918 Kilometers
Sampling Interval	63 μ radians across scan 88 μ radians down scene
Number of Bands	4
Number of Bits	7 (6 for band 4)

Table D.4 MSS Band and Noise Parameters.

Band	Full Scale Radiance	Shot Noise Constant	Thermal Noise Equivalent Radiance
1	2.48	0.008	0.006
2	2.00	0.007	0.005
3	1.76	0.005	0.005
4	4.60	0.005	0.010



D.3. Landsat Thematic Mapper

The data presented here are for the first six bands of the Landsat TM instrument. The spectral response was taken from Markham and Barker (1985), the spatial response from Markham (1985), and the noise levels from Malaret (1982). The rest of the information is from Salomonson, et al., (1980).

Table D.5 TM General Parameters.

Altitude	705 Kilometers
Sampling Interval	43 μ radians across scan 43 μ radians down scene
Number of Bands	6
Number of Bits	8

Table D.6 TM Band and Noise Parameters.

Band	Full Scale Radiance	Shot Noise Constant	Thermal Noise Equivalent Radiance
1	1.06	0.0073	0.00752
2	2.54	0.0079	0.00529
3	1.46	0.0066	0.00448
4	3.26	0.0049	0.00360
5	0.64	0.0055	0.00333
6	0.48	0.0127	0.00600

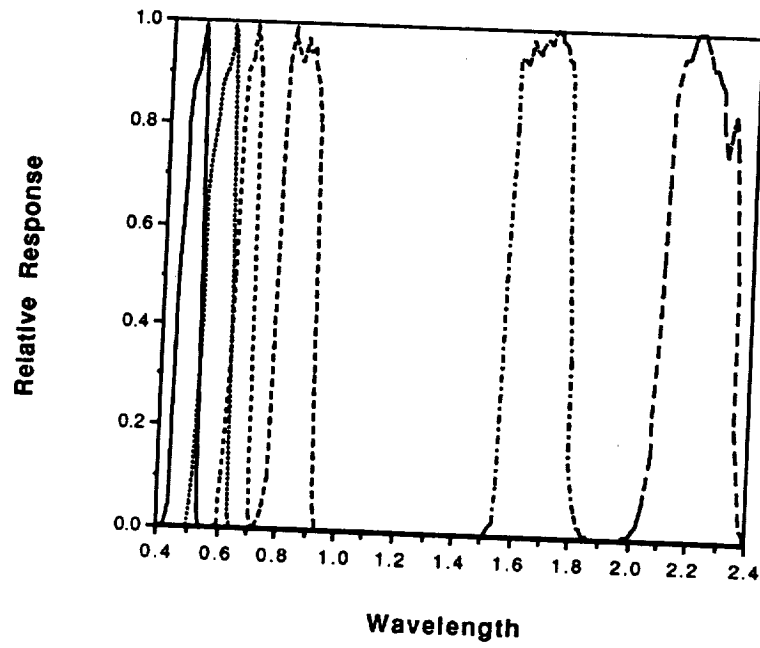


Figure D.5 TM Spectral Response.

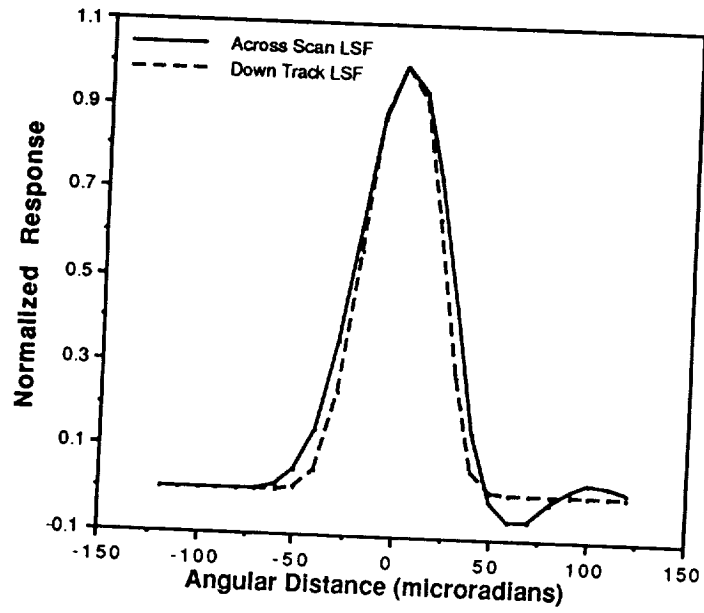


Figure D.6 TM Spatial Response.

Appendix E Analytical System Model Program Listing

C
C R S A N A John Kerekes May 29, 1989

C
C This program will compute the performance of a remote sensing
C system based on scene reflectance and system parameters.
C It is based on analytic models developed by Whitsitt (1977),
C Mobasser (1978), and Malaret (1982). It uses reflectance
C statistics obtained by the FSS and interpolated to 201 dimensions
C to work with the model HIRIS sensor. Feature selection based on
C combining bands is used to reduce the dimensionality. Tables
C generated by LOWTRAN 7 provide the atmospheric data under 125
C combinations of surface meteorological range, solar zenith angle,
C and view zenith angle. Classification accuracy is assessed through
C a function of the Bhattacharyya distance between classes.

C
C The program uses several data files as described below.

C
C "refstat" - Mean and covariance of reflectance for each class
C "scdesc" - Parameter file describing scene
C "irrad" - Table of total surface irradiance for varying
C meteorological ranges and sun angles
C "trans" - Table of atmospheric transmittance for varying
C meteorological ranges and view angles
C "prad0" - Table of path radiance for surface reflectance of 0, for
C varying meteorological ranges, solar angles, and view angles
C "prad1" - Table of path radiance for surface reflectance of 1, for
C varying meteorological ranges, solar angles, and view angles
C "senstat" - Parameter file describing sensor
C "feaset" - Table of processing features

C
C The format for these files is as follows.

C
C "refstat"
C Repeated for each class are the following
C (a10) Class Name
C (201f8.4) Mean Reflectance
C 201 rows of (201f8.4) Covariance Matrix

C
C "scdesc"
C (i3) Number of classes
C (f4.2) Across scene spatial correlation coefficient
C (f4.2) Down scene spatial correlation coefficient
C (i3) Meteorological range table index
C (i3) Solar zenith angle table index
C (i4) View zenith angle table index

C
C "irrad"
C Repeated for 5 solar angles (0°, 15°, 30°, 45°, and 60°)
C Repeated 201 times for spectral wavelengths
C 5(f7.2,a1) Spectral irradiance for 5 Met Ranges
C separated by tabs (2,4,8,16, and 32 Km)

C

```
c   "trans"
c       Repeated for 5 view angles (0°, 15°, 30°, 45°, and 60°)
c           Repeated 201 times for spectral wavelengths
c               5(f7.4,a1) Atm. Transmittance for 5 Met Ranges
c                   separated by tabs (2,4,8,16, and 32 Km)
c
c   "prad0"
c       Repeated for 5 view angles (0°, 15°, 30°, 45°, and 60°)
c           Repeated for 5 solar angles (0°, 15°, 30°, 45°, and 60°)
c               Repeated 201 times for spectral wavelengths
c                   5(f7.4,a1) Path Radiance for 5 Met Ranges
c                       separated by tabs (2,4,8,16, and 32 Km)
c
c   "prad1"
c       Repeated for 5 view angles (0°, 15°, 30°, 45°, and 60°)
c           Repeated for 5 solar angles (0°, 15°, 30°, 45°, and 60°)
c               Repeated 201 times for spectral wavelengths
c                   5(f7.4,a1) Path Radiance for 5 Met Ranges
c                       separated by tabs (2,4,8,16, and 32 Km)
c
c   "senstat"
c       (a24,a6) Label, Sensor Name
c       (a24,f4.1) Label, PSF Radius ( $r_0$ )
c       (a24,i3) Label, IMC Gain State
c       (a24,f11.1) Label, System Response Constant
c       (a24,2f8.1) Label, VNIR and SWIR Dark Current
c       (a24,f8.1) Label, Shot Noise Factor
c       (a24,2f8.1) Label, VNIR and SWIR Read Noise Std. Deviations
c       (a24,2f8.1) Label, VNIR and SWIR Quantization Noise St.Dvs.
c       (a24,f8.3) Label, Relative Calibration Error
c       (a24,f8.3) Label, Absolute Calibration Error
c       Repeated for 201 Wavelengths
c           (a24,f7.4) Label, Sensor Spectral Band Response
c
c   "feaset"
c       (a24,i4) Label, Number of Features to Use
c       Repeated for each feature
c           (a24,2i4) Label, Feature Beginning and Ending Band
c
c
c   Variables Used Include the Following:
c
c   absrad - level of absolute radiometric error (in decimal)
c   averef - average of class reflectances (in decimal)
c   avecov - covariance of average of reflectances (in decimal)
c   calstd - level of relative calibration error vector (in decimal)
c   dark - dark level current in detectors (in electrons)
c   feacov - covariance of feature set
c   feamat - feature selection matrix
c   feamean - mean of feature set
c   feaset - table of band edges for feature selection
c   gcon - conversion vector of received power to electrons
c           (electrons/watt)
c   irrads - table of total spectral irradiance at surface (mW/cm2-mm)
c           irrads(wavelength,met range, sun, angle)
```

```

c   mr - index for meteorological range
c   mu - Bhattacharyya distance
c   pcsun - overall average probability correct (in percent)
c   prad0 - table of path radiance when albedo=0 (mW/cm2-mm-sr)
c           prad0(wavelength, met range, sun angle, view angle)
c   prad1 - table of path radiance when albedo=1 (mW/cm2-mm-sr)
c           prad1(wavelength, met range, sun angle, view angle)
c   probcor - pairwise probability of correct (in decimal)
c   quantstd - variance of quantization noise (in electrons)
c   readstd - variance of read noise vector (in electrons)
c   refmean - mean reflectance array (in percent)
c   refcov - covariance of reflectance (in percent2)
c   rhox - across scene spatial correlation coefficient
c   rhoy - down scene spatial correlation coefficient
c   ro - sqrt(2) times the PSF radius in scene cells
c   senrsp - sensor response(product of optics transmittance and
c           quantum efficiency)
c   shtfac - shot noise factor
c   shotstd - standard deviation of shot noise vector(in electrons)
c   sigcov - covariance of received signal (in electrons2)
c   sigmean - mean of received signal (in electrons)
c   sigrad - signal radiance for 100% reflecting surface(in electrons)
c   sysrsp - system response constant (product of AΩ, Δλ, and 1/hc)
c   thsun - index of solar zenith angle
c   thvew - index of view zenith angle
c   trans - table of atmospheric transmittance
c           trans(wavelength, met range, view angle)
c   ws - spatial weight
c
c   IMSL version 10.0 routines used include the following:
c
c   erfc(x) - compute the error function complement of x
c   lftsf(*) - matrix factorization
c   lfdsf(*) - compute determinant given matrix factorization
c   linrg(*) - compute the inverse of a real general matrix
c
c   program rsana
c   parameter(irbrk=61,maxcls=4,maxdim=201,maxfea=16,maxopt=5)
c   character*1 tc
c   character*6 sename
c   character*10 covtype
c   character*24 label
c   integer feaset(maxfea,2)
c   integer imc,ipvt(maxfea),mr,numcls,numfea,thsun,thvew
c   real absrad,averef(maxdim)
c   real avecov(maxdim,maxdim)
c   real calval
c   real calstd(maxdim)
c   real dark(2),det1,det2,detave,det1,detk
c   real fac(maxfea,maxfea)
c   real feamat(maxfea,maxdim)
c   real feacov(maxfea,maxfea,maxcls),feamean(maxfea,maxcls)
c   real feacovk(maxfea,maxfea),feacovl(maxfea,maxfea)
c   real gcon(maxdim)

```

```

real irrad(maxdim,maxopt,maxopt),mu
real mxdiff(maxfea),matave(maxfea,maxfea),matinv(maxfea,maxfea)
real pcsum
real prad0(maxdim,maxopt,maxopt,maxopt)
real prad1(maxdim,maxopt,maxopt,maxopt)
real pthdif(maxdim)
real probcor(maxcls,maxcls)
real quantstd(2),readstd(2)
real refcov(maxdim,maxdim,maxcls),refmean(maxdim,maxcls)
real ro,roa,rob,rhox,rhoy,senrsp(maxdim)
real shtfac,shotstd(maxdim)
real sigrad(maxdim)
real sigmean(maxdim),sigcov(maxdim,maxdim)
real ws,sysrsp
real temp,tmpmean(maxdim),tmpcov(maxdim,maxdim)
real tmpvec(maxdim)
real trans(maxdim,maxopt,maxopt)
C
C
C
C
C*****
C
C   READ IN DATA PARAMETER FILES AND SET UP ARRAYS
C*****
C
C   Read in scene description and reflectance data
C
    open(unit=3,file="scdesc")
    rewind(3)
    read(3,'(i3)')numcls
    read(3,'(f4.2)')rhox
    read(3,'(f4.2)')rhoy
    read(3,'(i3)')mr
    read(3,'(i3)')thsun
    read(3,'(i3)')thvew
    close(3)
    open(unit=4,file="refstat")
    rewind(4)
    do 10 k=1,numcls
        read(4,'(a10)')covtype
        read(4,'(201f8.4)')(refmean(i,k),i=1,maxdim)
        do 20 j=1,maxdim
            read(4,'(201f8.4)')(refcov(i,j,k),i=1,maxdim)
20          continue
10        continue
    close(4)
C
C   Read in atmospheric data files
C
    open(unit=10,file="irrad")
    rewind(10)
    do 30 l=1,maxopt
    do 30 i=1,maxdim
        read(10,'(5(f7.2,a1))')irrad(i,1,l),tc,irrad(i,2,l),tc,
+          irrad(i,3,l),tc,irrad(i,4,l),tc,irrad(i,5,l)
    
```

```

30     continue
      close(10)
      open(unit=11, file="trans")
      rewind(11)
      do 40 l=1, maxopt
      do 40 i=1, maxdim
          read(11, '(5(f7.4, a1))') trans(i, 1, l), tc, trans(i, 2, l), tc,
+         trans(i, 3, l), tc, trans(i, 4, l), tc, trans(i, 5, l)
40     continue
      close(11)
      open(unit=12, file="prad0")
      rewind(12)
      do 50 l=1, maxopt
      do 50 m=1, maxopt
      do 50 i=1, maxdim
          read(12, '(5(f7.4, a1))') prad0(i, 1, m, l), tc, prad0(i, 2, m, l), tc,
+         prad0(i, 3, m, l), tc, prad0(i, 4, m, l), tc, prad0(i, 5, m, l)
50     continue
      close(12)
      open(unit=13, file="prad1")
      rewind(13)
      do 60 l=1, maxopt
      do 60 m=1, maxopt
      do 60 i=1, maxdim
          read(13, '(5(f7.4, a1))') prad1(i, 1, m, l), tc, prad1(i, 2, m, l), tc,
+         prad1(i, 3, m, l), tc, prad1(i, 4, m, l), tc, prad1(i, 5, m, l)
60     continue
      close(13)
c
c     Read in sensor parameter file
c
      open(unit=14, file="senstat")
      rewind(14)
      read(14, '(a24, a6)') label, senname
      read(14, '(a24, f4.1)') label, ro
      read(14, '(a24, i3)') label, imc
      read(14, '(a24, f11.1)') label, sysrsp
      read(14, '(a24, 2f8.1)') label, dark(1), dark(2)
      read(14, '(a24, 2f8.1)') label, shtfac
      read(14, '(a24, 2f8.1)') label, readstd(1), readstd(2)
      read(14, '(a24, 2f8.1)') label, quantstd(1), quantstd(2)
      read(14, '(a24, f8.3)') label, calval
      read(14, '(a24, f8.3)') label, absrad
      do 70 i=1, maxdim
          read(14, '(a24, f7.4)') label, senrsp(i)
70     continue
      close(14)
c
c     Read in feature file and fill up feature matrix
c
      open(unit=15, file="feaset")
      rewind(15)
      read(15, '(a24, i4)') label, numfea
      do 80 m=1, numfea
          read(15, '(a24, i4, i4)') label, feaset(m, 1), feaset(m, 2)
80     continue
      close(15)

```

```

      do 90 m=1,numfea
        do 100 i=1,maxdim
          feamat(m,i)=0.0
          if(i.ge.feaset(m,1).and.i.le.feaset(m,2))
+
            feamat(m,i)=1.0
100      continue
90      continue
c
c
c*****
c
c      SET UP CONVERSION AND SCALING VECTORS
c*****
c
      pi=4.0*atan(1.0)
      do 110 i=1,maxdim
        gcon(i)=0.01*(0.4+(i-1)*0.01)*sysrsp*senrsp(i)*imc
        sigrad(i)=(1.0/pi)*irrad(i,mr,thsun)*trans(i,mr,thvew)
        pthdif(i)=prad1(i,mr,thsun,thvew)-prad0(i,mr,thsun,thvew)
110      continue
c
c      Compute spatial weighting function
c      (Note, assume all bands have same spatial correlation)
c      (IMSL erfc function is 2 times erfc() as defined in thesis,
c      and also needs a division by sqrt(2) to normalize variable)
c      Now implemented scaling of PSF size by view angle in y direction
c
      a = -1.0*alog(rhox)
      b = -1.0*alog(rhoy)
      roa=ro
      rob=ro/cos(((thvew-1)*15.0*pi)/180.0)
      temp=4.0*exp(((a*a+b*b)/2.0)*roa*rob)
      ws=temp*0.5*erfc((a*roa)/sqrt(2.0))*0.5*erfc((b*rob)/sqrt(2.0))
c
c*****
c
c      COMPUTE AVERAGE REFLECTANCE FOR USE IN PATH
c      RADIANCE MODEL
c*****
c
      do 120 i=1,maxdim
        averef(i)=0.0
        do 130 k=1,numcls
          averef(i)=averef(i)+refmean(i,k)
130      continue
        averef(i)=(averef(i)/float(numcls))/100.0
120      continue
      do 140 i=1,maxdim
        do 140 j=1,maxdim
          avecov(i,j)=0.0
          do 150 k=1,numcls
            avecov(i,j)=avecov(i,j)+refcov(i,j,k)
150      continue

```

```

    avecov(i,j)=(avecov(i,j)/float(numcls*numcls))/10000.0
140    continue
c
c*****
c
c    COMPUTE FEATURE SPACE STATISTICS FOR EACH CLASS
c*****
c
c    Loop for all classes                START CLASS LOOP 1
c
c    do 390 k=1,numcls
c
c    Copy reflectance stats to temp files and convert from %
c
c    do 200 i=1,maxdim
c        tmpmean(i)=refmean(i,k)/100.0
c        do 210 j=1,maxdim
c            tmpcov(i,j)=refcov(i,j,k)/10000.0
210        continue
200    continue
c
c    Compute signal mean
c
c    do 220 i=1,maxdim
c        sigmean(i)=gcon(i)*(sigrad(i)*tmpmean(i)+
+           pthdif(i)*averef(i)+prad0(i,mr,thsun,thvew))
c        sigmean(i)=sigmean(i)*(1.0+absrad)
c        if(i.le.irbrk) then
c            sigmean(i)=sigmean(i)+dark(1)
c        else
c            sigmean(i)=sigmean(i)+dark(2)
c        endif
220    continue
c
c    Compute signal covariance
c
c    do 230 i=1,maxdim
c        do 240 j=1,maxdim
c            sigcov(i,j)=tmpcov(i,j)*gcon(i)*gcon(j)*sigrad(i)*
+           sigrad(j)+pthdif(i)*pthdif(j)*avecov(i,j)*
+           gcon(i)*gcon(j)
c            sigcov(i,j)=sigcov(i,j)*(1.0+absrad)*(1.0+absrad)
240        continue
230    continue
c
c    Apply spatial weighting function
c
c    do 250 i=1,maxdim
c        do 260 j=1,maxdim
c            sigcov(i,j)=ws*sigcov(i,j)
260        continue
250    continue
c
c    Compute signal dependent noise standard deviations
c
c    do 270 i=1,maxdim

```



```

do 395 m=1,numfea
  feamean(m,k)=feamean(m,k)/temp
  do 396 n=1,numfea
    feacov(m,n,k)=feacov(m,n,k)/(temp*temp)
396    continue
395    continue
393  continue
c
c                                     BEGIN CLASS LOOP 2
c
do 400 k=1,numcls
do 400 l=1,numcls
  if(l.eq.k) goto 400
  do 410 m=1,numfea
    mxdiff(m)=feamean(m,k)-feamean(m,l)
410    continue
  do 420 m=1,numfea
  do 420 n=1,numfea
    matave(m,n)=(feacov(m,n,k)+feacov(m,n,l))/2.0
    feacovk(m,n)=feacov(m,n,k)
    feacovl(m,n)=feacov(m,n,l)
420    continue
    call lftsf(numfea,feacovk,maxfea,fac,maxfea,ipvt)
    call lfdsf(numfea,fac,maxfea,ipvt,det1,det2)
    detk=det1*10.0**det2
    call lftsf(numfea,feacovl,maxfea,fac,maxfea,ipvt)
    call lfdsf(numfea,fac,maxfea,ipvt,det1,det2)
    detl=det1*10.0**det2
    call lftsf(numfea,matave,maxfea,fac,maxfea,ipvt)
    call lfdsf(numfea,fac,maxfea,ipvt,det1,det2)
    detave=det1*10.0**det2
    call linrg(numfea,matave,maxfea,matinv,maxfea)
    do 430 m=1,numfea
      tmpvec(m)=0.0
    do 440 n=1,numfea
      tmpvec(m)=tmpvec(m)+matinv(m,n)*mxdiff(n)
440    continue
430    continue
    mu=0.0
    do 450 m=1,numfea
      mu=mu+mxdiff(m)*tmpvec(m)
450    continue
    mu=(mu/8.0)+0.5*alog(detave/(sqrt(detk)*sqrt(detl)))
    probcor(k,l)=1.0-0.5*erfc(sqrt(mu))
400    continue
c
c                                     END CLASS LOOP 2
c
c
c*****
c
c    COMPUTE OVERALL PROBABILITY CORRECT
c
c*****
c
c
c    Output results
c

```

```
pcsum=0.0
do 500 k=1,numcls
do 500 l=1,numcls
  if(1.le.k) goto 500
  probcor(k,l)=probcor(k,l)*100.0
  print*,"The Pc of class ",k," and class ",l," was ",
+      probcor(k,l)
  pcsum=pcsum+probcor(k,l)
500  continue
pcsum=100.0-(100.0*((numcls*(numcls-1))/2)-pcsum)
print*,"The overall Pc was ",pcsum
stop
end
```